The University of Nottingham

UNITED KINGDOM · CHINA · MALAYSIA

Investigation of the spiral secretion pattern of the serine protease autotransporter, EspC using innovative fluorescent labelling approaches

---

Mahmoud M. Ashawesh, MSc

Submitted to The University of Nottingham for

the degree of Doctor of Philosophy



July 2016

Declaration

I declare that all the work presented in this thesis is my own, except where otherwise stated. No part has been submitted for the award any degree at the University of Nottingham or any other institute of learning.

M. Ashawesh

July 2016



Publications:

1. Ruparell, A., Dubern, J. F., Ortori, C. A., Harrison, F., Halliday, N. M., Emtage, A., **Ashawesh, M. M.**, Laughton, C. A., Diggle, S. P., Williams, P., Barrett, D. A., and Hardie, K. R. (2016) The fitness burden imposed by synthesising quorum sensing signals. *Scientific reports* **6**, 33101

2. Up close & personal: Pharmacologists' perspectives on the role of imaging technology. *Pharmacology Matters*, Volume **8**, issue 3 - December 2015 (ISSN No: 1757-8175)

Abstract

Enteropathogenic *Escherichia coli* (EPEC) is a diarrheagenic pathogen belonging to the Enterobacteriaceae and considered to be a leading cause of acute infantile diarrhoea in developing nations. During onset of infection, EPEC inject a variety of effector proteins into the host epithelial cells using the type III secretion system (T3SS). These effectors are encoded within the pathogenicity island (PAI) called the locus of enterocyte effacement (LEE). EPEC also secretes the non-LEE encoded serine protease EspC (**E**PEC **s**ecreted **p**rotein **C**) into the extracellular milieu. This autotransporter (AT) exits EPEC through a type V secretion system (T5SS) and is subsequently delivered into host cells by the T3SS. The precise steps by which EspC is secreted are still unknown. By using both traditional and advanced optical microscopes, it is shown here that EspC tagged with two different fluorescent labels locates to a structure that resembles the spiral bacterial cytoskeleton when it has its β-barrel domain attached. It was discounted that the spiral formation was an artefact of aggregation. Moreover, production of another AT (AaaA, derived from *Pseudomonas aeruginosa*) also generated spiral structures that resemble the ones observed with EspC. Perturbing the structure of the bacterial cytoskeleton actin homologue MreB with the *S*-(3,4-dichlorobenzyl) isothiourea compound (A22) disrupted the localization of EspC-mCherry. Furthermore, producing EspC-mCherry in an *E. coli* SecA mutant generated altered localization patterns. Collectively, these results indicate that the spiral localization of EspC is dependent upon its C-terminal β-barrel domain, the Sec translocon and the actin homologue MreB and this spiral secretion pathway seems to be conserved among ATs. Further analysis is required to reveal the molecular mechanism underlying spiral formation to unravel the mystery of AT secretion, thereby enabling the development of new therapeutic targets and treatments.

Acknowledgements

Foremost, I would like to take this opportunity to express my sincere gratitude to my supervisors Dr Kim R. Hardie and Dr Christopher Penfold for all continues support, excellent guidance and motivation during my PhD study. It is an honour to be my supervisors over the past four years. My deepest appreciation to Prof Miguel Camara for his kindest compliments and for the viva processes. Many thanks must also go to Dr James Lazenby who helped me to settle in during my arriving, Kathrin Boyle for showing me how to use the confocal microscope and Daniella Spencer for her assistance with carrying out the activity assay.

Thanks to Dr Robert Markus who run the super resolution microscope facility and helped me to process images and videos. Thanks to Dr Manuel Romero, Dr Muhammed Ehsaan and Dr Felix Dafhnis-Calas for their assistance with cloning at the beginning of my study. I would also like to thank my best friend and colleague Osman Dufailu for his generosity and hospitality. I hope that I have not forgotten someone, but thank you all my friends and colleagues for your encouragements and co-operation.

Special thanks to the School of Life Sciences for the unlimited support especially during the last two years of my study. Many thanks to Miss Leanne Mitchell (Postgraduate research student officer) who assisted me with the countless number of problems that faced me throughout my study, I do really appreciate her support and patience. The acknowledgement is also directed to my Libyan sponsor; the ministry of higher education and scientific research as well as to the Libyan Cultural Attache' in London.

Lastly, I would like to thank my family especially my father Prof Muhammed Ashawesh for his moral and financial supports during my studies here in UK and my sister Dr Hind Ashawesh for being such a supportive. A bouquet of roses must give to my wife "Ranim Kabbasa" who was always there cheering me up and stood by me through the good and bad times. Hats off to my daughters "Lugien and Layla" who gave me the strength and kept me going to finish this. Thousands of thanks to all of you‼

This Thesis is in dedication of the loving memory of my mother

Layla A. Kabbasa (1954-2001)

List of Contents

Page

Declaration i

Publications ii

Abstract iii

Acknowledgements iv

Dedication v

List of Contents vi

List of Figures xi

List of Tables xv

Abbreviations xvi

CHAPTER 1: Introduction 1

1.1 The commensal *Escherichia coli* (*E. coli*): the relationship that turned upside down! 2

1.2 History of EPEC disease 3

1.2.1 EPEC O127:H6 strain E2348/69 4

1.2.2 The attaching and effacing (A/E) lesion: a hallmark of EPEC infection 4

1.2.3 EPEC effector proteins and virulence factors: the attacking weapons! 7

1.2.4 The complex network behind LEE gene regulation 13

1.2.4.1 LEE-encoded regulators 13

1.2.4.2 Non-LEE-encoded regulators 14

1.2.4.3 *E. coli* global regulators 14

1.2.4.4 Environmental factors and quorum sensing 15

1.3 Autotransporters (ATs) in EPEC 16

1.3.1 The serine protease AT, EspC 16

1.3.1.1 The EspC journey; an autotransporter trip across membranes 20

1.4 Arginine-specific AT of *P. aeruginosa* (AaaA) 44

1.5 Localization patterns of AT secretion 44

1.5.1 Polar localization 45

1.5.2 Spiral localization 47

1.5.2.1 The bacterial cytoskeleton actin homologue, MreB 47
1.5.2.2 The bacterial IM Sec machinery 51
1.6 The pitfalls of fluorescent protein fusions 52
1.7 Main hypothesis and aims of this study 54
CHAPTER 2: Materials and Methods 56
2.1 General chemicals 57
2.2 Growth media 57
2.2.1 Luria Bertani (LB) media 57
2.2.2 Minimal Media P (MMP) 57
2.3 Antibiotics and gene expression 57
2.4 Growth and induction conditions 58
2.5 Bacterial strains 59
2.6 Plasmids 60
2.7 DNA Preparation, manipulation and analysis 64
2.7.1 Extraction of plasmid DNA 64
2.7.2 Quantifying DNA concentrations 64
2.7.3 Restriction enzyme digestion of DNA 64
2.7.4 Analysis and purification of DNA by agarose gel electrophoresis 65
2.7.5 Molecular weight marker 66
2.7.6 DNA ligation reactions 67
2.8 Polymerase Chain Reaction (PCR) amplification 67
2.8.1 Synthesis of oligonucleotide primers 67
2.8.2 PCR amplification 74
2.8.2.1 Conventional PCR 74
2.8.2.2 Site-directed mutagenesis PCR 74
2.9 DNA sequencing 76
2.10 Transformation 77
2.10.1 Preparation of chemically competent *E. coli* cells 77
2.10.2 Heat chock transformation 78
2.10.3 Heat chock transformation using the commercial provided Top10 *E. coli* cells 78
2.11 Protein sample preparation and analysis 79

2.11.1 *E. coli* whole cell protein preparation 79

2.11.2 *E. coli* secreted protein preparation 79

2.11.3 SDS-PAGE gel preparation 80

2.11.4 Western Blot 81

2.12 Cell fractionation 82

2.12.1 Cell fractionation using the protocol described for *P. aeruginosa* 82

2.12.2 Sucrose gradient fractionation 82

2.13 Trypsin assay 84

2.14 Arginine - *p* - nitroanalide assay 84

2.15 The *S*-(3.4-Dichlorobenzyl)-isothiourea (A22) 85

2.16 Expression of amber encoded recombinant proteins 86

2.17 Flow cytometry analysis 87

2.18 FlAsH labeling tetracysteine-tagged recombinant proteins 87

2.19 Confocal fluorescence microscope, fluorescent dyes and imaging study 88

2.20 Fluorescence recovery after photobleaching (FRAP) experiment 90

2.21 Super resolution microscope 90

CHAPTER 3: Investigating the localization of EspC using the monomeric red fluorescent protein (mCherry) as a tag in EPEC and *E. coli* K-12 92

3.1 Introduction 93

3.2 Results 96

3.2.1 Fusion of mCherry to EspC passenger domain in the presence and absence of the C-terminal transporter domain 96

3.2.2 EspC-mCherry is constitutively produced in a stable form 98

3.2.2.1 Construction of pMAC33 vector encoding EspC-mCherry from the lower copy number plasmid with the aim to prolong the production of a detectable fluorescent signal 98

3.2.2.2 Constructing pLA33mCherry vector encoding mCherry from pBAD33 101

3.2.3 As predicted, introduction of a stop codon decreases the observed molecular weight of EspC-mCherry indicative of a truncation that removes the transporter domain 103

3.2.4 EspC-mCherry locates to a spiral structure that resembles the bacterial cytoskeleton when it has the β-barrel domain attached. 105

3.2.5 EspC-mCherry forms spirals during the first hour of production, localizes to the bacterial outer membrane and presents in the culture supernatant 111

3.2.6 The spiral localization pattern of EspC-mCherry was missing in the parental EPECΔ*espC* strain E2348/69 119

3.2.7 Sucrose gradient analysis confirms that the EspC spiral formation is unlikely to be an artefact of aggregation 123

3.3 Discussion 127

CHAPTER 4: Localization of EspC is dependent upon its C-terminal β-barrel, the bacterial cytoskeleton actin homologue MreB, and the Sec translocon 133

4.1 Introduction 134

4.2 Results 136

4.2.1 Investigating the localization of the bacterial actin homologue MreB and its role in EspC secretion in *E. coli* 136

4.2.1.1 Cloning strategy used to construct pLA33mreBmc vector 136

4.2.1.2 MreB protein localizes in discrete patches with filaments that are short and cross the cells diagonally 141

4.2.1.3 Perturbing the actin homologue cytoskeleton MreB with A22 altered the localization of EspC-mCherry 144

4.2.2 Strains producing EspC with or without mCherry have cell wall defects and production of the 174 kDa EspC-mCherry makes cells bigger 156

4.2.3 Altering the serine protease motif of overproduced EspC did not repair the observed growth defect 173

4.2.4 Inactivation of the motor protein SecA alters the localization of EspC-mCherry 175

4.3 Discussion 180

CHAPTER 5: Can EspC be visualized with a single amino acid tag inserted using Amber suppression combined with click chemistry 188

5.1 Introduction 189

5.2 Results 193

5.2.1 Identification of optimal positions in *espC* to insert the amber stop codon (TAG) by SDM 193

5.2.1.1 Generation of a truncated version of EspC without the β-barrel domain via genetically encoded amber stop codon for UAA incorporation 193

5.2.2 Incorporation of N^{ε}-acetyllysine UAA into EspC using the *M. barkeri* *Mb*tRNA$_{CUA}$/*Mb*PylRSΔ pair 198

5.2.2.1 Cloning strategy used to insert EspC^{TAG533} and EspC^{TAG951} into p*Myo*4TAGPylT-his$_6$ vector 198

5.2.2.2 Inability to incorporate N^{ε}-acetyllysine into amber codons 200

5.2.3 Incorporation of TCOstar UAA into EspC using the *M. mazei* *Mm*tRNA$_{CUA}$/*Mm*PylRS^{AF} gene pair 204

5.2.3.1 Substitution of *M. barkeri* MS *pylS* gene in the pBKPylS vector for *M. mazei pylS* (*Mm*PylRS^{WT}) 207

5.2.3.2 Optimisation of the *M. barkeri* amber suppressor tRNA (*Mb*tRNA$_{CUA}$) to enable TCOstar incorporation efficiency with *Mm*PylRS^{AF} 210

5.2.3.3 Inability to incorporate TCOstar using *Mm*PylRS^{AF} and PylT$_m$ 210

5.2.4 Unexpectedly, N^{ε}-Boc-L-Lysine was successfully incorporated into EspC and myoglobin 211

5.3 Discussion 214

CHAPTER 6: The helical distribution of EspC is observed via the small tetracysteine tag technology, and shared by a different AT, AaaA 219

6.1 Introduction 220

6.2 Results 223

6.2.1 Labelling MreB and EspC with membrane-permeable FlAsH-EDT$_2$ 223

6.2.1.1 The TC-tag (CCPGCC) was incorporated into MreB and EspC efficiently 223

6.2.1.2 EspC is distributed in a spiral, patchy structure seen encircling cells in super-resolution microscope 226

6.2.2 The spiral localization of EspC is shared by the AT AaaA 234

6.2.2.1 Cloning strategy used to insert *aaaA* into pBAD33 vector 234

6.2.2.2 AaaA forms patchy helices resembling the EspC AT, but appears very bright 236

6.2.2.3 Substitution of cysteine for serine at position 233 in AaaA abolished the fluorescent signal 242

6.2.2.4 Super-resolution imaging of TC-tagged AaaA revealed the similarity of localization with EspC 243

6.2.3 FlAsH labelling of TC-tagged AaaA lacking the β-barrel domain shows distinct localization 246

6.2.3.1 Generation of a truncated version of TC-tagged AaaA without the C-terminal β-barrel domain 246

6.2.3.2 Truncated FlAsH-tagged AaaA without the β-barrel domain assumed a bulky spotty localization, and appeared to lack the helical organization 247

6.2.3.3 All forms of AaaA are active and detectable by immunoblotting 251

6.2.3.4 Overproduction of AaaA causes a significant reduction in the bacterial growth 257

6.2.4 EspC-mCherry fusion detects that the spiral structure is dynamic, but the FlAsH tagged AaaA control does not 259

6.3 Discussion 262

CHAPTER 7: Final conclusions and further directions 271

References 281

List of Figures

Page

Figure 1.1: Electron microscopy image of the hallmark A/E lesion of EPEC infection in intestinal epithelial tissue 6

Figure 1.2: Schematic representation of important virulence genes and their organization within EPEC strain E2348/69 8

Figure 1.3: Schematic overview of the EPEC T3SS apparatus 10

Figure 1.4: Schematic representation of the secretion systems in Gram-negative bacteria 22

Figure 1.5: The archetypical structure of autotransporters showing the main domains . 24

Figure 1.6: Schematic representation of the various sub-classes of the T5SS 26

Figure 1.7: Mechanistic models of passenger domain translocation across the OM 41

Figure 1.8: Schematic overview of the MreB interaction with PGEM in *E. coli*. 49

Figure 2.1: 1 kb DNA ladder visualized by SYBR® Safe DNA Gel Stain on 0.8% 1x TAE agarose gel transferred at 100V 66

Figure 3.1: Schematic of the cloning strategy for inserting mCherry into the EspC passenger domain 97

Figure 3.2: Confirmation of the genetic composition of plasmids encoding EspC-mCherry fusions 97

Figure 3.3: The cloning strategy of pMAC33 100

Figure 3.4: The cloning strategy of pLA33mCherry 102

Figure 3.5: Size verification of different versions of EspC 104

Figure 3.6: EspC-mCherry localizes to a helix unless the transporter domain is absent. 106

Figure 3.7: Formation of a spiral structure in *E. coli* producing EspC-mCherry from the plasmid pLA33C1mc 108

Figure 3.8: An extended helix is observed in *E. coli* expressing the full length EspC-mCherry 109

Figure 3.9: The Full length EspC-mCherry localizes as discrete patches in helical arrays 110

Figure 3.10: Truncated EspC-mCherry protein (lacking the β-barrel) is distributed in a diffuse and punctate pattern whilst the full length EspC-mCherry protein localizes to a spiral 114

Figure 3.11: Both full length and truncated EspC-mCherry are released into culture supernatants 116

Figure 3.12: Production of truncated EspC-mCherry reduces cell growth 116

Figure 3.13: Expression of the truncated EspC-mCherry causes severe growth defects in MG1655 strain compared to EPECΔ*espC* 116

Figure 3.14: Exogenously added trypsin degrades both forms of EspC in the *E. coli* MG1655 laboratory strain 118

Figure 3.15: Exogenously added trypsin did not degrade the cytoplasmic IscS protein in the control *E. coli* strain 118

Figure 3.16: Exogenous addition of trypsin degrades both forms of EspC-mCherry in the homologue *E. coli* EPECΔ*espc* strain 120

Figure 3.17: Truncated EspC-mCherry (lacking the β-barrel) causes notable growth defect in EPECΔ*espC* strain when the culture is immediately induced and is mainly distributed in a diffuse with some polar and few puncta 121

Figure 3.18: The full length EspC-mCherry protein localizes to patchy patterns during the first hour of induction in EPECΔ*espC* 122

Figure 3.19: The spiral localization of the full length EspC-mCherry was clearly observed at lower protein concentrations 124

Figure 3.20: Both versions of EspC-mCherry are associated with the bacterial outer membrane 126

Figure 4.1: The cloning strategy to fuse mCherry with MreB 139

Figure 4.2: The location of the amino acid selected for mutagenesis in the predicted MreB crystallographic structure 140

Figure 4.3: Production of MreB-mCherry protein in *E. coli* MG1655 142

Figure 4.4: The fluorescent localization patterns of MreB-mCherry observed over time in *E. coli* MG1655 strain 143

Figure 4.5: A22 causes bacterial cell shape changes 146

Figure 4.6: A22 alters the localization of EspC-mCherry with and without the β-barrel domain 147

Figure 4.7: Effects of A22 concentrations on full length EspC-mCherry localization 148

Figure 4.8: A22 perturbs the growth of MG1655 strains in a dose-dependent fashion 150

Figure 4.9: Full length EspC-mCherry does not form spirals in A22 treated MG1655, and some cells take up SYTOX® blue 151

Figure 4.10: Truncated EspC-mCherry localizes in a punctate pattern in A22 treated MG1655, and the majority of cells take up SYTOX® blue 152

Figure 4.11: Truncated EspC-mCherry associates with membranes in two different forms 154

Figure 4.12: Both forms of truncated EspC retain mCherry, with the larger form predominantly found in high A22 concentrations 155

Figure 4.13: Secretion of EspC-mcherry with and without the C-terminal transporter domain alters cell shape and integrity 157

Figure 4.14: 0.02% arabinose is the optimal arabinose concentration for the full length EspC-mcherry production to minimise cell integrity loss 159

Figure 4.15: 0.02% arabinose is the optimal arabinose concentration for truncated EspC-mCherry production with minimal loss in cell integrity 160

Figure 4.16: Switching the arabinose concentration from 0.2% to 0.02% in both MG1655 (pMAC33) and MG1655 (pLA33C1mc) did not dramatically improve growth 161

Figure 4.17: Construction of pMAO33 to generate truncated EspC lacking mCherry ... 163

Figure 4.18: 1% SDS reduces the viability of MG1655 producing EspC with or without mCherry or the β-barrel ... 163

Figure 4.19: Production of the full length 174 kDa EspC-mCherry makes cells larger . 167

Figure 4.20: Truncated EspC with or without mCherry release IM, OM and cytoplasmic proteins into the culture supernatant ... 168

Figure 4.21: MG1655 producing truncated EspC with or without mCherry generates small rounded structures visible by staining with the lipophilic fluorescent membrane dye, FM 1-43 ... 171

Figure 4.22: A22 reduces the release of outer membrane containing blebs from MG1655 (pMAC33) ... 172

Figure 4.23: No improvement in the growth during overproduction of the EspC serine protease mutant ... 174

Figure 4.24: EspC-mCherry is not found in culture supernatants of an *E. coli* SecA mutant ... 176

Figure 4.25: In *E. coli*Δ*SecA* the full length EspC-mCherry localization becomes predominantly bipolar whilst truncated EspC-mCherry is unipolar ... 178

Figure 4.26: Changing the cell shape by A22 did not alter the localization of EspC-mCherry produced from *E. coli* SecA mutant strains ... 179

Figure 5.1: The positions selected for UAA insertion mapped onto the EspC passenger domain ... 194

Figure 5.2: Production of short versions of EspC protein in *E. coli* MG1655 ... 196

Figure 5.3: Loss of the β-barrel domain in the newly generated EspC mutants causes reduced growth similar to those observed previously ... 197

Figure 5.4: The plasmids bearing the orthogonal amber suppressor $tRNA_{CUA}$/pyrrolysyl-tRNA synthetase mutant (*Mb*$tRNA_{CUA}$/*Mb*PylRSΔ) pair from *M. barkeri* received from the MRC Laboratory of Molecular Biology, UK ... 199

Figure 5.5: The cloning strategy used to replace myoglobin-His_6 encoding ORF with amber containing *espC* ... 201

Figure 5.6: Incorporation of N^{ε}-acetyllysine into EspC and Myoglobin-His_6 was initially unsuccessful ... 203

Figure 5.7: Sequence alignment of the pyrrolysyl-tRNA synthetase (PylRS) and the amber suppressor $tRNA_{CUA}$ from *M. barkeri* MS and *M. mazei* Go1 strains ... 206

Figure 5.8: Cloning strategy to replace the *Mb*$PylRS^{WT}$ in pBKPylS by the *Mm*PylRS hosting two mutations (Y306A and Y384F) to generate pBKPylS^{AF} vector ... 209

Figure 5.9: Incorporation of N^{ε}-Boc-L-Lysine into EspC and Myoglobin-His_6 ... 213

Figure 5.10: Schematic representation shows the predictive expression scenarios of *myo-espC* fusion containing amber codons upon N^{ε}-Boc-L-Lysine incorporation ... 217

Figure 6.1: The position selected for CCGKCC motif insertion on the predicted native EspC passenger domain structure ... 225

Figure 6.2: Detection of a helical patchy arrangement of TC-tagged MreB during FlAsH staining ... 227

Figure 6.3: Detection of bright spiral localization signals of FlAsH-tagged MreB and EspC hosting the optimal TC motif (CCPGCC) 229

Figure 6.4: EspC forms a spiral structure resembling the bacterial cytoskeleton actin homologue MreB 230

Figure 6.5: 3D rendering of structured illumination images reveal the spiral localization of FlAsH labelled TC-tagged EspC inside the living bacterium 232

Figure 6.6: High precision dSTORM image of FlAsH-tagged MreB reveals similar patchy distribution to EspC-mCherry fusion in MG1655 233

Figure 6.7: Cloning strategy adopted for construction of pLA33aaaA 235

Figure 6.8: Position of the optimal TC-tag insertion on the AaaA passenger domain structure 237

Figure 6.9: FlAsH-stained AaaA-TC AT adopts a bright helical patchy configuration 239

Figure 6.10: TC-tagged AaaA localizes as an extended helix in *E. coli* 240

Figure 6.11: AaaA distributes in patches in elongated cells when expressed during extended times 241

Figure 6.12: Replacement of the cysteine residue with serine at position 233 in AaaA leads to remarkable loss in background FlAsH signals 244

Figure 6.13: 3D rendering of structured illumination images reveal the spiral localization of FlAsH labelled AaaA-TC inside the living bacterium 245

Figure 6.14: Cells expressing FlAsH stained truncated AaaA-TC display a dense random distribution of fluorescent spots with no structured helical arrangement 248

Figure 6.15: An absence of the extended helix during production of TC-tagged AaaA lacking the β-barrel domain in MG1655 249

Figure 6.16: Inconsistent spotty distribution of FlAsH labelled truncated AaaA-TC at bacterial membranes appears bulky and lacking the helical organisation 250

Figure 6.17: All AaaA versions produce full length protein except for the truncated AaaA 252

Figure 6.18: All AaaA forms release arginine form the substrate 255

Figure 6.19: Truncated AaaA is active but was delayed and did not achieve the maximum activity compared with the full length AaaA forms during 24 h of incubation. 256

Figure 6.20: High doses of arabinose suppress the growth in cells producing AaaA 258

Figure 6.21: Fluorescence recovery after photobleaching reveals the dynamic nature of the molecules of EspC in patches 261

Figure 7.1: Schematic presentation of the AT secretion pathway and the prediction of possible targets for novel antimicrobials 280

List of Tables

Page

Table 1.1: AT encoding genes detected in EPEC 17

Table 1.2: Overview of the diversity of ATs, sub-categorized into five systems and their proposed role in virulence.....29

Table 2.1: Bacterial strains used in this study 59

Table 2.2: Plasmids used in this study.....63

Table 2.3: Standard recipes for agarose gel electrophoresis. 1x TAE was stored at RT..65

Table 2.4: Oligonucleotide primers used in this study.....74

Table 2.5: Routine PCR mixture and cycling parameters utilized in this study.....75

Table 2.6: SDM PCR mixture and cycling parameters used in this study 76

Table 2.7: The recipes for preparing stacking and separating gels used in this study....80

Table 2.8: Rabbit primary antibodies used in this study.....82

Table 2.9: Fluorescence spectra of fluorophores used in this study 90

Table 6.1: The advantages and disadvantages of FlAsH-tag technology.....221

Abbreviations

%	percentage
% (w/v)	percentage weight per volume
% (v/v)	percentage volume per volume
AT	autotransporter
AaaA	arginine-specific autotransporter of *P. aeruginosa*
aa	amino acid
APS	ammonium persulphate
ATP	adenosine triphosphate
ATPase	adenosine triphosphatase
Amp	ampicillin
A22	S-(3,4-dichlorobenzyl) isothiourea
BAM	β-barrel-assembly machinery
bp	base pair
BAL	British anti-Lewisite
$^{\circ}$C	degrees Celsius
Cm	chloramphenicol
$CaCl_2$	calcium chloride
CL	cardiolipin
dNTP	deoxynucleotide triphosphate
DNA	deoxyribonucleic acid
DNase	deoxyribonuclease
DTT	dithiothreitol
dH_2O	distilled water
DsRed	*Discosoma* sp. Red fluorescent protein
dSTORM	direct stochastic optical reconstruction microscopy
DMSO	dimethyl sulfoxide
DAPI	4',6-diamidino-2-phenylindole
DIC	differential interference contrast

EDT	1,2-ethanedithiol
ECL	enhanced chemiluminescence
EDTA	ethylenediaminetetraacetic acid
EspC	EPEC secreted protein C
ESPR	extended signal peptide region
FlAsH	fluorescein arsenical hairpin binder
$FeSO_4$	ferrous sulphate
Fig.	figure
GTP	guanosine triphosphate
GTPase	guanosine triphosphatase
GFP	green fluorescent protein
g	gram
HRP	horseradish peroxidase
HEPES	4-(2-hydroxyethyl)-1-piperazineethanesulfonic acid
HCl	hydrochloric acid
H_2O	water
HEp-2	human epithelial cell line 2
h	hour
IgA	immunoglobulin A
IgG	immunoglobulin G
IPTG	isopropylthio-β-D-galacto-pyranoside
IM	inner membrane
KH_2PO_4	monopotassium phosphate
kb	kilobase
Km	kanamycin
kDa	kilodalton
L	litre
LPS	lipopolysaccharides
LB	luria Bertani
M	molar

mM	millimolar
µM	micromolar
µm	micrometre
mg	milligram
µg	microgram
ml	millilitre
µl	microlitre
min	minute
ms	millisecond
mA	milliampere
MMP	minimal medium P
$MgSO_4$	magnesium sulphate
MeOH	methanol
myo	myoglobin gene
nm	nanometre
ng	nanogram
NaCl	sodium chloride
Na_2HPO_4	disodium phosphate
O/N	overnight
OD	optical density
OMP	outer membrane protein
OM	outer membrane
ORF	open reading frame
PAI	pathogenicity island
PBS	phosphate buffered saline
PBST	phosphate buffered saline 0.5% (v/v) Tween-20
psi or lb/in^2	pounds per square inch (pressure unit)
PCR	polymerase chain reaction
FACS	fluorescence-activated cell sorting
pfu	*Pyrococcus furiosus*

POTRA	polypeptide transport-associated
QMC	Queen's Medical Centre
RT	room temperature
ReAsH	resorufin arsenical hairpin binder
rpm	revolutions per minute
RNA	ribonucleic acid
RNase	ribonuclease
S/N	supernatant
SDS	sodium dodecyl sulphate
SDS-PAGE	sodium dodecyl sulphate polyacrylamide gel
SR-SIM	super resolution- structured illumination microscopy
SIM	structured illumination microscopy
SDM	site-directed mutagenesis
SOC	super optimal broth with catabolite repression
SPATE	serine protease AT of Enterobacteriaceae
SRP	signal recognition particle
Str	streptomycin
TC	tetracysteine motif
Tc	tetracycline
tRNA	transfer RNA
TAE	tris-acetate-EDTA
TCA	trichloroacetic acid
TEMED	tetramethylethylenediamine
Tris	tris hydroxymethyl aminomethane
TAM	translocation and assembly module
TPase	transpeptidae
T1SS	type 1 secretion system
T2SS	type 2 secretion system
T3SS	type 3 secretion system
T4SS	type 4 secretion system

T5SS	type 5 secretion system
T6SS	type 6 secretion system
T7SS	type 7 secretion system
T8SS	type 8 secretion system
T9SS	type 9 secretion system
UV	ultraviolet
UAA	unnatural amino acid
V	volts
WC or wc	whole cell
WT or wt	wild type

Chapter 1

Introduction

1.1 The commensal *Escherichia coli* (*E. coli*): the relationship that turned upside down!

E. coli is a rod-shaped, Gram-negative bacterium discovered in 1885 (1). The genus *Escherichia* is a division of gamma Proteobacteria belonging to the family Enterobacteriaceae. It is a facultative anaerobic commensal colonising the gastrointestinal tract in warm-blooded organisms thereby forming part of the normal flora of the host gut (2). However, because the *E. coli* genome is highly dynamic, acquisition of virulence genes as pathogenicity islands (PAI), prophages and/or plasmids by horizontal gene transfer from pathogenic strains promotes strain diversification and establishment of many potential pathogens of humans and animals (3,4).

In humans, pathogenic *E. coli* strains cause diarrheagenic (enteric) or extra-intestinal infections. The extraintestinal pathogenic *E. coli* (ExPEC) strains involved in the extraintestinal disease include sepsis-associated *E. coli* (SEPEC), neonatal meningitis *E. coli* (NMEC) and uropathogenic *E. coli* (UPEC) (5,6). The diarrheagenic *E. coli* have been classified into eight categories of pathotypes based on their mechanisms of pathogenicity; enteropathogenic *E. coli* (EPEC), enteroaggregative *E. coli* (EAEC), enterotoxigenic *E. coli* (ETEC), enterohemorrhagic *E. coli* (EHEC), enteroinvasive *E. coli* (EIEC), diffuse adherent *E. coli* (DAEC), adherent invasive *E. coli* (AIEC) and the Shiga Toxin (Stx) producing enteroaggregative *E. coli* (STEAEC) (2,5,7,8).

1.2 History of EPEC disease

EPEC was the first pathovar of *E. coli* to be associated with diarrhoeal illnesses (4). In the 17th century, infantile summer diarrhoea disease was very serious. Very high mortality rates were recorded that decimated the nonbreast-fed infant population due to a contaminated supply of cow's milk (9,10). Summer diarrhoea (also termed cholera infanturn) persisted for decades in Europe and the USA. The diarrhoea was characterized by severe gastroenteritis followed by death within hours. In the period between 1667 and 1720, the disease killed around 328,231 infants in London, which is more than 6000 deaths per year (9). In the 1940s, John Bary, first established the association of *Bacterium coli* or, as it is now known, *E. coli*, with infantile summer diarrhoea. Subsequently, the term EPEC was used to describe the causative strains of infantile diarrhoea (7,9).

It was believed that EPEC strains responsible for infantile diarrhoea belong to a limited set of O serogroups. However, a particular O:H serotype was found associated with virulence (9). In the 1990s, these EPEC strains were classified based on the absence or presence of the EPEC adherence factor (EAF) plasmid into atypical EPEC (aEPEC) and typical EPEC (tEPEC) respectively (11). Furthermore, to determine how tEPEC evolved, tEPEC strains were further classified into four different lineages designated EPEC1 to EPEC4 (12). Despite tEPEC having been considered as the main cause of acute infantile diarrhoea in developing countries for many years, aEPEC were found to be more prevalent than tEPEC in both developing and developed countries (13).

1.2.1 EPEC O127:H6 strain E2348/69

Doubts about the pathogenicity of EPEC strains were increased in the 1960s and 1970s due to their inability to secrete diffusible toxins or to invade host epithelial cells (4,14). However, in the late 1970s, a study conducted by Levine and her colleagues showed that feeding EPEC strain E2348/69 (serotype O127:H6 isolated from the outbreak of infantile diarrhoea in Taunton, UK in 1969) to adult volunteers caused diarrhoea indicating that E2348/69 pathogenesis may be independent of enterotoxins (4,15). Since this experiment, E2348/69 became the prototype strain used worldwide to study EPEC pathogenicity and genetics (4). E2348/69 is a tEPEC strain belonging to EPEC lineage 1 and to the B2 phylogroup that encompasses very simple T3SS and small effector repertoire making them a potential to fully dissect the whole virulence strategy of diarrheagenic pathogens in the genomic context (4).

1.2.2 The attaching and effacing (A/E) lesion: a hallmark of EPEC infection

During the onset of infection, EPEC colonise the small bowel and cause the formation of a characteristic histo-pathological feature on host intestinal epithelial cells termed attaching and effacing (A/E) lesions (Fig. 1.1) (16,17). A/E lesions are manifested by loss of microvilli, marked cytoskeletal changes and development of a cuplike pedestal underneath the intimately attached bacteria due to the induction of actin polymerisation (18-20). All the necessary genes required for the

formation A/E lesions are found encoded within a 35.6 kilobase (kb) PAI termed the locus of enterocyte effacement (LEE) (21,22). The ability to cause A/E lesions is dependent on the LEE as McDaniel *et al.,* 1997 found that cloning the LEE of EPEC strain E2348/69 into an avirulent *E. coli* strain conferred the recipient strain with the ability to cause infection and form A/E lesions (23). Other members of closely related pathogens were also shown to encode LEE and cause A/E lesions including enterohaemorrhagic *E. coli* (EHEC) and the animal pathogens such as *Citrobacter rodentium* (which infects mice) and rabbit EPEC (REPEC) (16). Interestingly, the LEE has a GC content of 38.4% which is considerably lower than that of the commensal *E. coli* chromosome (50.8%), suggesting that the LEE region was originally acquired by horizontal gene transfer from another A/E pathogenic species (16,17,24). Indeed, the evolution of EPEC seems to be a dynamic process requiring repeated acquisition of the LEE PAI and transmission of the plasmid, pEAF (12).

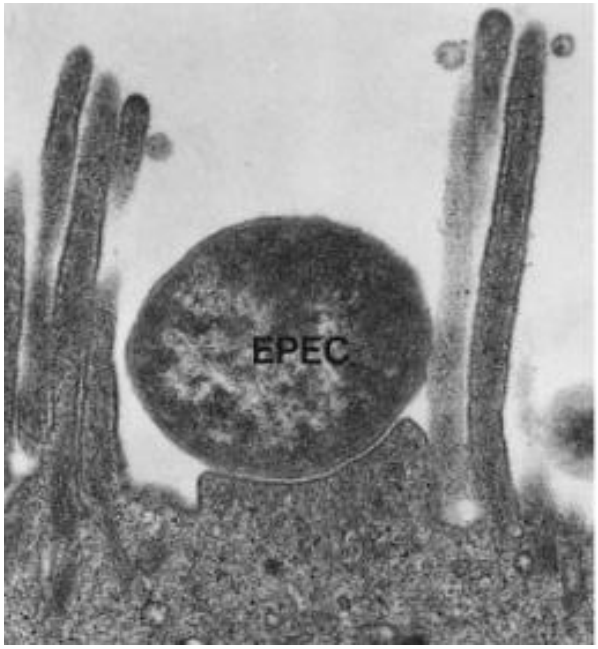


Figure 1.1: Electron microscopy image of the hallmark A/E lesion of EPEC infection in intestinal epithelial tissue. A/E lesions are characterized by disruption of intestinal cytoskeleton, membrane vesiculation, loss of absorptive microvilli and formation of a cuplike pedestal for intimate bacterial adhesion at the cell membrane. This figure was taken from Frankel *et al.*, 1998 (17).

1.2.3 EPEC effector proteins and virulence factors: the attacking weapons!

To cause A/E lesions, EPEC needs to secrete effector molecules and deliver them into host epithelial cells. This is achieved using a type III secretion system (T3SS) which is encoded by LEE genes (17,25,26). Within this genetic locus there are genes encoding; (i) T3SS machinery Sep (secretion of *E. coli* proteins) and Esc (*E. coli* secretion) components (25), (ii) EPEC-secreted proteins (Esp) such as the translocators EspA (27), EspD (28) and EspB (29), (iii) a variety of effector proteins, for example, EspF (30), EspG (31) and Map (32), (vi) chaperones such as Ces (chaperone for *E. coli* secreted proteins), (v) regulatory proteins, and (vi) an the intimin protein and its translocated intimin receptor (Tir) (11,24,33). In addition, EPEC delivers another 110 kDa protein to host cells which is not encoded within the LEE island. This EPEC-secreted protein C (EspC) is secreted into the extracellular milieu via the type V secretion system (T5SS) and then delivered into target host cell by the T3SS translocon (34,35). Interestingly, this protein is encoded by a second unique pathogenicity island called *espC* PAI (26,35,36). Other non-LEE encoded effector (nle) genes are also found in EPEC E2348/69 clustered in numerous pathogenicity islands which have been shown to have a role in virulence (4,37).

LEE contains 41 open reading frames (ORFs) arranged in at least five polycistronic operons (LEE1 to LEE5) as well as other shorter transcriptional units. (Fig. 1.2) (25,33,38). Briefly, LEE1, LEE2 and LEE3 operons encode T3SS components as well as a global regulator called

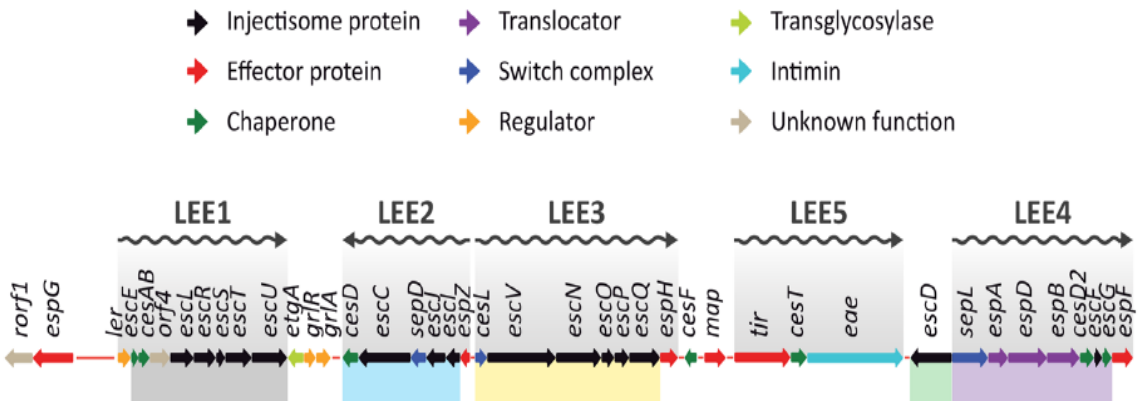


Figure 1.2: Schematic representation of important virulence genes and their organization within EPEC strain E2348/69. The chromosomally located LEE PAI that is arranged in at least five polycistronic operons (LEE1 to LEE5) plus other shorter transcriptional units. The 41 genes with the most known functions are specified with the colour code shown above the LEE. This figure was taken from Ruano-Gallego *et al*., 2015 (38).

LEE-encoded regulator (Ler). The fourth operon (LEE4) encodes the Esp proteins; EspA, EspB, EspD and EscF that are considered to encode the main T3SS apparatus by which bacterial proteins can translocate across the inner membrane (IM) and outer membrane (OM) and be delivered to the host cell cytosol or plasma membrane (depending on protein function) during cell contact (35). The last operon (LEE5) encodes Tir, Tir-chaperones CesT and intimin (25,35). In addition to the effector protein EspG (called EspG1) being encoded within LEE region, another EspG homolog, Orf3 (designated as EspG2) was found located in the *espC* PAI, suggesting the existence of a set of related effectors targeting the host cytoskeleton (31,39-41).

The T3SS plays an important role in pathogenicity of EPEC (16) and other enteric Gram-negative pathogens (42) by injecting virulence factors directly from the bacterial cytoplasm to the host cytosol (Fig. 1.3) (43). The hydrophilic translocator EspA protein polymerizes into a filamentous structure to form a surface appendage (a needle-like structure) with an internal pore linking the bacteria with its target cell (17,27). A study conducted by Luo *et al*., 2011, demonstrated that the creation of this linking translocation pore in the host plasma membrane is dependent on the interaction between two hydrophobic EspB and EspD translocators, in a process that occurs after bacterial attachment. Furthermore, this research also revealed a direct interaction between hydrophobic EspD and the hydrophilic translocator protein, EspA, providing greater definition of the function of EspB (44). EspD appears to have a role in EspA appendage elongation because a deletion mutant in *espD* reduced EspA appendage elongation and prevented

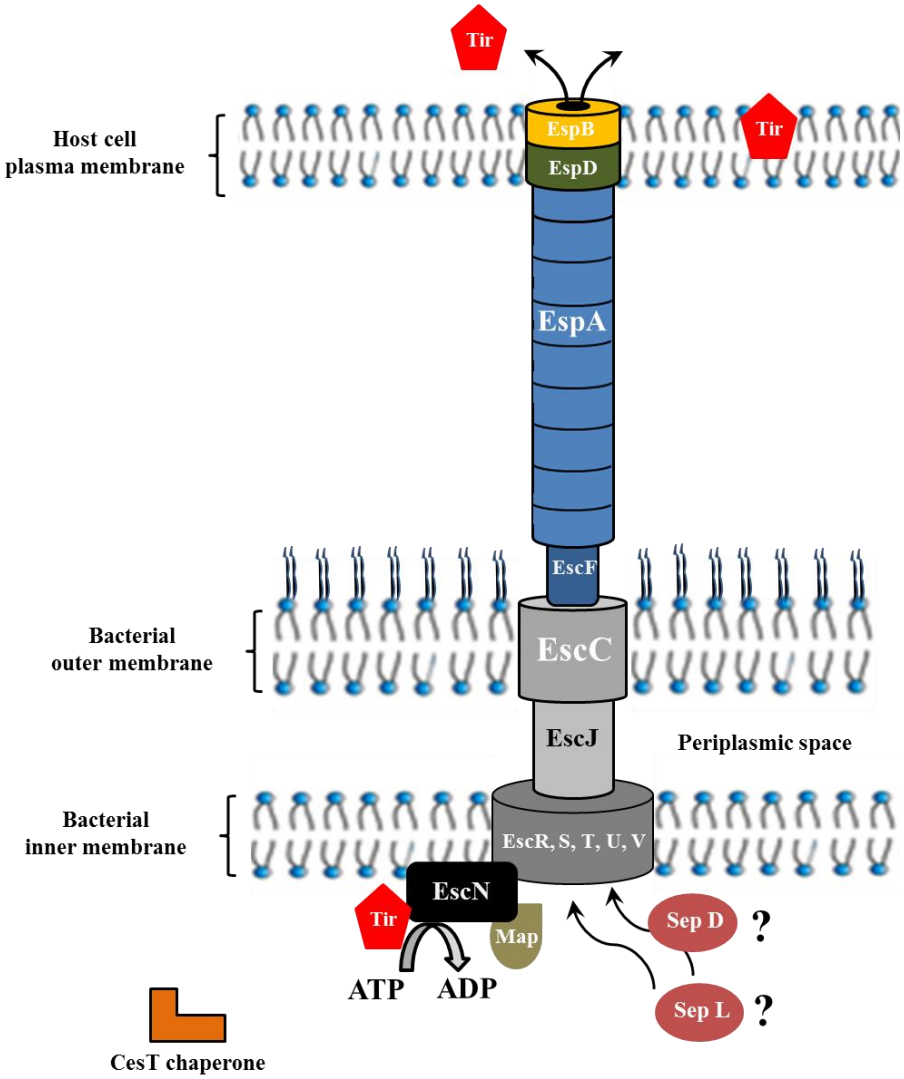


Figure 1.3: Schematic overview of the EPEC T3SS apparatus. The basal body of the system is comprised of two ring structures located at the bacterial inner and outer membranes. The IM ring is composed of proteins EscT, EscU, EscS, EscV and EscR that are connected to the OM ring formed by the secretin, EscC by the connector lipoprotein, EscJ. The projection channel is formed by the EscF needle which used to directly bind to the EspA filament (mediated by coiled-coil combinations between EspA subunits). EspD and EspB create the translocation pore in the target host plasma membrane to link the host target with the bacteria via EspA filaments. The cytoplasmic energy supplier motor protein EscN is shown with some examples of effector proteins Tir and Map with their chaperone CesT. The cytoplasmic components of T3SS SepD and SepL are predicted to play a role in controlling the system to switch from secretion of translocator protein to secretion of effector proteins. This figure was adapted from Garmendia *et al*., 2005 (32).

adhesion to target host cells compared to wild-type leading to the conclusion that EspD played a role in formation or stabilization of the T3SS apparatus. (24,45).

Intimate adherence and pedestal formation are important characteristics of EPEC infection which involves an attachment strategy that requires a 94 kDa bacterial OM protein called intimin and its receptor (Tir). Intimin is encoded by the *eae* gene, found downstream of *tir* gene in the LEE (3,16). Previously, Tir was thought to be a host cell protein as it is located on the surface of the plasma membrane of host cells during an EPEC infection (2). However, in 1997, Kenny and coworkers revealed that Tir was in fact a bacterial protein encoded within LEE and is translocated by the T3SS apparatus into host cells to serve as a receptor for intimin (3,46). This finding was supported by Kenny, 1999 who showed that disruption of genes encoding T3SS components prevented the translocation of Tir (47). Interestingly, multimerisation of protein-protein interactions of Tir and intimin results in a higher order clustering of Tir, that triggers tyrosine phosphorylation of Tir by the host cell Src-family kinase (SFK), c-Fyn, culminating in a signalling cascade that breaks microvilli (effacement) and promotes actin accumulation (polymerization) just beneath the intimately attached bacteria (2,19,48,49).

In addition to the A/E lesion, a study by Scaletsky *et al*., 1984 showed that the tEPEC forms a distinctive pattern of adherence characterized by formation of three-dimensional clusters known as localized adherence (LA) on the host epithelial cell (50). Interestingly, this pattern was

accompanied by the presence of a large EAF plasmid containing an operon of 14 genes encoding a functional pilus called the bundle-forming pilus (BFP) (4,8). Removal of the EAF plasmid from EPEC strains resulted in attenuated virulence and loss of the ability to cause localized adherence (3,8). BFP is composed of the bundlin protein (also called pilin or BfpA) encoded by diverse *bfpA* alleles separated into two bundlin allelic groups, α and β (51). BFP belongs to the type IV fimbria family which is also found on the surface of other Gram-negatives including *P. aeruginosa, Neisseria meningitidis* and *Neisseria gonorrhoea*, and Gram-positives such as *Clostridium perfringens* (52). BFP was found to be responsible for bacterial clusters due to its capability to aggregate into cordlike bundles. Interestingly, these bacterial aggregates could also disaggregate and disperse. The opposing behaviours are triggered by two ATPases, BfpD which drives pilus assembly (extension) and BfpF which mediates pilus retraction (51). Consistent with this finding, a disruption of any those genes led to an inability to express BFP, aggregate and cause localized adherence (53). An earlier study by Bieber and coworkers also showed that EPEC containing disrupted *efpF* displayed reduced virulence, suggesting a significant role for dispersal during infection (54). Moreover, Zahavi *et al*., 2011 reported that EPEC containing an *efpD* mutation did not produce BFP or autoaggregate in tissue culture medium, and was unable to develop a localized adherence pattern (52). In general, EPEC 2348/69 secretes a variety of effectors which appear to display overlapping functions and cooperation in these virulent activities (37).

1.2.4 The complex network behind LEE gene regulation

The main transcriptional regulator in the LEE PAI is the global regulator, Ler, a 15 kDa DNA binding protein. Ler is encoded within the LEE1 operon that modulates the expression of other LEE operons (55). Elliott and coworkers showed the importance of this global regulator when they found that nonpolar *ler* mutants were unable to form A/E lesions or even to express T3SS secreted proteins, concluding that ler is the central regulator that controls the expression of LEE (56). However, the expression of Ler itself is under the control of a large number of regulatory factors such as environmental factors, LEE and non-LEE encoded regulators as well as *E. coli* global regulators, making the regulatory cascade far more complex (11). Interestingly, besides regulating genes within the LEE PAI, Ler also regulates the expression of genes outside the LEE island such as *espC* (56).

1.2.4.1 LEE-encoded regulators

In addition to the master regulator, Ler, there are two other LEE-encoded regulators termed as the global regulator of LEE activator (GrlA) and repressor (GrlR). These are encoded by the *grlRA* operon located between the LEE2 operon and *etgA* (57). GrlA has been found to positively regulate Ler expression by interacting with the *LEE1* promoter. Interestingly, Ler also activates the expression of the *grlRA* operon, forming a positive regulatory circuit to guarantee the suitable level of Ler to switch on the expression of LEE genes (22). GrlR represses LEE

gene expression by its specific binding to GrlA, thereby preventing it interacting with the *LEE1* promoter (58).

1.2.4.2 Non-LEE-encoded regulators

The LEE genes are also regulated by an operon called plasmid encoded regulator (Per) located on the EAF plasmid in tEPEC. The *perABC* operon encodes the regulator proteins PerA, PerB, and PerC (59). PerA activates *perABC* and *bfp* expression while PerC activates only LEE1 promoter leading to the switching on of the Ler regulator and thus the other LEE promoters independently of GrlA (22,55).

1.2.4.3 *E. coli* global regulators

One important global regulator of LEE is the histone-like nucleoid structuring protein (H-NS) of *E. coli*, which influences gene expression, mostly negatively, by its ability to non-specifically bind to DNA, causing changes in DNA supercoiling and packing (56). H-NS represses the regulatory regions of EPEC *LEE1*, *LEE2*, *LEE3* and *LEE5*, thus directly controlling LEE transcription. In fact, Ler can counteract the repression exerted by H-NS on LEE genes but not on its own promoter (22,60). To overcome this issue, activation of the Ler *LEE1* promoter can be promoted by the integration host factor (IHF) (61). IHF is required to activate expression of Ler by perturbing the Ler repression by H-NS. Importantly, the ability to overcome the H-NS silencing of the *ler* promoter depends on the combined antirepressor activity of IHF with PerC or GrlA (55). Moreover, EPEC has the H-NS truncated protein (H-

NST) which also has been shown to counteract the H-NS repressive activity (62).

E. coli contains numerous other transcriptional regulators that control the expression of LEE genes for example; the factor for inversion stimulation (Fis) that positively regulates Ler and *LEE4* expression (63), the ribosome-binding GTPase (BipA) which increases LEE transcription by indirectly activating Ler expression (64) and the Cpx envelope stress response which down regulates the expression of T3SS components upon activation which also can occur at post-transcriptional levels via the chaperone DegP (65). A post-transcriptional regulator, CsrA (RNA-binding protein) has also been shown to be involved in switching on and off the expression of LEE genes in a concentration dependent manner (22,66).

1.2.4.4 Environmental factors and quorum sensing

During EPEC infection, the optimal LEE gene expression is detected during exponential growth, at pH 7, at normal body temperature 37°C, and at physiological osmolarity in the existence of calcium and sodium bicarbonate. Therefore, any changes in these environmental conditions would cause a tight negative regulation of virulence genes expression (18). Moreover, the addition of ammonium to the culture media has shown to significantly reduce *bfpA* expression, and thus prevent EPEC adherence (67). Another distinctive regulatory mechanism shown to be involved in the regulation of the expression of EPEC LEE genes is quorum sensing (68). Quorum sensing is a mechanism of bacterial

communication that controls the behaviour of bacterial populations via production of signal molecules, called autoinducers (69). Autoinducers can interfere with gene expression when they reach a critical threshold concentration (69). In EPEC, quorum sensing activates expression of the quorum-sensing *E. coli* regulator A (QseA) which in turn activates expression of Ler (69,70). A mutation in both *luxS* (a widely distributed quorum-sensing system) and *qseA* reduces the expression of T3SS, and thus decreases A/E lesion formation (68).

1.3 Autotransporters (ATs) in EPEC

Abreu and coworkers identified numerous AT-encoding genes of diarrheagenic *E. coli* pathotypes in EPEC (Table 1.1). The frequencies of these genes in the tEPEC and aEPEC groups were inconsistent. Among these ATs, EspC was the most frequent serine protease AT found in both groups of EPEC (71).

1.3.1 The serine protease AT, EspC

EspC belongs to the serine protease AT of Enterobacteriaceae (SPATEs) family (72). EspC has been shown to (i) be an enterotoxin (36), (ii) have enterotoxic, cytotoxic and cytopathic effects on HEp-2 cells (a human epithelial cell line) (34,73), and (iii) degrade haemoglobin to enable the bacteria to utilize the released iron for growth (74). Nevertheless, whether EPEC virulence is linked to these EspC biological properties is still unknown (74).

Gene	Encoded Products	Strain	Function	Reference
espC	*E. coli* secreted protein C (EspC)	EPEC	Serine protease	(75)
espP	Extracellular serine Protease plasmid-encoded (EspP)	EHEC	Serine protease	(76)
espI	*E. coli* secreted protease, island encoded (EspI)	EHEC	Serine protease	(77,78)
pet	Plasmid-encoded toxin (Pet)	EAEC	Serine protease	(79)
pic	Protein involved in colonization (Pic)	EAEC	Serine protease	(80)
eatA	ETEC autotransporter A (EatA)	ETEC	Serine protease	(81)
sat	Secreted autotransporter Toxin (Sat)	DAEC	Serine protease	(82)
tibA	TibA	ETEC	Biofilm formation/ autoaggregation	(83)
cah	Calcium-binding antigen 43 homologue (Cah)	EHEC	Biofilm formation/ autoaggregation	(84)
ehaA	EHEC autotransporter A (EhaA)	EHEC	Biofilm formation	(85)
ehaB	EHEC autotransporter B (EhaB)	EHEC	Biofilm formation	(85)
ehaC	EHEC autotransporter C (EhaC)	EHEC	Unknown	(85)
ehaD	EHEC autotransporter D (EhaD)	EHEC	Biofilm formation	(85)
ehaJ	EHEC autotransporter J (EhaJ)	EHEC/ EPEC	Biofilm formation	(86)

Table 1.1: AT encoding genes detected in EPEC.

Recent studies have shed more light on the functionality of EspC. For example, Fernando Navarro-Gracia's group demonstrated that EspC is the major cause of epithelial cell cytotoxicity during EPEC infection, by cleaving fodrin (an important component of the actin cytoskeleton structure organization and epithelial morphogenesis) into two parts. As a consequence of fodrin degradation, the two products trigger a cascade of events including focal adhesion kinase (FAK) and paxillin (the two main focal adhesion proteins) degradations, leading to cell rounding and cell detachment that creates the hallmark of EPEC disease (87). In addition, using immunoblot analysis, Guignot and coworkers demonstrated a novel function for EspC. They showed that the levels of cell-associated EspA and EspD were significantly elevated in an EPECΔ*espC* mutant compared to the EPEC WT after 45 min of cell contact. This indicated that EspC mediated proteolysis of the EspA/D T3SS translocator components, and thereby controlled the T3SS-dependent pore formation at the host plasma membrane (88).

EspC was initially identified as one of three proteins secreted by EPEC. Amino acid sequence data analysis identified considerable homology between the 110 kDa EspC and a family of immunoglobulin A (IgA) protease-like proteins that are conserved in virulent bacteria (75). This study also showed that EspC was the principal exported protein in EPEC strain E2368/69. Allelic exchange deletion of *espC* in this background indicated that EspC did not play a significant role in adherence or invasion of tissue culture cells (75). The ability of EPEC to cause cytotoxic effects was however dependent on the successful internalization of the 110 kDa EspC AT into the host cell and presence of

the catalytic serine residue in the serine protease motif (GDSGS) (35,73,89). Interestingly, this motif is widely conserved among several members of the AT family such as EspP from EHEC, Sat from UPEC and Pic from EAEC and *Shigella flexneri* (more examples are shown in Table 1.1) (89,90). Serine protease activity requires two more residues, His and Asp that are included in the formation of the catalytic triad (His, Asp and Ser) (89). Besides the serine protease motif, SPATEs also share other features which will be discussed through the following sections.

Although SPATE family members share a characteristic serine protease motif, their functions are extremely diverse (90,91). Evolution studies conducted by Yen and coworkers proposed that all members of the AT family evolved through speciation and late gene duplication events within the microbe and that horizontal gene transfer was a very rare evolutionary event with regard to ATs (89,92).

The term AT derives from the hypothesis that all the necessary information required for secretion across the inner and outer membranes of Gram-negative bacteria is present in the protein itself, and that there is no need for any kind of assistance from other bacterial molecules or chaperones (93). ATs are defined by having an amino-terminal signal peptide that is cleaved off during translocation across the IM plus a characteristic C-terminal domain that forms a β-barrel in the OM and is required for translocation of the passenger domain to the external surface of the bacterial cell. The structure and processing of EspC is consistent with it being an AT. Whilst the *espC* open reading frame (ORF) encodes a protein of approximately 140 kDa (1,306 amino

acids), the secreted version found in culture supernatants migrates with a size of approximately ~110 kDa which corresponds to the passenger domain that spans from amino acids 54 to 1,030. The secreted 110 kDa form of EspC lacks the first 53 amino acid signal sequence and potentially the C-terminal β-barrel domain that starts between amino acids 1,031 to 1,306 (26,75). Despite recent insights into the role of EspC in EPEC pathogenesis (87,88), a detailed mechanism of EspC secretion and the role of any accessory factors involved are still under debate.

1.3.1.1 The EspC journey; an autotransporter trip across membranes

EspC uses a unique translocation mechanism to target the host cell which involves collaboration between both EPEC T5SS and T3SS. In agreement with such a mechanism, internalization of exogenous added EspC into HEp-2 cultured cells in absence of EPEC occurs in 8 h while it was faster (after 1 h) when EPEC was present (34). In support of this finding and as stated earlier, the global regulator Ler, part of the Per-mediated regulatory cascade, was found to co-regulate the expression of *espC* with secretion of T3SS-secreted Esp proteins, intimin and Tir (35,56). However, the precise contribution of T3SS in translocation of the milieu-secreted EspC and how exactly EspC gets access to T3SS translocon to be delivered into host cell cytosol are still obscure (35).

1.3.1.1.1 Type V secretion system (T5SS)

Gram-negative bacteria secrete a variety of virulence proteins by different secretion pathways (93). At least nine secretion pathways are currently known, these include T1SS to T8SS (94,95). Recently, another system has been uncovered in Bacteroidetes named T9SS (also called the Por secretion system) (96-98). These secretion systems are different in terms of their complexity, structural features and methods of protein translocation (93). Basically, these secretion machineries can be classified into two categories; those that span both bacterial IM and OM traversing the periplasmic space as one large secretion complex, and those that span the OM only (99), and thus utilize a two-step translocation pathway. A brief description of such secretion systems are represented in Fig. 1.4

T5SS, which is used by ATs to exit the cell, is considered to be the simplest secretion system and the most commonly used system amongst Gram-negative bacteria for delivering effector virulence proteins externally (100,101). Pohlner *et al.,* 1987 were the first to identify and describe the T5SS after dissecting the extracellular location of immunoglobulin A1 (IgA protease) secreted by *Neisseria gonorrhoeae* (102). Since that description, a large number of proteins which are secreted by similar mechanisms have been discovered among other Gram-negative bacteria (103).

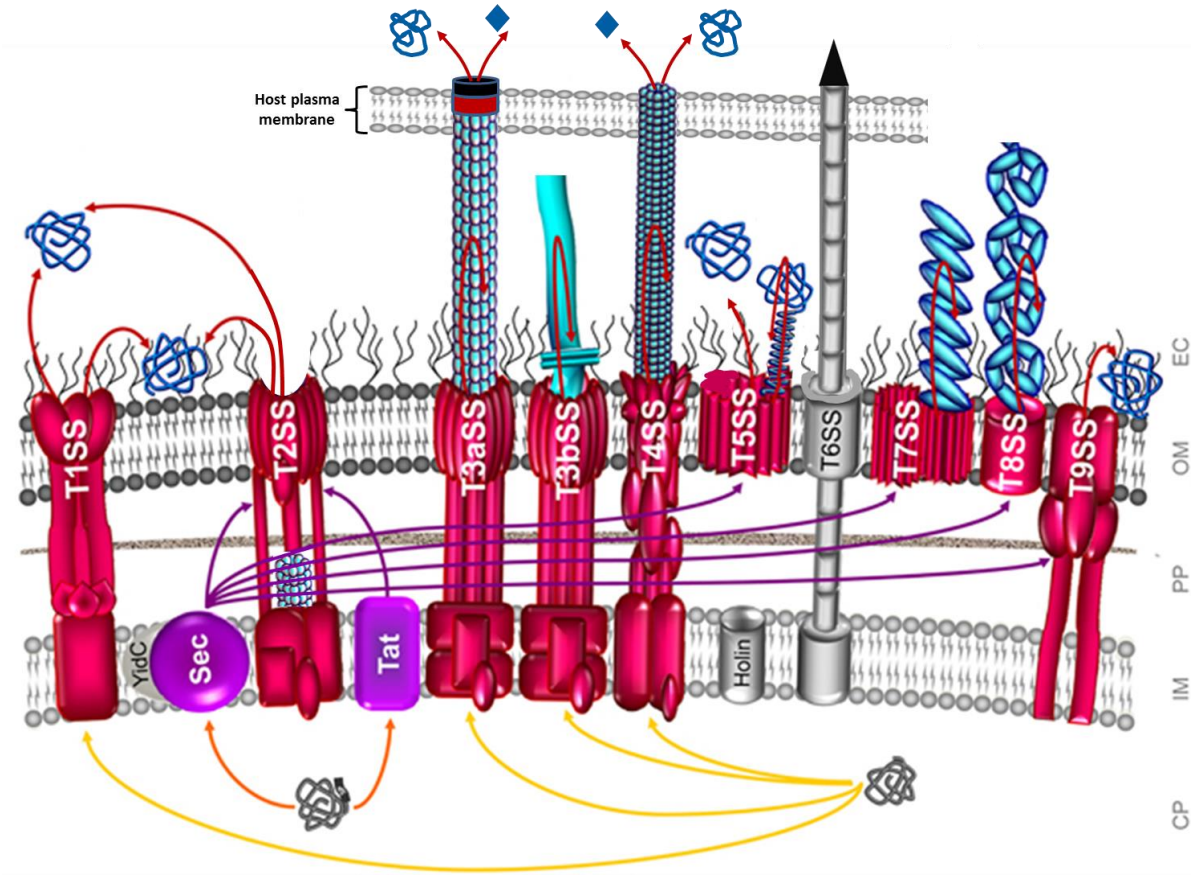


Figure 1.4: Schematic representation of the secretion systems in Gram-negative bacteria. Nine distinct secretion machineries have been identified to date, T1SS to T9SS. T1SS, T2SS, T3SS, T4SS, T6SS and T9SS are double-membrane-spanning-secretion systems while T5SS, T7SS (type 1 or P pilus biogenesis) and T8SS (curli secretion system) span the OM only. Moreover, T2SS, T5SS, T7SS, T8SS and T9SS are Sec-dependent whereas T1SS, T3SS, T4SS and T6SS are sec-independent. Furthermore, T2SS might use the twin arginine translocation (Tat) system to cross the IM. Two types of T3SS are shown: T3aSS can be involved in the formation of needle-like structures (injectosome) and T3bSS is involved in flagellum assembly. T7SS is the Chaperone usher pathway (CUP) that is involved in the biogenesis of the P pilus. T8SS is the extracellular nucleation-precipitation pathway (ENP) involved in the formation curli pilus. This figure was adapted from Chagnot *et al*., 2013 (98).

ATs share sequence and structure homology as well as relying on the general secretion pathway components for translocation across the IM (specifically the Sec-dependent pathway comprising the SecYEG translocon) (93). Interestingly, other secretion machineries are required Sec machinery for their function such as T2SS, T7SS, T8SS and T9SS (Fig. 1.4) (95,96). The signal sequence, located at the N-terminus of ATs (Fig. 1.5), directs the secretion of the precursor across the IM via the Sec system. The central AT domain called the passenger domain (also called α-domain or N-domain) carries the functional moiety of the protein. The last domain, known as the carboxy domain (β-barrel domain or translocator/transporter domain) inserts as a β-barrel into the OM, potentially to form a channel through which the passenger domain may subsequently travel for OM translocation (72,93,94). Additionally, several ATs including all SPATE ATs such as EspC, EspP, *Bordetella* serum-resistance killing protein A (BrkA), IgA protease and adhesin involved in diffuse adherence (AIDA-I) from EPEC strain 2787 contain a unique short region termed the linker region (also called α-helical region or α-helix) found just adjacent to the N-terminus of the β-barrel domain, suggesting a role in passenger domain processing. This region along with β-barrel domain is called the translocation unit (104,105) as mutations in some residues within the linker region abolish the translocation of the passenger domain across the OM (106).

An additional feature was identified in a study conducted by Oliver *et al*., 2003 who demonstrated the presence of an intramolecular chaperone domain (also known as the autochaperone domain) in a subgroup of ATs

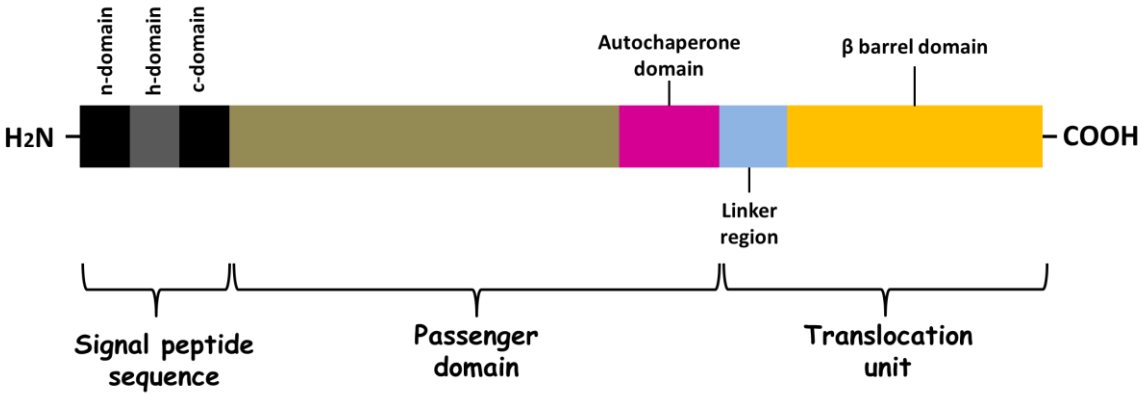


Figure 1.5: The archetypical structure of autotransporters showing the main domains. This figure was adapted from Desvaux *et al.*, 2004 (107).

that is just proximal to the C-terminal passenger domain and plays a significant role in maintaining the proper folding of the AT to ensure function of the passenger domain following translocation across the OM (72,104,107) (Fig. 1.5). Consistent with this finding, mutation of the hydrophobic residues located near the C-terminus of EspP (from EHEC) and Hemoglobin binding protein (Hbp) (from pathogenic *E. coli*) passenger domains affect the folding of the autochaperone domain which had a knock on effect of the translocation of their passenger domains (101,108-110). Moreover, multiple autochaperone domain sequence alignments demonstrated that EspC has a conserved sequence motif comprising amino acids Gly-Phe-Ser (termed as GFS motif) which has been shown by site-directed mutagenesis (SDM) to be important in the translocation of EspC (111).

The export of ATs to the bacterial cell surface is dependent on the type of the AT in question. It is influenced by the size of the transporter domain as well as the position of the passenger domain in the precursor (95,101). T5SS currently has been sub-classified into five categories: (i) a classical AT system (type Va system), (ii) the two-partner secretion (TPS) system (type Vb system), (iii) the trimeric AT adhesion (TAA) system (type Vc system), (vi) the classical AT and TPS fusion pathway (type Vd system), and (v) the inverted ATs pathway (type Ve system) (Fig. 1.6) (100).

The main difference between classical ATs and TPS systems is that in the TPS system, the passenger domain (the TpsA partner) and transporter domain (the TpsB partner) are synthesized as two separate

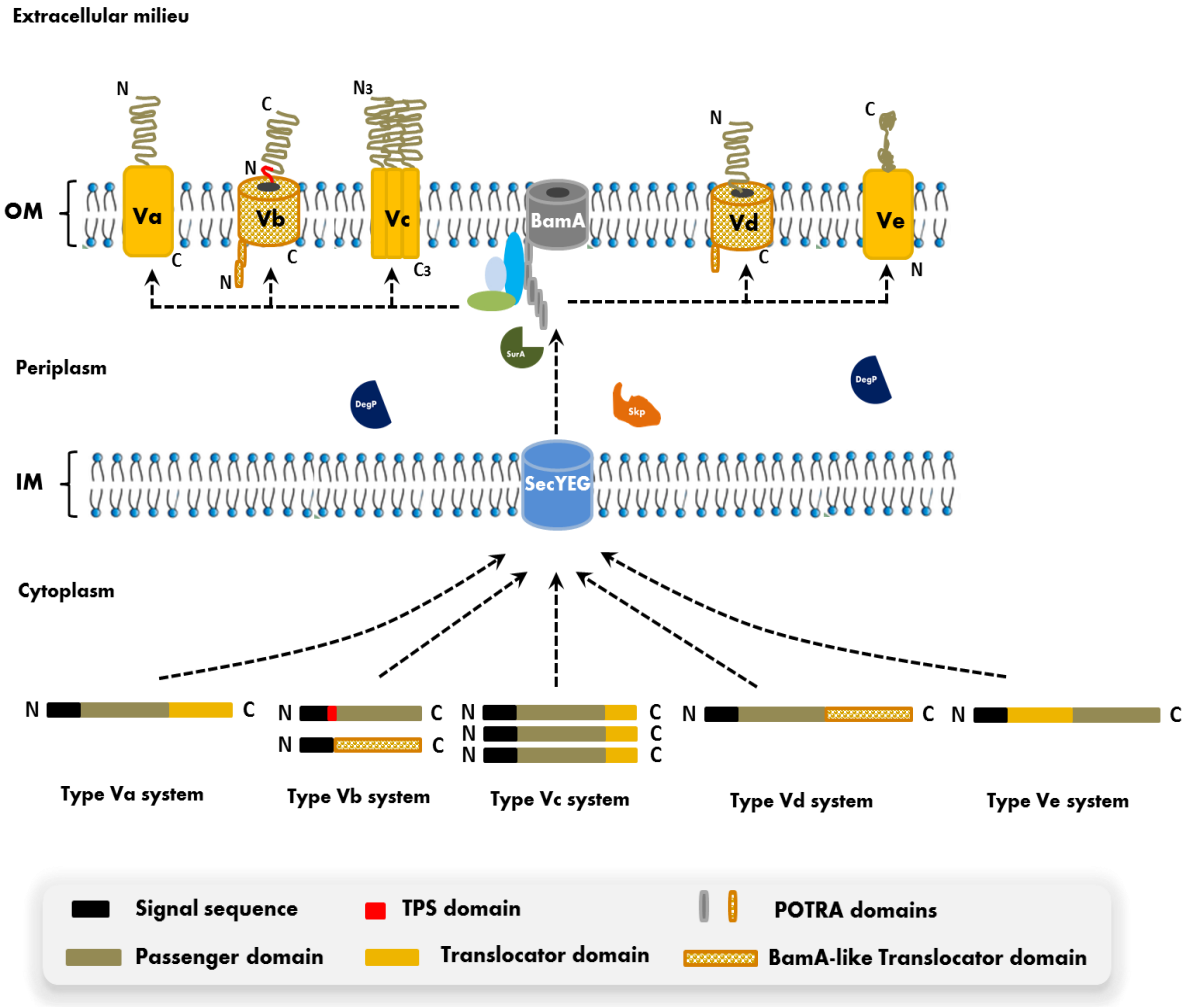


Figure 1.6: Schematic representation of the various sub-classes of the T5SS. T5SS has been sub-classified according to the differences within the precursor protein architecture. The transporter domain is the main cause of this variation. It may (i) be located at a different position relative to the passenger domain, (ii) trimerize or monomerize to form a functional β-barrel at the OM, (iii) form β-barrels with 12 or 16 strands that resemble BamA, and (iv) be contained with its cognate passenger domain in one polypeptide chain or synthesized separately (type Vb). The passenger domain in type Vb system hosts the TPS domain for recognition of its specific transporter domain. The positions of N- and C-terminus of such AT proteins are shown. This figure was adapted from Grijpstra *et al*., 2013 (101).

proteins which are transported independently through the IM using their respective signal sequences (93,95,101). Once translocated into the periplasm, TpsB inserts first into the OM as a 16-stranded β-barrel with two polypeptide transport-associated (POTRA) domains (112). Subsequently, TpsA (after crossing the Sec translocon and cleavage of its leader signal peptide sequence), targets TpsB at the OM via its N-terminal conserved Tps domain (95,101,112). Following attachment to the TpsB POTRA domains in the periplasm, secretion of TpsA across the OM by the TpsB channel is initiated (112).

Although the TAAs have one intact polypeptide, their carboxyl termini encodes only one-third of a β-barrel, therefore these proteins need to trimerize to form a functional β-barrel at the OM (93,113). On the other hand, inverted ATs have an inverted orientation, i.e. the order of passenger and transporter domains are reversed (93,95,101). In the fused two-partner secretion pathway, the obvious difference to the TPS system is that in the fusion pathway, the passenger domain is actually attached to its partner via a POTRA domain and they are synthesized as one protein (95). Notably, SPATEs represent a typical example of classical ATs (91). More examples of ATs using such pathways are listed in Table 1.2

Type Va system (Classical ATs)			
Protein name	**Bacterial spp.**	**Function**	**Reference**
EspC	EPEC	Enterotoxin, haemoglobin protease and cleaved fodrin	(36,74,87)
EspP	EHEC	Degrades pepsin, complement factors and contributes to biofilm formation	(114)
Pet	EAEC	Cytotoxin and proteolytic toxin	(79)
Pic	EAEC/*S. flexneri*/ EPEC	Degrades gelatine and mucin	(80,115)
Sat	UPEC	Cytopathic activity	(82,90)
SepA	*S. flexneri*	Proteolytic activity	(90,116)
SigA	*S. flexneri*	Cytotoxin	(72)
Vat	APEC	Vacuolating cytotoxin	(117)
Hbp	EPEC	Heme-sequestering protein	(90,118)
NalP	*N. meningitidis*	Proteolytic activity	(119)
Hap	*H. influenzae*	Adhesin and protease activity	(120)
VacA	*H. pylori*	Vacuolating cytotoxin	(121)
IgA protease	*N. meningitides*/ *H. influenzae*	Degrades IgA1	(102)
IcsA	*S. flexneri*	Mediates intracellular motility	(122)
BrkA	*B. pertussis*	Serum resistance and adhesion	(104)
AIDA-I	*E. coli*	Adhesin	(123)
TibA	ETEC	Adhesin and invasion	(124)
Ag43	*E. coli*	Autoaggregation factor	(125)
AaaA	*P. aeruginosa*	Arginine aminopeptidase	(126)

EstA	*P. aeruginosa*	lipolytic enzyme involved in motility and biofilm formation	(127)
MapA	*M. catarrhalis*	Phosphatase activity	(128)
Type Vb system (TPS)			
HMW1 and HMW1B	*H. influenzae*	Adhesin	(129)
FhaB and FhaC	*B. pertussis*	Adhesin	(130)
HpmA and HpmB	*P. mirabilis*	Hemolysin	(131)
Sh1A and Sh1B	*S. marcescens*	Hemolysin	(131,132)
Type Vc system (TAAs)			
Hia	*H. influenzae*	Adhesin	(133)
YadA	*Y. enterocolitica*	Adhesin, serum resistance	(134)
Msf (NhhA)	*N. meningitidis*	Adhesin, serum resistance	(135,136)
EibD	*E. coli*	IgA and IgG binding proteins,	(137)
Type Vd system (The classic AT and TPS fusion model)			
PlpD	*P. aeruginosa*	lipase activity (phospholipase)	(138,139)
Type Ve system (Inverted ATs)			
Intimin	EPEC	Adhesin (the major component in A/E lesion)	(95,101)
Invasin	Yersinia spp.	Adhesin activate autophagy	(95,101)

Table 1.2: Overview of the diversity of ATs, sub-categorized into five systems and their proposed role in virulence.

1.3.1.1.1.1 Translocation across the IM; the first gate to the surface!

Some ATs are synthesized in the cytoplasm with a characteristic Sec-dependent signal peptide of the typical 20-30 amino acid residue length (93). The structure of such signal peptides is well understood; they have a tripartite structure comprising an N-domain with positively charged amino acids, H-domains hosting hydrophobic amino acids and a C-domain incorporating a proteolytic cleavage site for IM signal peptidase (72). Such ATs are exported via the Sec translocon to which they are ushered by the cytoplasmic chaperone SecB, which keeps the AT in a translocation-competent state (72,140). The translocation process across SecYEG channel is driven by the motor protein ATPase (SecA) which requires cardiolipin (CL) for energy coupling and efficient proprotein translocation (141). Other ATs including members of SPATEs are made with unusually long signal peptides (between 50-60 amino acid residues long) e.g. EspC, EspP, Hbp, Pet, TpsA domains and TAA proteins. Such signal peptides contain five domains called the N1, H1, N2, H2 and C domains (93). The unique N1 and H1 domains contain a well conserved amino-terminal extended signal peptide region (ESPR), which presumably harbours a specific additional function (72,93,142). Interestingly, ESPR is not required for Sec machinery targeting but rather ESPR is involved in the optimal biogenesis of a number of ATs (91,112).

Initial investigations of two SPATE proteins EspP and Hbp secreted from *E. coli* have led to the hypothesis that ESPR is recognised by another cytoplasmic accessory protein different from SecB called signal

recognition particle (SRP) which promotes a co-translational translocation of the AT proprotein (72,93,112,143). However, some observations have contradicted this notion. Although recognition is strictly SRP independent, it occurs post-translationally rather than co-translationally (144,145). Several studies hint that the function of ESPR is to prevent AT aggregation and premature folding in the periplasm by delaying or slowing passage of the AT to the periplasm due to its interaction with the specialized IM integrase called YidC which is associated with the SecYEG translocon during IM translocation (144-147).

Some ATs such as substatin-like protease (SphB1) of *Bordetella pertussis*, neisserial autotransported lipoprotein (NalP) of *N. meningitides*, capsule biosynthesis protein A (CapA) from *Campylobacter jejuni* and adherence-associated lipoprotein A (AlpA) from *Helicobacter pylori* are considered lipoproteins due to the presence of a lipid box located at the carboxyl terminus of the signal sequence (93). The lipid box targets lipoproteins to be cleaved by the specialized lipoprotein signal peptidase LspA (also known as single peptidase II) after Sec-dependant translocation. The first N-terminal cysteine residue in the mature protein is then N-acylated by the transacylase enzyme, Lnt (93,101,148). Subsequently, the new processed lipoproteins destined for the OM are localized by the Lol pathway. However, the exact role of the Lol pathway in periplasmic transit of both NalP and SphB1 is still obscure (101). In agreement with this, an observation was conducted by Roussel-Jazede *et al*., 2013, concluding that NalP translocation is not

actually dependent on the Lol pathway despite the necessity of lipid moiety for accurate attachment and function at the cell surface (149).

1.3.1.1.1.2 Transit through the periplasm

As ATs include an integral OM domain (translocation unit) and utilize a secretion mechanism largely resembling the biogenesis of OM proteins (OMPs), it was postulated that ATs co-operate with periplasmic proteins (including chaperones) to keep them in a translocation competent state and target them to the OM (93,101). According to Ruiz-Perez *et al*., 2009 and Purdy *et al*., 2007, a number of periplasmic chaperones such as the survival protein A (SurA), seventeen kilodalton protein (Skp), a protease member of HtrA family called DegP and a peptidyl-prolyl cis/trans isomerase FkpA are shown to play a significant role during periplamic transit of some AT members (150,151). To investigate their contribution to AT biogenesis, yeast two-hybrid assays (Y2H) and surface plasmon resonance (SPR) approaches were used to dissect protein-protein interactions between these chaperones and ATs (150,152). These studies revealed for the first time direct protein-protein interaction between DegP and SurA chaperones with highly conserved aromatic amino acids (aro-x-aro motifs) within the EspP passenger domain. Interestingly, four of these motifs were highly conserved among the entire SPATE subfamily (150). Subsequent investigations also demonstrated the interaction of periplasmic chaperones to different ATs, for example Hbp was found to interact with Skp (152), IgA protease with FkpA (153) and Pet with newly identified 37 kDa VirK and Skp (154).

In general, ATs utilize chaperones to maximise secretion e.g. reduced secretion of the non-SPATE IcsA and the SPATE EspP ATs occurred from *surA*, *degP* and *skp* mutants of *S. flexneri* and *E. coli* respectively, despite the mutants being capable of translocating the protein across the OM and correctly folding the β-barrel domain (93,100,150,151,155). These results point out the main roles of periplasmic chaperones in AT biogenesis which includes (i) protecting ATs from degradation by protease enzymes present in the periplasm, (ii) keeping ATs in an extended translocation competent state to successfully continue their journey toward the bacterial surface, and (iii) degrading misfolded or prematurely folded/aggregated AT passenger domains (93,150,151). Interestingly, due to the existence of chaperone redundancy, their contribution to keeping ATs in a translocation competent state varies and there is a possibility that they have overlapping roles that can be substituted if one chaperone becomes impaired in *E. coli* (151,152,156,157).

1.3.1.1.1.3 The exit gate

Based on the original AT model (102), the insertion of the transporter domain into the OM to form a β-barrel channel is a necessary step to guarantee the secretion of the passenger domain (101). Sequence homology as well as the emergence of crystal structures of transporter domains in a set of classical ATs including Hbp, EspP, NalP, BrkA and EstA has clearly shown a common, characteristic 12-stranded β-barrel linked to a periplasmic hairpin turn and extracellular loops forming an anti-parallel β-barrel with an internal α-helix that sits inside the channel

(93,101). This feature has also been reported to be present in other AT systems such as in trimeric AT and inverted AT transporter domains, but not in TpsB which instead shows sequence homology with the BamA (previously known as Omp85 or YaeT) component of the β-barrel-assembly machinery (Bam) complex (93,158). An additional feature conserved between these domains is the α-helix in which passenger domain cleavage occurs (101). Several studies have indicated possible additional roles of the α-helix including (i) controlling and maintaining the β-barrel lumen by blocking it, (ii) processing of the passenger domain, and (iii) folding of the β-barrel (106,159-161). Furthermore, a study conducted by Zhai *et al*., 2011 demonstrated the presence of a conserved hydrophobic cavity comprising hydrophobic patches on loop L4 and β-strand S5 and S6 in three classical β-barrel structures (NalP, EspP and EstA), suggesting a possible role in passenger domain secretion (162).

Passenger domain translocation across the OM, the proposed models

This is the final step in the secretion of ATs in which the passenger domains adopt a translocation-competent conformation for successful transit through a channel previously made during the insertion of cognate β-barrel domains in the OM followed by folding on the bacterial external surface. Many, but not all passenger domains of classical ATs adopt characteristic β-helical stalk-like structures with N-terminal global domain (101,163). Several models of passenger translocation across the OM have been proposed, such as the threading, the hairpin, the multimeric and the BamA models (93). Furthermore, more recently, the

new discovery of a new translocation and assembly module (TAM) has led to an alternative model which combines both hairpin and BamA models (94,164). The currently available data does not support the threading and multimeric models leading to their rejection, whereas the remaining models are still being supported and investigated (93,165-168). It was proposed in the threading model that the passenger domain translocates through the β-barrel channel in the N- to C-terminus direction. However, due to the lack of the specific N-terminal sequences in the passenger domain to target it to the β-barrel, the threading secretion model has become an unlikely scenario. In the multimeric model, multiple AT β-barrel domains were predicted to be inserted and oligomerized to form a central hydrophobic channel which facilitates passenger domain translocation. As most AT β-barrel domains are inserted into the OM as monomeric structures this again makes the multimeric model controversial (165,167,168).

- **The Hairpin Model**

In this model, it was originally proposed that after insertion of the β-barrel into the OM, a unique hairpin structure formed at the C-terminal region of the passenger domain. The β-barrel then threads the unfolded passenger domain into the OM β-barrel pore in a C- to N-terminus direction (94,95). As shown in the Fig. 1.7 A, the consequence of this event is that the appearance of the C-terminus of the passenger domain at the outer surface would occur before its periplasmic N-terminus (94). This folding feature was suggested to stop the passenger from slipping back to the periplasm via the channel and would give energy to pull out

the N-terminus from periplasm to the external surface (94,169). Generally, the hairpin model is accepted because both the periplasm and the cell surface are devoid of ATP to drive translocation (101). Substantial evidence exists supporting the potential for the central channel of the β-barrel to accommodate a hairpin structure. The hairpin model is underpinned by: (i) the role of the autochaperone domain in driving the folding of the rest of passenger domain once it emerges from the bacterial surface where no external energy source is available (104,105,109,170), (ii) the translocation of folded chimeric passenger domains containing disulphide bonds across the outer membrane (167), (iii) AT crystal structures which show that the linker between the passenger domain and the translocator domain creates an α-helix that traverses the β-barrel channel (91,99,101), (iv) loss of secretion of Pet AT when large disulphide-bounded loops were introduced into the peptide sequence (163), and (v) identification of a conserved extracellular cavity formed by hydrophobic patches of Loop 4 and strand 5 and 6 of the 3D structure of BrkA β-barrel domain which is speculated to provide favourable conditions for insertion of the hairpin-like structure and thereby facilitate quick and efficient folding of the translocated N-terminal of the passenger domain (162).

Certainly, OM translocation is affected by passenger domain conformation. Many AT passengers exhibit a long right-handed β-helical stem-like structure linked by several loops (163,171-173). However, the crystal structure of the AT β-barrel shows that the internal channel is relatively narrow (~1.2 nm) and thus incompatible with the secretion of folded or even partially folded passenger domains. This contradicts the

hypothesis that there is formation of an α-helical linker during the translocation process (90,94,101,174), suggesting instead that to achieve effective translocation, passenger domains would have to be maintained in a linear format (an extended conformation) to be secreted without causing jamming in the β-barrel channel (163). However, since numerous AT passengers can be secreted in a partially folded state, alternative models were proposed (101,174). In an interesting study by Ieva *et al*., 2008 it was suggested that the α-helical linker is integrated into a partially folded β-barrel-like structure (proto-barrel) in the periplasm prior to the incorporation into the OM (165). It is conceivable that the mechanism of AT secretion is more complicated than it was thought and that additional factors might be involved to facilitate the secretion of passenger domains across the OM, which as a consequence has placed the term "autotransporter" under scrutiny (100,167).

- **The BamA Model**

Previous works have speculated that AT secretion involves the participation of an exogenous factor that has been called Omp85 or YaeT (175-177). Omp85 was originally identified in *N. meningitidis* and is now known as BamA (175). It is the archetypal protein of the Omp85 family that has major roles in the biogenesis of bacterial OM proteins (OMPs) and is found in all Gram-negative bacteria (178). Other members of the Omp85 family, including TpsB (the OM translocator in the TPS) and the newly identified TamA (the core component in the TAM), are also to be involved in AT biogenesis (158,164).

In Gram-negative bacteria, BAM complex consisted of five proteins; one integral β-barrel protein, BamA and four OM associated lipoproteins, BamB, C, D and E (179-181). BamA is the central component of the complex comprising two domains; an N-terminal periplasmic domain divided into a set of five POTRA domains (numbered 1 to 5 from the N- to C-terminus, with POTRA 5 occupying a central position closest to the β-barrel domain), and a C-terminal domain which forms a 16-stranded β-barrel structure with 2.5 nm pore embedded in the OM (179,182). BamD interacts with BamA via the POTRA domain 5, and that these two components are essential proteins for cell viability since mutation in each of these proteins causes a block in the assembly of OMPs (183,184). However, all BAM complex protein components are necessary for efficient incorporation of OMPs into the bacterial OM (180).

Potential functions for BAM complex components include BamA opening laterally in the membrane upon binding with BamCDE to enable insertion of OMP substrates into the OM (185,186). BamB appears to act as a scaffold to facilitate the handoff of chaperone-bound OMP substrates to BamA (184). BamC, BamD and BamE are involved in the regulation of the conformational state of BamA (182). Certainly, the process of folding and insertion of OMPs (and ATs) into the bacterial OM is dynamic and involves conformational changes within the BAM complex machinery (187). However, the functional roles of individual components and how the complex exactly works, remains unknown (188).

In SPATEs, two key conserved residues have been identified (F1360 and F1377 located at the C-terminus of the SPATE β-barrel domain). The substitution mutation F1360A caused cell lysis, but F1377A did not, suggesting that the phenylalanine at position 1360 is involved in the targeting and insertion of the β-barrel into the OM (presumably with assistance from BamA). Phenylalanine 1377 is required (possibly alongside periplasmic chaperones) for β-barrel formation and function in the periplasm as a proto-barrel-like structure (189).

Various studies have illustrated the role of periplasmic chaperones in the interaction between ATs and the BAM complex. For instance, Sauri *et al*., 2009 demonstrated a role for the periplasmic chaperone SurA in the delivery of Hbp AT to the BAM complex (174). Moreover, Ieva *et al*., 2011 and Pavlova *et al*., 2013 proposed that the chaperone Skp targets the EspP transporter domain to the BAM complex, whereas SurA is involved in transfer of polypeptide segments of the passenger domain to BamA via POTRA domains, concluding that the chaperones delivered the passenger domain to the translocation machinery in an appropriate secretion competent state (190,191). Precisely how AT proteins interact with the Bam complex is still under investigation. Different scenarios have been proposed (93), and Fig. 1.7 B presents the recently revised model, based mainly on the experimental evidence obtained from EspP (191,192).

- **The alternative Model**

In addition to the BAM complex, another distinctive secretion complex has recently been discovered called TAM which appears to contribute to

AT biogenesis (164). TAM is found in Proteobacteria, and comprises of the integral OM protein TamA and the integral IM protein TamB (94,112,164). Interestingly, TamA is a member of the Omp85 family with a 16-stranded transmembrane β-barrel and three POTRA domains (193). Both TamA and TamB can form a hetero-oligomeric complex that spans the bacterial periplasmic space (164,194).

The evidence implicating TAM in AT secretion includes the observation that a mutant of *C. rodentium* lacking either *tamA* (formerly *ytfM*) or *tamB* (formerly *ytfN*) failed to secrete the AT p1121 (164). Furthermore, double *tamA/tamB* mutants in *E. coli* failed to produce the adhesins Ag43 or EhaA ATs (94,99,164). However, a mutant of *E. coli* lacking *tamA* did not affect the secretion of Hbp, suggesting this system likely contributes to secretion of a particular subclass of ATs that may not include the SPATEs (112,174). A brief overview on the translocation process of ATs via the alternative model is illustrated in Fig. 1.7 C

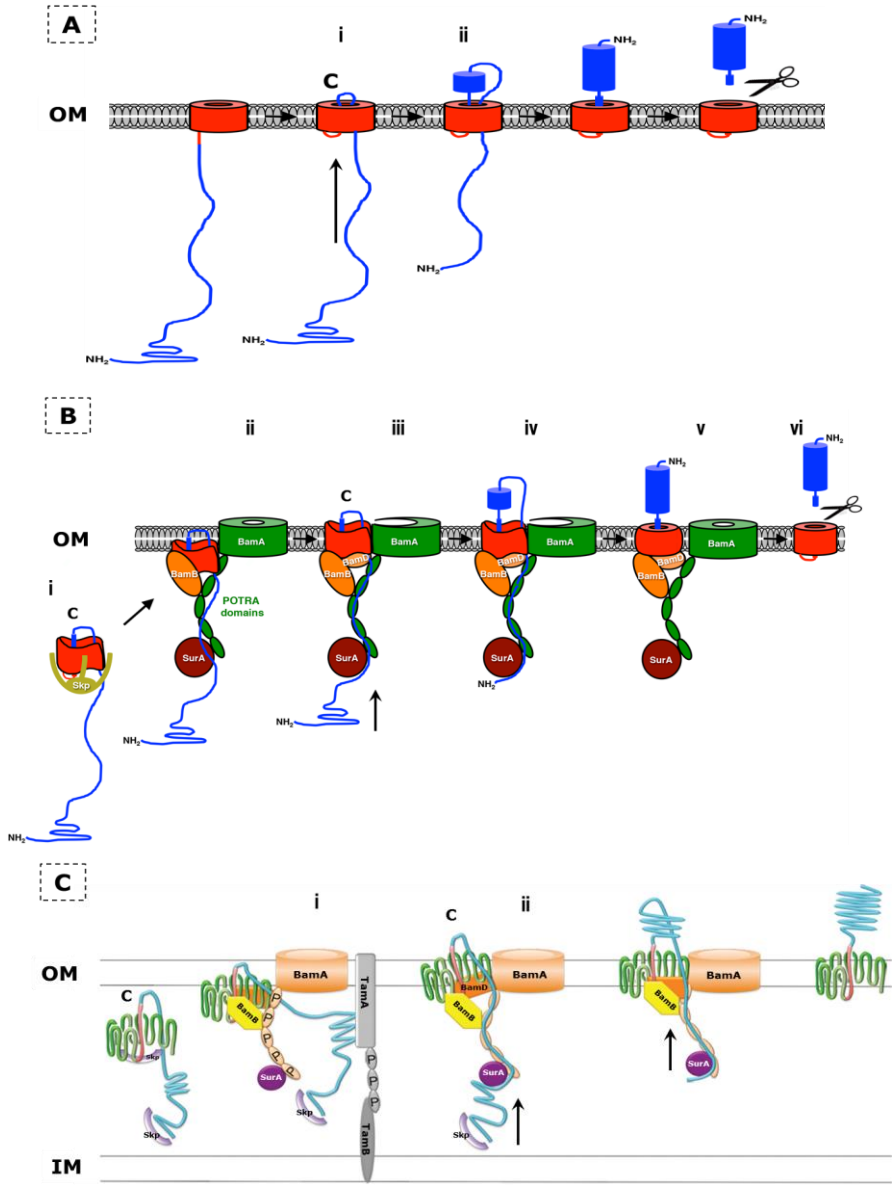


Figure 1.7: Mechanistic models of passenger domain secretion across the OM. (A) The hairpin model in which the secretion of the AT passenger domain (Blue) occurs from C- to N-terminal direction in an unfolded confirmation through a channel created by its cognate β-barrel domain (Red) at the OM (i). Formation of the hairpin structure inside the β-barrel channel facilitates the gradual threading of the passenger through the β-barrel channel. The translocation is then driven by the folding of passenger domain at the outer surface (ii). Subsequently, the protein may be released by a proteolytic cleavage or remain attached. **(B)** BAM model. Here in the periplasm the β-barrel domain folds first into a proto-barrel structure which incorporates the C-terminus of the passenger domain in a hairpin structure in presence of the periplasmic chaperone, Skp (i). Next, the β-barrel domain is targeted to the BAM complex via a combined interaction with BamA, BamB and BamD and at this stage Skp chaperone disassociates (ii). Next, translocation of the passenger domain is started just after the β-barrel reaches a specific stage of assembly (iii) which is predicted to move progressively from SurA to BamA POTRA domains towards the channel formed collectively by the AT β-barrel and BamA (iv). Following the complete translocation of the passenger domain and release as described in (A), both BamB and BamD remain in contact with the β-barrel during these events (v) but later dissociate (vi). **(C)** The alternative model that involves a combination of hairpin, BAM models as well as TAM. Here, the β-barrel is depicted as green, the passenger domain as blue and the linker domain as a pale red. TAM is predicted here to provide an essential step by stabilizing the periplasmic intermediate that is targeted to BamA (i) and is disassociated immediately after initiation of passenger domain translocation (ii). Both BamC and BamE components of the BAM complex are not shown for clarity. A and B were adopted from Bernstein H., 2015 (192) whereas C was adopted from Gawarzewski I.*, et al*., 2013 (94).

1.3.1.1.1.4 Release to the target; ready to fire!

Once the ATs are located at the surface of the bacterium, the passenger domains have alternative fates. Some are cleaved and released into the extracellular milieu by an autoproteolytic mechanism or by the action of proteases found on the cell surface. Others are cleaved but remain non-covalently and strongly linked with the β-barrel domain. A few remain covalently attached to the β-barrel domain (93). The proteolytic release mechanisms are widely diverse. For instance, the cleavage of the passenger from SPATE ATs including EspC is dependent on the β-barrel domain itself rather than on the passenger serine protease motif. This intramolecular autoproteolytic cleavage occurs immediately after passenger domain secretion at two conserved consecutive asparagines (Asn1023-Asn1024) found in the linker domain, and is catalysed by the β-barrel (90,93). Dautin and coworkers found that the cleaving mechanism of the SPATE AT EspP is triggered by an interaction between two conserved residues; an aspartate (Asp1120) located inside the β-barrel domain and asparagine (Asn1023) present at the cleavage junction. This cleavage inside the pore of the β-barrel leads to Asn1023 cyclization (169,195). Interestingly, this mechanism also seems to be present in non-SPATE ATs such as pertactin and BrkA from *B*. *pertussis* (90,195). Furthermore, unlike SPATE ATs, ADIA-I does not contain a serine protease motif but is intramolecularly cleaved at the bacterial cell surface in a process that requires two acidic residues that locate in the autochaperone domain (196).

Other examples of cleavage mechanisms include; (i) release of the passenger domain by an integral OM protease such as *S. flexneri* IcsP which cleaves IcsA passenger (197), (ii) autoproteolytic cleavage e.g. IgA protease and Hap (102,198), and (iii) processing by another AT protease for instance NalP serine protease cleaves various *N. meningitidis* ATs including the peptidase AusI (also known as MspA) and the adhesion and penetration protein (App) (93).

1.3.1.1.2 Entering Host cells using the T3SS

As mentioned in section 1.3.1.1, extracellular EspC gains access to the host cytosol by interacting with the T3SS (26,34,35). The association between T3SS and EspC was discovered by Vidal *et al.*, 2008 who examined infection of HEp-2 cells by a set of EPEC T3SS mutants. This group found that the EPECΔ*espB* mutant (defective in the pore forming T3SS translocator), the EPECΔ*espA* mutant and the EPECΔ*espF* mutant (defective in extracellular translocators) secrete EspC at levels similar to wild-type EPEC, but that EspC was not observed in the HEp-2 cytoplasm, and concluded that EPEC recruits the T3SS to facilitate translocation of EspC into the host cells (35). However, how EspC can access the closed T3SS translocon to be delivered into the host target is still under investigation.

1.4 Arginine-specific AT of *P. aeruginosa* (AaaA)

The AT AaaA was used in this study as a comparison to confirm the novel EspC findings. In contrast to EspC, AaaA is secreted from a different microbe, *P. aeruginosa* and has a very different function. However, AaaA uses the same route of secretion, the classical route (type Va system) (126). A study conducted by Luckett *et al*., 2012 showed that AaaA is degraded by exogenously added trypsin at the cell surface suggesting that AaaA remains tethered to the OM of the bacterium with its passenger domain exposed to the medium (126). Interestingly, a mutant of *P. aeruginosa* lacking *aaaA* exhibited reduced infection in a mouse chronic wound model suggesting that AaaA enables the opportunistic pathogen *P. aeruginosa* to establish chronic infections in a murine skin wound model although the underlying pathogenicity mechanism is currently unknown (126). How AaaA is regulated and precisely localized in *P. aeruginosa* are still under investigation.

1.5 Localization patterns of AT secretion

ATs are large proteins ranging from 90 to 200 kDa. They have diverse functions and share a tripartite structure of organization widely distributed and conserved among the double layered Gram-negative bacteria. The details of their journey inside the highly organized bacterial cell are not fully uncovered. Thus, understanding the mechanisms involved in their secretion across the bacterial cellular compartments as well as their spatial organization is important for the development of novel anti-virulence compounds.

1.5.1 Polar localization

It has been demonstrated that several ATs from different Gram-negative pathogens such as IcsA, SepA, AIDA-I and BrkA are localized at the bacterial pole dependent upon the existence of complete lipopolysaccharides (LPS), and this localization occurs in the cytoplasm prior to secretion, suggesting the existence of a conserved specialized machinery located at the poles among Gram-negative bacteria (199). In agreement with this finding, Charles *et al.*, 2001 showed that the IcsA AT fused to green fluorescent protein (GFP) lacking the signal peptide sequence or the β-barrel domain is still localized at the old pole of the bacterium, suggesting that the two protein domains are not required for the protein polar targeting. Moreover, this study also revealed that two regions within IcsA were necessary for polar targeting of IcsA-GFP and when produced in a number of bacterial strains including *E. coli*, they found similar results, indicating that the mechanism of polar targeting is conserved among Enterobacteriaceae (200). Furthermore, another similar study also showed that the IcsA AT is located at the bacterial pole when expressed in a SecA depleted strain of *E. coli* (temperature-sensitive strain, MM52), concluding that IcsA uses the Sec machinery to cross the IM only after it has localized to the pole and that the polar translocation event of IcsA occurs in the cytoplasm and is independent of the Sec machinery (201).

The polar localization of IcsA AT was dependent on several bacterial factors including the structure of LPS which can interfere with OM fluidity, i.e. if the strain has incomplete LPS (O-antigen lacking strain) at

its surface, then the rate of protein diffusion at the OM of bacteria will be high and as a consequence would affect the protein localization (199). A more recent study conducted by Doyle *et al*., 2015 contradicted against this notion by finding that IcsA surface distribution is equivalent in strains with complete and incomplete LPS, and that differences in cellular IcsA levels may have confused previous findings (202). A cytoplasmic chaperone (DnaK) was identified as being required for IcsA polar secretion during screening of a genome-wide library of polar secreted *E. coli* proteins, leading to the speculation that it plays a role in the chaperoning of polar AT in the bacterial cytoplasm (203). In addition, a conserved cell division molecule called FtsQ was also shown to be involved in localization of IcsA and other ATs to the bacterial poles (204).

Non-AT proteins with diverse functions are also targeted to the cell poles e.g. proteins involved in motility, adhesion, cell division, virulence and chemotaxis (205,206). Polar localization could utilize the bacterial cytoskeleton actin homologue, MreB. In support of this notion, perturbing MreB in *P. aeruginosa* by A22 affected the polar localization of the type IV pilus retraction ATPase (PilT) and caused mislocalization of PilT as well as attenuation of twitching motility (207). Furthermore, production of IcsA-GFP and GFP-EpsM (a polar IM protein from *Vibrio cholerae*, tagged with GFP at the N-terminus) in *mreB* mutant cells resulted in multiple fluorescent foci that appeared asymmetrically scattered over the entire cell surface, indicating the important role of MreB in organization the polar positioning (208). Interestingly, this study also demonstrated that the localization defect observed in *mreB*

mutant cells upon production of polar proteins was indistinguishable from that which appeared in cells treated with A22. In general, numerous publications have suggested that MreB provides a mechanism for the determination of cell polarity (209-211).

1.5.2 Spiral localization

To date, no evidence in the literature shows that ATs are localized in helices. Preliminary data from the Hardie group have shown that EspC AT can locate to a spiral conformation in a manner resembling the spiral cytoskeleton of *E. coli* when it is tagged with the fluorescent protein mCherry.

1.5.2.1 The bacterial cytoskeleton actin homologue, MreB

MreB is the main helical cytoskeletal component. It is widely conserved and essential for elongation, determining and maintaining the rod cell shape of bacteria (212-214). Other different functions have been assigned to the MreB cytoskeleton, including the establishment of the chromosome segregation and cell polarity (209,215,216). Two lines of recent work have uncovered more specific roles of MreB. First, Strahl and colleagues have shown that in *B. subtilis*, MreB is involved in the distribution and organization of membrane proteins via creation of specific membrane regions with increased fluidity (RIFs). This leads to an overall reduction in membrane fluidity, and disruption of MreB influences the distribution of a number of integral membrane proteins suggesting that the specific role of MreB in providing a fluid membrane

environment is necessary for optimal cell wall synthesis (217). In more recent work, it has been demonstrated that MreB controls the spatiotemporal organization of the cytoplasmic membrane as well as regulating the dynamics of trans-membrane proteins (TMPs) and lipids (218).

Importantly, It has also been suggested that the MreB cytoskeleton could act as a scaffold to provide paths for membrane protein localization and diffusion (207). In rod-shaped bacteria, MreB is essential and found encoded within the *mreBCD* operon with two other adjacent protein components required for cell shape maintenance (219). A study conducted by Vats *et al*., 2009 has actually given insight into the structure of MreB cytoskeleton before cell division, proposing that MreB is split into two equivalent rings that are structurally comprised of multiple proteins including MreC, MreD, PBP2 and RodA which assemble into the cytoskeletal ring (220). This assembly is dependent on the presence of an important component of the cell division apparatus (the FtsZ ring) adjacent to MreB rings (220,221). In *E. coli*, MreB connects directly to the membranes though it's N-terminal amphipathic helix and at the same time interacts directly to the cytoplasmic helix-turn-helix motif (HTH) of the bitopic membrane (single transmembrane α-helix) protein, RodZ (Fig. 1.8), an assembly that has been elucidated to be crucial for controlling the topological growth in *E. coli* (221-226).

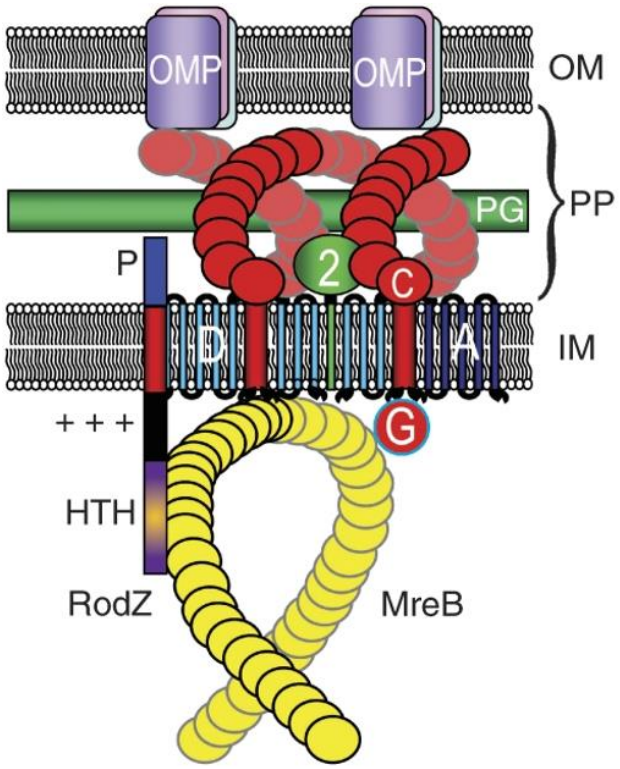


Figure 1.8: Schematic overview of the MreB interaction with PGEM in *E. coli*. MreB filaments interact directly to the IM by its N-terminal amphipathic helix via membrane targeting sequence (MTS) and indirectly through the RodZ HTH motif. MreB firmaments (Yellow) bind to the IM via two regions (see text). RodZ (vertical bar) has four domains. HTH domain that directly interact with MreB, the positively charged Juxta-membrane (JM) domain (+++) presumably provides a strict angular movement of the transmembrane helix via interaction with the negatively charged membrane polar lipids and the transmembrane region. The red helix (MreC) also interacts with MreB as well as with PBP2 (green) and other OMPs. PP, periplasm; PG, peptidoglycan layer; D, MreC; A, RodA. This figure was taken from Gerdes K., 2009 (226).

MreB forms cytoplasmic antiparallel double filaments which dynamically rotate around the cell circumference at the long axis of the cell in a manner reliant on the cell wall synthesis machinery (213,227). The addition of antibiotics targeting specific sites in peptidoglycan synthesis caused rapid termination of filament movement, leading to the proposal that peptidoglycan drives the movement of MreB and not the opposite (212-214,228).

Previously, it was thought that MreB motion is due to the filament polymerization or treadmilling (229,230). However, evidence provided by Garner *et al*., 2011 showed that GFP-MreB containing a mutant to perturb ATP hydrolysis still displayed a circumferential motion, leading to the proposal that a mechanism apart from the filament polymerization dynamics is the driving force of MreB motion (212). This study also brought into doubt the presence of continual helices. Instead it postulated that MreB proteins assembled into discrete patches that move around the cell circumference, independent of each other in both directions perpendicular to the axis of the cell (212). By using total internal reflection fluorescent microscopy (TIRFM) to study major events at the cell surface of *Bacillus subtilis* and to visualize the dynamic collaboration between three MreB isoforms (MreB, MreBH and Mbl), patch-like localization and dynamics were observed. This was also found in *Caulobacter crescentus* and *E. coli*, indicating that these structures are widely conserved (212,228,231).

To understand the exact role of peptidoglycan cell wall synthesis in the dynamics of MreB filaments, most of the studies have focused on the

relationship between MreB filament motion and the elongation of the peptidoglycan cell wall machinery. The thickness of the peptidoglycan layer varies. Gram-positives harbour an external thick peptidoglycan layer and Gram-negatives have a very thin layer between their inner and OMs (212,214,232). In both cases, the peptidoglycan elongation machinery (PGEM) is required for rod-shaped growth and composed of conserved membrane proteins (RodZ, RodA, MreC and MreD) and number of penicillin binding proteins (PBPs) that are responsible for assembling and crosslinking these subunits (232). The class B TPase PBP (PBP2) is essential for cell elongation and require MreB filament for localization as disruption in this specific elongation TPase PBP2 causes cessation in MreB movement, leading to the conclusion that the synthesis of peptidoglycan itself is responsible for providing the driving force which is required for MreB filament motion (212,213,231,233). In agreement with these observations, both peptidoglycan synthesis subunits and MreB paralogs were shown to move around the cell circumference at similar directions and speed (212,231).

1.5.2.2 The bacterial IM Sec machinery

Interestingly, different fluorescent labelling techniques such as GFP-fusions, the biarsenical labelling (fluorescein arsenical hairpin binder (FlAsH) tag) and immunofluorescence have provided evidence that the Sec translocon is distributed in a spiral-like structure. For example, a study conducted by Campo *et al*., 2004 showed that SecA and SecY (the main component of Sec machinery) in *B. subtilis* strains are organized in helix-like structures along the cells similar to the spiral cytoskeleton of

E. coli. The localization of these Sec components in *mreB* or *mbl* mutants was similar, indicating that localization does not rely on the spiral cytoskeleton component, MreB or MbI (234). Consistent with this finding, both SecG without GFP fusion (native SecG detected by employing indirect immunofluorescence microscopy (IFM)) and SecE tagged with green fluorescent protein (GFP) were arranged in a helical conformation in *E. coli*, suggesting that the Sec machinery is arranged into a helical structure distinct from the helical filament of MreB (235). FlAsH-tagged SecY or SecE were also observed in a helical arrangement (141). It is possible that the actin homologue MreB might be implicated in targeting some cytoplasmic proteins toward the Sec translocon machinery, as secretion of colibactin-maturating enzyme (CIbp) across the IM was MreB and Sec/SRP/YidC dependent (236).

Supporting the hypothesis that MreB helical filaments in combination with the Sec machinery may act as a pathway to deliver proteins toward bacterial poles, MreB filaments were implicated in polar localization of IcsA, aspartate chemoreceptor Tar, some polarized proteins in *C. crescentus* and PilT in *P. aeruginosa*, and depletion in MreB causes disturbance in localization of such proteins (207,210). It is apparent that MreB helical filaments are somehow in combination with Sec machinery, and may act as a pathway to deliver proteins toward bacterial poles.

1.6 The pitfalls of fluorescent protein fusions

In recent years, the use of fluorescent tags such as fluorescent proteins and fluorescently labelled antibodies in protein localization studies has

had a huge impact in discovering and understanding the molecular basis of molecular mechanisms in both eukaryotic and prokaryotic cells. However, the use of large fluorescent tags such as mCherry or GFP (~27 kDa) comes with the risk of causing localization artefacts, more likely due to protein aggregation and thus must be carefully controlled (237).

The studies on MreB localization that support the extended MreB helices concluded their results on the basis of fluorescent images generated by fluorescence microscopy of proteins fused with fluorescent tags or cells probed with fluorescently labelled antibodies (238). New super imaging techniques such as electron cryotomography can examine molecules in near-native states increasing the certainty about localization (237). The use of cryotomographic microscopy to localize MreB by Swulius *et al*., 2012 revealed that the spiral filament conformation observed when MreB is fused with yellow fluorescent protein at its N-terminus is an artefact, whereas when MreB is tagged with mCherry within an internal loop, a patchy localization pattern similar to that observed with wild type MreB is detected (228,238). Another study using electron cryotomography also failed to observe long extended spiral filaments adjacent to the membrane and encircling rod-shaped bacteria. Instead, short MreB filaments were seen that could act as a scaffold for peptidoglycan strands (239). Moreover, an analysis using a super resolution variant of total internal reflection microscopy with structured illumination (TIRF-SIM) microscopy could not detect a complete GFP-MreB spiral helix, although it did reveal disconnected filaments of MreB of variable lengths in live *B. subtilis* cells (240). Super resolution fluorescence microscopy also revealed that the synthesis of

peptidoglycan in Gram-negative bacteria occurs in a discontinuous patchy manner mirroring the localization of the MreB cytoskeleton (241). Collectively, this evidence suggests that the use of advanced imaging techniques to monitor protein localization provides greater certainty about their behaviour than conventional fluorescence microscopy (242).

1.7 Main hypothesis and aims of this study

We hypothesize that the bacterial cytoskeleton MreB is important for directing the localization of EspC toward the cell poles by a mechanism that recruits the AT C-terminal β-barrel domain. The spiral distribution of EspC at the cell membranes along the bacterial cytoskeleton is dependent on the dynamic interaction with the actin homologue MreB and Sec translocon.

Building on the preliminary data that revealed a spiral-like structure of EspC-mCherry reminiscent of the bacterial cytoskeleton, this study set out to understand more about the underlying mechanism of AT secretion by:

- monitoring the localization of EspC-mCherry with and without the C-terminal β-barrel domain and comparing this in laboratory strains of *E. coli* and the original host, EPEC.
- evaluating the consequences of utilizing the fluorescent protein mCherry as a tag to localize EspC.

- determining if the pathway of EspC secretion required the actin homologue MreB or the Sec translocon, and whether these are recruited by the AT's β-barrel domain.
- establishing the localization of more than one AT (EspC and AaaA) using a range of fluorescent labels in partnership with advanced super resolution techniques.

Chapter 2

Materials and Methods

2.1 General chemicals

The majority of chemicals used in this study were purchased from Sigma (UK) unless otherwise stated.

2.2 Growth media

2.2.1 Luria Bertani (LB) media

All bacterial strains were routinely grown in Luria Bertani media (LB). The media ingredients were obtained from Oxoid Ltd and prepared as described Sambrook *et al*., 1989 (243). The LB broth was composed of 5 g yeast extract, 10 g tryptone and 10 g NaCl in 1 L of dH_2O. To prepare LB agar, addition of 0.8% (w/v) technical agar No. 3 (Oxoid) to LB broth was applied. The prepared media was autoclaved at 121°C for 20 min at 15 psi prior to use (243).

2.2.2 Minimal Media P (MMP)

Where stated, *E. coli* strains were cultured in MMP. MMP consisted of 0.2 g/L $MgSO_4$, 1.47 g/L Na_2HPO_4, 0.648 g/L KH_2PO_4 and 0.001 g/L $FeSO_4$ (126). For sterilisation, the media was filtered under vacuum.

2.3 Antibiotics and gene expression

Antibiotics were supplemented to the media at the following final concentrations: ampicillin (Amp) (100 µg/ml); chloramphenicol (Cm) (30 µg/ml); kanamycin (Km) (25 µg/ml); tetracycline (Tc) (25 µg/ml)

and streptomycin (Str) (100 µg/ml) unless otherwise stated. For gene expression, L-Arabinose was used to induce the expression of genes under the control of araBAD promoter in pBAD vector. 20% (w/v) L-arabinose was prepared as a stock solution and was mainly added to working concertation of 0.2% (w/v) unless otherwise stated. The preparation of all stock solutions was according to Sambrook *et al*., 1989 (243), and filter sterilised using before 0.22 µm filters provided by Sartorius Stedim Biotech (Minisart®) and stored for further use according to the manufacturers' guidelines.

2.4 Growth and induction conditions

Bacterial strains were routinely grown at 37°C on LB broth shaking at 200 rpm. Strains were maintained on LB agar plates and kept frozen at -80°C in 25% (v/v) glycerol for future use. *E. coli* Δ*secA* strains were grown at 30°C up to OD_{600} of 0.1 then switched to non-permissive temperature at 42°C. To express the recombinant protein, bacterial overnight cultures were diluted 1:100 in LB and either (i) induced concurrently with 0.2% L-arabinose for up to 4 h shaking at 37°C (termed as direct induction), or (ii) induced after reaching OD_{600} of 0.5 for period up to 2 h (referred as indirect induction) unless otherwise stated. Growth of bacterial cultures was measured by absorbance readings at a wavelength of 600 nm (optical density (OD), OD_{600}) using a Thermo Biomate 3 Spectrophotometer.

2.5 Bacterial strains

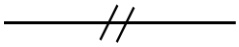
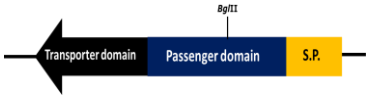
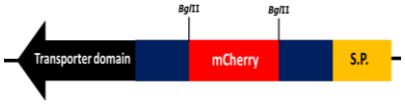
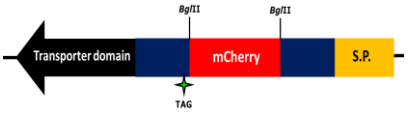
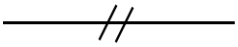
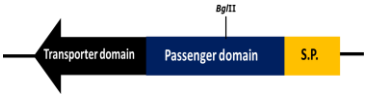
The bac*t*eria strains used in this study are listed in table 2.1.

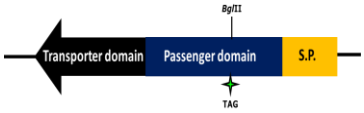
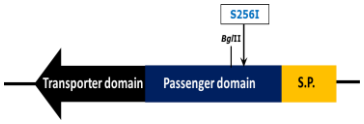
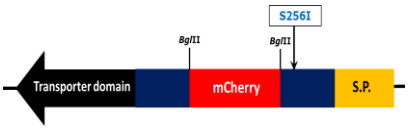
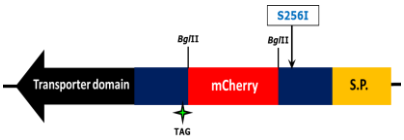
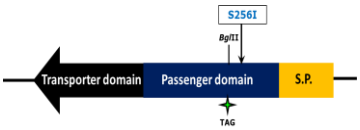
Strain	Genotype or Description	Reference
MG1655	*F- λ- ilvG- rfb-50 rph-1.*	(244)
DH5α	F'/*end*A1, *hsd*R17(R- M+), *supE*44, thi-1, recA1, gyrA, relA1, Δ(*lacZYA-argF*) U169, *deoR* [Φ80d *lac*Δ(*lacZ*) M15].	(243)
EPEC E2348/69	Wild-type EPEC O127:H6 isolated in Taunton (UK) during an outbreak of infantile diarrhea in1969.	(4)
EPECΔ*espC*	EPEC O127:H6 E2348/69 has *espC* gene deletion.	(111)
MM52	*E. coli* has *SecA* mutant (temperature sensitive mutant).	(245)
E. coli Top10	F- *mcr*A Δ(*mrr-hsd*RMS-*mcr*BC) Φ80*lac*ZΔM15 Δ*lac*X74 *rec*A1 *ara*Δ139 Δ(*ara-leu*)7697 *gal*U *gal*K *rps*L (Str^R) *end*A1 *nup*G.	iba company

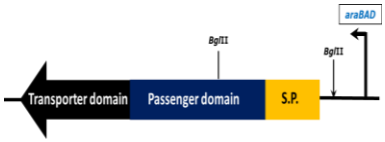
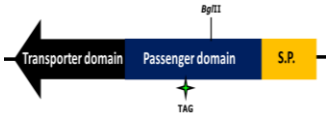
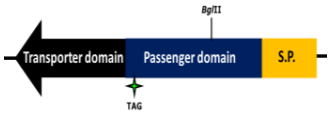
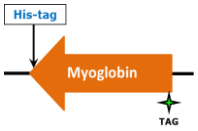
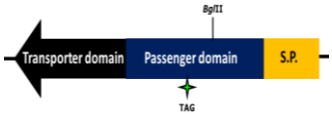
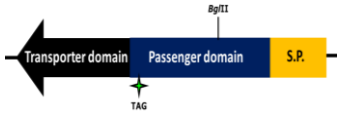
Table 2.1: Bacterial strains used in this study.

2.6 Plasmids

All plasmids used in this study are listed in table 2.2.

Plasmid	Description	Construct depiction	Protein size	Antibiotic resistance	Reference
pBAD18	High copy number with ColE1 and F1 ori. Empty vector under the control of an *araBAD* promoter.		#	Amp^r	Stephanie Pommier
pLADC1	pBAD18 containing native *espC* gene under the control of *araBAD* promoter.		140 kDa	Amp^r	(246)
pLA18C1mc	pBAD18 hosting EspC-mCherry fusion (mCherry was inserted at the *BglII* site approximately in the middle of passenger domain) under the control of an *araBAD* promoter.		174 kDa	Amp^r	Stephanie Pommier
pMAC18-75	pBAD18 containing truncated EspC-mCherry (a stop codon introduced at the end of *mCherry* gene causes a frameshift to truncate translation before the transporter domain) under the control of an *araBAD* promoter.		~70 kDa	Amp^r	(247)
pBAD33	Medium copy number with p15A and F1 ori. Empty vector under the control of an *araBAD* promoter.		#	Cm^r	Stephanie Pommier
pLA33C1	pBAD33 containing native *espC* gene under the control of an *araBAD* promoter.		140 kDa	Cm^r	(246)
pLA33C1mc	pBAD33 hosting EspC-mCherry fusion (mCherry was inserted at the *BglII* site approximately in the middle of passenger domain) under the control of an *araBAD* promoter.		174 kDa	Cm^r	Stephanie Pommier

pMAC33	pBAD33 containing truncated EspC-mCherry (a stop codon introduced at the end of *mCherry* gene causes a frameshift to truncate translation before the transporter domain) under the control of an *araBAD* promoter.		~70 kDa	Cm^r	This study
pMAO33	pBAD33 containing truncated EspC (Opal stop codon inserted after *BglII* site) under the control of an *araBAD* promoter.		~35 kDa	Cm^r	This study
pmCherry	Prokaryotic expression vector encoding red *mCherry* gene under the control of an *araBAD* promoter.		~34 kDa	Amp^r	Stephanie Pommier
pLA33mCherry	pBAD33 containing the *mCherry* gene under the control of an *araBAD* promoter.		~34 kDa	Cm^r	This study
pLA33C1$_{S256I}$	pLA33C1 derivative carrying a substitution of Ser for Ile at codon 256 of the *espC* ORF.		140 kDa	Cm^r	This study
pLA33C1mc$_{S256I}$	pLA33C1mc derivative carrying a substitution of Ser for Ile at codon 256 of the *espC-mCherry* ORF.		174 kDa	Cm^r	This study
pMAC33$_{S256I}$	pMAC33 derivative carrying a substitution of Ser for Ile at codon 256 of the *espC-mCherry* ORF.		~70 kDa	Cm^r	This study
pMAO33$_{S256I}$	pMAO33 derivative carrying a substitution of Ser for Ile at codon 256 of the *espC* ORF.		~35 kDa	Cm^r	This study
pLA33mreB	pBAD33 containing native *mreB* gene under the control of an *araBAD* promoter.		~40 kDa	Cm^r	This study
pLA33mreB$_{AvrII}$	pLA33mreB derivative carrying a substitution of Gly for Arg at codon 228 of *mreB* ORF for encoding *Avr*II restriction site.		~40 kDa	Cm^r	This study

pLA33mreBmc	pBAD33 containing MreB-mCherry fusion (mCherry was inserted at the *AvrII* site) under the control of an *araBAD* promoter.		~74 kDa	Cm^r	This study
pLA33C1$_{BglII}$	pLA33C1 derivative containing additional *Bgl*II restriction site inserted upstream of the *espC* ORF by SDM.		140 kDa	Cm^r	This study
pLA33C1^{TAG533}	pLA33C1 derivative containing an Amber stop codon inserted at 533 aa position of the *espC* ORF.		55 kDa	Cm^r	This study
pLA33C1^{TAG951}	pLA33C1 derivative containing an Amber stop codon inserted at 951 aa position of the *espC* ORF.		110 kDa	Cm^r	This study
p*Myo*4TAGPylT-*his6*	Plasmid carrying a sperm whale myoglobin (*myo*) gene with an amber stop codon replaced the codon 4 of *myo* ORF and His-tagged at the C-terminal. This gene is under the control of *araBAD* promoter. This plasmid also hosts the *PylT* gene from *Methanosarcina barkeri* (*Mb*) (strain MS) with an *lpp* promoter and *rrnC* terminator.		~19 kDa	Tc^r	(248,249)
pBK-PylSΔ	pBK plasmid encompassing The *Mb* MS *PylS* mutant gene under the control of *E. coli GlnRS* promoter and terminator.		~47 kDa	Km^r	(248,250)
p*Esp*C533TAGPylT	p*Myo*4TAGPylT-*his6* derivative containing *espC* gene encoded with TAG at position 522 replacing the *myo* gene under the control of an *araBAD* promoter.		55 kDa	Tc^r	This study
p*Esp*C951TAGPylT	p*Myo*4TAGPylT-*his6* derivative containing *espC* gene encoded with TAG at position 951 replacing the *myo* gene under the control of an *araBAD* promoter.		110 kDa	Tc^r	This study

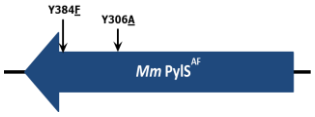
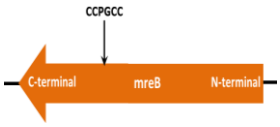
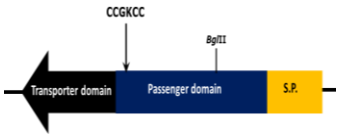
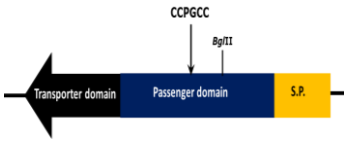
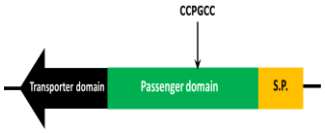
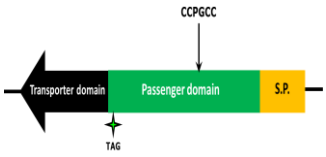
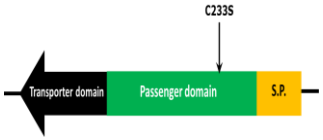
pBK-PylS^{WT}	pBK-PylSΔ derivative carrying *Methanosarcina mazei* (*Mm*) *PylS* gene replacing the *Mb MS PylS* mutant gene.		~51 kDa	Km^r	This study
pBK-PylS^{AF}	pBK-PylS^{WT} derivative carrying *Mm PylS* gene with double mutant (Y306A and Y384F).		~51 kDa	Km^r	This study
pLA33mreB-TC	pLA33mreB derivative carrying CCPGCC tagged MreB. The TC motif inserted after Tyr residue at codon 226 of the *mreB* ORF.		~40 kDa	Cm^r	This study
pLA33C1-TC^{CCGKCC}	pLA33C1 derivative carrying CCGKCC tagged EspC. The TC motif inserted after Gly residue at codon 896 of the *espC* ORF.		140 kDa	Cm^r	This study
pLA33C1-TC^{CCPGCC}	pLA33C1 derivative carrying CCPGCC tagged EspC. The TC motif inserted after Gln residue at codon 530 of the *espC* ORF.		140 kDa	Cm^r	This study
pET21a::aaaA	Plasmid containing *aaaA* gene under control of an IPTG inducible promoter.		80 kDa	Amp^r	(126)
pLA33aaaA	pBAD33 containing native *aaaA* gene under the control of an *araBAD* promoter.		80 kDa	Cm^r	This study
pLA33aaaA-TC	pLA33aaaA derivative carrying CCPGCC tagged AaaA. The TC motif inserted after Leu residue at codon 291 of the *aaaA* ORF.		80 kDa	Cm^r	This study
pLA33aaaA-TCΔ	pLA33aaaA-TC derivative carrying CCPGCC tagged AaaA, with codon 343 replaced by an amber codon.		~38 kDa	Cm^r	This study
pLA33aaaA^{C233S}	pLA33aaaA derivative carrying a substitution of Cys for Ser at codon 233 the *aaaA* ORF.		80 kDa	Cm^r	This study

Table 2.2: Plasmids used in this study.

2.7 DNA Preparation, manipulation and analysis

2.7.1 Extraction of plasmid DNA

High or medium copy-number plasmids were routinely isolated from the *E. coli* cultures using GenElute™ plasmid miniprep kit (Sigma) according to the manufacturers' protocols. Plasmid DNA was eluted into 25-35 µl molecular biology grade H_2O (Fisher Scientific, UK).

2.7.2 Quantifying DNA concentrations

To measure the concentration of DNA, the NanoDrap® ND-1000 (Nanodrop Technologies) was utilized. 1.2 µl of DNA sample was applied to determine characteristic absorbance and concentrations. Whole spectra of samples could also be measured to evaluate purity.

2.7.3 Restriction enzyme digestion of DNA

Restriction enzymes were purchased form New England Biolabs (UK) and from Promega (UK) and were used according to the manufacturer's recommendations. In general, the digestion reactions contained 0.1-0.9 µg DNA, 0.5-1 µl restriction enzyme(s) and 10x suitable restriction buffer made to a total volume of 10-20 µl with molecular biology grade H_2O (Fisher Scientific, UK). Samples were incubated at 37°C for 1-2 h dependent on the quantity of DNA in the reactions.

2.7.4 Analysis and purification of DNA by agarose gel electrophoresis

DNA samples were mixed with DNA blue gel loading dye purchased from New England Biolabs (UK) and loaded on 0.8-1% (w/v) agarose gels using a horizontal gel apparatus (Biorad, UK). The preparation of the gels were carried out according the procedure described by Sambrook e*t al*., 1989 using agarose bioreagent dissolved in 1x tris-acetate-ethylenediaminetetraacetic acid (TAE) buffer (table 2.3) with the addition of 10,000X SYBR® Safe DNA Gel Stain concentrate (dissolved in dimethyl sulfoxide (DMSO)) (Invitrogen) used at dilution 1:10,000 in 1X TAE buffer (243). The gels were run in 1× TAE buffer and electrophoresis was performed at 95-100 V. DNA fragments were visualized on Biorad Gel DOC™ XR+ with image Lab™ Software. For cutting the DNA fragments, a UV safe Visi-Blue™ Transilluminator was utilized. DNA fragments were extracted from agarose gel slices using the QIAquick® Gel Extraction Kit [50] (QIAGEN, Ltd) following the manufacturers' protocols. Final elution of the purified DNA product was carried out using 15-20 µl molecular biology grade H_2O (Fisher Scientific, UK).

1x TAE	Concentrations
EDTA pH 8.0	50 mM
Tris-acetate-EDTA base	40 mM
Glacial acetic acid	0.1142% (v/v)

Table 2.3: Standard recipes for agarose gel electrophoresis. 1x TAE was stored at RT.

2.7.5 Molecular weight marker

To measure or estimate the size of DNA fragments, 1 kb DNA ladder (New England Biolabs (N3232S), UK) was used in this study. 1 µg of 1 kb DNA ladder was mixed with 1x blue DNA loading dye and made to final volume of 6 µl with molecular biology grade H_2O (Fisher Scientific, UK). Loading this mixture on 0.8% agarose gels reveals the size of DNA bands hosted in the 1 kb DNA ladder (Fig. 2.1).

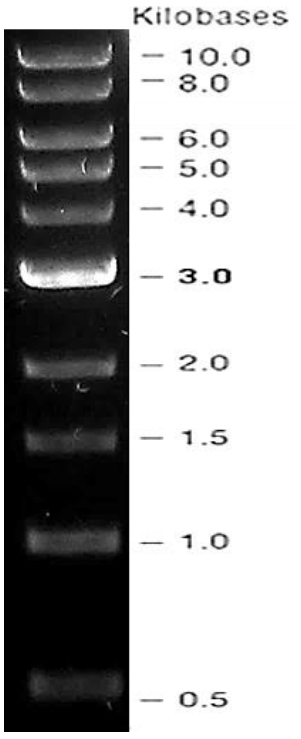


Figure 2.1: 1 kb DNA ladder visualized by SYBR® Safe DNA Gel Stain on 0.8% 1x TAE agarose gel transferred at 100V. The DNA fragments appears clearly ranging from 0.5 to 10.0 kilobases (kb).

2.7.6 DNA ligation reactions

All ligation reactions were performed using T4 DNA ligase (Promega, UK). The reaction volume was routinely prepared in a final volume of 20 µl contained 1 µl T4 DNA Ligase, 2 µl T4 ligation buffer and 1:5 ratio of vector to insert following by incubated O/N at 16°C. To calculate the appropriate volumes of vector and insert needed for achieving successful ligation reaction, the following formula was used according to manufacturers' protocol; (ng vector X Kb size insert / Kb size of vector) X Molar ratio of (5/1) = ng insert.

2.8 Polymerase Chain Reaction (PCR) amplification

2.8.1 Synthesis of oligonucleotide primers

All oligonucleotide primers were designed using American SnapGene® software and synthesised by Sigma-Aldrich Ltd (UK). Designed primers were further analysed using oligonucleotide properties calculator website (http://www.basic.northwestern.edu/biotools/OligoCalc.html). A variety of primers were made in this study contained a minimum of 18 bases to ensure a correct hybridization. Primer sequences used in this study are listed in table 2.4.

Primer Name	Primer Sequence (5`to 3`)	Description
F-*Bgl*II-mCherry	**CT**AGATCT**T***ATG*GTGAGCAAGG GCGAG	Forward primer used to amplify the *mCherry* ORF region with the underlined *Bgl*II restriction site directly upstream of the start codon (italic). The bold nucleotides are additional bases to make mCherry in frame with *espC*. This primer designed by Stephanie Pommier for generating EspC-mCherry fusion.
R-*Bgl*II-mCherry-FL	**AG**AGATCT**AA**CTTGTACAGCTC GTCCAT	Reverse primer used to amplify the *mCherry* ORF region with the underlined *Bgl*II restriction site directly downstream of *mCherry* gene replacing the stop codon. The bold nucleotides are additional bases to make mCherry in frame with *espC*. This primer designed by Stephanie Pommier for generating full length EspC-mCherry fusion.
R-*Bgl*II-mCherry-Δ	**AG**AGATCT**AAA***A*CTTGTACAGCT CGTCCA	Reverse primer used to amplify the *mCherry* ORF region with the underlined *Bgl*II restriction site directly downstream of *mCherry* gene replacing the stop codon. This primer in particular contains an extra italic bold base to create a frameshift that led to create short EspC-mCherry fusion version (pMAC33). This primer designed by Stephanie Pommier.
F-*Bgl*II mCherry	**ATA**AGATCT*ATG*GTGAGCAAGG GCGAGGAGGAT	Forward primer used to amplify the *mCherry* ORF region with the underlined *Bgl*II restriction site directly upstream of the ATG start codon (italic). The bold nucleotides are additional bases to ensure accurate *Bgl*II restriction site digestion. This primer used to create pLA33mChery vector.
R-*Sal*I mCherry	**TAT**GTCGACCTTGTACAGCTCG TCCATGCCGCCG	Reverse primer used to amplify the *mCherry* ORF region with the underlined *Sal*II restriction site directly downstream of *mCherry* gene. The bold nucleotides are additional bases to ensure accurate *Bgl*II restriction site digestion. Please note that the stop codon was autonomously introduced downstream the restriction site. This primer used to create pLA33mCherry vector.
F-TGA-*Bgl*II	GCAAAAAATAATAATAACTATAA **AGATCT**AAGTTGATTTAGTGGT GGTGGAAGTATTAATTTCGACA	Forward primer used to amplify pLA33C1 plasmid for encoding the *espC* ORF region with the underlined opal stop codon at 344 aa position. The bold nucleotides represent the *Bgl*II restriction site.

R-TGA-*Bgl*II	TGTCGAAATTAATACTTCCACCA CCACTAAATCAACTT**AGATCT**TT ATAGTTATTATTATTTTTTGC	Reverse primer used to amplify pLA33C1 plasmid for encoding the *espC* ORF region with the underlined opal stop codon at 344 aa position. The bold nucleotides represent the *Bgl*II restriction site.
F-pLA33C1-*Bgl*II	CCATACCCGTTTTTTTGGGCTAG CGAAT**AGATCT**TCGAGCTCGAT CTGGTGATAA	Forward primer used to amplify pLA33C1 plasmid to insert the bold *Bgl*II restriction site in pBAD33 vector backbone downstream of *araBAD* promoter.
R-pLA33C1-*Bgl*II	TTATCACCAGATCGAGCTCGA**A GATCT**ATTCGCTAGCCCAAAAA AACGGGTATGG	Reverse primer used to amplify pLA33C1 plasmid to insert the bold *Bgl*II restriction site in pBAD33 vector backbone downstream of *araBAD* promoter.
F-MreB-*Bgl*II	**TAT**AGATCT*ATG*TTGAAAAAATT TCGTGGCAT	Forward primer used to amplify the *mreB* ORF region with the underlined *Bgl*II restriction site directly upstream of the ATG start codon (italic). The bold nucleotides are additional bases to ensure accurate *Bgl*II restriction site digestion.
R-MreB-*Sal*I	**ATA**GTCGAC*TTA*CTCTTCGCTGA ACAGGTC	Reverse primer used to amplify the *mreB* ORF region with the underlined *Sal*I restriction site directly downstream of TAA stop codon (italic). The bold nucleotides are additional bases to ensure accurate *Sal*I restriction site digestion.
F-MreB-*Avr*II	GAAATCGGTTCGGCTTATCC**TA G****G**GATGAAGTCCGTGAAATCGA	Forward primer used to amplify pLA33mreB for encoding the *mreB* ORF region with the underlined *Avr*II restriction site. The bold nucleotides represent the changed bases that required for encoding *Avr*II restriction site.
R-MreB-*Avr*II	TCGATTTCACGGACTTCATC**C**C**T A**GGATAAGCCGAACCGATTTC	Reverse primer used to amplify pLA33mreB for encoding the *mreB* ORF region with the underlined *Avr*II restriction site. The bold nucleotides represent the changed bases that required for encoding *Avr*II restriction site.
mCherry-F-MreB	**ATA**CCTAGG*ATG*GTGAGCAAGG GCGAGGAGGAT	Forward primer used to amplify the *mCherry* ORF region with the underlined *Avr*II restriction site directly upstream of the start codon (italic). The bold nucleotides are additional bases to ensure accurate *Avr*II restriction site digestion.
mCherry-R-MreB	**TAT**CCTAGGCTTGTACAGCTCG TCCATGCCGCCG	Reverse primer used to amplify the *mCherry* ORF region with the underlined *Avr*II restriction site directly downstream of *mCherry* gene replacing the stop codon. The bold nucleotides are additional bases to ensure accurate *Avr*II restriction site

		digestion.
EspC-F S256I	CGGTGGAGAC**A<u>T</u>T**GGTTCCGGT TTCTATCTGTATGATAACGT	Forward primer used to amplify the *espC* ORF region with bold codon for substitution of Ser for Ile. The bold underlined nucleotide represent the changed base that required for encoding Ile instead of Ser.*****
EspC-R S256I	ACGTTATCATACAGATAGAAACC GGAACC**A<u>A</u>T**GTCTCCACCG	Reverse primer used to amplify the *espC* ORF region with bold codon for substitution of Ser for Ile. The bolded underlined nucleotide represent the changed base that required for encoding Ile instead of Ser *****
F-TAG533espC	TCAGGTAATACAGAGATAAACCA CCAGTTTGAT**TAG**ACCCAAAAAA ATAATAGTCGCCTGATTCTGG	Forward primer used to amplify pLA33C1 and target the *espC* ORF region for insertion the bold amber stop codon at positon 533 aa.
R-TAG533espC	CCAGAATCAGGCGACTATTATTT TTTTGGGT**CTA**ATCAAACTGGTG GTTTATCTCTGTATTACCTGA	Reverse primer used to amplify pLA33C1 and target the *espC* ORF region for insertion the bold amber stop codon at positon 533 aa.
F-TAG951espC	GTCCTGGTCGACTTTTTAAACAA GCCAGCCAGT**TAG**GAAATGAAC GTGACGTTAATTACCGCACCGA	Forward primer used to amplify pLA33C1 and target the *espC* ORF region for insertion the bold amber stop codon at positon 951 aa.
R-TAG951espC	TCGGTGCGGTAATTAACGTCAC GTTCATTTC**CTA**ACTGGCTGGCT TGTTTAAAAAGTCGACCAGGAC	Reverse primer used to amplify pLA33C1 and target the *espC* ORF region for insertion the bold amber stop codon at positon 951 aa.
F-espC	TTTATCGCAACTCTCTACTGTTT	Forward primer used to amplify the *espC* ORF region. This primer was designed to flank *araBAD* region to enable amplifying *Sac*I restriction site that situated between the promotor and *espC* ORF region in pLA33C1 vector.
R-*Apa*I-espC	TGCATGCCTGCA**GGGCCC**GGTC GACTCTAGG	Reverse primer used to amplify the *espC* ORF region with the bold *Apa*I restriction site downstream of *espC* gene in pLA33C1 vector.
F-pBK-*Sal*I	AGCACGAACCTG<u>TAA</u>**GTCGAC**T TTCAAACGCTAAATTGCCTGATG CGCTACGC	Forward primer used to amplify pBK-PylSΔ plasmid with bold *Sal*I restriction site directly downstream of the stop codon (underlined) of *MbpylS* ORF region.
R-pBK-*Sal*I	GCGTAGCGCATCAGGCAATTTA GCGTTTGAAA**GTCGAC**<u>TTA</u>CAG GTTCGTGCT	Reverse primer used to amplify pBK-PylSΔ plasmid with bold *Sal*I restriction site directly downstream of the stop codon (underlined) of *MbpylS* ORF region.

F-Mazei-*Nde*I	**ATA**CATATG*ATG*GATAAAAAAC CACTAAAC	Forward primer used to amplify the *MmPylS* ORF region with an underlined *Nde*I restriction site directly upstream of the start codon (italic). The bold nucleotides are additional bases to guarantee accurate *Nde*I restriction site digestion.
R-Mazei-*Sal*I	**TAT**GTCGAC*TTA*CAGGTTGGTA GAAATCC	Reverse primer used to amplify the *MmPylS* ORF region with an underlined *Sal*I restriction site directly downstream of the stop codon (italic). The bold nucleotides are additional bases to guarantee accurate *Sal*I restriction site digestion.
F-*Mm*PylS-Y306A	TTGCTCCAAACCTT**GCC**AACTAC CTGCGCAAGCTTGACAGGGCCC TGCC	Forward primer used to amplify pBK-PylS plasmid (hosting *Mm*PylS^{WT}) for encoding the *MmPylS* ORF region with bold codon for substitution of Tyr for Ala at aa position 306. The underlined nucleotides represent the changed bases that required for the mutation.
R-*Mm*PylS-Y306A	GGCAGGGCCCTGTCAAGCTTGC GCAGGTAGTT**GGC**AAGGTTTGG AGCAA	Reverse primer used to amplify pBK-PylS plasmid (hosting *Mm*PylS^{WT}) for encoding the *MmPylS* ORF region with bold codon for substitution of Tyr for Ala at aa position 306. The underlined nucleotides represent the changed bases that required for the mutation.
F-tRNA mut	TCGATCTACATGATCAGGTT**T**CC GCGGCCGCGAATTCAGCGTTAC AAGTA	Forward primer used to amplify p*Myo*4TAGPylT-*his6* plasmid for substitution guanine nueclotide for adenenie at the acceptor stem of the suppressor tRNA.
R-tRNA mut	TACTTGTAACGCTGAATTCGCGG CCGCGG**A**AACCTGATCATGTAG ATCGA	Reverse primer used to amplify p*Myo*4TAGPylT-*his6* plasmid for substitution guanine nueclotide for adenenie at the acceptor stem of the suppressor tRNA.
F-*Mm*PylS-Y384F	TCGTAGGCGATTCCTGCATGGT C**TT**GGGGATACCCTTGATGTA ATG	Forward primer used to amplify pBK-PylS plasmid (hosting *Mm*PylS ^{Y306A}) for encoding the *MmPylS* ORF region with bold codon for substitution of Tyr for Phe at aa position 384. The underlined bold nucleotide represents the changed base that required for the mutation.
R-*Mm*PylS-Y384F	CATTACATCAAGGGTATCCCC**A AA**GACCATGCAGGAATCGCCTA CGA	Reverse primer used to amplify pBK-PylS plasmid (hosting *Mm*PylS ^{Y306A}) for encoding the *MmPylS* ORF region with bold codon for substitution of Tyr for Phe at aa position 384. The underlined bold nucleotide represents the changed base that required for the mutation.

F-MreB CCXXCC	TCGGTTCGGCTTAT**TGTTGC**CC GGGC**TGTTGC**GATGAAGTCCGT GAAAT	Forward primer used to amplify pLA33mreB plasmid for encoding the *mreB* ORF region with the bold codons to generate the optimal CCPGCC motif. XX are representing Pro-227–Gly228 residues.
R-MreB CCXXCC	ATTTCACGGACTTCATC**GCAAC A**GCCCGG**GCAACA**ATAAGCCG AACCGA	Reverse primer used to amplify pLA33mreB plasmid for encoding the *mreB* ORF region with the bold codons to generate the optimal CCPGCC motif. XX are representing Pro-227–Gly228 residues.
F-EspC CCXXCC	GTTGAACTGGGGGGC**TGTTGC** GGGAAA**TGCTGT**GACTTTGCCA CCCTGCGGGT	Forward primer used to amplify pLA33C1 plasmid for encoding the *espC* ORF region with the bold codons to generate CCGKCC motif. XX are representing Gly-897–Lys-898 residues.
R-EspC CCXXCC	ACCCGCAGGGTGGCAAAGTC**AC AGCA**TTTCCC**GCAACA**GCCCCC CAGTTCAAC	Reverse primer used to amplify pLA33C1 plasmid for encoding the *espC* ORF region with the bold codons to generate CCGKCC motif. XX are representing Gly-897–Lys-898 residues.
F-EspC CCPGCC	CAGAGATAAACCACCAG**TGCTG TCCAGGCTGCTGC**TTTGATACC CAAAAAAATAATAGTCGC	Forward primer used to amplify pLA33C1 plasmid for encoding the *espC* ORF region with the bold codons to generate the optimal CCPGCC motif. This motif sequence is inserted between Gln-530 and Phe-531 residues.
R-EspC CCPGCC	GCGACTATTATTTTTTGGGTAT CAAA**GCAGCAGCCTGGACAGC A**CTGGTGGTTTATCTCTG	Reverse primer used to amplify pLA33C1 plasmid for encoding the *espC* ORF region with the bold codons to generate the optimal CCPGCC motif. This motif sequence is inserted between Gln-530 and Phe-531 residues.
F-AaaA CCPXCC	AGTACTGACCAACGCCCTC**TGC TGTCCA**GGC**TGCTGC**CAGGAG CGCATCGAGC	Forward primer used to amplify pLA33aaaA plasmid for encoding the *aaaA* ORF region with the bold codons to generate the optimal CCPGCC motif. X is representing Gly-292 residue.
R-AaaA CCPXCC	GCTCGATGCGCTCCTG**GCAGCA** GCC**TGGACAGCA**GAGGGCGTT GGTCAGTACT	Reverse primer used to amplify pLA33aaaA plasmid for encoding the *aaaA ORF* region with the bold codons to generate the optimal CCPGCC motif. X is representing Gly-292 residue.
F-AaaA C233S	CGGCGGGTACCGGCTGC**TC**AAG CGACGGCGAAAGCTTCAACGG	Forward primer used to amplify pLA33aaaA plasmid for encoding the *aaaA* ORF region with the bold nucleotides for substitution of Cys for Ser at 233 aa position.
R-AaaA C233S	CCGTTGAAGCTTTCGCCGTCGCT	Reverse primer used to amplify pLA33aaaA plasmid for encoding the *aaaA* ORF region

	T**GA**GCAGCCGGTACCCGCCG	with the bold nucleotides for substitution of Cys for Ser at 233 aa position.
F-AaaATAG343	ATGGAAGACCAGTTG**<u>T</u>AG**CGCC AGCATCAGGCACT	Forward primer used to amplify pLA33aaaA-TC plasmid for encoding the *aaaA* ORF region with the bold amber stop codon at aa positon 343. The underlined bold nucleotide is representing the changed base that required for the mutation.
R-AaaATAG343	AGTGCCTGATGCTGGCG**CTA<u>A</u>**CA ACTGGTCTTCCAT	Reverse primer used to amplify pLA33aaaA-TC plasmid for encoding the *aaaA* ORF region with the black bold amber stop codon at aa positon 343. The underlined bold nucleotide is representing the changed base that required for the mutation.
Primers for sequencing		
espCFNO1	GATCTGGTGATAAAAACATTA	Primer to sequence *espC* (246).
espCF12	AAGTTTGTTGTTGAAACA	Primer to sequence *espC* (246).
mCherry MA-F MID	TCCCCGACTACTTGAAGCTG	Primer to sequence *mCherry*.
pLADCBP3f	TTAGAGAGGGTGGGGGTTACCT GCATGCTGC	Primer to sequence *espC* (246).
Primer MA2-F	GAAACAGGAGTATTACTCCC	Primer to sequence *mCherry*.
espCKHf1	GAACAAGCGTATGGGTGA	Primer to sequence *espC* (246).
AaaA upstream F1	CACGGCGTCACACTTTGCTATGC CA	Primer to sequence *aaaA*.
AaaA-F2	GGTTCGCGTGCCTACGTCGAGT CCCT	Primer to sequence *aaaA*.
AaaA-F3	GTTTCGACATGCCTGGCAATCC GG	Primer to sequence *aaaA*.
AaaA-F4	GACATGGGCGGCGTGGACAAG GATTTCG	Primer to sequence *aaaA*.
MreB-F2	TGGTACCACTGAAGTTGCTGTTA T	Primer to sequence *mreB*.
F-Myo4TAG	ATGACAAAAACGCGTAACAAAA GTG	Primer to sequence *myoglobin*.
F-tRNA syn 1	AGATCATACGCCGTTATACGTTG TTT	Primer to sequence *MbpylS*Δ.
F-tRNA syn 2	TATACCAACGATCGTGAAGATTA TCT	Primer to sequence *MbpylS*Δ.

M-mazei F1	AGCCTGTCCCGCTTATAAGAT	Primer to sequence *MmpylS*^{AF}.
M-mazei F2	GCACAGGCTCAACCTTCTGGATC	Primer to sequence *MmpylS*^{AF}.
M-mazei F3	GGATGGGCATTGATAATGATA	Primer to sequence *MmpylS*^{AF}.
M-mazei F4	ATACCGCTTGACCGGGAATGG	Primer to sequence *MmpylS*^{AF}.
F-pylT	ACCGGAAGGAGCTACCGGC	Primer to sequence tRNA-Pyl (*pylT*) gene.

Table 2.4: Oligonucleotide primers used in this study.
* These primers used to create pLA33C1$_{S256I}$, pLA33C1mc$_{S256I}$, pMAC33$_{S256I}$ and pMAO33$_{S256I}$ plasmids.

2.8.2 PCR amplification

2.8.2.1 Conventional PCR

A standard PCR amplification was performed according to methods described by *Saiki et al*., 1988 in a final volume of 25 µl using Q5® High-fidelity PCR Kit (New England BioLabs (E0555S/L), UK) (251). Reactions were carried out in SensoQuest Labcycler (SensoQuest GmbH) for a total of 35 cycles. The components of the PCR reaction as well as the thermocycling conditions used in this study are shown in table 2.5.

2.8.2.2 Site-directed mutagenesis PCR

Site-directed mutagenesis (SDM) was carried out by following the principles described in the QuikChange II Site-Directed Mutagenesis Kit, Instruction manual (from Agilent Technology). To obtain high mutation efficiencies, the high fidelity *Pfu* DNA polymerase was used (Promega,

PCR Mix		
Components	**Volumes**	**Final concentration**
Q5 High-Fidelity 2X Master Mix	12.5 µl	1X
10 µM Forward primer	1.25 µl	0.5 µM
10 µM Reverse primer	1.25 µl	0.5 µM
DNA template	variable	25 ng-75 ng
Nuclease-Free Water	to 25 µl	
Thermocycling conditions		
Cycle Stage	**Temperature**	**Time and Repetitions**
Initial denaturation	98°C	30 sec / one cycle
Denaturation	98°C	10 sec
Annealing	55°C *	30 sec
Extension	72°C	30 sec every 1kb
Final Extension	72°C	2 min / one cycle
Hold	4°C	Pause

35 cycles

Table 2.5: Routine PCR mixture and cycling parameters utilized in this study.
***** The annealing temperature was changed depending on the nature of the primers used and the stringency levels required.

M7741). To avoid the existence of any parental templates in the PCR products, the products were digested by *Dpn*I enzyme (Promega, R6231) at 37°C for 1 h following by transformation into *E. coli* Top10 torepair the nicks. Mutated plasmids were further extracted and transformed into freshly prepared $CaCl_2$ MG1655 for further analysis. The PCR reaction and conditions are shown in table 2.6.

PCR Mix		
Components	**Volumes**	**Final concentration**
Pfu Buffer 10X	5 µl	1X
10 µM forward primer	1 µl	0.2 µM
10 µM Reverse primer	1 µl	0.2 µM
DNA template	variable	35 ng-50 ng
dNTP mix, 10 mM each	1 µl	200 µM each
DMSO (optional) *	1 µl	2%
Pfu DNA polymerase	1 µl	2-3 units/µl
Nuclease-Free Water	to 50µl	

Thermocycling conditions			
Cycle Stage	**Temperature**	**Time and Repetitions**	
Initial denaturation	95°C	30 sec / one cycle	
Denaturation	95°C	30 sec	12-16 cycles
Annealing	55°C **	1 min	
Extension	68°C	1 min every 1kb	
Hold	4°C	Pause	

Table 2.6: SDM PCR mixture and cycling parameters used in this study.
***** To enhance the PCR amplification DMSO sometimes added in some reactions.
****** The annealing temperature was changed depending on the nature of the primers used and the stringency levels required.

2.9 DNA sequencing

When necessary, DNA sequencing was conducted by Source BioScience, Nottingham, using Sanger sequencing services and ABI3730XL sequencer. Prepared sequence data were download via Source BioScience SpeedREAD automated data delivery system and analysed using the SnapGene® software. Alignment of DNA or protein sequences to identify homology was achieved using the Basic Local Alignment

Search Tool 'BLAST' provided by NCBI (http://blast.ncbi.nlm.nih.gov/Blast.cgi). The Sequences of the pre-determined DNA and protein were obtained from the NCBI (http://www.ncbi.nlm.nih.gov/) using gene and protein databases respectively. Furthermore, the *E.coli* K-12 MG1655 genome sequence database (http://www.ecogene.org/) was also used to analyse MG1655 sequences.

2.10 Transformation

2.10.1 Preparation of chemically competent *E. coli* cells

To prepare chemical competent *E. coli* cells, 1 ml from an overnight (O/N) *E. coli* culture was added to 99 ml of sterile LB broth (1:100 dilution) in 500 ml flasks and grown at 37°C with shaking at 200 rpm until reaching OD_{600} of 0.4-0.5. Subsequently, Cells were harvested by centrifugation at 5500 rpm (Allegra™X-22R centrifuge, Beckman Coulter) for 10 min at 4°C and resuspended in ice cold sterile 50 ml 100 mM $CaCl_2$ before being incubated in ice for 40-60 min. Once incubated, cells were harvested again at the same conditions and finally resuspended in ice cold sterile 5 ml 100 mM $CaCl_2$. Cells were aliquoted into 300 µl and immediately used for heat shock transformation. If necessary, cells were aliquoted into 300 µl containing 10% (v/v) sterile glycerol in sterile Eppendorf tubes before quick freezing in liquid nitrogen and storage at -80°C freezer for future use.

2.10.2 Heat chock transformation

Heat shock was performed by first adding 100 ng of DNA (or 8-10 µl from the ligation reaction) to 300 µl of $CaCl_2$ competent *E. coli* cells followed by 45 min on ice, 1-2 min shock at 42°C and 2 min on ice. Then, 700 µl of SOC outgrowth broth (New England BioLabs, B9020S) added followed by incubation at 37°C (shaking at 200 rpm) for 60 min in absence of antibiotics. Subsequently, after finishing the incubation period, centrifugation 2 min at 5500 rpm and 800 µl of the supernatant was discarded and the reminder was resuspeneded and platted in 50 µl aliquots onto LB agar plates containing appropriate antibiotics for selection of transformants. Finally, plates were incubated O/N at 37°C. Likewise, Negative controls of heat shocked cells with no plasmids were prepared.

2.10.3 Heat chock transformation using the commercial provided Top10 *E. coli* cells.

The competent *E. coli* Top10 cells (IBA) were only used to perform site directed mutagenesis. Top10 cells were transformed with mutated plasmid DNA according to the manufacturer's recommendations. Briefly, 100 µl of Top10 *E. coli* cells were mixed with 10 µl of *Dpn*I digested PCR reaction followed by 30 min incubation on ice, shock at 37°C for 5 min and cooling between 2-5 min on ice. Then, 900 µl of SOC broth added followed by incubation at 37°C (shaking at 200 rpm) for 45 min. After finishing the incubation period, centrifugation 2 min at 5500 rpm and continue as described in section 2.10.2.

2.11 Protein sample preparation and analysis

2.11.1 *E. coli* whole cell protein preparation

E. coli strains to be investigated were grown in LB broth as previously described. After finishing the induction time, the OD_{600} of the culture was measured and 1 ml aliquots removed from the culture and used to prepare the samples. The aliquots were pelleted by centrifugation for 1-2 min at 13,000 rpm and then resuspended in 200 µL of 1 X sodium dodecyl sulphate-polyacrylamide gel electrophoresis (SDS-PAGE) loading buffer (50 mM Tris-HCl, pH 6.8, 100 mM dithiothreitol (DTT), 2% (w/v) sodium dodecyl sulphate (SDS), 0.1% (w/v) bromophenol blue and 10% (v/v) sterile Glycerol). When necessary, samples were sonicated at amplitude 5-10 microns for 10 s to avoid the sample viscosity using an MSE Soniprep 150. To guarantee the denaturation of the proteins, the lysates were boiled at 100°C for 10 min before loading onto the gel.

2.11.2 *E. coli* secreted protein preparation

Supernatant samples containing proteins were collected by centrifugation 5 min at 13,000 rpm then precipitated with 10 % (v/v) trichloroacetic acid (TCA) for 30 min on ice followed by 15 min centrifugation to obtain the precipitated proteins. Subsequently, samples were washed with ice cold acetone and allowed to air dry by inverting the tubes for 15 min. Dried pellets were then resuspended in 1X SDS-PAGE loading buffer and boiled 5 min at 100°C prior loading onto the SDS-PAGE gel for analysis.

2.11.3 SDS-PAGE gel preparation

The analysis of proteins and SDS-PAGE were performed as described by Cooksley *et al*., 2003 (252). Dependent on the molecular weight of the investigated proteins, both 9% and 12% polyacrylamide separating gels were used in this study. To allow separation of protein mixture through the separating gel, protein samples had first been electrophoresed through a 5% stacking gel. The composition of both separating and stacking gels are shown in table 2.7. Once prepared samples were loaded into the stacking gel, the electrode assembly containing the gel was placed inside Bio-Rad Mini-Protein® Tetra Cells system and electrophoresis was started in 1X electrophoresis running buffer (0.025 M Tris base, 0.19 M Glycine and 0.08% (w/v) SDS) using a PowerPac™ HC power supply at 16 mA per gel until the protein arrived the running gel. Subsequently, 40 mA per gel was used to allow samples to separate, until the loading buffer had reached to the bottom of the gel. 6-8 µl of ColorPlus Prestained Protein Marker, Broad Range (7-175 kDa) (New England Biolabs, P7709V) was also loaded in parallel to the samples, allowing estimation of protein molecular weight.

Stacking Gel (5%)	Separating Gel (9%)	Separating Gel (12%)
Stacking gel buffer: 1ml (0.5M Tris pH 6.8 + 0.4% SDS)	Separating gel buffer (2.5ml) (1.5M Tris pH 8.8 + 0.4% SDS)	Separating gel buffer (2.5ml) (1.5M Tris pH 8.8 + 0.4% SDS)
Acrylamide: 400 µl	Acrylamide: 3 µl	Acrylamide: 4 µl
Water: 723 µl	Water: 4.44 µl	Water: 3.44 µl
APS: 50 µl	APS: 150 µl	APS: 150 µl
TEMED: 5 µl	TEMED: 15 µl	TEMED: 15 µl

Table 2.7: The recipes for preparing stacking and separating gels used in this study.

2.11.4 Western Blot

Once the components of the protein mixture were separated on SDS-PAGE gel, they next were transferred from SDS-PAGE gel onto the nitrocellulose membrane via a Mini Trans-Blot® Electrophoretic Transfer Cell (Biorad, UK). Blotting was carried out in cold 1x transfer buffer (20 mM Trise base, 150 mM Glycine and 20% (v/v) MeOH) at 150 mA for 60 min at RT. After this, the nitrocellulose membrane was blocked without shaking at 4°C O/N in blocking solution (PBS containing 0.5% (v/v) Tween-20 (PBST) and 5% (w/v) dried skimmed milk powder).

To detect the protein of interest, next day the blocking solution was discarded and the membrane incubated with the primary antibody at desirable dilution (table 2.8) in freshly prepared blocking solution at RT for 60 min. The membrane was washed (3 x 5 min) with 0.5% PBST before addition of the secondary antibody (commercially available Anti-rabbit IgG horseradish peroxidase (HRP) at 1:10,000 dilution in 0.5% PBST and resuming incubation at RT shaking for another 60 min. After incubation, the membrane was again washed as described above. On the other hand, for His tagged protein detection, the membrane was incubated only once with Penta-His HRP conjugate (QIAGEN) in 0.5% PBST at RT and washed as before. Subsequently, the blots were developed using the Pierce® ECL Western Blotting substrate (Thermo Scientific) and the Amersham Hyperfilm™ chemiluminescence film (GE Healthcare Limited, UK) according to the manufacturer's instructions.

Rabbit Antibodies	Dilution	Reference
α-EspC	1:1000	(111)
α-dsRed	1:10,000	Source Bioscience
α-TolC	1:2000	(126)
α-AcrB	1:2000	(126)
α-IscS	1:1000	(126)
α-AaaA	1:2000	(126)

Table 2.8: Rabbit primary antibodies used in this study.

2.12 Cell fractionation

2.12.1 Cell fractionation using the protocol described for *P. aeruginosa*

To split the bacterial compartments and determine the localization of the protein of interest, the samples of cytoplasmic, inner membrane, periplasmic and outer membrane fractions were prepared according to a protocol published by Luckett *et al*., 2012 (126). The protocol is also available online (http://www.bio-protocol.org/e922).

2.12.2 Sucrose gradient fractionation

To provide a clear separation of membrane associated proteins and clarify the localization of the protein of interest, a flotation sucrose gradient analysis was performed using a protocol described by Hardie *et al*., 1996 (253). Briefly, the LB O/N cultures of each strain were diluted

1:100 next day in fresh LB supplemented with suitable antibiotic and induced concurrently either by 0.2% or 0.02% arabinose for 4 h at 37°C shaking 200 rpm. The cultures were grown in 100 ml LB broth volume using 500 ml flasks. After 4 h of induction, Cells were harvested by centrifugation at 5000 rpm for 5 min at 4°C and washed with 10 ml 25 mM HEPES (pH 7.5) then finally resuspended in 3 ml 25 mM HEPES (pH 7.5) containing 1 mg/ml DNase and 1 mg/ml RNase. Following disruption in a French pressure cell at 14000 lb/in^2 (two or three times until lysates become clear), on ice. Whole cell extracts were made ›60% (w/w) sucrose. In parallel, sucrose gradient solutions spanning from 31% to 60% (w/w) were also prepared in 25 mM HEPES (pH 7.5) buffer.

To enable separation of proteins from the whole cell lysate, 1 ml from whole cells extracts ›60% (w/w) sucrose was first loaded at the bottom of Ultra-Clear™ centrifuge tube (Thinwall tubes, 13.2 mL, 14 x 89 mm) (Beckman Coulter, 334059) followed by loading with care equivalent amount of prepared sucrose solutions start with 60% up to 32% sucrose (w/w) solutions. Samples were centrifuged at top speed 41,000 rpm (Optima™ LE-80k Ultracentrifuge, Beckman Coulter) using SW41Ti rotor for 24 h at 10°C. Next day, the fractions of 1 ml were carefully aspirated from the top of the tube and subjected to TCA precipitation before Western blotting analysis. To determine the precise percentage of sucrose in every gradient, the refractive index in all sucrose gradients was measured by the refractometer before and after the centrifugation.

2.13 Trypsin assay

To confirm the localization of EspC at the bacterial surface, bacteria expressing such protein were exposed to digestion by an exogenously added trypsin (Trypsin from bovine pancreas from Sigma) and its susceptibility to trypsin enzyme was examined. O/N cultures of the strains to be studied were prepared and diluted 1:100 in fresh LB broth containing appropriate antibiotics. Each culture was divided into two groups to be induced directly and indirectly (see section 2.4) and kept to grow at 37°C shaking 200 rpm. Whole cells samples were collected overtime by centrifugation at 6000 rpm for 5 min at 4°C (Allegra™X-22R, Beckman Coulter), washed twice and resuspended to 1.0 OD_{600} units/ml in 100 mM Tris-HCl (pH 8.0). After this, the samples were divided into two sets, whole and lysate cells (cells lysed by sonication 1-2 min, on ice). Subsequently, both whole and lysate cells were incubated at 37°C for 60 min in three aliquots, independently, one with trypsin (1 µg/ml), one with trypsin (1 µg/ml) plus soybean trypsin inhibitor (10 µg/ml) (Invitrogen) and one kept without trypsin treatment. Finally, all samples were centrifuged as before and the pellets were then resuspended in 200 µl 1X SDS-PAGE loading dye and boiled for 10 min for further protein analysis.

2.14 Arginine - *p* - nitroanalide assay

To assess the activity of AaaA, arginine-*p*-nitroanilide degradation assay was carried out according to a protocol described by Luckett *et al*., 2012 (126). The O/N of bacterial strains to be tested were prepared and

diluted 1:100 in LB supplemented with appropriate antibiotics and grown at 37°C shaking until reaching OD_{600} of 0.05. Then, the cultures were induced by 0.02% arabinose. After a further 2:30 h, cells were harvested and washed twice with sterile MMP using centrifugation 6000 rpm for 5 min and subsequent resuspension was normalised to 0.25 OD_{600} unit in a final volume of 1 ml of MMP. Subsequently, 150 µl of each sample were inoculated in wells of sterile clear bottomed 96 well plates (Costar) and mixed with 150 µl of arginine-*p*-nitroanilide solution (at final concentration of 1 mM). The plate was placed in Lucy plate reader for 11-24 h at 37°C for monitoring the degradation of *p*-nitroanilide measured by OD_{405}.

2.15 The *S*-(3.4-Dichlorobenzyl)-isothiourea (A22)

To perturb the bacterial actin homologue cytoskeleton MreB, A22 (Calbiochem, 475951) was used in this study according to the previous study made by Gitai *et al*., 2005 (254). A22 was prepared at concentration 5 mM (stock concentration) and used whether at zero µg/ml ($A22^0$) as untreated controls, 2.5 µg/ml ($A22^{2.5}$) to get lemon shaped cells or 10 µg/ml ($A22^{10}$) to have completely circular cells. Bacterial strains to be tested were grown in LB broth plus appropriate antibiotics O/N at 37°C shaking 200 rpm. Next day, 1 ml of cultures was used to inoculate 99 ml of fresh LB broth supplemented with antibiotics (1:100 dilution) using 500 ml flask and concurrently induced by 0.2% arabinose. The cultures kept to grow shaking at 37°C for approximately 1 h (until reach 0.05 of OD_{600nm}). At this particular point, the cultures were aliquoted into 3 sets (25 ml each in 100 ml flasks). One set of

culture was treated with $A22^0$ (control), the second set was treated with $A22^{2.5}$ and the third with $A22^{10}$. Subsequently, treated cells were incubated to grow at 37°C shaking for further 4 h, harvested by centrifugation at 6000 rpm for 5 min, washed once with ice cold PBS, and resuspended to 0.5 OD_{600} units/ml. Finally, 8 µl of washed cells were applied on microscopic slides for microscope analysis.

2.16 Expression of amber encoded recombinant proteins

To express the amber encoded sperm whale myoglobin, the plasmid p*Myo*4TAGPylT-*his6* was co-transformed with the plasmid pBK-PylSΔ (ACKRS-1) into the $CaCl_2$ competent MG1655 cells. For expression of *espC* that that contains amber codon either at position 533 or 951, the plasmid p*EspC*533TAGPylT or p*EspC*951TAGPylT was co-transformed with the plasmid pBK-PylSΔ (ACKRS-1) into the similar competent cells. The cells were incubated O/N at 37°C shaking 200 rpm in LB broth supplemented with Km 25 µg/ml and Tc 12.5 µg/ml as recommended by Neumann *et al*., 2008 (248). Next day, bacterial cultures were diluted 1:100 in fresh LB broth containing the selected antibiotics plus supplemented with 1 mM (final concentration) of unnatural amino acid (UAA). After 2 h shaking at 37°C (OD_{600} 0.2-0.4), induction of the protein expression was performed by addition 0.02% arabinose and grown for further 3-4 h. Finally, cells were harvested by centrifugation at 6000 rpm for 5 min, washed with PBS and the pellets were then resuspended in 200 µl 1X SDS-PAGE loading dye and boiled for 10 min for immunoblotting analysis.

2.17 Flow cytometry analysis

To allow discrimination between different cell populations according to fluorescent intensity, membrane integrity and size, cell suspensions were analysed in duplicate with a Beckman Coulter MoFlo XDP flow cytometry. Bacterial viability was assessed by staining cells with SYTOX® blue dead cell stain (Invitrogen, S11348). The stain has high affinity to nucleic acid and gives a bright blue fluorescence when excited with violet laser. Staining procedure was manipulated according to the manufacturer's instructions. Briefly, 4 h arabinose induced cultures were harvested by centrifugation at 5000 rpm for 5 min, washed and resuspended in sterile ice cold PBS to 0.5 OD_{600} units/ml (~5 x 10^8 cells/ml). 1 ml of cell suspensions were transferred to 1.5 ml eppendrof tubes, sealed and safely taken to the flow cytometry facility in QMC hospital for analysis. Before start measuring, samples were stained by adding 1 µl of the blue stain at a final concentration of 1 µM to tubes and incubated at room temperature for 5 min, protected from light. Samples were excited with violet and green lasers to detected blue cells and mCherry respectively. Signals were amplified using liner mode for forward scattering and side scattering while logarithmic mode was the choice to use to amplify the fluorescence signals.

2.18 FlAsH labeling tetracysteine-tagged recombinant proteins

To enable detection of recombinant proteins hosting tetracysteine motif, the green membrane-permeable biarsenical dye, FlAsH-EDT_2 (Invitrogen, T34561), was used in this study. Cultures of the strains to

be tested were prepared and induced by 0.02% arabinose as previously described unless otherwise stated. Cells producing TC-tagged protein were harvested by centrifugation at 5500 rpm for 2 min and washed once with 1x HEPES buffered saline BioUltra (Sigma, 51558) ice cold, and resuspended in 1 ml to 1.0 of OD_{600} using the same buffer. The cells were centrifuged once more and the pellet was resuspended (slowly) in 500 µl 1x HEPES buffer containing 3-5 µM (final concentration) FlAsH-EDT_2 substrate followed by incubation for 35-45 min in darkness at RT. After incubation, cells were harvested by centrifuging as before and the supernatant discarded according to the University of Nottingham guidelines. Subsequently, cells were washed twice with 1 ml 1x British Anti-Lewisite (BAL) wash buffer at final concertation of 0.25 mM as recommended by the manufacturer (added twice volume of wash buffer to the volume of added substrate). Lastly, cells were further washed once again with the 1x HEPES buffered saline, ice cold and resuspended to approximately 0.5 of OD_{600}. 8 µl of washed cells were mounted on microscope slide, covered with coverslip, sealed with transparent nail polish and examined under fluorescent microscope.

2.19 Confocal fluorescence microscope, fluorescent dyes and imaging study

To generate more detailed images, a Zeiss LSM 700 compact confocal laser scanning microscope was used fitted with HXP 120C lamp for light illumination and a Zeiss alpha-Plan-Apochromat 60x/1.46 Oil objective lens. Images were captured by using AxioCam digital microscope

camera connected to ZEN software and analysed using image J software.

In order to facilitate visualization of the EspC-mCherry fluorescent patterns, cells were stained with the lipophilic fluorescent membrane stain, FM 1-43 (Invitrogen, T3163) according to the manufacturer's instructions. Briefly, cell pellets were resuspended in 1 ml ice cold PBS containing 5 µg/ml FM-1 43 (final concertation) and incubated on ice for a maximum 1 min in darkness and washed twice with ice cold PBS before mounting on microscope sides. FM 1-43 was also used in this study to determine the shapes of cells. To assess the integrity of bacterial cells expressing EspC, cells were stained with the nucleic acid stain, SYTOX® blue dead cell stain. Staining procedure was manipulated according to the manufacture's recommendation. Briefly, Induced bacterial cultures were centrifugation 5000 rpm for 5 min, washed once with PBS and resuspended to 0.5 OD_{600} units/ml followed by staining with 1 µM (final concertation) SYTOX® blue stain then incubation at room temperature for 5 min in dark. Immediately following incubation, stained cells were washed twice and finally reusupended in 500 µl PBS for further microscope analysis. When necessary, DAPI (4',6-Diamidino-2-Phenylindole, Dihydrochloride) (Invitrogen) was also used in this study to stain bacterial DNA at the final concentration of 1 µg/ml in PBS, and manipulated as recommended by manufacturer's instructions. The fluorescence excitation and emission spectra of all fluorophores used in this study are summarised in table 2.9.

Fluorophore name	Excitation maximum	Emission maximum	Fluorescence colour	Laser channel
mCherry	587 nm	610 nm	Red	561 nm
FM 1-43	479 nm	589 nm	Green	488 nm
SYTOX® blue	444 nm	480 nm	Bright blue	405 nm
DAPI	358 nm	461 nm	Blue	405 nm
FlAsH-EDT_2	508 nm	528 nm	Bright green	488 nm

Table 2.9: Fluorescence spectra of fluorophores used in this study.

2.20 Fluorescence recovery after photobleaching (FRAP) experiment

The microscope Zeiss Elyra PS.1, with alpha-Plan-Apochromat 100x/1.46 Oil DIC M27 Elyra objective in confocal mode was used for FRAP experiment. Images acquired using 561 nm laser at 2.0% or 488 laser at 0.3% form mCherry and FlAsH-tag respectively. Zeiss Zen Black 2012 software was used to extract the intensity values from the bleached and control regions over time. Drift correction was applied using Zen Blue 2012 software. Values were exported to Microsoft Excel and normalization was done by dividing the values from the bleached zone with the values from the control zone before values were plotted.

2.21 Super resolution microscope

For super-resolution imaging a Zeiss Elyra PS.1 microscope was used in SIM or dSTORM modes. In SIM mode, either Plan-Apochromat 63x/1.4 Oil DIC M27 or C-Apochromat 63x/1.2W Korr M27 objectives were used. For FlAsH labelled bacteria the following setting were used; filter set

LBF-488/561, laser power 488 nm at 4.0% and cmos camera exposure time 25.0 ms. On the other hand, BP 570-620+LP 750 filter, 561 nm laser at 2.1% and camera exposure 100.0 ms were used for mCherry expressing bacteria. With regarding to the dSTORM mode, the following setting was utilized; alpha Plan-Apochromat 100x/1.46 Oil DIC M27 Elyra objective, BP 495-550+LP 750 filter and 405 nm laser at 0.7000% (this is used to increase the number of molecules which return to ground state, and therefore more molecules will emit light).

Chapter 3

Investigating the localization of EspC using the monomeric red fluorescent protein (mCherry) as a tag in EPEC and *E. coli* K-12

3.1 Introduction

During the onset of an EPEC infection, a diverse set of virulence associated proteins are injected into the host epithelial cells through the T3SS injectisome (16). On of these effectors is the non-LEE encoded EspC. EPEC secrets EspC into the extracellular milieu by the T5SS which is subsequently delivered into host cells by the T3SS (26,35,36). Although the SPATE EspC is a member of the AT family, how EspC is secreted from the bacterium itself and what accessory factors are involved remains uncharacterized (74,142).

The majority of studies characterizing EspC AT have focused on its role in epithelial cell infection. For instance, it has been shown that EspC is the major cause of epithelial cell cytotoxicity during an EPEC infection because it cleaves fodrin, an important component of the actin cytoskeleton, forming cytoskeletal contraction phenotypes such as cell rounding and cell detachment (87). EspC also controls the pore formation mediated by the T3SS by targeting EspA associated with EspD to regulate their levels (88). However, how it utilizes the T3SS to reach its target still undefined.

Predictive options of how EspC can access the T3SS needle are summarized as follows (i) as EspC preferentially targets EspA accociated with EspD (88), it is likely to interact with the surface of the needle and use it as a guide to migrate towards host cells, perhaps powered along by components of T3SS needle (ii) or probably enter the injectosome from the culture supernatant and delivered it this way (iii) EspC has less affinity to target EspA alone (88), therefore other possibility could be

that EspC targets or replaces the T3SS pore component (EspD) at the host epithelial membrane (iv) because T3SS is assembled as an intact needle complex with a closed secretion channel (to prevent leakage), the more likely scenario is that EspC interacts with a yet unknown surface receptor that is secreted by T3SS and reminiscent of the other AT, intimin.

In order to track, monitor and study the molecular mechanism of EspC secretion, it is necessary to visualize EspC as it matures and is translocated out of the cell. To do this, the monomeric version of the tetrameric dsRed fluorescent protein, mCherry was chosen as a fusion tag to monitor protein translocation (237). Previous data had indicated that EspC-mCherry locates to a spiral reminiscent of the bacterial cytoskeleton actin homologue, MreB. However, this is had not yet been characterized.

MreB forms cytoplasmic helical filaments which dynamically rotate around the cell circumference at the long axis of the cell in a manner reliant on the cell wall synthesis machinery (212,213). Different functions have been assigned to the MreB cytoskeleton, including maintenance of the bacterial bacillus cell shape, chromosome segregation and cell polarity as well as possibly acting as a scaffold for transporting proteins to different positions throughout the bacterial cell (207,209,217). This chapter reveals for the first time that EspC AT localizes in helix during the secretion and provides evidence discounting the artefactual localization. Moreover, the chapter reports the different localization patterns obtained during the secretion of different versions

of EspC fused with mCherry fluorescent protein and compare it with the bacterial cytoskeleton MreB helix, extending the analysis to monitoring the bacterial growth and morphology in both *E. coli* MG1655 and EPEC.

3.2 Results

3.2.1 Fusion of mCherry to EspC passenger domain in the presence and absence of the C-terminal transporter domain

The insertion of the transporter domain (β-barrel) into the OM is a necessary step for the secretion of the AT passenger domain (189). To establish the importance of the EspC β-barrel in EspC localization, EspC-mCherry with (pLA33C1mc and pLA18C1mc) and without (pMAC18-75) a functional β-barrel transporter domain had been previously prepared. This was achieved by PCR amplification of the gene encoding mCherry from pmCherry, and insertion of the amplicon into a *Bgl*II site in the middle of the passenger domain of EspC (Fig. 3.1). To create the β-barrel transporter domain truncation, two versions of the reverse primer were used, one containing a single base pair insertion to create a frameshift that led to a premature translational termination (Fig. 3.1). It was envisaged that this truncated EspC version would facilitate a comparative investigation of EspC secretion without its β-barrel domain (the transporter domain).

To determine whether these vectors contained the correct mCherry inserts, plasmid preparations were performed after transformation into *E. coli* MG1655. Following digestion by *Bgl*II restriction enzyme, and separation through a 0.8% agarose gel, the expected ~710 bp mCherry digestion product was observed in all the plasmids (Fig. 3.2).

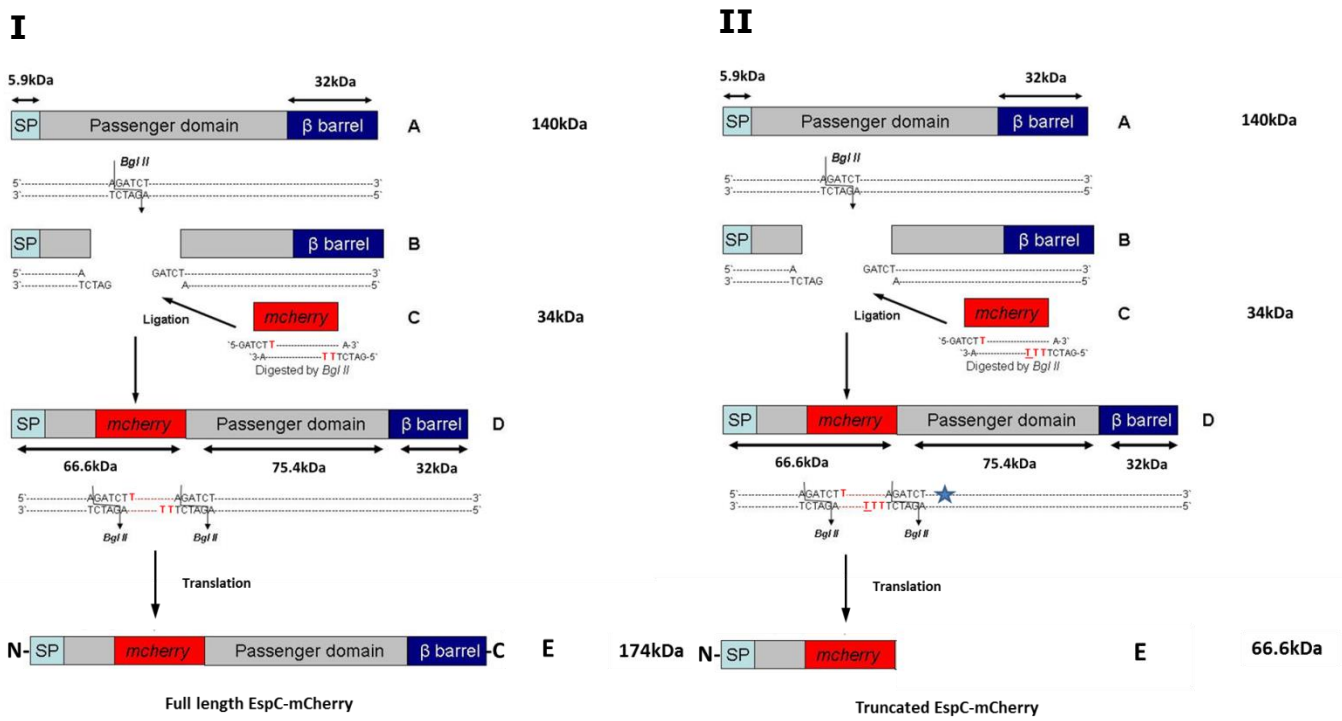


Figure 3.1: Schematic of the cloning strategy for inserting mCherry into the EspC passenger domain. (A) The native 145 kDa EspC protein is shown with the relative position of the *Bgl*II restriction site on its encoding DNA. **(B)** Digestion of the DNA template by *Bgl*II opened *espC*. Ligation to a DNA fragment (encoding the 34 kDa mCherry protein) which had been digested by the same enzyme was then undertaken. **(I-D)** Successful insertion of the fluorescent mCherry protein into passenger domain results in formation of full length 174 kDa EspC-mCherry protein **(I-E)**, whereas in **(II-D)** a stop codon was introduced immediately downstream of the mCherry gene (indicated by the blue asterisk) producing a truncated version of the EspC-mCherry protein with a size of ~70 kDa **(II-E)**.

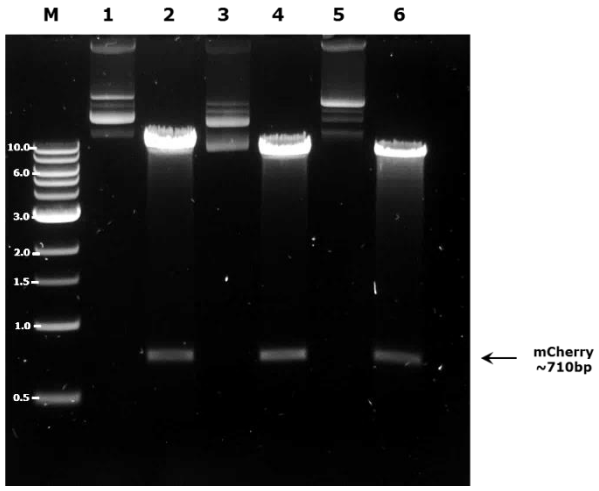


Figure 3.2: Confirmation of the genetic composition of plasmids encoding EspC-mCherry fusions. Plasmids pLA33C1mc (1 and 2), pLA18C1mc (3 and 4) and pMAC18-75 (5 and 6) were separated through a 0.8% agarose gel run alongside the 1 kb DNA ladder (M). Lanes 1, 3 and 5 are uncut, while 2, 4 and 6 are digested with *BglII*. The expected DNA product bearing mCherry (~710 bp) is indicated by the black arrow. Note the digested product of the pLA33C1mc vector (lane 2) is ~9260 bp reflecting the pBAD33 backbone, whilst for both pLA18C1mc and pMAC18-75 it is smaller at ~8540 bp) as these two are derived from pBAD18.

3.2.2 EspC-mCherry is constitutively produced in a stable form

Protein production analysis showed that the strength of the fluorescent signal from mCherry was affected by the nature of the plasmid backbone into which EspC-mCherry was inserted. For cells harbouring plasmids derived from pBAD18, such as *E. coli* MG1655 (pLA18C1mc) and *E. coli* MG1655 (pMAC18-75), very weak fluorescence that bleached quickly upon exposure to green light was observed. In contrast, much stronger fluorescence over extended times was observed for recombinant clones having the pBAD33 backbone such as *E. coli* MG1655 (pLA33C1mc). Since the truncated EspC-mCherry or solo mCherry gene were not present in pBAD33, it was necessary to clone these genes into pBAD33 to generate a set of comparable plasmids allowing for rigorous and efficient molecular mechanistic and protein localization investigations.

3.2.2.1 Construction of pMAC33 vector encoding EspC-mCherry from the lower copy number plasmid with the aim to prolong the production of a detectable fluorescent signal

Plasmid pMAC33 was engineered by swapping the full length EspC-mCherry gene fusion in pLA33C1mc with the truncated gene fusion lacking the β-barrel domain of pMAC18-75 according to Fig. 3.3. The restriction enzyme sites *Sac*I and *Hind*III, peripheral to EspC-mCherry in both parent plasmids, were used to remove EspC-mCherry from pLA33C1mc and truncated EspC-mCherry from pMAC18-75 so that the truncated EspC-mCherry gene fragment could be cloned into

complementary restriction enzyme sites of pBAD33. *Sac*I and *Hind*III digestion of pLA33C1mc produced two digested fragments, ~5.3 kb digested pBAD33 vector and ~4.6 kb full length EspC-mCherry which were easily separated on agarose gel. However, *Sac*I and *Hind*III digestion of pMAC18-75 yielded two fragments of similar sizes, ~4.6 kb pBAD18 vector and ~4.6 kb truncated EspC-mCherry (Fig. 3.3 A) which needed a second round of digestion with *Nde*I to split the pBAD18 vector in half enabling separation from the truncated EspC-mCherry gene insert (Fig. 3.3 B). The 4.6 kb truncated EspC-mCherry gene fragment was ligated with the 5.3 kb pBAD33 backbone to produce the recombinant plasmid, pMAC33 (Fig. 3.3 B).

Prospective pMAC33 plasmids were subsequently verified by *Sac*I/ *Hin*dIII digestion (Fig. 3.3 C), and the presence of the expected TAG stop codon at the end of the mCherry gene was confirmed by DNA sequencing.

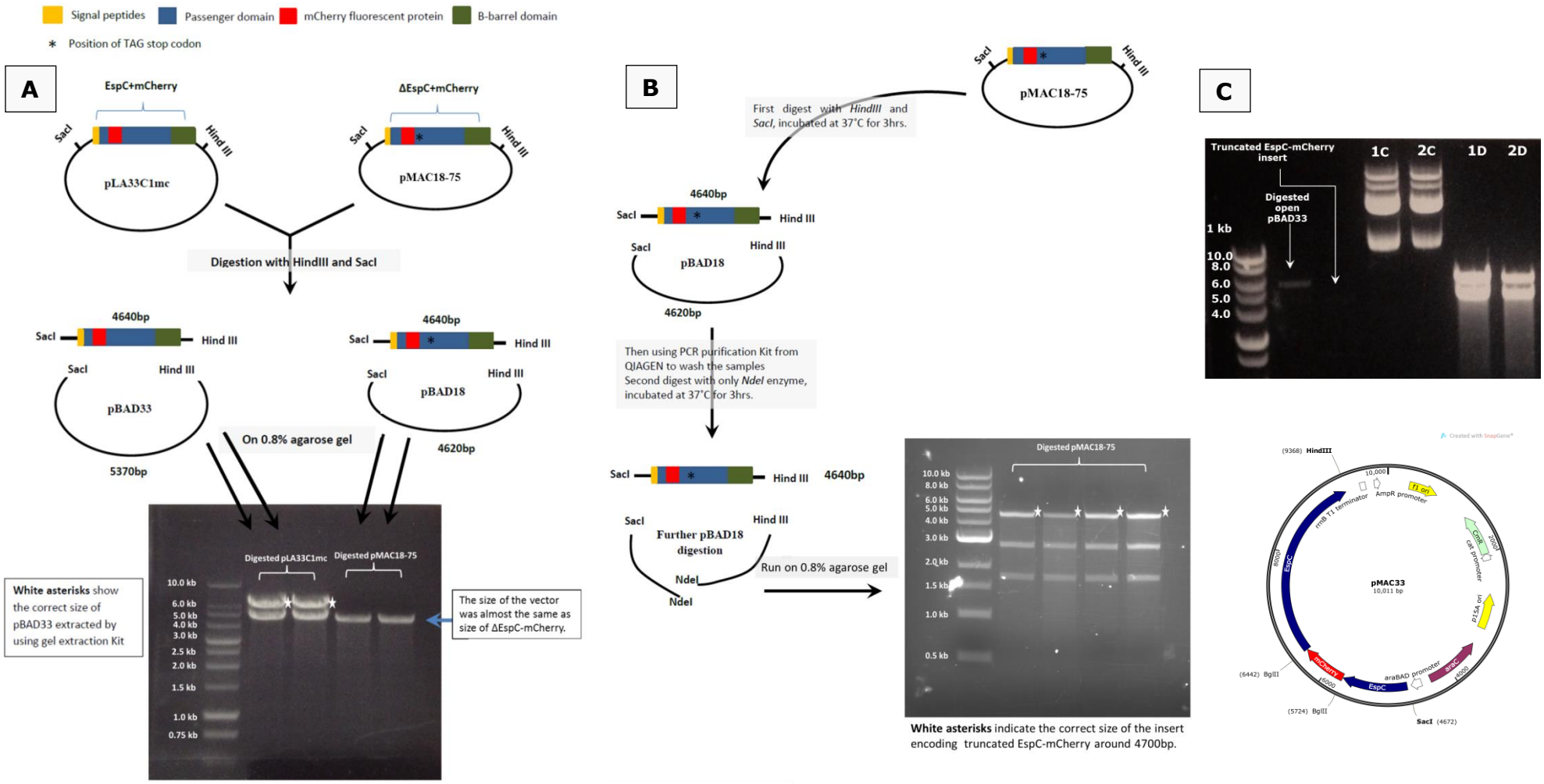


Figure 3.3: The cloning strategy of pMAC33. (A) pLA33C1mc and pMAC18-75 were digested with *Sac*I and *Hind*III. As expected, pLA33C1mc digestion yielded the first target fragment of approximately 5.3 kb comprising the pBAD33 vector (white asterisks) in addition to the ~4.6 kb full length EspC-mCherry. It was not possible to differentiate the separate digested products of pMAC18-75 due to the size similarity between the pBAD18 vector (~4.6 kb) and truncated EspC-mCherry (~4.6 kb) products. **(B)** To enable separation of vector and insert DNA on agarose gel electrophoresis, pMAC18-75 was further digested with *Nde*I to produce two smaller fragments. **(C)** The confirmation of the new pMAC33 construct was via *Sac*I/*Hind*III digestion (Agarose C, two different colonies were evaluated 1 & 2 (with (D) and without (C) digestion) alongside the controls; open pBAD33 vector and *Sac*I/*Hind*III digested truncated EspC-mCherry. All DNA samples are separated through 0.8% agarose gel alongside the DNA ladder. A copy of the new plasmid (pMAC33) map obtained from SnapGene software is included.

3.2.2.2 Constructing pLA33mCherry vector encoding mCherry from pBAD33

pLA33mCherry was generated by amplifying the mCherry encoding gene from pmCherry using F-*Bgl*II mCherry/R-*Sal*I mCherry primers designed to introduce *Bgl*II and *Sal*I sites at the 5' and 3' ends of the mCherry coding region respectively (see table 2.4, chapter 2). Subsequently, the purified PCR product was digested with *Bgl*II and *Sal*I. The destination plasmid was created by inserting a *Bgl*II site into pLA33C1 downstream of the arabinose promoter by SDM yielding pLA33C1$_{Bgl\text{II}}$ (see table 2.2, chapter 2) (Fig. 3.4 A). Digestion of pLA33C1$_{Bgl\text{II}}$ with *Bgl*II and *Sal*I yielded the pBAD33 backbone which was ligated to the similarly digested PCR product bearing *mCherry* to create the control plasmid pLA33mCherry (Fig. 3.4 B and C).

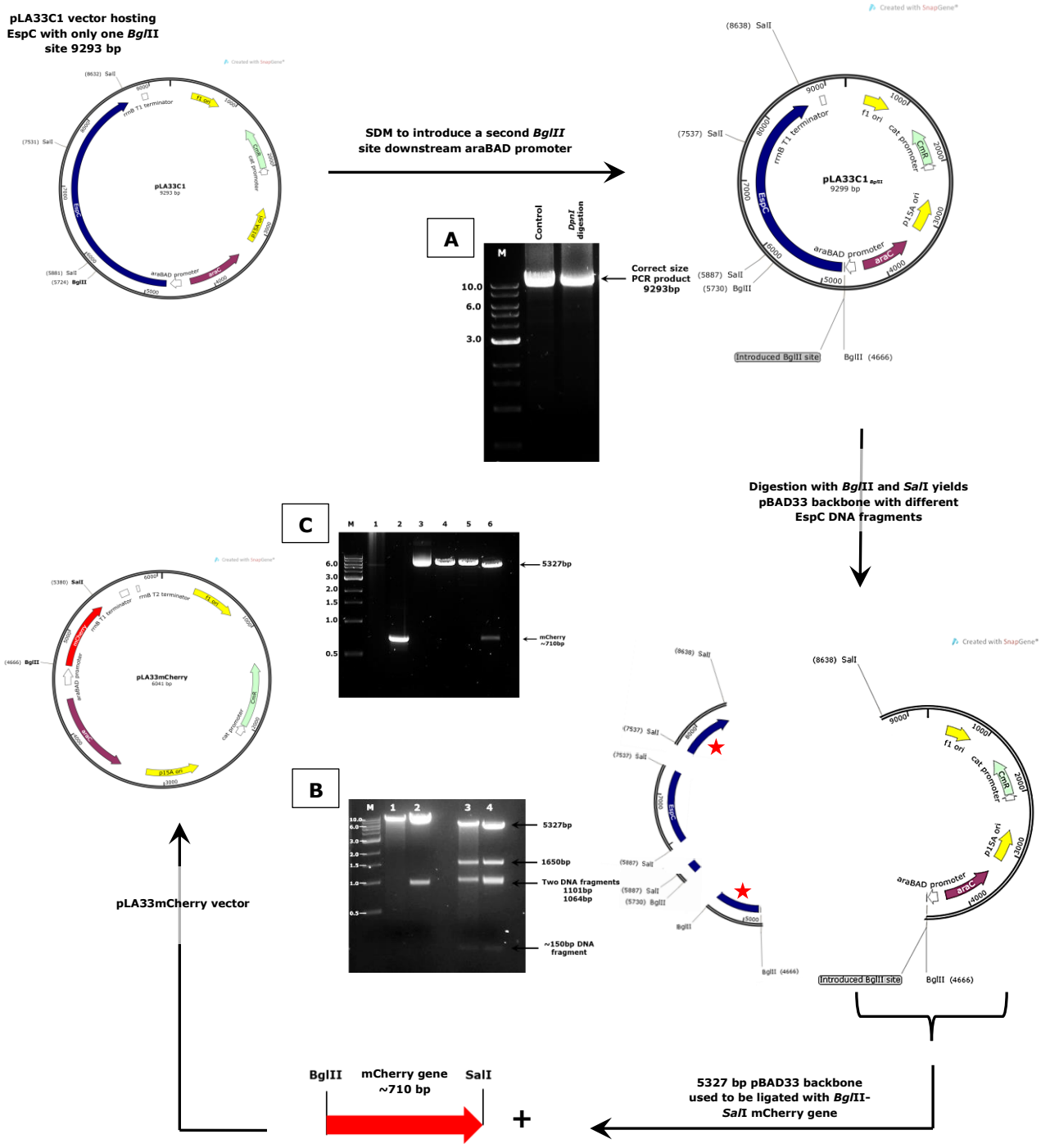


Figure 3.4: The cloning strategy of pLA33mCherry. Plasmid pLA33C1 harbouring *espC* was subjected to site directed mutagenesis using primers F-pLA33C1-*Bgl*II/R-pLA33C1-*Bgl*II to insert a *Bgl*II restriction site downstream of the arabinose promoter (see table 2.4, chapter 2). **(Agarose A)** shows the successful of the mutagenic PCR containing the expected size DNA product ~9293 bp (undigested as a control and digested with *Dpn*I restriction enzyme. The confirmation of the new construct called pLA33C1$_{BglII}$ was through a single digestion using *Bgl*II enzyme. **(Agarose B)** showing the digestion of original pLA33C1 (1) and the new construct pLA33C1$_{BglII}$ (2) with only *Bgl*II enzyme which clearly shows the generation of second DNA fragment ~1000 pb in the lane 2 as proof of the successful second *Bgl*II restriction site insertion. To enable cloning *mCherry* gene into pBAD33 backbone, pLA33C1$_{BglII}$ was digested with *Bgl*II and *Sal*I enzymes **(Agarose B,** lane 4**)** in parallel with the control pLA33C1 **(Agarose B,** lane 3**)**. Notably, Introduction of a second *Bgl*II site causes production of four DNA fragments, two of which were very similar ~1101 bp and ~1064 bp (red asterisks) **(Agarose B, lane 4)**. Subsequently, the open pBAD33 vector generated from pLA33C1$_{BglII}$ was ligated to the similarly digested PCR product bearing *mCherry* to yield pLA33mCherry. The new construct was verified by sequencing and by digestion with the restriction enzymes **(Agarose C;** Lane 1 is opened pBAD33 vector digested with *Bgl*II and *Sal*I enzymes (control), Lane 2 is the control PCR similarly digested mCherry, Lane 3 is for the control non digested plasmid DNA sample, Lane 4 showing plasmid DNA digested with only *Sal*I, or *Bgl*II (Lane 5) or double digestion (Lane 6)**)**. All DNA samples are separated through 0.8% agarose gel alongside 1 kb DNA ladder.

3.2.3 As predicted, introduction of a stop codon decreases the observed molecular weight of EspC-mCherry indicative of a truncation that removes the transporter domain

Preliminary data had indicated that the introduction of a stop codon adjacent to the mCherry inserted within the passenger domain of EspC might result in an altered cellular localization that could be attributed to the lack of the transporter domain. First it was necessary to verify that the size of the EspC-mCherry fusion was indeed reduced according to this hypothesis. Thus, the production of native EspC (as control), native mCherry (as control), full length EspC-mCherry and the truncated EspC-mCherry proteins in *E. coli* MG1655 whole cell lysates were compared. Each strain was prepared by centrifugation of 1 ml of cell culture treated with 0.2% arabinose to induce recombinant protein production. Bacterial pellets were resuspended in 200 µl of 1x SDS-PAGE loading buffer and immunoblotted with α-EspC following SDS-PAGE electrophoresis. Proteins of the expected sizes were observed: 174 kDa full length EspC-mCherry produced from pLA33C1mc, ~70 kDa truncated EspC-mCherry produced by pMAC33 and the native control 140 kDa EspC protein from pLA33C1 (Fig. 3.5 A). Incubation of the membrane with α-dsRed detected the ~34 kDa native mCherry protein, the ~70 kDa truncated EspC-mCherry produced by pMAC33 and the 174 kDa full length EspC-mCherry without any detection to the native control 140 kDa EspC in whole cell lysates (Fig. 3.5 B). Interestingly, there was a second protein detected by both antisera in MG1655 (pMAC33) lysates which corresponded to the EspC lacking the 5 kDa signal peptide, defined as a smaller ~65 kDa truncated form (black arrows, Fig. 3.5).

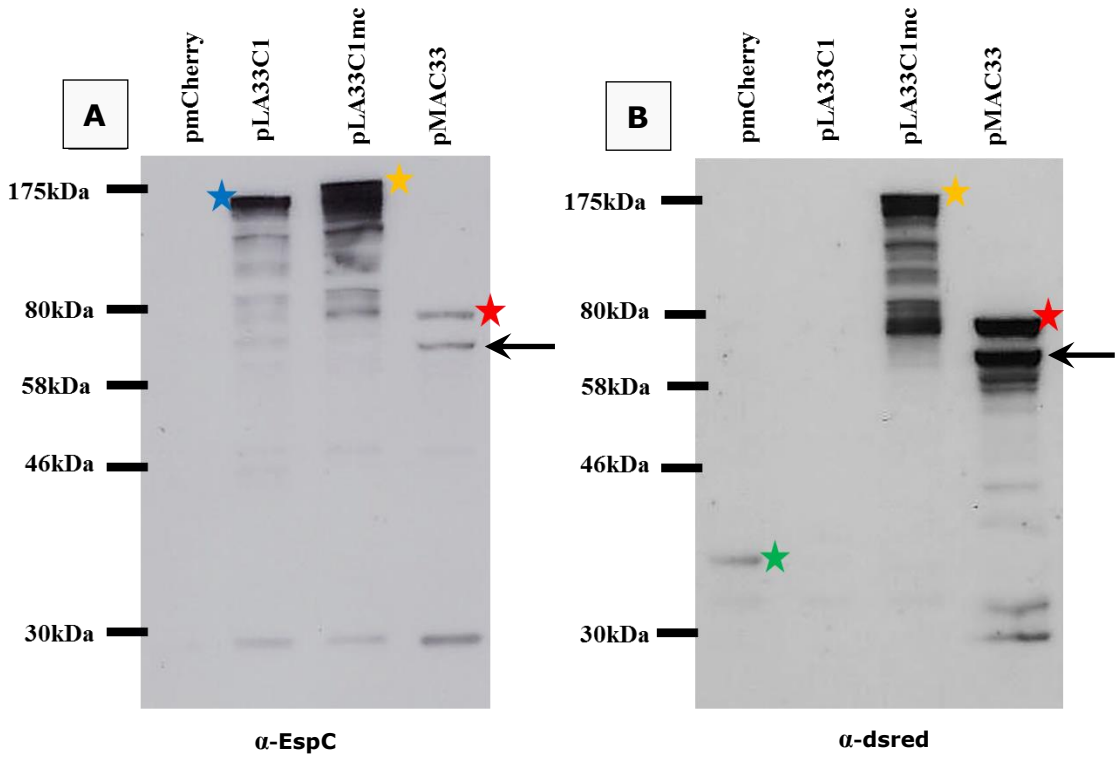


Figure 3.5: Size verification of different versions of EspC. Strains MG1655 (pmCherry), MG1655 (pLA33C1), MG1655 (pLA33C1mc) and MG1655 (pMAC33), were grown in LB and immediately induced with 0.2% arabinose for 4 h. Whole cell lysates were prepared by spinning down 1 ml of cell culture, resuspended in 200 µl 1x SDS-PAGE loading dye and separated through 9% SDS-PAGE gel. Western blot analysis of cell lysates incubated with α-EspC **(Panel A)** or α-dsred **(Panel B)**. The positions of the full length EspC in the absence (blue asterisk) or presence of the fusion to mCherry (orange asterisks) is indicated. Red asterisks and black arrows indicate the positions of the truncated version of EspC-mCherry protein with ~70 kDa and without ~65 kDa the signal peptide respectively. A lysate containing native mCherry (green asterisk) was applied to the left hand lane of both western blots.

3.2.4 EspC-mCherry locates to a spiral structure that resembles the bacterial cytoskeleton when it has the β-barrel domain attached.

To verify that EspC-mCherry locates to a spiral-like structure when it has its C-terminal transport domain attached in *E. coli*, the localization of EspC-mCherry was monitored by confocal microscopy from induced cultures of MG1655 (pLA33C1mc), MG1655 (pMAC33) and MG1655 (pLA33mcherry). As shown in Fig. 3.6, all cells displayed a bright red fluorescence when visualized microscopically using green laser exposure but interestingly, each type of cell had a different patterns of fluorescence.

The confocal imaging revealed that the majority of *E. coli* MG1655 (pMAC33) cells (which produces truncated EspC-mCherry) had an apparent growth defect and exhibited diffuse patterns of fluorescence with some polar localization and punctate of fluorescence (Fig. 3.6 B). In contrast, *E. coli* MG1655 (pLA33C1mc) cells (containing full length EspC-mCherry) grew much better and had a fluorescent localization pattern that was mainly patchy with some polar localization (Fig. 3.6 A). Strikingly, a few cells clearly exhibited either complete or partial helical localization (Fig. 3.6 A). The control *E. coli* MG1655 (pLA33mCherry) cells illustrated only diffuse cytoplasmic localization as expected (Fig. 3.6 C). It is apparent that the lack of the transporter domain alters the intracellular distribution of EspC.

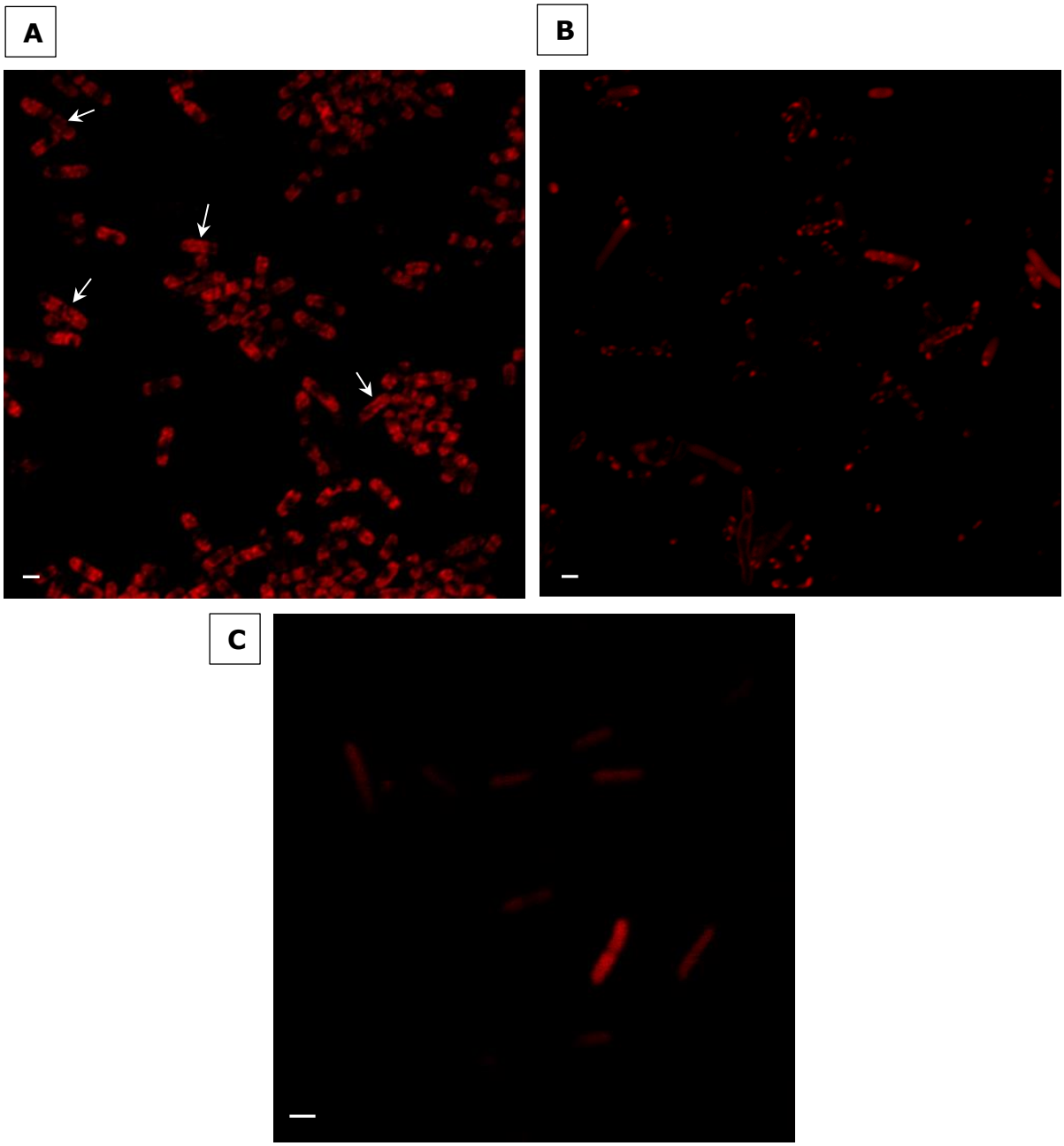


Figure 3.6: EspC-mCherry localizes to a helix unless the transporter domain is absent. Confocal images of *E. coli* MG1655 producing the full length EspC-mCherry from the plasmid pLA33C1mc **(image A)** or truncated EspC-mCherry pMAC33 **(image B).** *E. coli* MG1655 (pLA33mCherry) which produces mCherry which was not fused to EspC was similarly analysed **(image C)**. The red colour indicates the position of mCherry. The white arrows indicate cells producing a distinctive EspC spiral localization. The scale bar shown indicates 2 μm.

The spiral localization pattern of the full length EspC-mCherry was very interesting. Although the majority of the observed cells produced patchy distribution over the cell surface that appear sometimes connected with variably length of helical filaments structures rotating circumferentially the long axis of the bacterial cell (Fig. 3.6 A), a complete spiral pattern was observed in some cells, but this was very rare (Fig. 3.7 A). Focal stacks of those cells revealed the extended helical patterns along the cell membranes (Fig 3.8). To investigate this further, Super Resolution Structured Illumination Microscopy (SR-SIM) was employed. Using this more refined imaging technique, the full length EspC-mCherry appeared to localize as discrete patches that were arranged in helices and wrapped around the cell circumference towards the bacterial poles (Fig. 3.9). These patches sometimes appears connected by cross-streaks in a manner that resembled the bacterial actin homologue MreB (242) (Fig. 3.7 B).

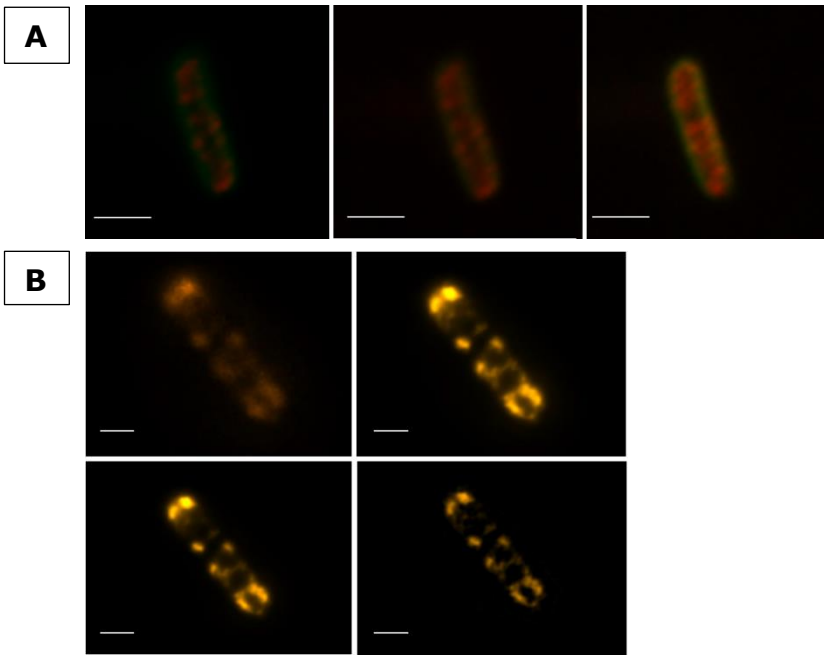


Figure 3.7: Formation of a spiral structure in *E. coli* producing EspC-mCherry from the plasmid pLA33C1mc. Imaging DH5α *E. coli* strain by confocal microscope after staining with FM 1-43 as described in Materials and Methods **(A)** or *E. coli* MG1655 strain by SR-SIM **(B)**. Cells were grown for 4 h, induced by 0.02% arabinose and prepared for microscope imaging as described in Materials and Methods. Scale bar represents 2 μM in **(A)** and 1 μM in **(B)**.

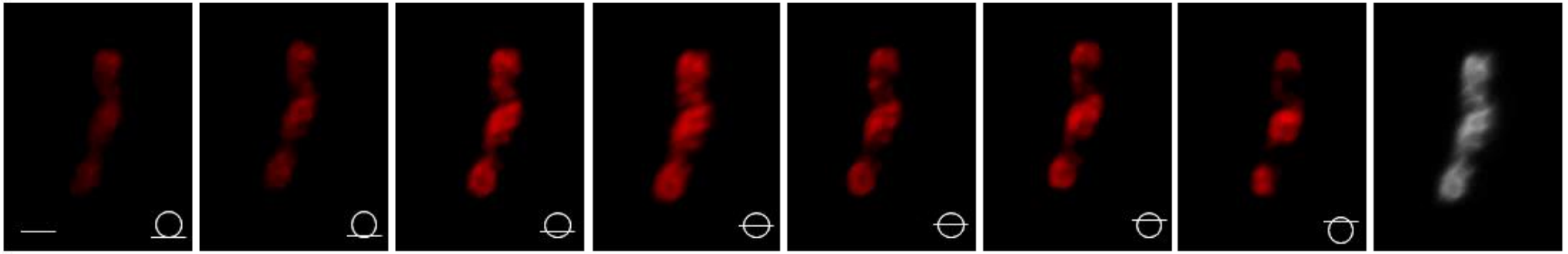


Figure 3.8: An extended helix is observed in *E. coli* expressing the full length EspC-mCherry. Individual confocal images of a focal stack through a cell with an extended spiral fluorescent pattern. MG1655 (pLA33C1mc) culture were grown in LB induced by 0.02% arabinose for 4 h and prepared for microscope imaging as described in Materials and Methods. The diagram presented in each image corresponds to the position of the focal stack. For clarification, an image with fully extended spiral structure was further processed by using ImageJ software which clearly shows the helix in grey. Scale bar represents 1 μM.

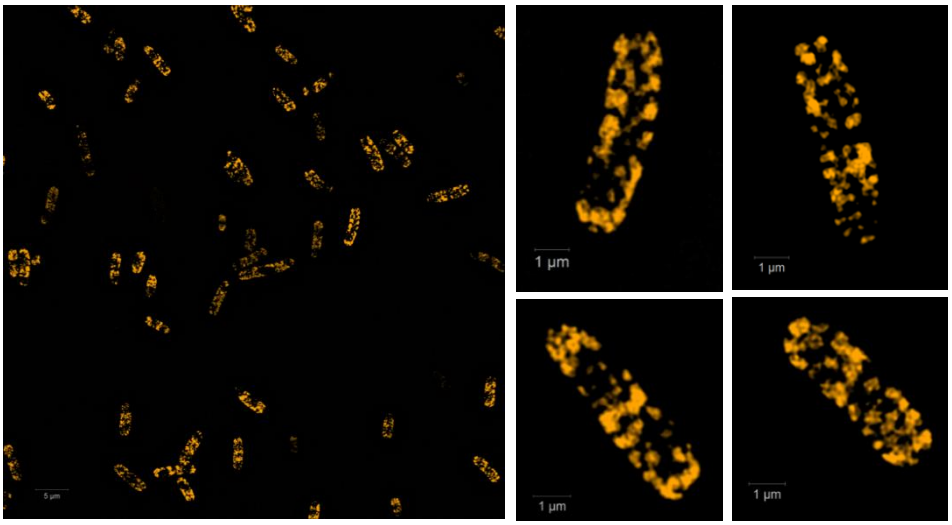
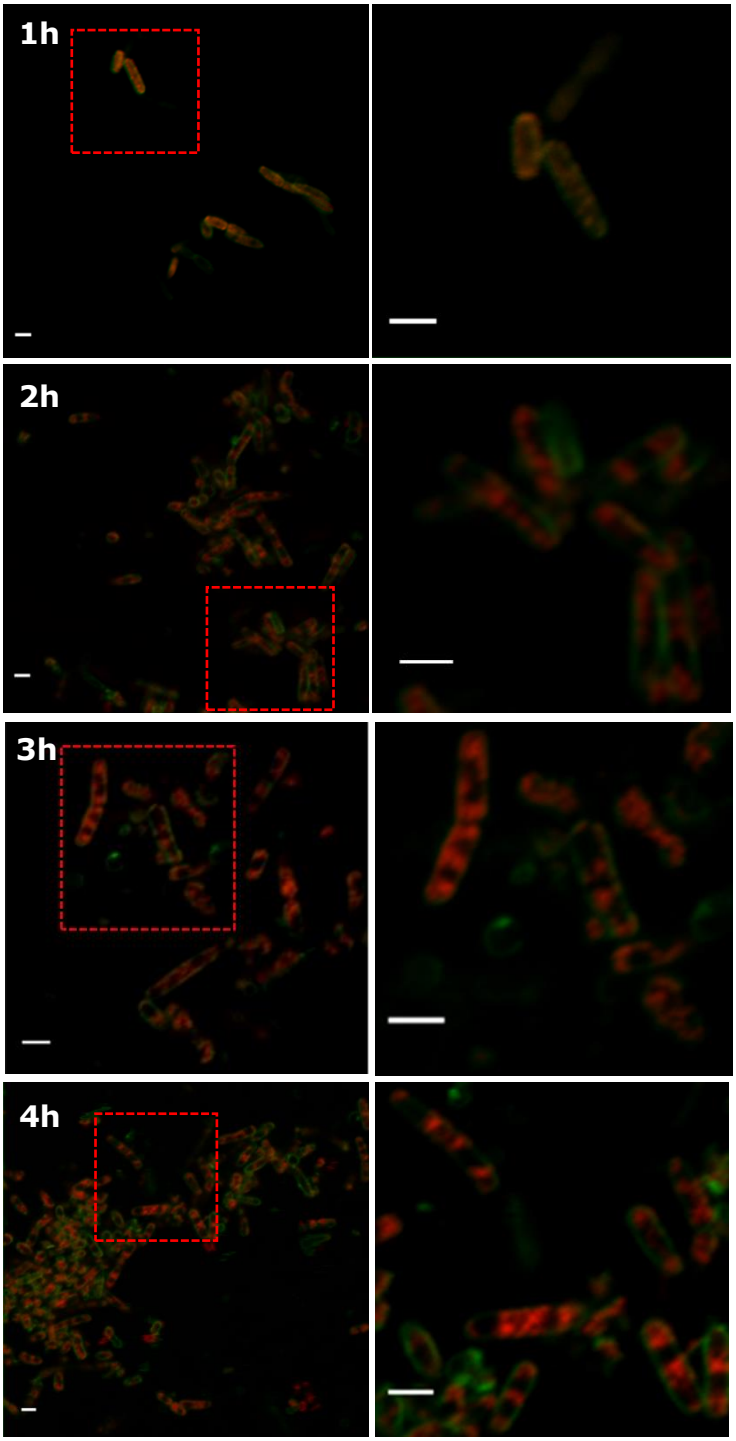


Figure 3.9: The Full length EspC-mCherry localizes as discrete patches in helical arrays. Super resolution images of *E. coli* MG1655 (pLA33C1mc) showing the population of cells producing the full length EspC-mCherry **(left side)**. Individual bacteria (four different cells) displaying a patchy localization are shown **(right side)** which were digitally cropped from the original left side highly resolution SIM image and displayed using Zen black 2012 software with interpolation filter. Cells were grown, induced by 0.02% arabinose for 4 h and prepared for microscope imaging as described in Materials and Methods. Scale bar represents 1 µM.

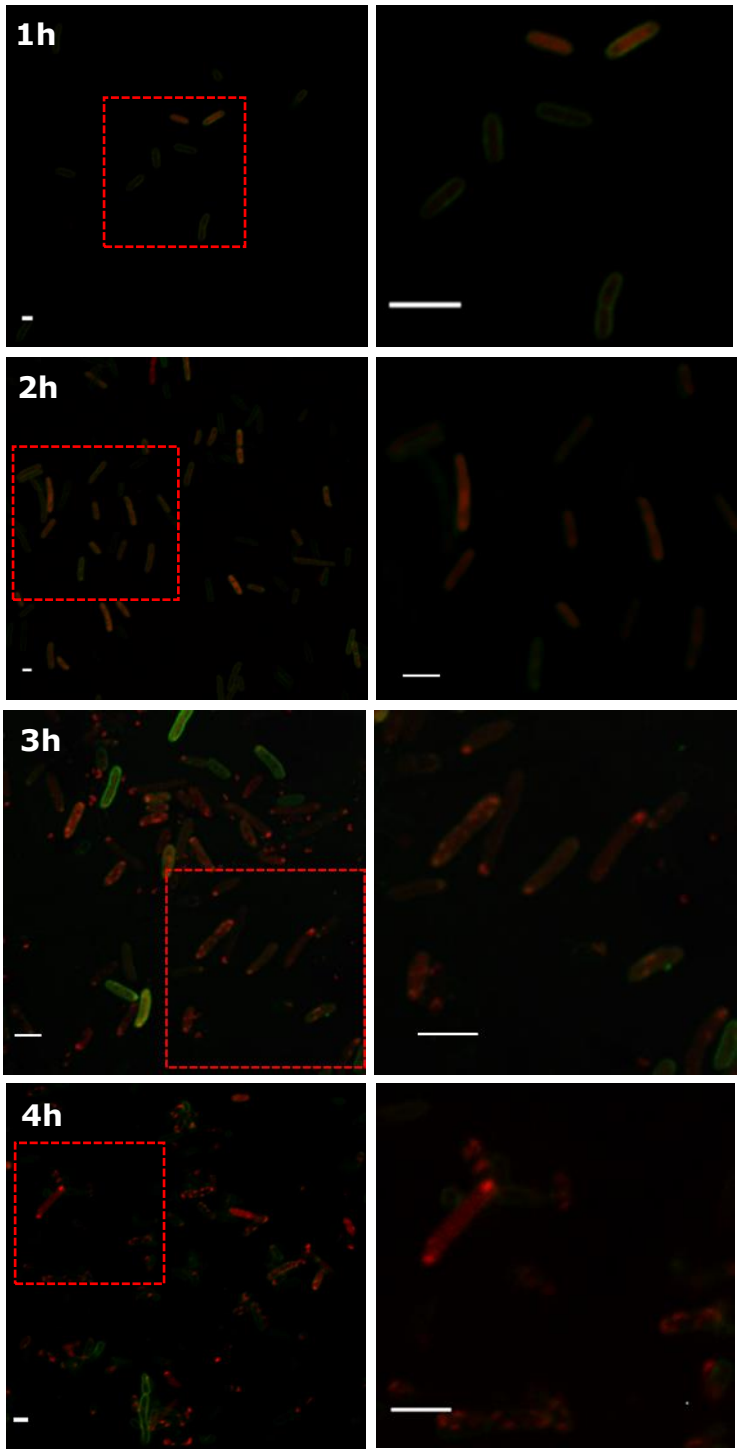
3.2.5 EspC-mCherry forms spirals during the first hour of production, localizes to the bacterial outer membrane and presents in the culture supernatant

To explore the processes involved in the localization and secretion of EspC, the expression of full length and truncated versions fused with mCherry were monitored in *E. coli* MG1655 over time using confocal microscopy (Fig. 3.10). The spiral localization pattern was observed in cells producing full length EspC-mCherry (174 kDa) during the first hour of induction and the fluorescence became more defined over time (Fig. 3.10 A). Helical structures were only rarely observed. Instead, fluorescent patches or incomplete turns of short filaments were evident. In contrast, a diffuse localization pattern was more apparent during the first hour of induction in cells harbouring the truncated version of EspC-mCherry (Fig. 3.10 B). Brighter fluorescence was observed over time, with more polar and punctate patterns (clearly distinguishable from the patchy distribution of the full length EspC-mCherry) becoming evident especially after 3 h of induction. The helical localization was not observed (Figs. 3.10 B and 3.6 B). The control cells producing mCherry exhibited only diffuse fluorescence throughout the period of induction indicating no structured export pathway (Fig. 3.10 C). EspC-mCherry localization was constant and independent of the bacterial growth phase and time of induction.

A- MG1655 (pLA33C1mc)



B- MG1655 (pMAC33)



C- MG1655 (pLA33mCherry)

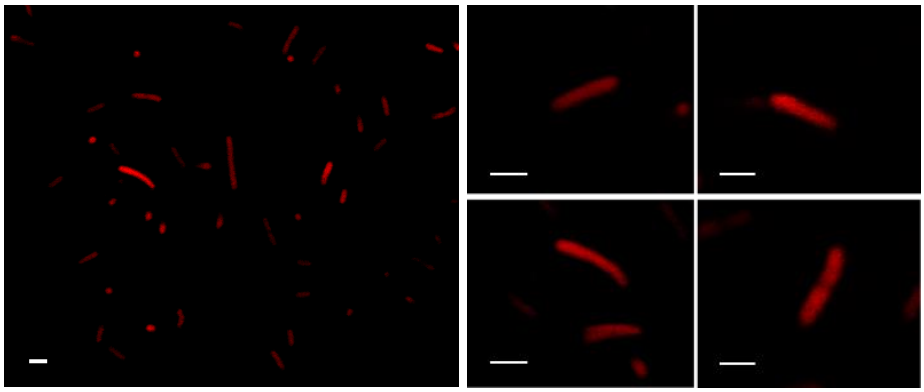


Figure 3.10: Truncated EspC-mCherry protein (lacking the β-barrel) is distributed in a diffuse and punctate pattern whilst the full length EspC-mCherry protein localizes to a spiral. Confocal images showing the spiral localization of the full length EspC-mCherry protein formed within 1 h and monitored up to 4 h **(A)**. The diffuse localization of truncated version EspC-mCherry is shown at 1 h with a more polar and punctate pattern evident after 4 h **(B)**. The diffuse pattern of fluorescence of MG1655 (pLA33mCherry) is shown in **(C)**. The green colour indicates cells were treated with the membrane stain FM 1-43, scale bars represent 2 μm.

To examine whether EspC with or without the C-terminal transporter domain could reach the extracellular milieu, culture supernatant samples were collected from the same cultures over time. The results revealed that the full length 174 kDa EspC-mCherry was detected in the supernatant after 2 h of immediate induction or after 1 h of delayed induction (Fig 3.11). Surprisingly, the truncated 70 kDa EspC-mCherry version without the β-barrel domain was also detected in the supernatant (Fig 3.11).

The existence of the truncated EspC-mCherry in the culture supernatant was initially perplexing. It is well known that the C-terminal of ATs is required to facilitate the secretion of its cognate passenger domain because it inserts as a β-barrel in the OM in combination with the β-barrel assembly machinery (BAM) complex, potentially forming a

channel through which the passenger domain may subsequently translocate (72,93). So, how could EspC lacking its C-terminal reach the external milieu? Confocal images revealed that the cells producing the truncated EspC-mCherry had abnormal shapes compared to the cells producing the full length EspC-mCherry and the control mCherry (Figs. 3.6 B and 3.10 B). It was thus predicted that the production of the truncated version of EspC might cause bacterial growth defects accompanied with cell lysis.

To determine whether the presence of the truncated EspC-mCherry in culture supernatant may be related to cell lysis, the growth of all strains was monitored over time (Fig. 3.12), and measured after 4 h induction in triplicate (Fig. 3.13). Cells producing the truncated version of EspC-mCherry had a significant growth defect compared to cells producing the full length EspC-mCherry. Interestingly, parallel analysis of EPEC containing all plasmids rather than MG1655, revealed that production of truncated EspC-mCherry in EPECΔ*espC* did not show such a major defect in growth (Fig. 3.13).

To establish whether EspC with or without the C-terminal domain is localized at the bacterial OM, both versions were exposed to digestion by an exogenously added protease, trypsin. To verify whether the usage of trypsin would be suitable for this application, the Peptide Cutter software (http://web.expasy.org/peptide_cutter/) was utilized to calculate the number of trypsin cleavage sites in EspC. In total, 102 trypsin cleavage sites were detected in EspC and these sites were

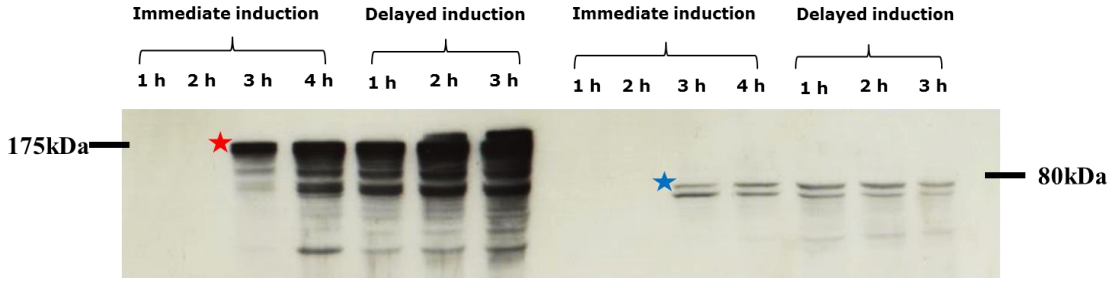


Figure 3.11: Both full length and truncated EspC-mCherry are released into culture supernatants. α-EspC immunoblot of culture supernatants from MG1655 (pLA33C1mc) **(on the left)** and MG1655 (pMAC33) **(on the right)**. Cultures were diluted 1:100 and either concurrently induced with 0.2% arabinose (immediate induction) or were diluted and grown to OD_{600} of 0.5 and then induced (delayed induction). Samples were collected every 1 h after arabinose induction and precipitated as described in Materials and Methods. Red asterisk indicates the full length 174 kDa EspC-mCherry protein while the blue asterisk shows the truncated 70 kDa EspC-mCherry protein. Samples were separated through 12% SDS-PAGE gels.

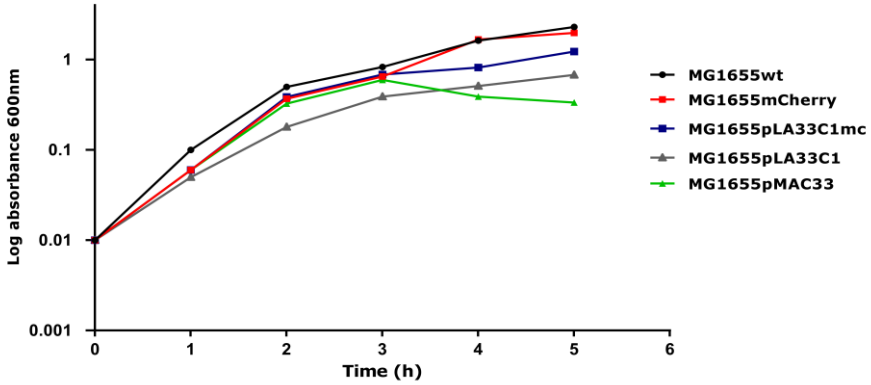


Figure 3.12: Production of truncated EspC-mCherry reduces cell growth. The growth of cultures of untransformed MG1655 wt (Black line), MG1655 containing native mCherry (red line), MG1655 with full length EspC-mCherry (blue line), MG1655 with native EspC (grey line) or MG1655 with truncated EspC-mCherry (green line) were monitored over time by measuring the OD_{600} at the indicated times after immediate induction with 0.2% arabinose. Strains were prepared as described in material and methods.

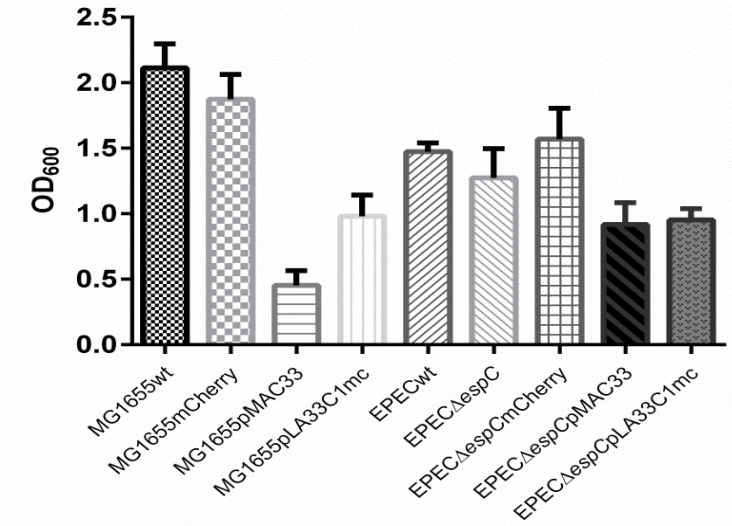


Figure 3.13: Expression of the truncated EspC-mCherry causes severe growth defects in MG1655 strain compared to EPECΔ*espC*. MG1655 and EPECΔ*espC* hosting mCherry, pMAC33 or pLA33C1mc were grown in LB after dilution, and concurrently induced with 0.2% arabinose. The optical density OD_{600} was measured after 4 h of induction. Error bars represent standard deviation (n=3 replicate reads).

scattered along the length of the protein. Hence If exposed on the surface of the bacterial cell, EspC would be degraded in whole cells and also in a cell lysate, but stable in controls containing soybean trypsin inhibitor.

E. coli MG1655 strains hosting the full length EspC-mCherry, truncated EspC-mCherry and empty pBAD33 vector were grown, induced via utilizing two different induction times and subjected to exogenous trypsin digestion as described in materials and methods. To compare the localization of both EspC-mCherry forms, whole cell samples were collected over time. Immunoblotting with α-EspC was used to detect EspC and α-IscS was used as a control since IscS is a cytoplasmic *E. coli* protein, and should thus only be degraded by trypsin in cell lysates in the absence of the trypsin inhibitor. As expected from the predicted OM localization, trypsin degraded the full length EspC in both whole and lysed *E. coli* MG1655 cultures (Fig. 3.14 A). Unexpectedly, trypsin was also able to cleave the truncated EspC as well as the cytoplasmic IscS protein in both sets of cultures (Fig. 3.14 C, B and D) whereas IscS protein was not accessible to the trypsin in cells expressing the empty vector pBAD33 (Fig. 3.15). Trypsin inhibitor prevented this trypsin-mediated degradation (Fig. 3.14). Due to the similarity in the data collected over time, only the 4 h immediate induced and the 1 h delayed induced samples are shown (Fig. 3.14).

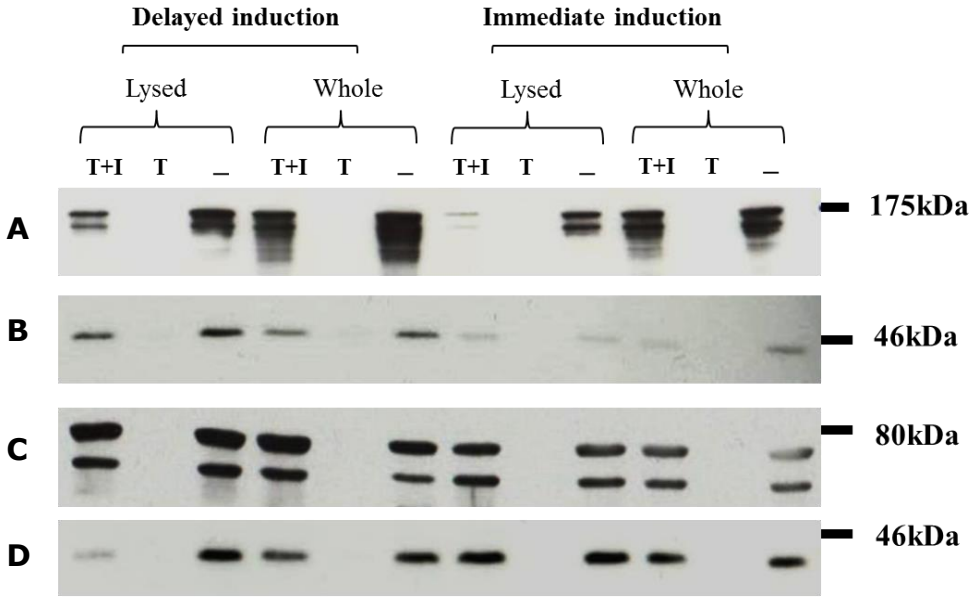


Figure 3.14: Exogenously added trypsin degrades both forms of EspC in the *E. coli* MG1655 laboratory strain. Both MG1655 (pLA33C1mc) **(A** and **B)** and MG1655 (pMAC33) **(C** and **D)** were grown in LB and induced in two different ways. Immediate induction where samples were diluted and concurrently induced for up to 4 h or delayed induction where samples were grown to OD_{600} of 0.5 then induced for 3 h. Whole and lysed cells were divided into three equal aliquots and treated with (T) trypsin or without (–) trypsin. As a control, the third aliquot was subjected to the protease inhibitor before adding trypsin (T+I) according to material and methods. Both full length 174 kDa EspC-mCherry **(A)** and the truncated 70 kDa EspC-mCherry **(C)** proteins were degraded by trypsin in whole and lysed cells. As a second control, the cytoplasmic protein (IscS) ~45 kDa also was degraded by trypsin **(B** and **D)**. Samples were separated by 9% SDS-PAGE gel and immunoblotted with α-EspC antisera **(A** and **C)** and α-IscS antisera **(B** and **D)**.

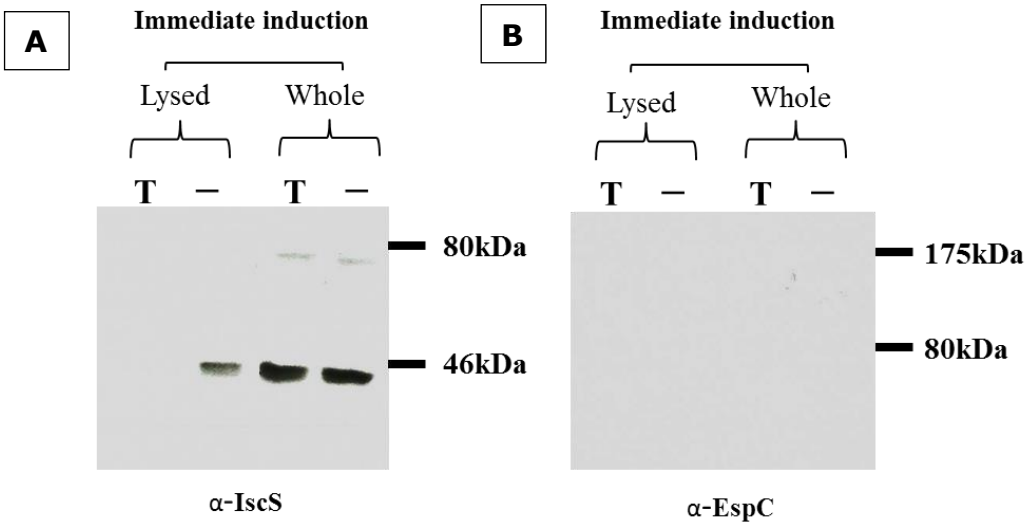


Figure 3.15: Exogenously added trypsin did not degrade the cytoplasmic IscS protein in the control *E. coli* strain. The overnight culture of MG1655 (pBAD33) was diluted 1:100 in LB and concurrently induced with 0.02% arabinose. After 4 h the samples were prepared for trypsin degradation as described in material and methods. Whole and lysed cells were divided into two aliquots and treated with (T) trypsin or without (–) trypsin. The samples separated through 9% SDS-PAGE gel and immunoblotted with α-IscS antisera to detect the cytoplasmic protein (IscS) ~45 kDa **(A)** or with α-EspC antisera to detect EspC protein **(B)**.

3.2.6 The spiral localization pattern of EspC-mCherry was missing in the parental EPECΔ*espC* strain E2348/69

To determine if the observations obtained from MG1655 strain were consistent in different strain backgrounds, the localization of both EspC-mCherry versions was examined in the EPECΔ*espC* strain. As shown in Fig. 3.16 A, the full length EspC-mCherry was accessible to the exogenously added trypsin. Similarly, the truncated EspC-mCherry was degraded by trypsin (Fig. 3.16 B). Interestingly, only one form of the truncated EspC-mCherry (~65 kDa) subsequently shown to lack the protein signal peptide was detected in the delayed induced culture (Fig. 3.16 B), suggesting the ability of the parental strain to process all targeted EspC-mCherry products toward the cytoplasmic membrane. Hence, preventing accumulation or stalling at the IM SecYEG gates.

Consistent with this notion, confocal images of EPECΔ*espC* cells producing truncated EspC-mCherry protein represented normal cell shapes when induced after reached 0.5 of OD_{600} compared to the immediately induced cells (Fig. 3.17 A and B respectively). In the latter case, cells were morphologically changed and lysed especially after long induction period (Fig. 3.17 B). When compared to EPECΔ*espC* expressing the full length EspC-mCherry, there were no obvious changes due to the time of induction. In general, no spirals of full length EspC-mCherry were detected except some patchy localization (Fig. 3.18 A). Over the 2 h of induction, a proportion of circular, elongated and lysed cells were spotted (Fig. 3.18 B). The control EPECΔ*espC* cells producing native mCherry exhibited only diffuse fluorescence (data not shown).

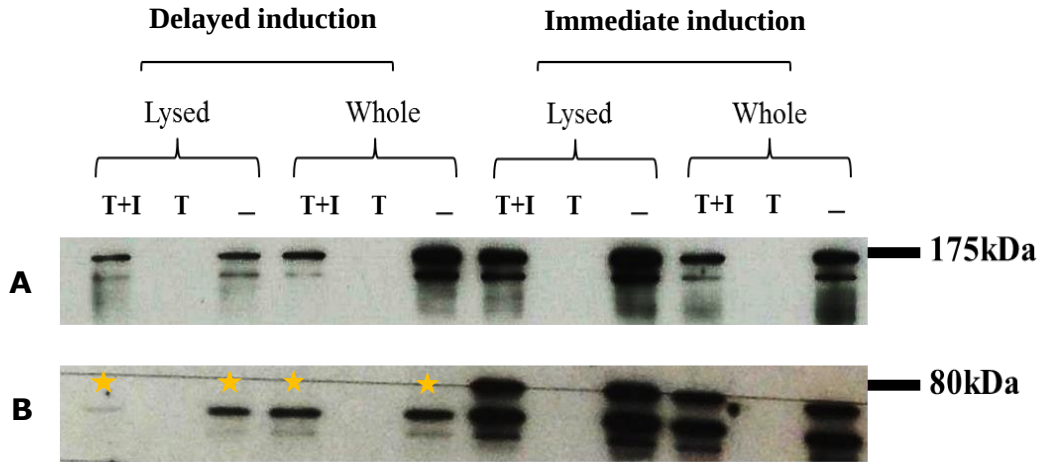


Figure 3.16: Exogenous addition of trypsin degrades both forms of EspC-mCherry in the homologue *E. coli* EPECΔ*espc* strain. Both EPECΔ*espc* (pLA33C1mc) **(A)** and EPECΔ*espc* (pMAC33) **(B)** were grown in LB and induced in two different ways as described previously. Whole and lysed cells were divided into three aliquots and treated with (T) trypsin or without (–) trypsin. As a control, one aliquot was subjected to the protease inhibitor before adding trypsin (T+I) according to material and methods. Both full length 174 kDa EspC-mCherry **(A)** and the truncated EspC-mCherry (70 kDa and 65 kDa) **(B)** forms were degraded by trypsin in whole and lysed cells. Yellow asterisks indicate the position of the missing truncated EspC-mCherry 70 kDa form. Samples were separated by 9% SDS-PAGE gel and immunoblotted with α-EspC antisera.

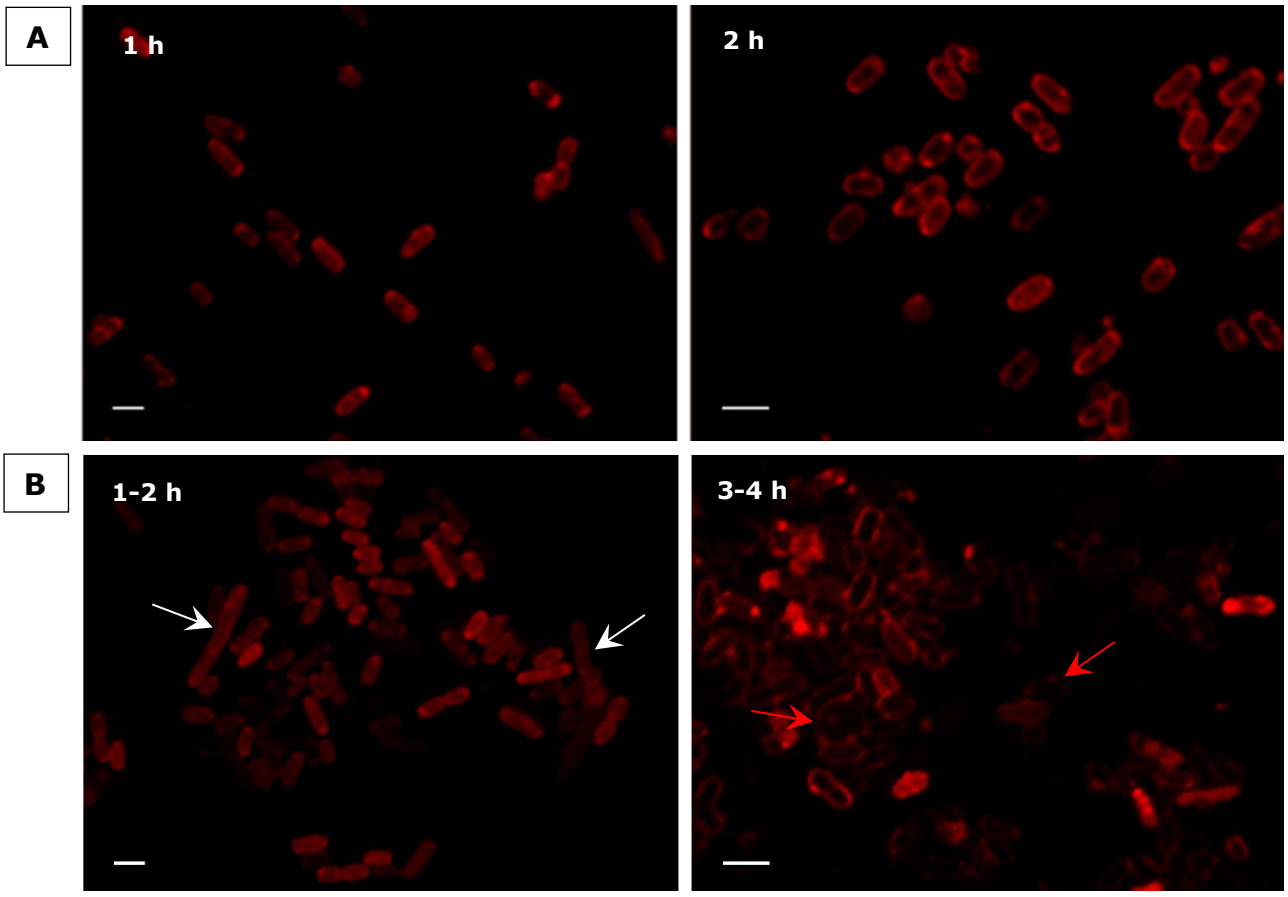


Figure 3.17: Truncated EspC-mCherry (lacking the β-barrel) causes notable growth defect in EPECΔ*espC* strain when the culture is immediately induced and is mainly distributed in a diffuse with some polar and few puncta. (A) The strain EPECΔ*espC* (pMAC33) was grown in LB to OD_{600} of 0.5 then induced with 0.02% arabinose for 2 h (Delayed induction) or **(B)** concurrently induced with 0.02% arabinose for period up to 4 h (immediately induction). Normal cell shapes were observed by confocal microscopy in samples that induced after reaching OD_{600} of 0.5 **(A).** However, abnormal cells were detected over time in the samples that immediately induced (straighter cells: white arrows; rounded cells: red arrows) **(B)**. Scale bar represents 2 μm.

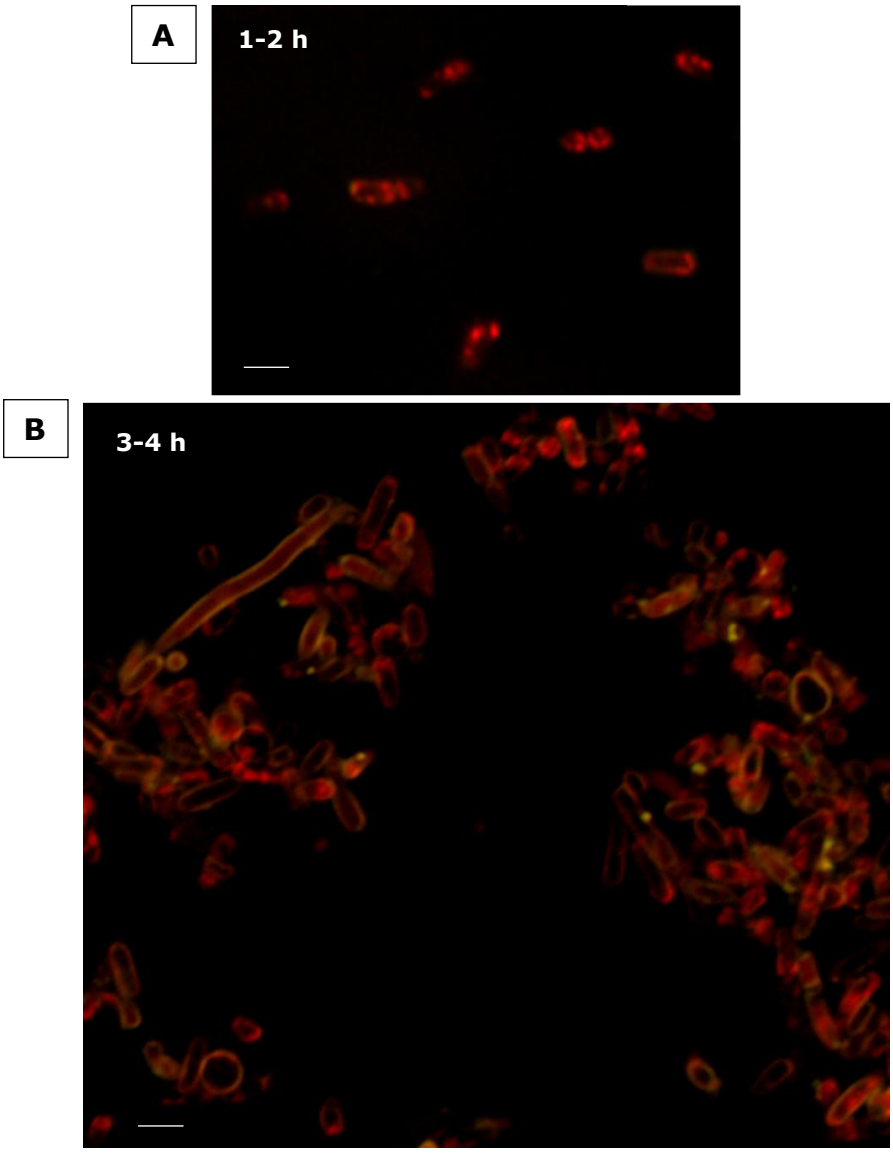


Figure 3.18: The full length EspC-mCherry protein localizes to patchy patterns during the first hour of induction in EPECΔ*espC*. The overnight of EPECΔ*espC* (pLA33C1mc) culture producing full length EspC-mCherry was diluted in LB and concurrently induced by 0.02% arabinose for up to 4 h. Samples were prepared for confocal fluorescent microscopy after 1-2 h **(panel A)**, 3-4 h **(panel B)** as described in Materials and Methods. Cells were collected by centrifugation, washed with PBS and stained with FM 1-43 for staining bacterial OM. scale bar represents 2 μm.

3.2.7 Sucrose gradient analysis confirms that the EspC spiral formation is unlikely to be an artefact of aggregation

Having established that EspC tagged with mCherry fluorescent protein forms a spiral structure when it has been induced with arabinose at 0.2% and 0.02% concentrations, it was necessary to verify that the formation of such spirals was not an artefact arising from high protein production levels (237). Thus, we first reduced the protein production to the lowest level possible to be enough to observe the mCherry inside the cells. Interestingly, cultures induced for 4 h with 0.002% arabinose was more than enough to still observe the discrete patches and formation of the spiral structure of EspC-mCherry in certain cells (Fig. 3.19) suggesting that the spiral pattern of protein localization seen was a genuine phenomenon.

Nevertheless, labelling EspC with the large 34 kDa mCherry fluorescent protein may interfere with its journey toward the bacterial surface and cause protein misfolding or premature folding (aggregated) resulting in fluorescence artefacts (255). To discount this, whole cell extracts induced by 0.02% arabinose from MG1655 (pLA33C1mc), MG1655 (pMAC33) and the control MG1655 (pBAD33) strains were subjected to flotation sucrose gradient fractionation as described in material and methods. This method was selected because it provides a good separation of membrane associated proteins which float up the gradient from aggregated proteins which remain at the bottom resulting from differences in relative densities (253). Remarkably, the full length EspC-

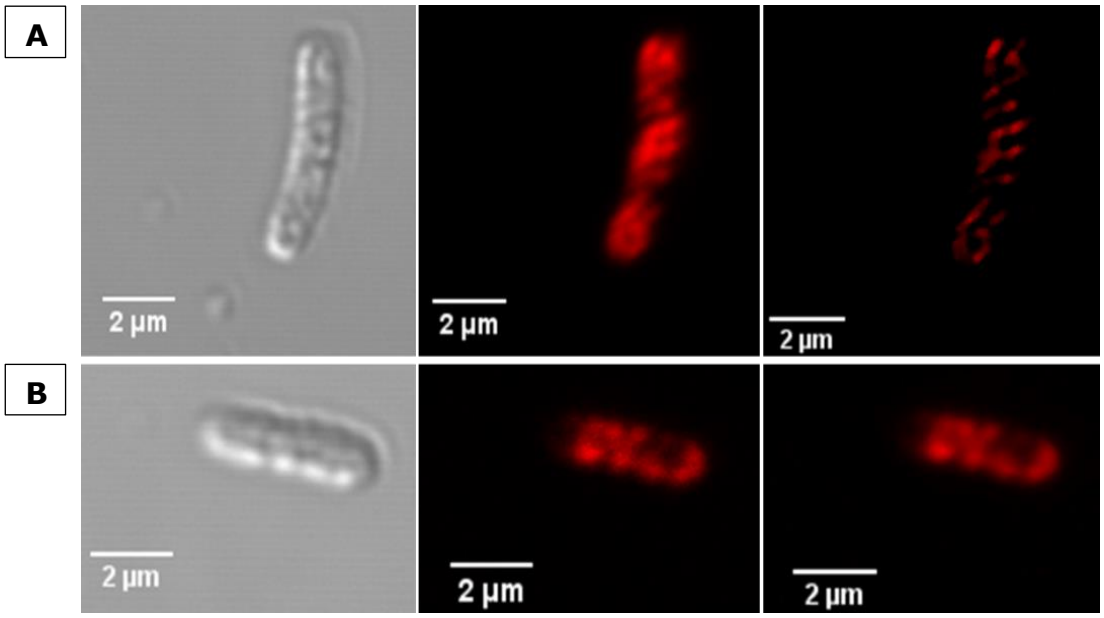


Figure 3.19: The spiral localization of the full length EspC-mCherry was clearly observed at lower protein concentrations. Full length EspC-mCherry induced for 4 h with 0.02% arabinose **(A)** and 0.002% arabinose **(B)**. Pictures are taken by confocal microscope and shown in a contrast phase plus in different filters provided by imageJ software.

mCherry protein was mostly located in the fraction containing 55% sucrose which is the same fractions as the OM protein TolC. There was also no detection of any aggregated EspC at higher sucrose concentrations (58-61%) suggesting that the full length EspC-mCherry is associated with this membrane (Fig. 3.20 A). Likewise, the truncated version of EspC-mCherry did not form aggregates and clearly co-migrated with the fractions containing 55-53% sucrose (Fig. 3.20 B). The lower ~65 kDa form of truncated EspC-mCherry (with a cleaved signal peptide) migrated toward lower sucrose concentrations at 52% and showed in particular to be located in the same fractions as the OM protein TolC (Fig. 3.20 B), together with the full length EspC-mCherry version, indicating that it could be associated with the bacterial OM. No EspC was detected in total cell extracts from control MG1655 (pBAD33) strain (Fig. 3.20 D).

To further explore if the higher expression level of EspC-mCherry might cause localization artefacts as a consequence of formation of aggregates, the flotation gradient analysis was repeated using whole cell extracts from MG1655 (pLA33C1mc) induced with the highest dose of arabinose 0.2% used in this study. Similar results were obtained (Fig. 3.20 C). Consistent with the previous results, the localization of the native 140 kDa EspC produced from the MG1655 (pLA33C1) strain also floated up to the fraction containing 55% sucrose (data not shown). Together, these observations indicate that the EspC helix forms at different protein production levels, discounting the possibility of it being an artefact.

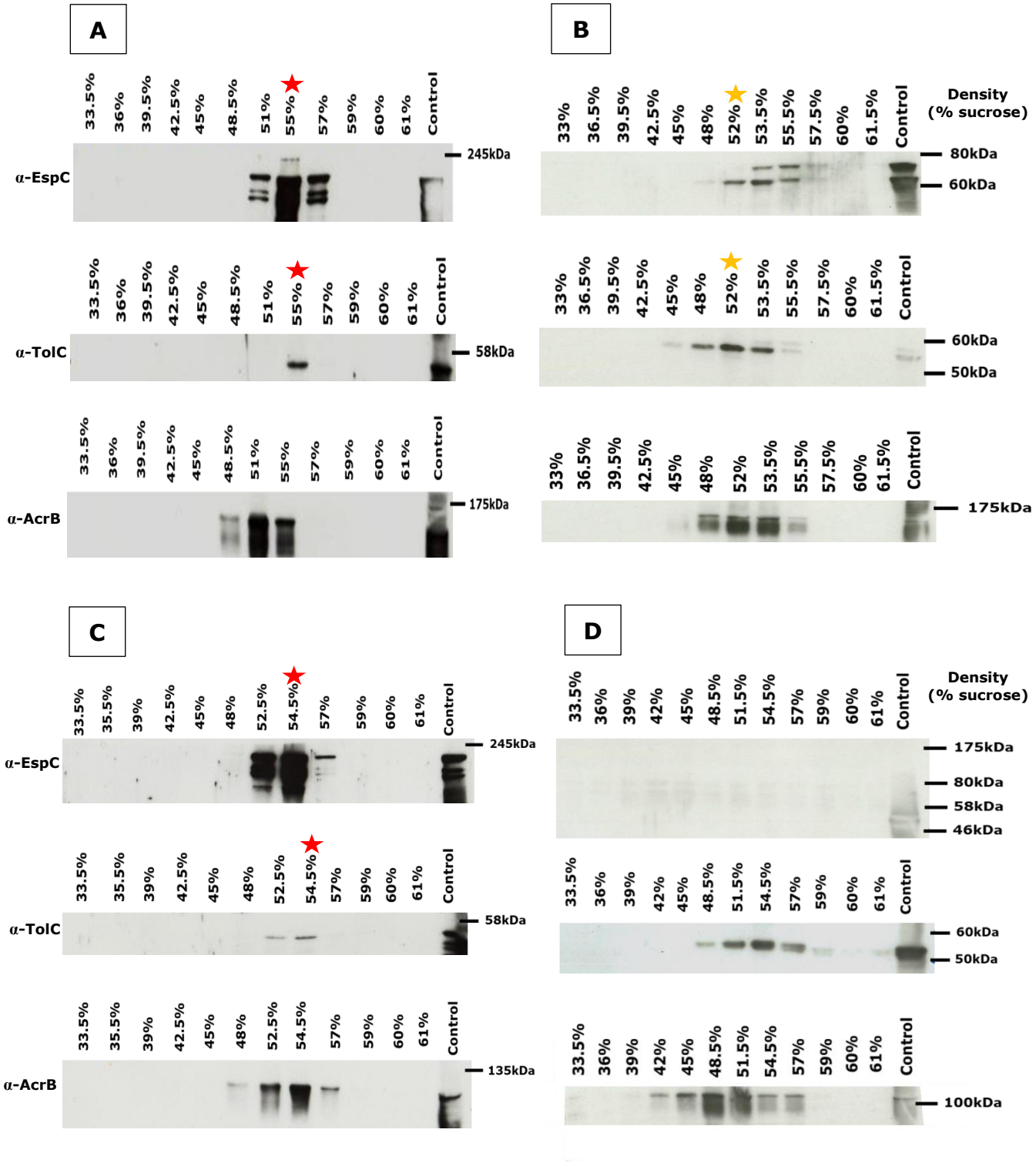


Figure 3.20: Both versions of EspC-mCherry are associated with the bacterial outer membrane. Cell lysates of MG1655 (pLA33C1mc) **(A** and **C)**, MG1655 (pMAC33) **(B)** and the control MG1655 (pBAD33) **(D)** were applied to the bottom of a 32-60% sucrose gradient which was prepared as described in Materials and Methods. The samples in panels **A**, **B** and **D** were induced by 0.02% arabinose except in panel **C** which was induced by 0.2% arabinose. The sucrose concentration (% w/w) in each fraction is also shown. In each panel, aliquots from each fraction of the gradient were separated by SDS-PAGE and immunoblotting using α-EspC (top row), the OM control α-TolC (middle row) and the IM control α-AcrB (bottom row). Red asterisks indicate the location of the full length EspC-mCherry in the fraction containing 55% sucrose, which is similar to the location of TolC, an OM protein. Yellow asterisks point to the position of the truncated EspC-mCherry (~65 kDa) that was mostly located in fraction containing 52% sucrose in which TolC is also densely present. No EspC was found in the control MG1655 (pBAD33) strain **(D)**. Molecular weight markers (kDa) are shown.

3.3 Discussion

In previous work conducted by Kim R. Hardie group, EspC tagged with the mCherry fluorescent protein was shown to locate to a spiral structure that resembles the spiral cytoskeleton of *E. coli* when it has its C-terminal transporter domain attached whereas when lacking the C-terminal β-barrel domain, the localization becomes diffuse. It was proposed that EspC secretion somehow relies on the bacterial helical cytoskeleton for secretion when it has an intact C-terminal β-barrel domain, assuming possible cytoskeleton components integrate with the Sec machinery or Bam complex to facilitate EspC secretion.

Monitoring and tracking protein secretion using fluorescent proteins in living cells is particularly useful for determining and clearly understanding the dynamics and mechanistic details of protein biogenesis processes (256). Such knowledge could impact upon the development of new antimicrobials and healthcare benefits as well as improving our understanding of other protein secretion systems (257,258). The usage of the red fluorescent monomer mCherry in this particular study was due to its unique properties. For instance, mCherry contains GFP-type termini which result in a higher stabillity of N- or C-terminal fusions. Morover, it offers higher photostability, fastest maturation and excellent pH resistance. In addition, it provides long excitation and emission wavelengths (587/610 nm) respectively with a weaker fluorescent background and better fluorescence quality and most importantly it minimizes the generation of artefacts (237,255,259). This

study has clearly shown the usefulness of mCherry to track EspC localization.

The successful cloning of the truncated EspC-mCherry gene from pMAC18-75 (with its pBAD18 backbone) and the native mCherry from the control pmCherry into pBAD33 resulted in the recombinant plasmids called pMAC33 and pLA33mCherry respectively. This will facilitate further studies as pBAD33 constructs generate stronger and more persistent fluorescence that can be monitored and tracked more readily.

The data presented here demonstrates that the localization of the full length EspC-mCherry was shown to be spiral during the onset of secretion and detectable during the first hour of induction. Subsequently, the predominant localization was mostly patchy (arranged in helix) with some polar and some extended helical localization. In contrast, the truncated EspC-mCherry version was totally diffuse during the first two hours of induction and then became polar and distributed in localized spots over time. Super resolution images revealed that the full length EspC-mCherry was localized in discrete patches dispersed circumferentially throughout the cell in helix. The formation of spirals due to the expression of the full length EspC-mCherry at concentrations that exceed those of the endogenous protein was questioned initially as the localization pattern could have resulted from protein aggregation (255). Protein aggregation was also a potential outcome for the truncated EspC-mCherry during secretion due to it missing the β-barrel domain (the transporter domain) that guides the AT

toward BamA. Any deficiencies in this step of secretion would be predicted to infringe upon AT secretion. (150,189).

In an attempt to resolve this issue, flotation sucrose gradient analysis was chosen to confirm whether EspC is aggregating or not during the secretion. As stated previously, this method was chosen because it provides clear separation of ordered protein from disordered aggregates due to significant differences in relative densities (253). Interestingly, the analysis confirmed that both versions of EspC-mCherry as well as the native EspC were integrated into the bacterial OM without detection of any aggregates (Fig. 3.20). Formation of aggregates was also discounted when the spiral structure was still detectable after induction of full length EspC-mCherry at the lowest arabinose concentration used, 0.002% (Fig. 3.19). To evaluate the efficacy of the separation, the integral OM TolC was analysed in parallel (260,261). Unfortunately, the chosen IM control protein (AcrB) unexpectedly co-localized with the OM TolC (260). As shown on Fig. 3. 20, the co-fractionation of AcrB with TolC in the sucrose density gradients was more evident in the strains expressing the recombinant protein compared to the control strain hosting the empty vector, pBAD33. This could be explained by EspC stalling in the periplasm or in one or both membranes due to its overproduction thereby encouraging the bacteria to form intermembrane AcrAB-TolC complexes that span both membranes and make bridges across the periplasmic space as tight links between IM and OM to protect the bacteria from cell death (260). Collectively, the results presented confirm that the EspC spiral formation is unlikely to be an

artefact of aggregation and that the truncated version is somehow integrating with the bacterial OM but causing a significant growth defect.

Exogenously adding trypsin revealed that both versions of EspC-mCherry were located at the surface of bacteria in both *E. coli* backgrounds. It is not surprising that the full length EspC-mCherry was digested by trypsin however unexpectedly degraded as much as the truncated version. It was interesting that truncated EspC-mCherry was also detected in culture supernatants. The hypothesis was that the absence of the C-terminal β-barrel domain would prevent truncated EspC-mCherry secretion from cells due to an inability to recognise the β-barrel-assembly machinery (Bam) complex (189). However, digestion by exogenously added trypsin appeared to confirm localization at the OM. It is difficult to envisage how the truncated EspC-mCherry incorporates into the bacterial OM without the presence of the β-barrel domain. Indeed, the significant growth defect caused due to truncated EspC-mCherry expression that was observed in Fig. 3.13 could provide hints to decipher this conundrum. Additionally, the cytoplasmic protein IscS was also degraded in all strains except the control strain containing the empty vector, pBAD33. It is likely that the cell membranes had been rendered leaky by production of truncated EspC-mCherry. Low OD_{600} measurements and non-compact cell pellets supported this conclusion by indicating a growth defect and cellular fragility. An important question raised by these finding that deserves further investigation is; why was truncated AT missing the β-barrel domain was able to integrate into OM and be secreted into the medium? This could perhaps be investigated by generating a similar truncated EspC version that lacks

the mCherry protein fusion to examine the growth in the absence of mCherry, supporting this with confocal microscopy localization analysis, and cellular fractionation.

To compare and further study the localization of the EspC-mCherry fusion in its natural parental host, the EPECΔ*espC* mutant was complemented with WT EspC produced from the arabinose inducible promoter of the medium copy number plasmid, pBAD33. Interestingly, the full length EspC-mCherry also localized in patches in EPEC which was visible after 1 h of induction. However, the fluorescent spiral localization pattern seen in MG1655 was completely absent (Fig. 3.18 A). The morphological changes that were observed as a consequence of secretion of the full length 174 kDa EspC-mCherry in EPECΔ*espC* were similar to those observed following overexpression of essential proteins that maintain the rod-shape of Gram-negative bacteria. For instance, overproduction of RodZ (that acts with MreB to maintain the cell shape) causes formation of straighter cells (224). Likewise, overproduction of WT *E. coli* PBP2 caused rounded cells after 2 h of induction (262). Thus, it could be suggested that EspC may depend on the bacterial cytoskeleton components to continue its journey toward the bacterial surface. Clearly, however, further detailed investigation will be required to validate this prediction.

On the other hand, the truncated EspC-mCherry did not cause significant growth defects in EPECΔ*espC* compared to MG1655 strain especially when the culture was induced after a period of extended growth. Explanations for this could be that EPEC may have chaperones

to aid folding or more efficient targeting of EspC, or EPEC may have factors more able to degrade misfolded or prematurely folded AT passenger domains (26,150,151). A comparative sequencing analysis between the genome of the EPEC strain E2348/69 with the genomes of eight sequenced *E. coli* strains including the K-12 strain MG1655 revealed that the chromosomes of these organisms are highly conserved and showing a high degree of overall synteny. However, E2348/69 contains specific genes most of which are carried on mobile genetic elements which are often associated with EPEC pathogenicity (4). These might encompass extra factors not present in the laboratory strain.

Overall, it is apparent that the spiral fluorescent localization pattern of full length EspC-mCherry is an orchestrated secretion mechanism dependent upon its C-terminal transporter domain. The SR-SIM data presented here clearly showed that the pattern appears as small patches that are distributed around the cell circumference of rod-shaped bacteria and arranged in helices. These data suggest that EspC secretion appears to depend on the bacterial cytoskeleton, the MreB helix. However, it still remains uncertain if EspC incorporates into the bacterial cytoskeleton via the actin homologue MreB during secretion or uses different bacterial cell wall machineries reported previously to organize into spirals e.g. the Sec machinery (234,235). This will become clearer by investigating the consequences of perturbing MreB and the Sec machinery upon EspC secretion.

Chapter 4

Localization of EspC is dependent upon its C-terminal β-barrel, the bacterial cytoskeleton actin homologue MreB, and the Sec translocon

4.1 Introduction

Having established (see previous chapter) that fluorescently tagged EspC containing its β-barrel locates to a structure that resembles the spiral cytoskeleton of *E. coli*, it was an interesting next step to investigate the role of MreB on EspC secretion. It was hoped that this might shed light upon the secretion of ATs and reveal why spiral localization was only observed when the C-terminal translocator domain was present.

Based on the similarity between the spiral localization of EspC and the bacterial helical cytoskeleton, it was hypothesized that the secretion of EspC depends on MreB helical filaments. It is possible that the Sec machinery may act as a pathway to deliver proteins to this structure and the dynamic nature of the cytoskeleton may facilitate relocation towards bacterial poles where protein secretion has been reported for some ATs (199). Supporting this notion, MreB filaments have been implicated in polar localization of the aspartate chemoreceptor Tar, several polarised proteins in *C. crescentus*, and the AT IcsA, with depletion in MreB causing a disturbance to this localization pattern (210). Indeed, perturbing MreB in *P. aeruginosa* with A22 [*S*-(3,4-dichlorobenzyl) isothiourea], a compound that inhibits the formation of MreB fibres and rapidly perturbs its function causes mis-localization of the type IV pilus retraction ATPase PilT and attenuation of twitching motility (207). Polar localization has been demonstrated in several ATs (199), and the spiral localization pattern of the full length EspC-mCherry was accompanied by

a degree of accumulation of EspC in both bacterial poles (Figs. 3.7 B and. 3.8).

Numerous studies have provided examples of the Sec translocon distributed in a spiral structure as well (141,234,235). Moreover, the actin homologue MreB might be implicated in targeting cytoplasmic proteins toward the Sec translocon machinery. For example, secretion of Colibactin-maturating enzyme (CIbp) across the IM was MreB and Sec/SRP/YidC dependent (236).

As mentioned in section 2.15, the A22 compound was used in this study to perturb the bacterial cytoskeleton MreB. Addition of A22 to the bacterial cells disrupts the helical localization of MreB *in vivo* and causes loss of rod-shaped cell morphology (254). A22 was shown to function as a competitive inhibitor of ATP binding by MreB due to its ability to bind with high affinity and specificity to the nucleotide-binding pocket of MreB, overlapping with the position that would be occupied by the *β*- and *γ*- phosphates of ATP. This eventually leads to disassembly and diffusion of MreB in the cytoplasm (263).

To further understand the relationship between MreB, Sec and protein translocation, we set out to dissect the consequences of perturbing the function of MreB, the Sec translocon and the β-barrel AT domain on the localization of EspC.

4.2 Results

4.2.1 Investigating the localization of the bacterial actin homologue MreB and its role in EspC secretion in *E. coli*

4.2.1.1 Cloning strategy used to construct pLA33mreBmc vector

To test the possibility that the bacterial cytoskeleton actin homologue MreB is directly responsible for the spiral arrangement of EspC at the cell membrane, the localization of MreB itself was initiated in single cells. To visualize the localization pattern of MreB in live cells, an *E. coli* MG1655 strain bearing an arabinose inducible *mreB-mCherry* fusion was constructed. The strategy adopted for creation of the *mreB-mCherry* fusion in a pBAD33 backbone is shown in the Fig. 4.1. The open reading frame (ORF) sequence of the *E. coli* MG1655 *mreB* gene was PCR amplified using the primer pair F-MreB-*Bgl*II/R-MreB-*Sal*I (see table 2.4, chapter 2) to introduce *Bgl*II and *Sal*I sites at the 5' and 3' ends of *mreB* coding region respectively. The resultant products were separated using agarose gel electrophoresis, which confirmed the presence of the expected *mreB* fragment (~1044 bp) (Fig. 4.1 A). The purified DNA was digested with restriction enzymes *Bgl*II and *Sal*I and ligated into similarly digested pBAD33 vector (Fig. 4.1 B). Following ligation and transformation into *E. coli* MG1655, the resultant construct was extracted from selected transformants and confirmed by either single *Bgl*II or double *Bgl*II/*Sal*I digestion, and named pLA33mreB (Fig. 4.1 C). An absence of point mutations was also verified by DNA sequencing.

After successful cloning of *mreB* into pBAD33, the next stage in the strategy was to insert mCherry into the recombinant MreB protein. To do this, it was important first to delineate a suitable position in the crystal structure of MreB to insert mCherry, thus minimising any potential loss of function following insertion of the mCherry fluorescent protein into MreB. Previously, it was demonstrated that a fully functional *mreB-mCherry* fusion was successfully made when the fluorescent protein was inserted in subdomain IIB of MreB between helices 6 and 7 (222,237,264). To identify the ideal position, a predictive MreB crystal structure model was first created using the I-TASSER (Iterative Threading ASSEmbly Refinement) server for protein structure and function predictions (http://zhanglab.ccmb.med.umich.edu/I-TASSER/), and then mapped onto a 3D model using PyMol 3D Zalman software. As shown in Fig. 4.2, the crystal structure of MreB facilitated the identification of the position of helix 6. This position appears ideal for the insertion of mCherry as it is situated laterally and distant from a cleft between domains I and II which holds the nucleotide-binding site. Thus, a strategy was devised to insert mCherry into the loop preceding helix 6 of MreB (Fig. 4.2).

In order to insert mCherry into the chosen site, SDM was performed to insert an *Avr*II restriction site into the DNA corresponding to the amino acid position 228 in MreB using the primer pair F-mreB-*Avr*II/R-mreB-*Avr*II (see table 2.4, chapter 2) (Figs. 4.1 D and 4.2). Subsequently, the PCR product (6377 bp) was digested with *Dpn*I enzyme to remove the parental DNA copies followed by transformation into commercially prepared *E. coli* Top10 competent cells. To confirm the mutation, the

plasmid extracted from the selected transformants was successfully linearized with *Avr*II, (Fig. 4.1 E), and DNA sequenced to confirm the existence of the desired base substitutions (including the *Avr*II restriction site) with no point mutations. Finally, to introduce the fluorescent protein into MreB, the *mCherry* gene was amplified using primers mCherry-F-mreB/mCherry-R-mreB (see table 2.4, chapter 2) to introduce *Avr*II recognition sites at both termini of the gene (Fig. 4.1 F). The PCR product was digested with *Avr*II, and ligated into pLA33mreB$_{AvrII}$ which was digested with the same restriction enzyme resulting in the formation of the new recombinant plasmid, pLA33mreBmc (Fig. 4.1 G). Plasmid pLA33mreBmc was verified by digestion with *Sal*I and *Avr*II and compared with the digestion profile of the parent plasmid, pLA33mreB$_{AvrII}$ (Fig. 4.1 G). DNA sequencing was repeated for a final confirmation. The successful clone was subsequently transformed into competent *E. coli* MG1655 cells for analysis.

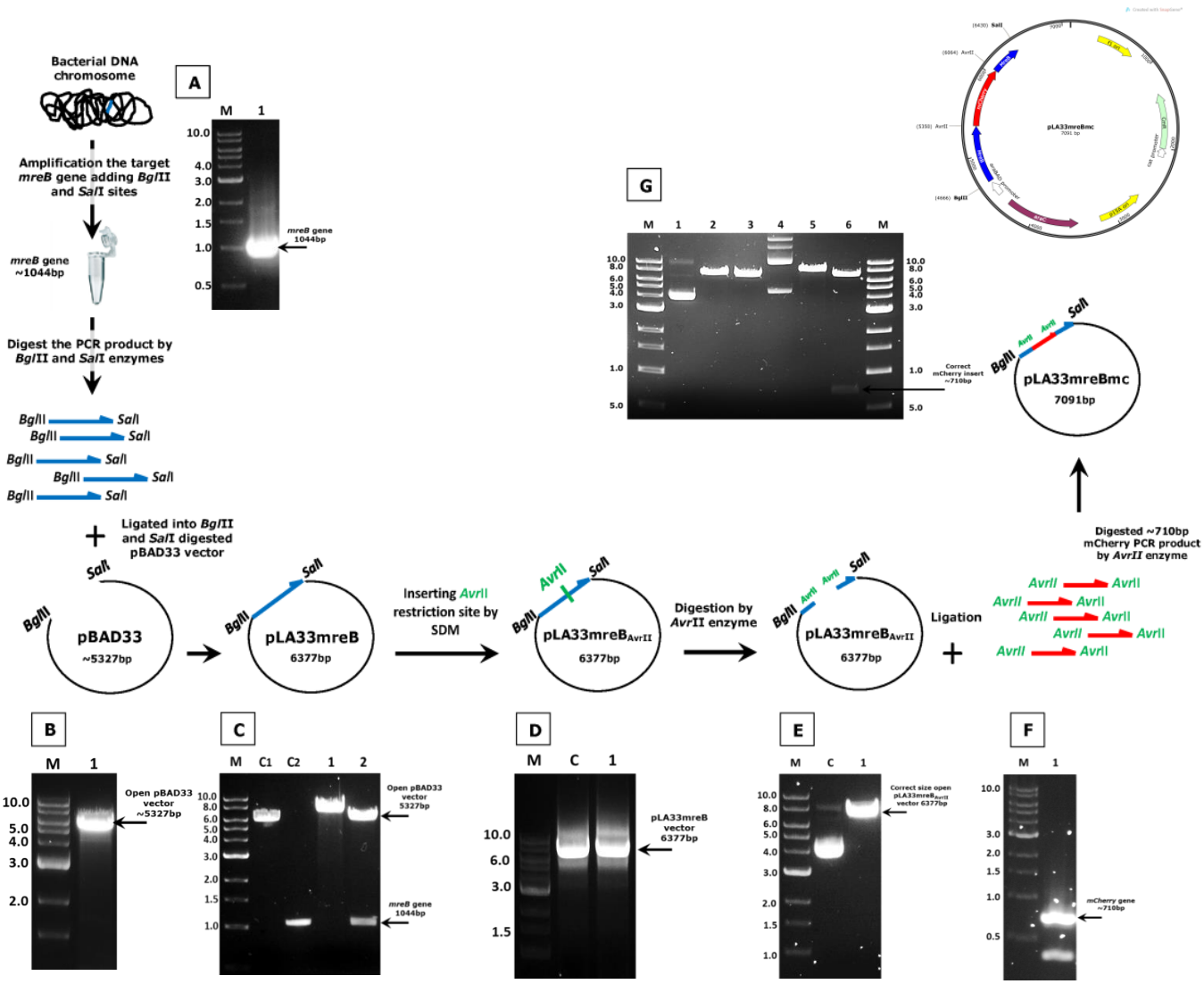


Figure 4.1: The cloning strategy to fuse mCherry with MreB. The ORF of *mreB* gene was PCR amplified to incorporate *Bgl*II and *Sal*I restriction sites at the 5' and 3' ends of *mreB* coding region respectively. Splitting of ~1044 bp PCR product confirms the successful amplification **(Agarose A)**. Digestion of the PCR product with *Bgl*II and *Sal*I enzyme and ligation into pBAD33 vector which was digested with the same enzymes **(Agarose B)**. To confirm whether *mreB* had been cloned into the pBAD33 backbone, selected Plasmids were digested with the same set of enzymes and yielded the expected digestion profile (5327 bp plus 1044 bp fragments), which were named pLA33mreB **(Agarose C**: Lane C_1 and C_2 showing the controls of only open pBAD33 vector and digested *mreB* fragment respectively: Lane 1 representing a single *Bgl*II digestion while Lane 2 illustrating double *Bgl*II and *Sal*I digestion**).** To enable insertion of mCherry into MreB, SDM was first utilized to introduce *Avr*II restriction site to chosen site (see text) yields pLA33mreB$_{AvrII}$ **(Agarose D**: Lane C control of non-digested and Lane 1 *Dpn*I digested PCR products**)**. Subsequently, mCherry gene was amplified using primers designed (See primer table chapter 2) to include *Avr*II restriction site at both gene ends **(Agarose F)**. This mCherry PCR product was digested with *Avr*II enzyme and ligated into open pLA33mreB$_{AvrII}$ vector which was digested with the same restriction enzyme **(Agarose E** : Lane C showing control of plasmid DNA and Lane 1 displaying the correct size open vector after digestion with *Avr*II enzyme**)**. The new construct termed as pLA33mreBmc was successfully made and verified by single *Sal*I and *Avr*II digestion and comparison with similarly digested pLA33mreB$_{AvrII}$ vector **(Agarose G**: Lane 1, 2 and 3 are for pLA33mreB$_{AvrII}$ vector showing the control DNA plasmid, digestion with *Sal*I and digestion with *Avr*II enzyme respectively whereas Lane 4, 5 and 6 are for the new pLA33mreBmc vector illustrating the control DNA plasmid, digestion with *Sal*I and digestion with *Avr*II enzyme respectively**)**. M indicates the 1 kb DNA molecular marker. A copy of the new plasmid map obtained from SnapGene software is included.

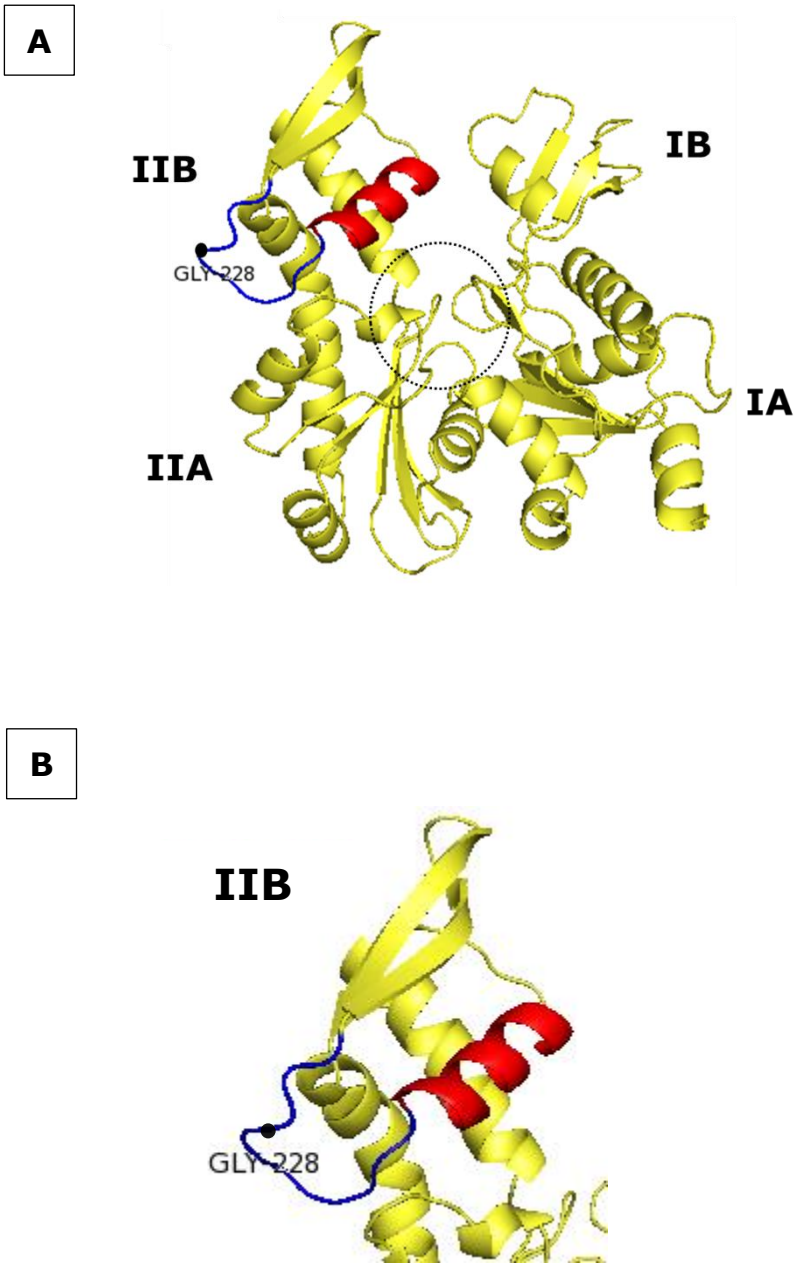


Figure 4.2: The location of the amino acid selected for mutagenesis in the predicted MreB crystallographic structure. The predicted 3D model of MreB developed in PyMol Zalman software showing the typical four-domain architecture IA, IB, IIA and IIB. Black circle indicates the ATP binding pocket and the helix 6 is highlighted in red **(A)**. A closer view at the subdomain IIB clearly reveals the position of glycine amino acid (black spot) in the blue loop preceding the helix 6 **(B)**.

4.2.1.2 MreB protein localizes in discrete patches with filaments that are short and cross the cells diagonally

Following the successful construction of pLA33mreBmc hosting the *mreB-mCherry* fusion, and transformation into *E. coli* MG1655, production of MreB-mCherry was confirmed. Using a specific antibody (α-dsRed) to detect mCherry protein, immunoblotting revealed the presence of the expected ~65 kDa protein corresponding to the MreB-mCherry in lysates induced with 0.2% or 0.02% arabinose, with higher quantities being produced with greater concentrations of arabinose induction (Fig. 4.3).

To reveal the localization pattern of the actin homologue MreB, the production of MreB-mCherry fusion was monitored in *E. coli* MG1655 over time using confocal microscopy. Interestingly, during the first 2 h of induction, the majority of cells showed a diffuse MreB-mCherry localization pattern with distinguishable dark areas in the cytoplasm (Fig. 4.4 B). A small proportion of cells exhibited discrete spots of fluorescence at the cell surface and short filaments could be discerned spanning the cells (Fig. 4.4 A). Strikingly, after 3 to 4 h, all cells had completely changed their shape from rods to lemon shapes with a punctate pattern of fluorescence at their surface (Fig. 4.4 C). To further explore if the dark regions observed in the cytoplasm were occluded by the bacterial chromosome, the experiment was repeated and after 2 h of induction, cells were stained with the nucleic acid stain, DAPI. As expected, a bright blue colour has coincided with a lack of red fluorescence from MreB-mCherry (Fig. 4.4 C).

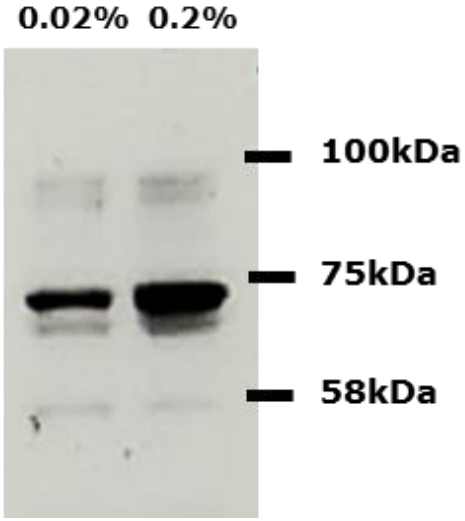


Figure 4.3: Production of MreB-mCherry protein in *E. coli* MG1655. The overnight culture of *E. coli* MG1655 containing pLA33mreBmc was diluted 1:100 and concurrently induced with 0.2% and 0.02% arabinose. After 4 h of induction, whole cell lysates were prepared and separated through 9% SDS-PAGE gel. Subsequently, Western blotted using α-dsRed detected the expected ~65 kDa MreB-mCherry protein.

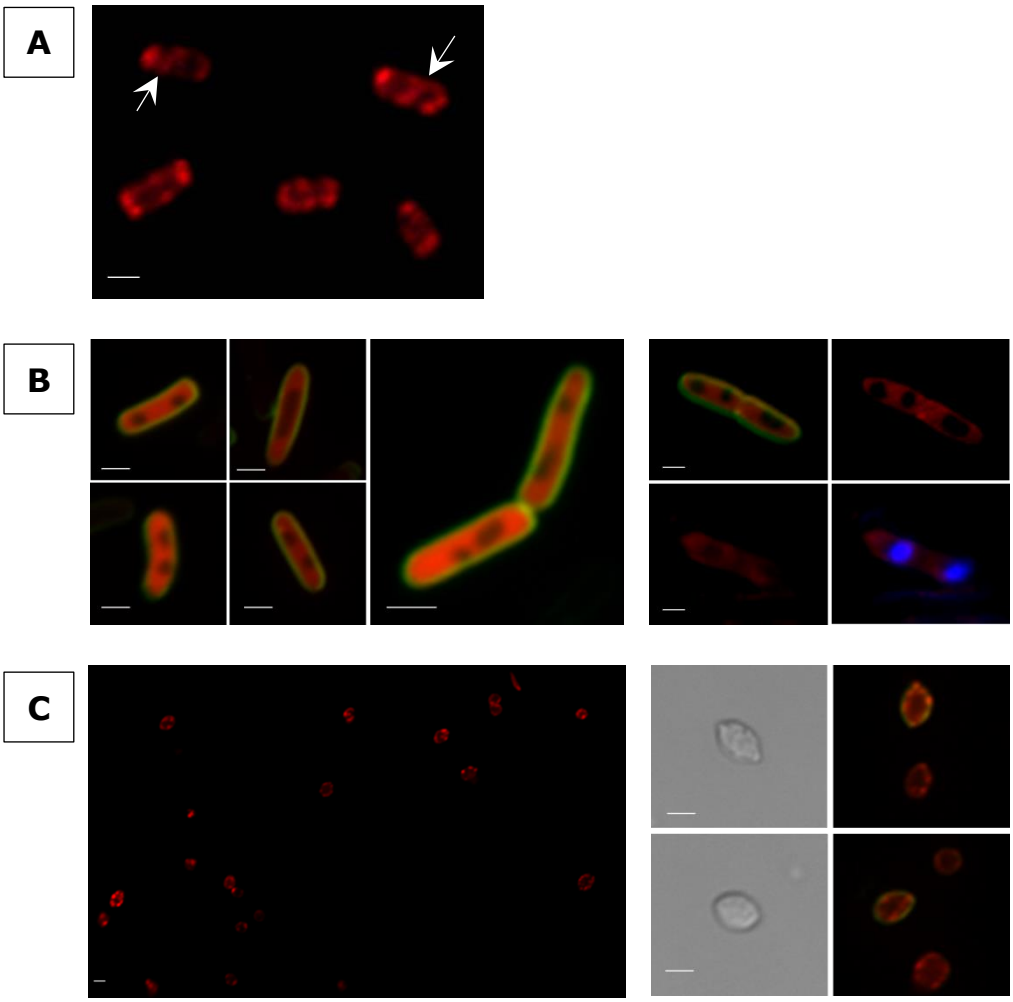


Figure 4.4: The fluorescent localization patterns of MreB-mCherry observed over time in *E. coli* MG1655 strain. *E. coli* MG1655 (pLA33mreBmc) producing MreB-mCherry was grown in LB, induced by 0.02% arabinose and monitored up to 4 h by confocal microscopy as described in materials and methods. Bright red spots at cell surfaces and short bands crossing some cells during the first 2 h of induction are indicated by white arrows **(A).** Blue fluorescence reveals where DAPI has stained the chromosome in the majority of cells **(B)**. Lemon shaped cells with cell surface spots of red fluorescence observed after 3 h of induction **(C).** The green colour indicates cells that were treated with the membrane stain FM 1-43, scale bars represent 2 μm.

4.2.1.3 Perturbing the actin homologue cytoskeleton MreB with A22 altered the localization of EspC-mCherry

To explore the hypothesis that the bacterial cytoskeleton actin homologue MreB is directly involved in the helical localization of EspC, we next sought to determine whether disrupting this cytoskeleton actin homologue might perturb the localization of EspC. MreB is essential for bacterial survival and making an mreB null mutant will cause cell lysis (219,265). Using A22 compound was an alternative approach chosen in this work to try to inhibit MreB filament assembly. It has been reported that the effect of A22 is similar to the effect of the MreB null mutant (254,266). In order to determine the growth-inhibitory levels of A22 on *E. coli* (K-12) MG1655 strain, 0.2% arabinose induced wild-type MG1655 culture was treated with A22 at zero µg/ml ($A22^0$), 2.5 µg/ml ($A22^{2.5}$) and 10 µg/ml ($A22^{10}$), and subjected to confocal microscopy as described in materials and methods. As shown in Fig. 4.5, the lower concentration of A22 had a moderate effect on cell shape, changing it from a rod to a lemon shape, whereas at higher concentration the cells completely converted to cocci.

In order to monitor EspC-mCherry localization patterns in the presence of A22, 0.2% arabinose induced MG1655 (pLA33C1mc) and MG1655 (pMAC33) cultures were treated with $A22^{2.5}$ and $A22^{10}$. As a control, a set of samples were induced and grown without treatment ($A22^0$). As a consequence of using A22, the fluorescent localization patterns of both EspC-mCherry forms dramatically changed. The fluorescent localization pattern for the full length EspC-mCherry became diffuse. Treatment with

$A22^{10}$ completely disrupted the EspC-mCherry localization resulting in no distinct spiral patterns being detected (appeared diffuse with no spirals detected) (Figs. 4.6 A and. 4.7 B). At a concentration of $A22^{2.5}$, the localization appeared to have lost its organization with only a few irregular punctate pattern of fluorescence being detected (Fig. 4.7 A). The diffuse fluorescence pattern observed in those cells sometimes appeared condensed at the cell periphery due to the space occupied by the bacterial chromosomal DNA in the cytoplasm (Fig. 4.7 B). In contrast, the truncated version of EspC-mCherry lacking the beta barrel was observed as strong diffuse fluorescence with irregular punctate foci (Fig. 4.6 B).

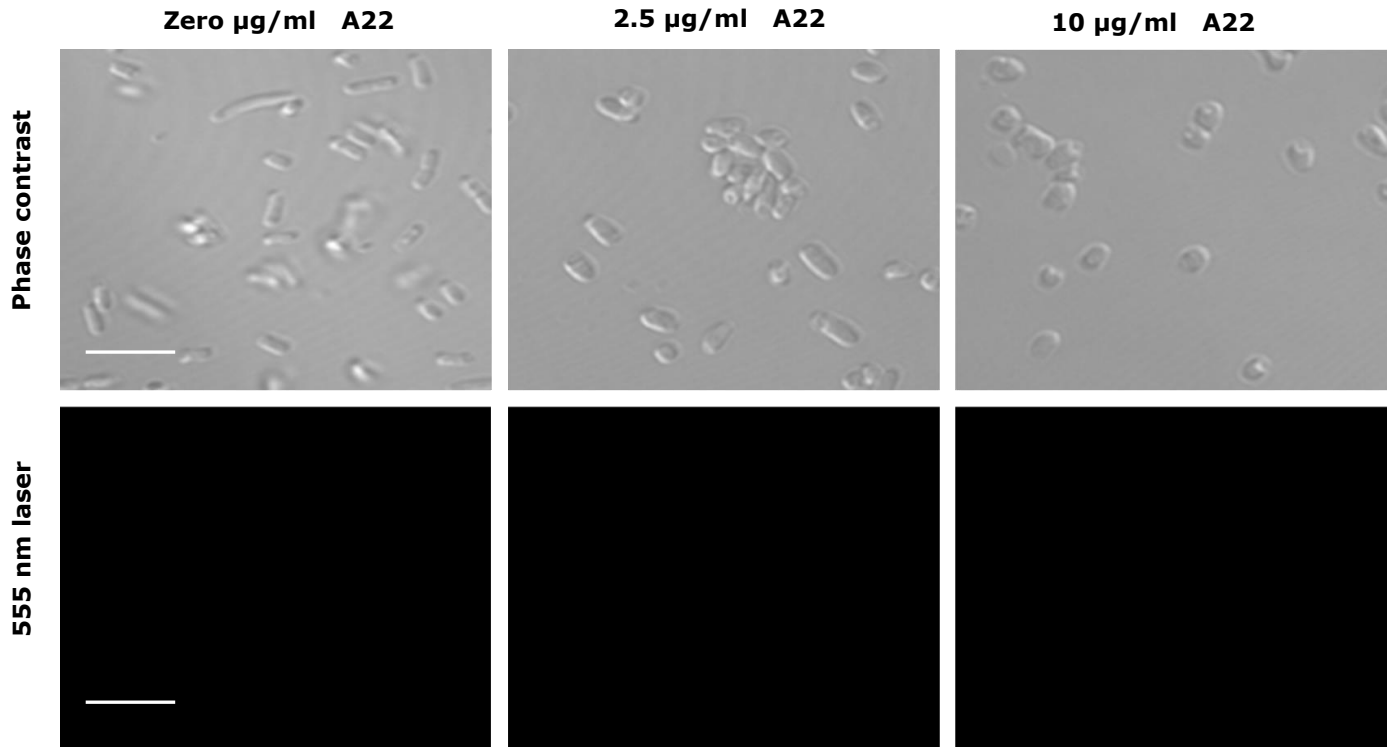


Figure 4.5: A22 causes bacterial cell shape changes. 0.2% arabinose induced MG1655 wt was grown in LB to OD_{600} of 0.05 then treated with $A22^{0}$, $A22^{2.5}$ or $A22^{10}$ and incubated at 37˚C shaking for up to 4 h as described in materials and methods. Representative lemon shaped bacteria (middle image; $A22^{2.5}$) and rounded cells (right hand column; $A22^{10}$) are shown. Phase contrast and mCherry fluorescence pictures were taken by confocal microscopy. The green 555 nm laser was used to detect mCherry. No red fluorescent was detected in the wild type strain. Scale bar represents 5 µm.

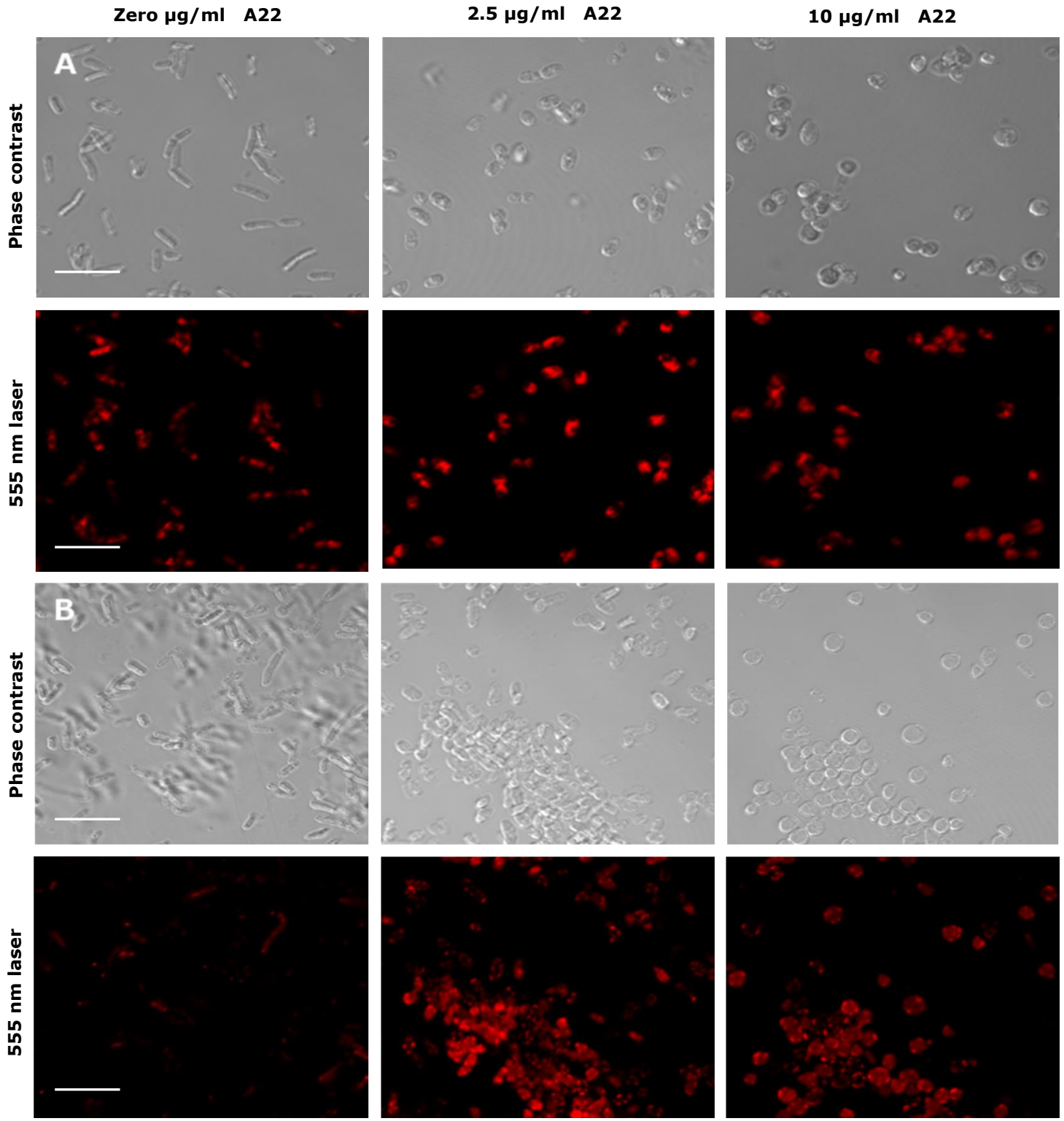


Figure 4.6: A22 alters the localization of EspC-mCherry with and without the β-barrel domain. 0.2% arabinose induced MG1655 (pLA33C1mc) **(A)** and MG1655 (pMAC33) **(B)** strains were grown in LB to OD_{600} of 0.05 then treated with $A22^{0}$, $A22^{2.5}$ or $A22^{10}$ and incubated at 37°C shaking for up to 4 h. Phase contrast and mCherry fluorescence pictures were taken by confocal microscopy. The green 555 nm laser was used to detect mCherry. Scale bars represent 5 µm.

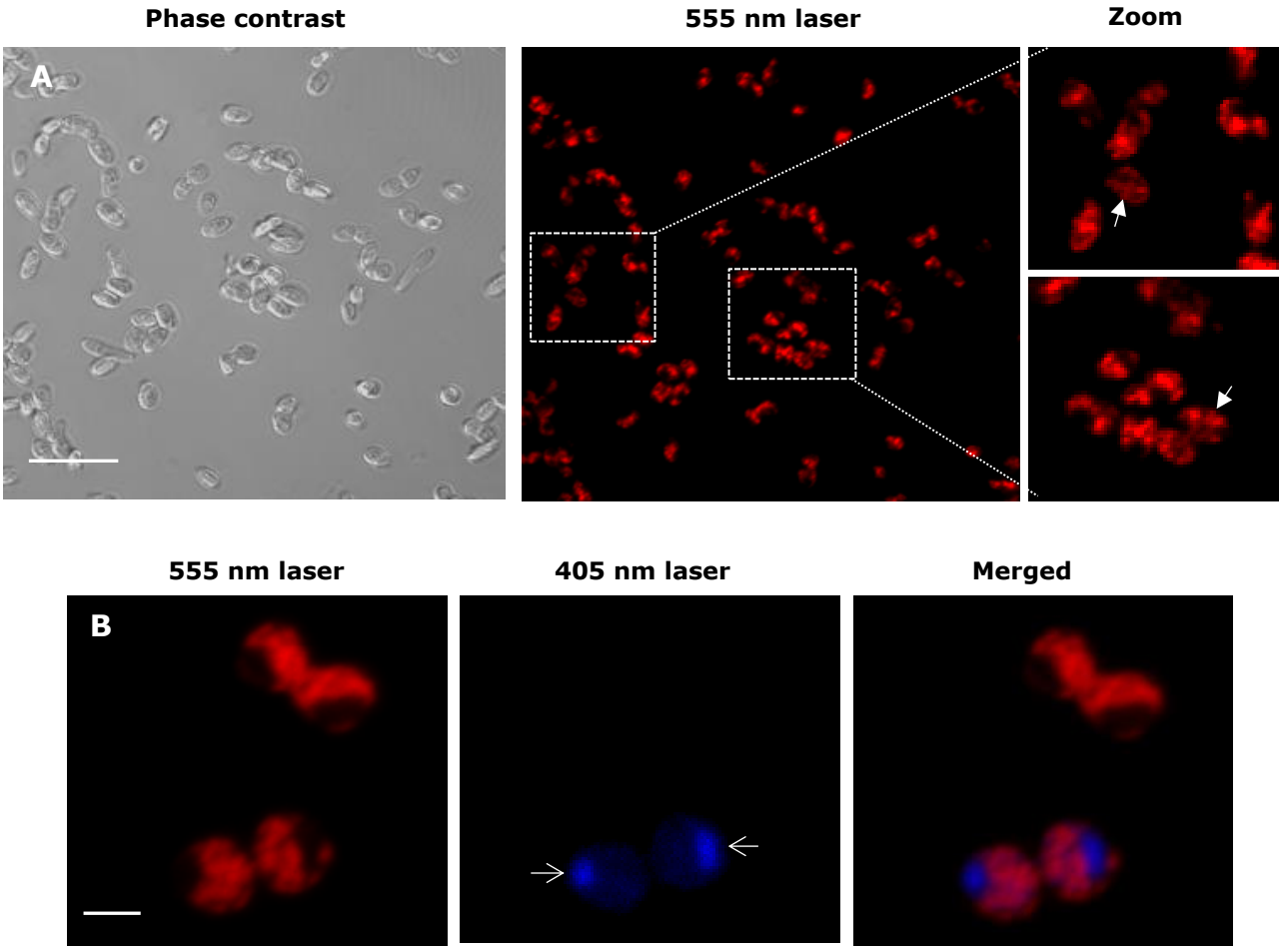


Figure 4.7: Effects of A22 concentrations on full length EspC-mCherry localization. Distorted fluorescent localization pattern was apparent in cells treated with $A22^{2.5}$, the closed white arrows indicate some irregular bands detected in particular cells **(A)**. No bands or spiral structure were observed in cells treated with $A22^{10}$ and staining with SYTOX dead blue stain indicates the position of the bacterial chromosome (open white arrows) **(B)**. 0.2% arabinose induced MG1655 (pLA33C1mc) strain was grown in LB to OD_{600} of 0.05 then treated with $A22^{2.5}$ **(A)** $A22^{10}$ **(B)** and incubated at 37°C shaking for up to 4 h as described in materials and methods. Phase contrast and mCherry fluorescence pictures were taken by confocal microscopy. The green 555 nm laser was used to detect mCherry while 405 nm violet laser was used to detect SYTOX stained dead cells. White rectangles indicate zoomed view, and merged images combine red and blue fluorescence. Scale bar represents 5 µm **(A)** or 2 µm **(B)**.

To test the influence of A22 on the growth of MG1655 strains, 0.2% arabinose induced MG1655 (pLA33C1mc), MG1655 (pMAC33) as well as MG1655 wt were treated with the same set of A22 concentrations as previously. The optical density (OD) was monitored over time (Fig. 4.8). The growth rates between samples treated with $A22^{0}$, $A22^{2.5}$ and $A22^{10}$ were almost similar (Fig. 4.8 A and B). The growth of MG1655 (pMAC33) in A22 mirrored that of MG1655 wt and MG1655 (pLA33C1mc) for the first hour, but was considerably lower from 2 h onwards (Fig. 4.8 C). The growth profile of MG1655 (pMAC33) without A22 was consistent with previous observations (Figs.3.12 and 3.13).

Although the OD measurements clearly showed that A22 had no dose-dependent effect on the growth of MG1655, it remained to be determined if viability was also affected. To ascertain this, MG1655 (pLA33C1mc) and MG1655 (pMAC33) cultures were treated with $A22^{10}$ followed by staining with the live-dead stain SYTOX® blue. As before, no spiral structures were visible in cells producing full length EspC-mCherry (Fig. 4.9), while truncated EspC-mCherry was localized in a punctate pattern (Fig. 4.10). Notably, suggestive of a leaky membrane, the number of cells stained by SYTOX was higher for MG1655 (pMAC33) than MG1655 (pLA33C1mc) (Figs. 4.10 A and 4.9 A, respectively).

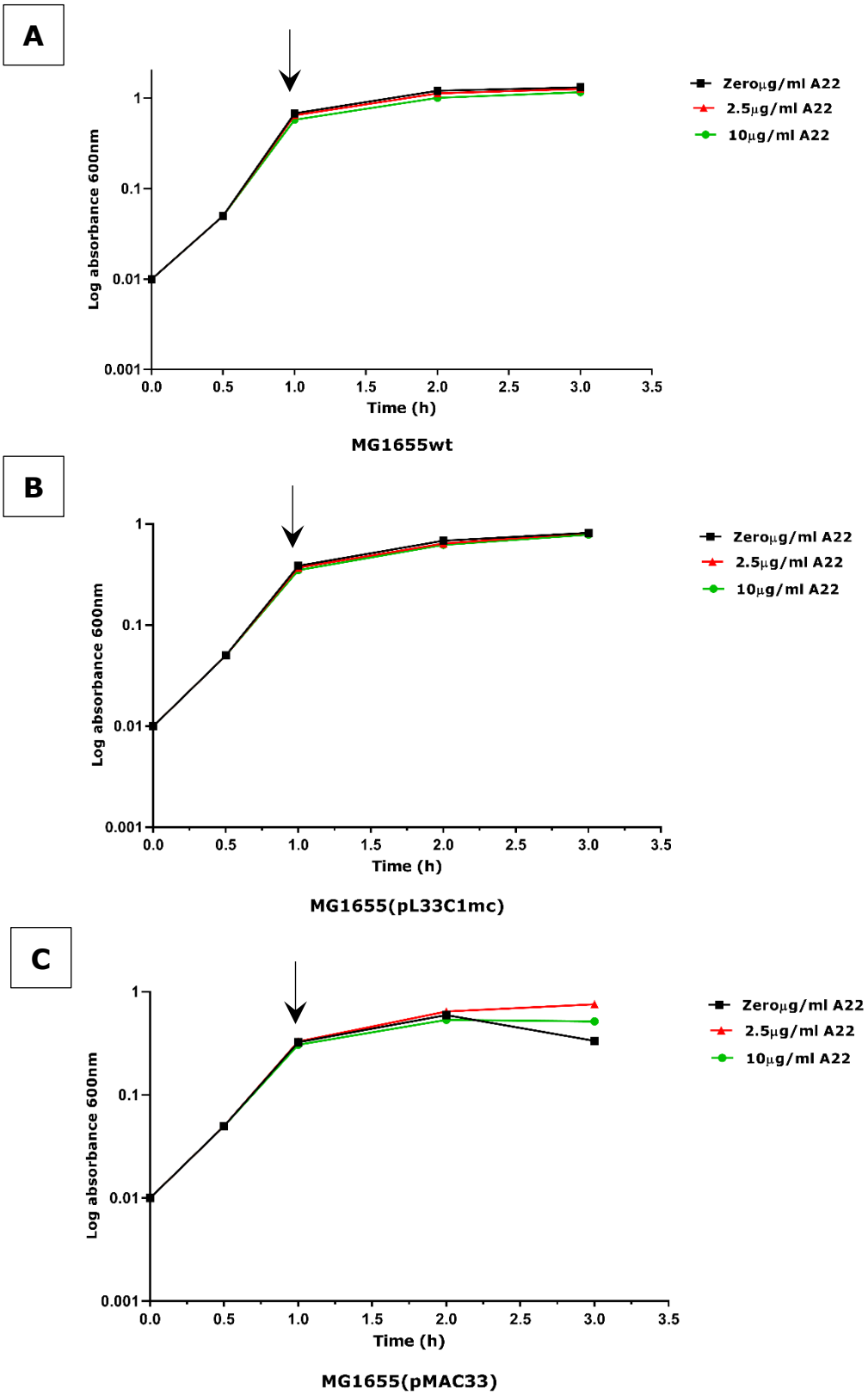


Figure 4.8: Addition of small concentrations of A22 did not perturb the growth of MG1655 strains. 0.2% arabinose induced MG1655 wt **(A)**, MG1655 (pLA33C1mc) **(B)** and MG1655 (pMAC33) **(C)** strains were grown in LB to OD_{600} of 0.05 then treated with $A22^{0}$, $A22^{2.5}$ or $A22^{10}$. Growth was monitored over time by OD_{600} for up to 3 h after addition of A22. Black arrows indicate the time point of addition of A22.

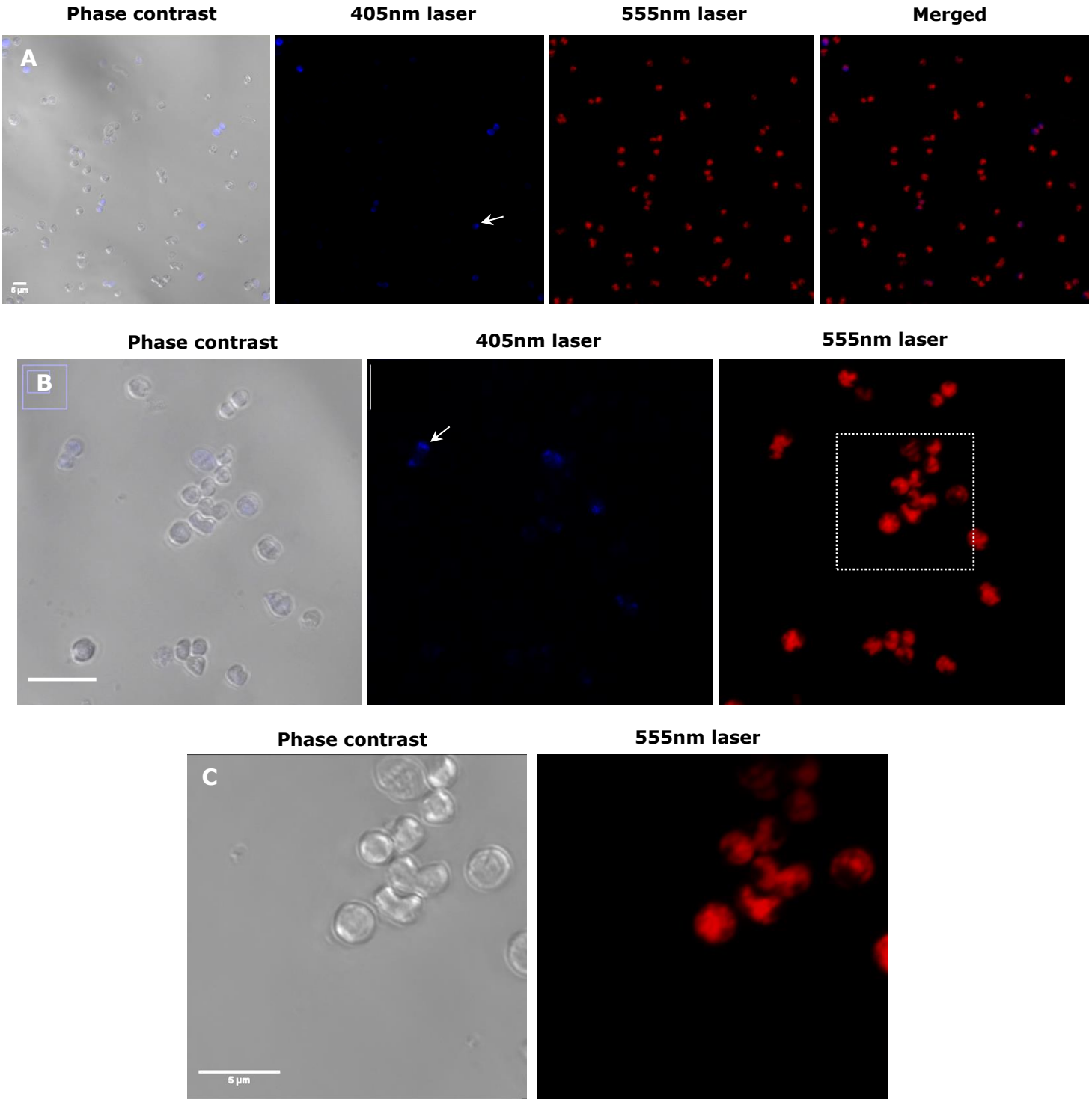


Figure 4.9: Full length EspC-mCherry does not form spirals in A22 treated MG1655, and some cells take up SYTOX® blue. MG1655 (pLA33C1mc) was induced with 0.2% arabinose, treated with A22[10] and stained with SYTOX® blue. Images show treated cells with gradual zooming from smallest **(A)** to the medium **(B)** and largest magnification **(C)**. The 405 nm violet laser was used to detect the dead cells whilst the 555 nm green laser was used to excite mCherry. White rectangles in (B) indicate zoomed view shown in (C), and white arrows show stained DNA and merged images combine red and blue fluorescence. Scale bars represent 5 µm.

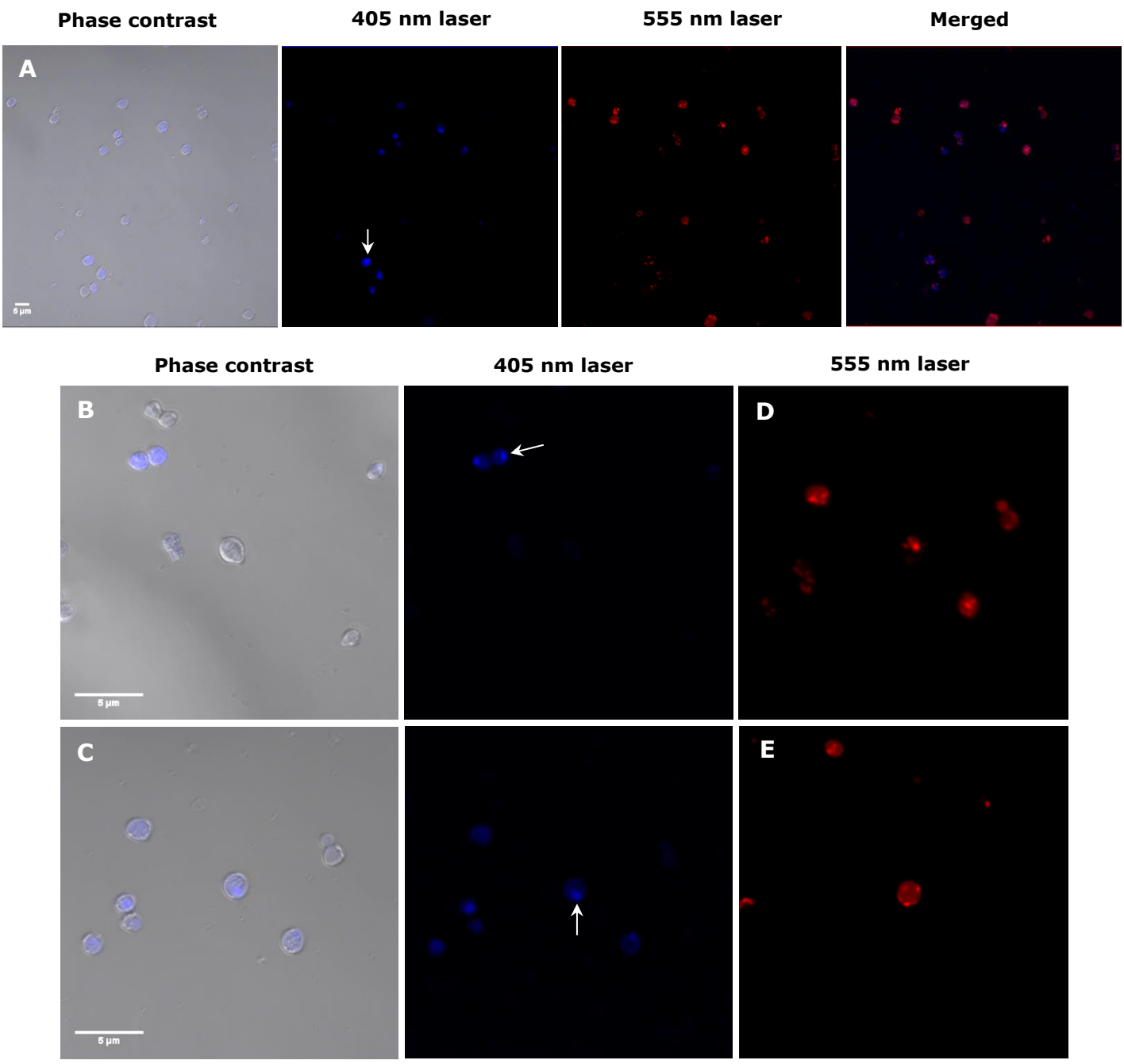


Figure 4.10: Truncated EspC-mCherry localizes in a punctate pattern in A22 treated MG1655, and the majority of cells take up SYTOX® blue. MG1655 (pMAC33) was induced with 0.2% arabinose, treated with A22[10] and stained with SYTOX® blue. Images show treated cells with gradual zooming from smallest **(A)** to largest magnification **(B** - **E)**. Images D and E were chosen from a different field of that shown in B and C. 405 nm violet laser was used to detect the dead cells while 555 nm green laser to excite mCherry. White arrows show stained DNA and merged images combine red and blue fluorescence. Scale bars represent 5 µm.

4.2.1.3.1 Truncated EspC-mCherry associates with membranes in two forms

In order to determine if the altered localization of EspC in cells treated with A22 was reflected in changes in processing, cells were fractionated into membranes and soluble compartments. Both MG1655 (pLA33C1mc) and MG1655 (pMAC33) were induced with 0.2% and 0.02% arabinose and treated with $A22^{0}$, $A22^{2.5}$ and $A22^{10}$. OM and IM fractions were confirmed by immunoblotting with α-TolC and α-AcrB respectively. Whilst no obvious differences in processing of the full length 174 kDa EspC-mCherry were detected upon addition of A22 (Fig. 4.11 A and C), two forms of truncated EspC-mCherry (upper ~70 kDa and lower ~65 kDa) were detected and both clearly localized with membranes. The larger form (~70 kDa) was primarily associated with the OM fraction, and became more abundant there with increasing A22 concentration (Fig. 4.11 B and D). In contrast, the smaller form (~65 kDa) was primarily associated with the IM and became fainter with increasing A22 concentration (Figs. 4.11 B and 4.12 B). In line with this, the loss of the 65 kDa form of truncated EspC-mCherry with increasing A22 was evident in whole cell extracts.

Surprisingly, both forms of truncated EspC-mCherry were detected in the culture supernatant of untreated bacteria. This had not been expected as the β-barrel transporter domain was not present. It was clear that the ~65 kDa form was not lost from the whole cells due to export as it was gradually absent from the culture supernatant when A22 was added for increasing time or at higher concentrations (Fig. 4.12

A). Immunoblotting whole cell extracts with α-dsRed confirmed that both forms of the protein retained mCherry (Fig. 4.12 B).

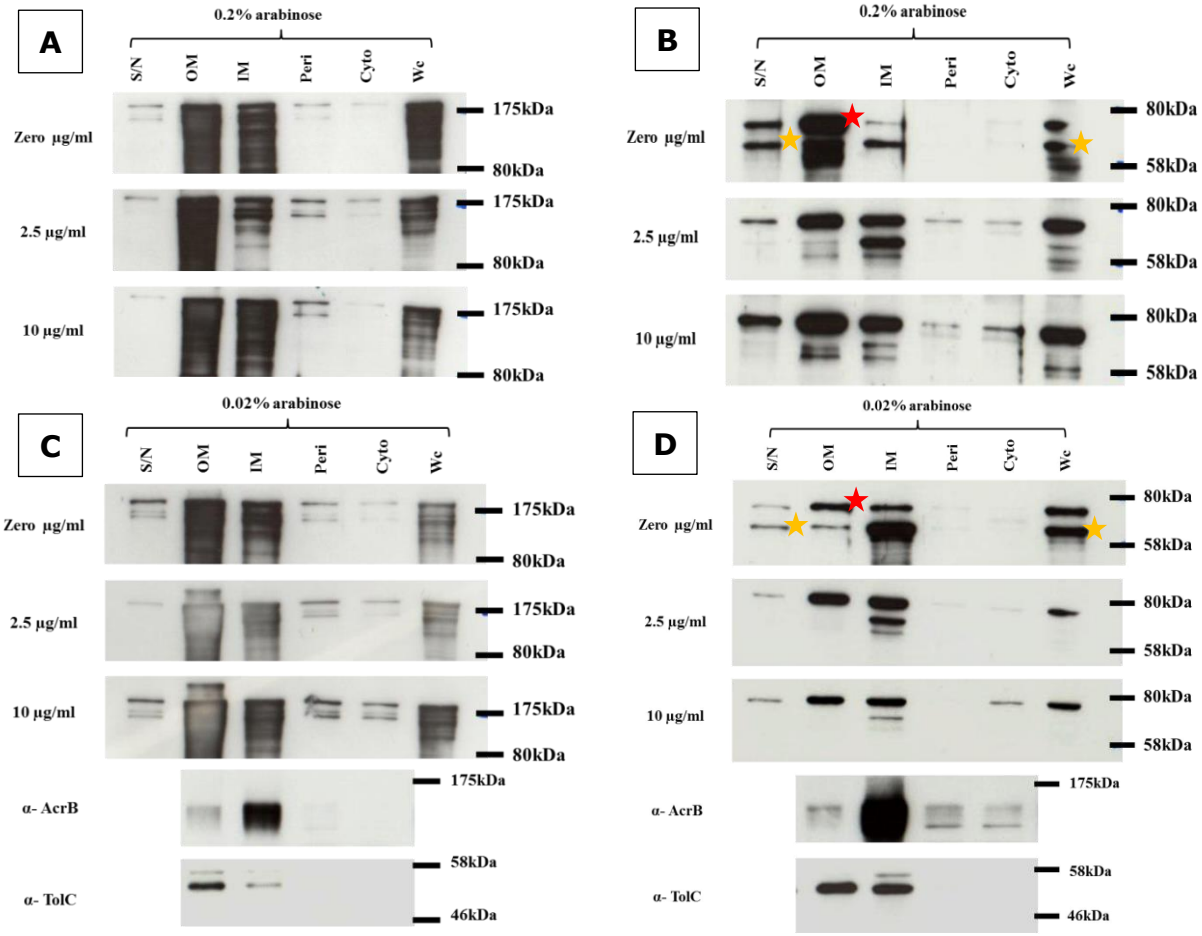


Figure 4.11: Truncated EspC-mCherry associates with membranes in two different forms. α-EspC immunoblots of cellular fractionation following treatment with $A22^{0}$, $A22^{2.5}$ or $A22^{10}$ as described in materials and methods. MG1655 (pLA33C1mc) induced for 4 h with 0.2% **(Panel A)** or 0.02% arabinose **(Panel C)**. MG1655 (pMAC33) induced for same period with 0.2% **(Panel B)** or 0.02% **(Panel D)**. Fractionation was performed as described in chapter 2 to generate whole cell (Wc), cytoplasmic (Cyto), inner membrane (IM), periplasmic (Peri) and outer membrane (OM) fractions. The control IM protein has being confirmed by α-AcrB (110 kDa) and the OM with α-TolC (~50 kDa) **(Panel C** and **D)**. The larger form of truncated version of truncated EspC-mcherry (~70 kDa: red asterisk), the smaller form of truncated version of truncated EspC-mcherry (yellow asterisk) are indicated in supernatant (S/N), WC, or OM fractions. Proteins were separated in 9% SDS-PAGE.

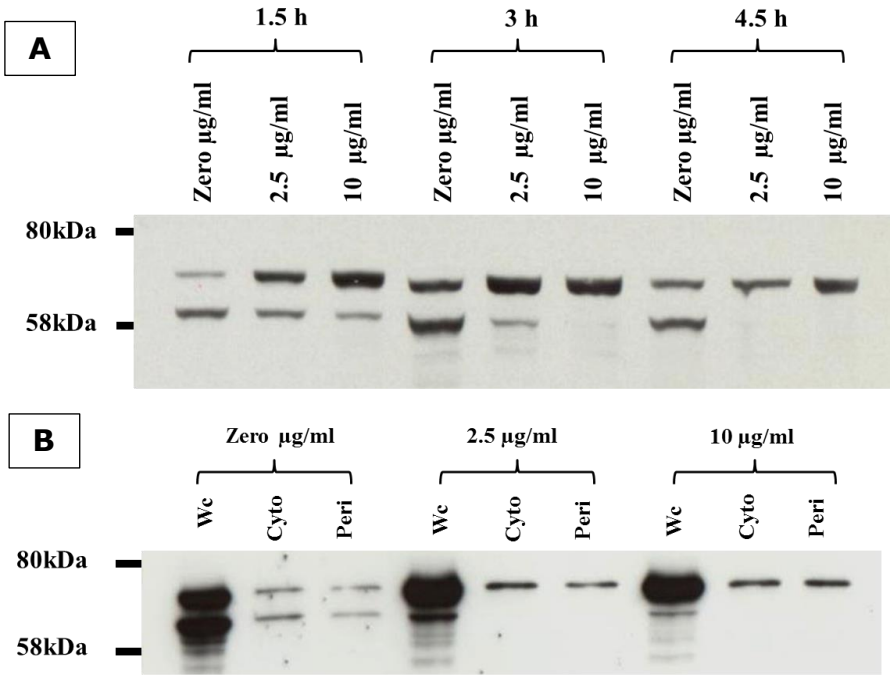


Figure 4.12: Both forms of truncated EspC retain mCherry, with the larger form predominantly found in high A22 concentrations. α-EspC immunoblot of supernatant samples from MG1655 (pMAC33) culture induced with 0.2% arabinose, treated with different A22 concentrations and collected over time **(A)**. α-dsRed immunoblot of whole cells (Wc), cytoplasmic (Cyto) and periplasmic (Peri) fractions from the same strain induced with 0.2% arabinose and treated with the same A22 concentrations but collected after 4 h of A22 treatment **(B)**. Proteins were separated in 9% SDS-PAGE.

4.2.2 Strains producing EspC with or without mCherry have cell wall defects and production of the 174 kDa EspC-mCherry makes cells bigger

Since the expression of truncated EspC-mCherry lacking the C-terminal transporter domain alters the growth of MG1655, and because the localization of EspC-mCherry in MG1655 and EPECΔ*espC* backgrounds was different, microscopy was performed to examine the cell integrity. Propidium iodide (PI) uptake could not be utilized due to its overlapping red fluorescence with mCherry. Thus, SYTOX® blue dead cell stain was utilized. This stain has high affinity for DNA and can easily enter cells with compromised membranes whilst being excluded from viable cells. Four h induced cultures were stained with SYTOX® blue at room temperature and incubated for 5 min in the dark as described in materials and methods. MG1655 wt and MG1655 (pmCherry) were only minimally fluorescent (Fig. 4.13 A and B, respectively). Cells producing the truncated EspC-mCherry exhibited a remarkable blue fluorescence (Fig. 4.13 C) while a moderate blue fluorescence was evident in cells producing the full length EspC-mCherry (Fig. 4.13 D). Only MG1655 data is shown as it was not significantly different to that obtained for EPECΔ*espC* except that lower levels of staining was observed.

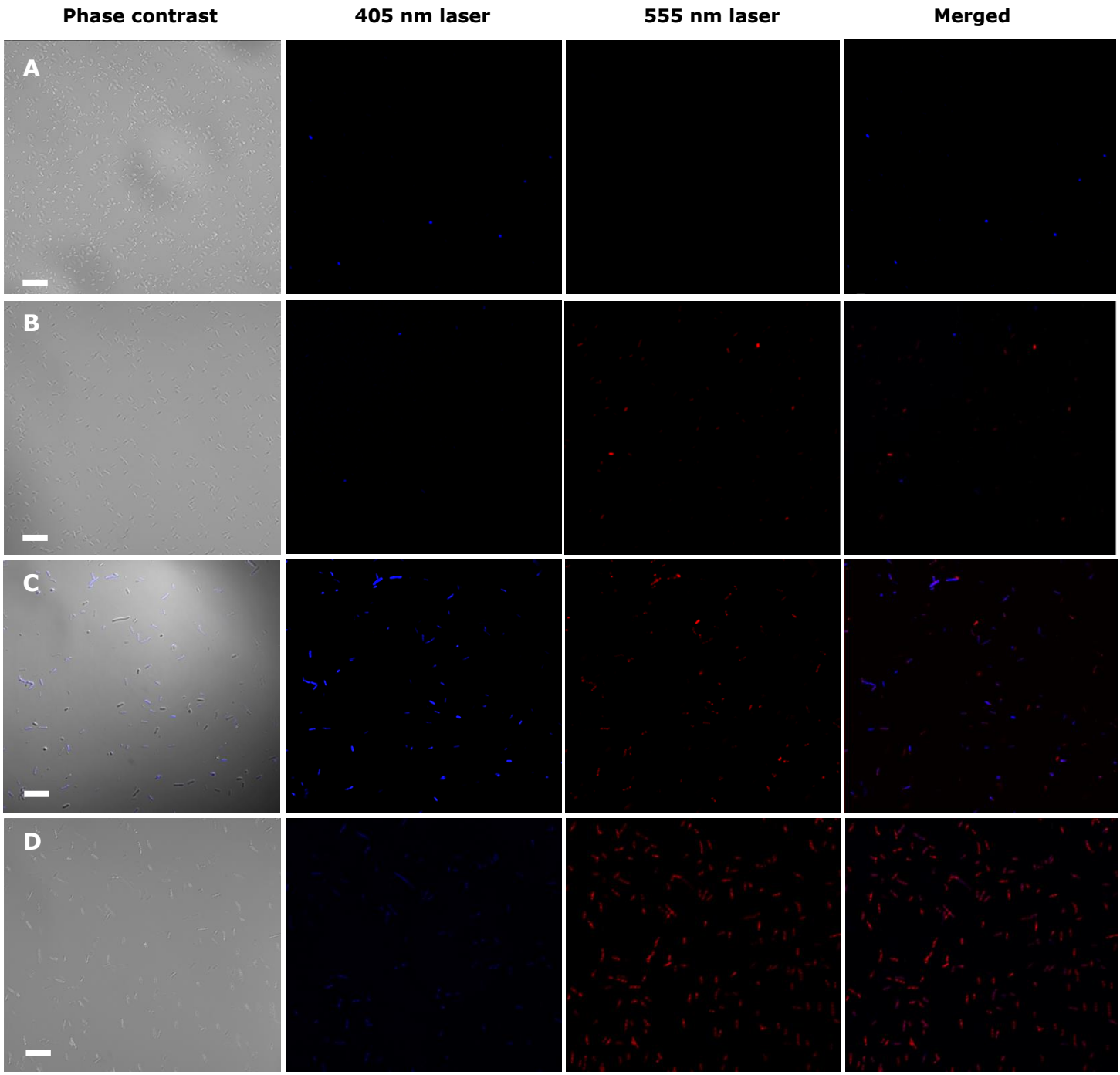


Figure 4.13: Secretion of EspC-mcherry with and without the C-terminal transporter domain alters cell shape and integrity. Four h 0.2% arabinose induced cultures of MG1655 wt **(A)**, MG1655 (pmCherry) **(B)**, MG1655 (pMAC33) **(C)**, MG1655 (pLA33C1mc) **(D)** were washed with PBS and resuspended to OD_{600} of 0.5 following staining with SYTOX® dead blue stain. Images were taken by confocal microscopy and subjected to 405 nm violet laser to excite the blue stain while the 555 nm green laser was used in parallel to stimulate the mCherry fluorescent protein. Images were merged to combine both fluorescence signals. Scale bars represent 5 µm.

It was possible that the high concentration of arabinose used to induce the production of EspC might be responsible for the growth defects and membrane leakiness. To optimise a suitable arabinose concentration for *espC* induction without causing any defective growth, both MG1655 (pLA33C1mc) and MG1655 (pMAC33) cultures were induced by 10 fold decreasing arabinose concentrations (0.2%, 0.02%, 0.002% and 0.0002%) for up to 4 h (Figs. 4.14 and 4.15, respectively). Samples were taken to measure the cell density (OD_{600}) over time and SYTOX® blue dead cell stain was applied. Interestingly, the proportion of cells staining blue fell significantly at 0.02% arabinose concentration in both strains while the proportion of the red cells was almost similar to cultures induced with 0.2% arabinose (Figs. 4.14 C and 4.15 C). However, the numbers of red cells were substantially decreased at arabinose concentrations lower than 0.02% suggesting that 0.02% is optimal for detecting the red fluorescence with minimal growth defects (Figs. 4.14 D and 4.15 D). Parallel induction with similar arabinose concentrations and SYTOX® blue staining revealed no growth defects encountered in MG1655 wt and MG1655 (pmCherry) strains. MG1655 (pLA33C1) and MG1655 (pMAC33) exhibited similar phenotypes (data not shown).

To determine whether 0.02% arabinose was the best option to use to detect fluorescently labelled EspC from pLA33C1mc and pMAC33 without harming the cells, the changes in cell density (OD_{600}) were monitored and the growth rate calculated for all strains. Surprisingly, growth rates in cultures induced with 0.02% were not recovered to the extent anticipated from the microscopy (Fig. 4.16).

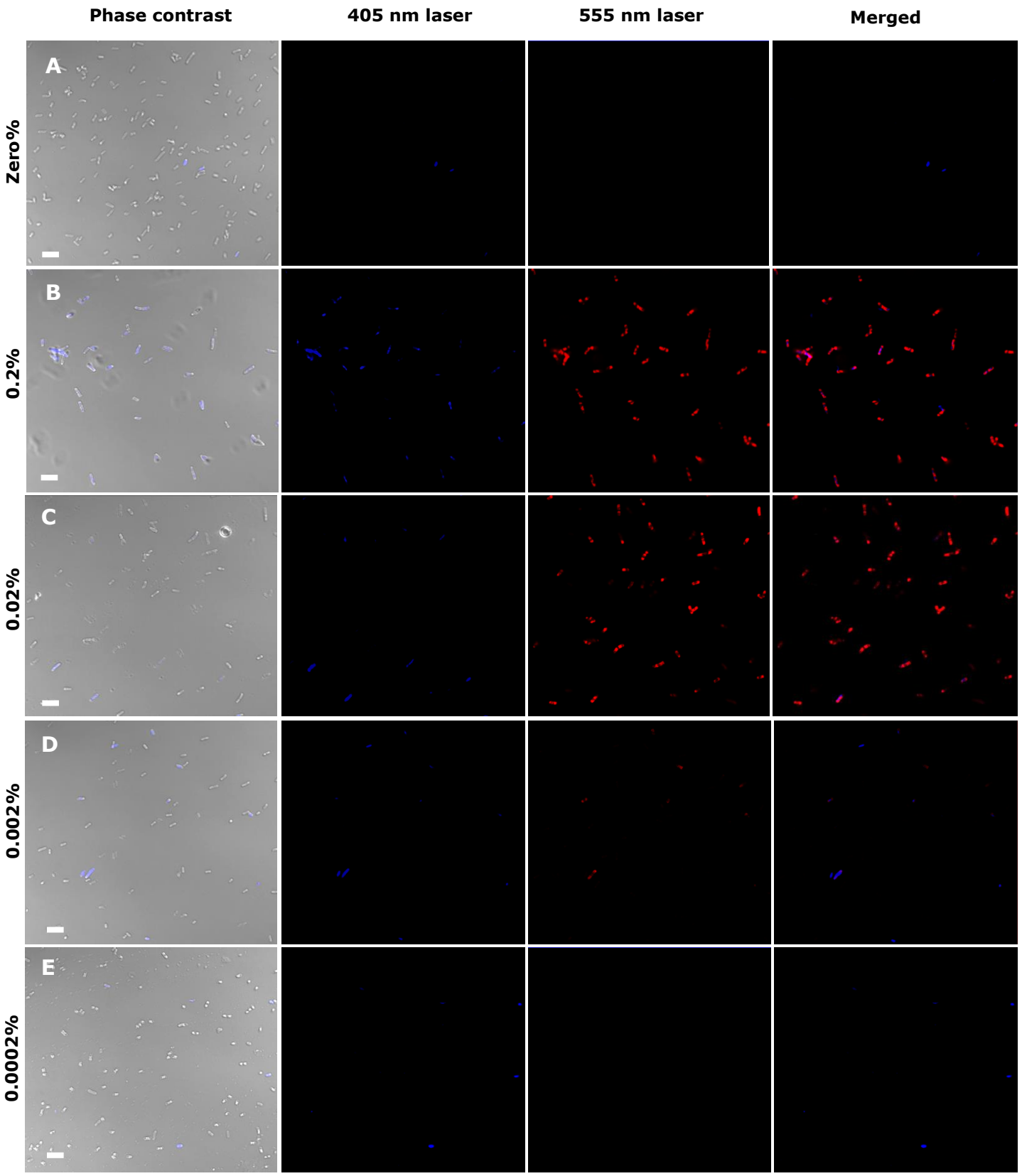


Figure 4.14: 0.02% arabinose is the optimal arabinose concentration for the full length EspC-mcherry production to minimise cell integrity loss. MG1655 (pLA33C1mc) strain induced with Zero% **(A)**, 0.2% **(B)**, 0.02% **(C)**, 0.002% **(D)** and 0.0002% **(E)** arabinose for 4 h following by washing with PBS and resuspension to OD_{600} of 0.5 then staining with SYTOX® dead blue stain as described in materials and methods. Images were taken by confocal microscope and subjected to 405 nm violet laser to excite the blue stain while the 555 nm green laser was used in parallel to stimulate mCherry. Images were merged to combine the fluorescence. Scale bar represent 5 µm.

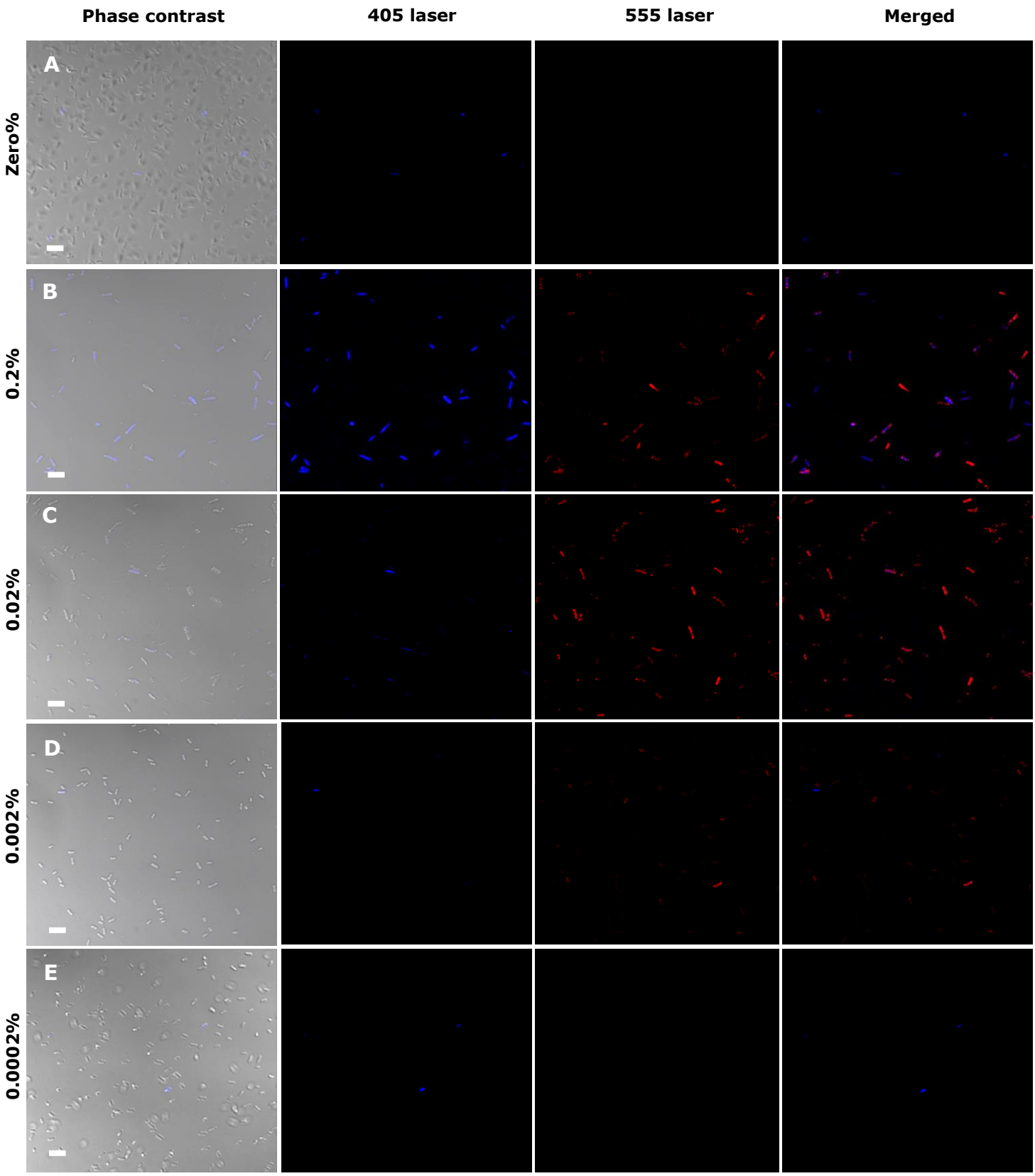


Figure 4.15: 0.02% arabinose is the optimal arabinose concentration for truncated EspC-mCherry production with minimal loss in cell integrity. MG1655 (pMAC33) strain induced with Zero% **(A)**, 0.2% **(B)**, 0.02% **(C)**, 0.002% **(D)** and 0.0002% **(E)** arabinose for 4 h following by washing with PBS and resuspension to OD_{600} of 0.5 then staining with SYTOX® dead blue stain as described in materials and methods. Images were taken by confocal microscopy and subjected to 405 nm violet laser to excite the blue stain while the 555 nm green laser was used in parallel to stimulate mCherry. Images were merged to combine the fluorescence. Scale bar represent 5 µm.

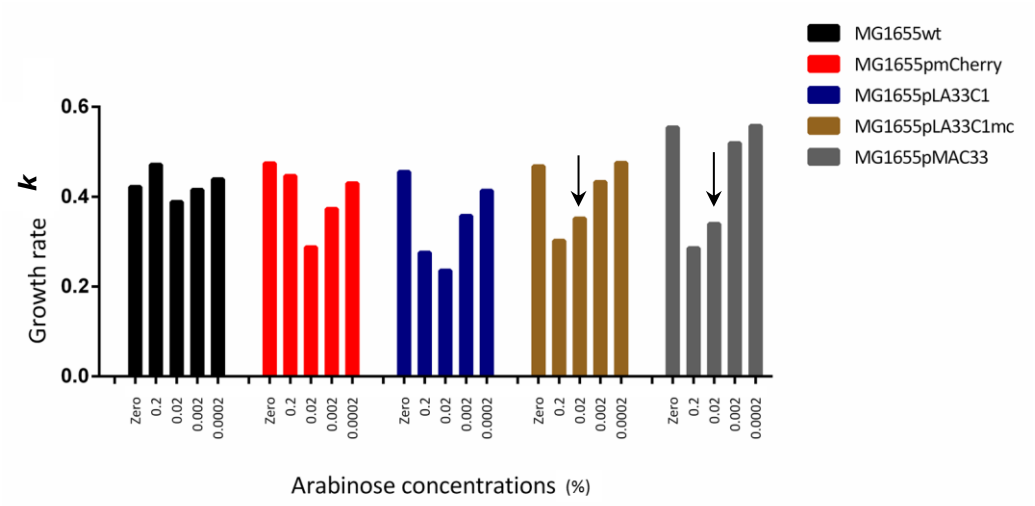


Figure 4.16: Switching the arabinose concentration from 0.2% to 0.02% in both MG1655 (pMAC33) and MG1655 (pLA33C1mc) did not dramatically improve growth. Monitoring the changes in the growth rate in MG1655 wild type (black bars), MG1655 (pmCherry) (red bars), MG1655 (pLA33C1) (blue bars), MG1655 (pLA33C1mc) (brown bars) and MG1655 (pMAC33) (grey bars) induced with decreasing arabinose concentrations over 4 h. The cell density of samples was taken every 60 min. Black arrows indicate the slight growth recovery in 0.02% arabinose compared with 0.2% arabinose for MG1655 (pLA33C1mc) and MG1655 (pMAC33) strains. The formula used to calculate the growth rate is: $k = \frac{log(X_t) - log(X_0)}{0.301t}$

To determine whether the apparent membrane leakiness in MG1655 (pMAC33) is due to the insertion of mCherry into the truncated EspC, a derivative of *espC* with an opal stop codon (TGA) downstream of the *Bgl*II restriction site was constructed using SDM (Fig. 4.17 A). The position chosen aligned with the amber stop (TAG) downstream of *mCherry* in pMAC33 (Fig. 3.1 I). The expected size of the protein containing the introduced mutation and the encoded ~35 kDa product was detected by immunoblotting with α-EspC (Fig. 4.17 B). The new construct was verified by sequencing and called pMAO33. Like truncated EspC-mCherry, the new truncated EspC was detected in culture supernatants despite lacking the β-barrel transporter domain (data not shown). However, cell density measurements indicated that MG1655 (pMAO33) grew much better than MG1655 (pMAC33) reaching OD_{600} of 1.67 after 4 h induction with 0.02% arabinose. Despite this improved growth, MG1655 (pMAO33) was as sensitive to 1% SDS as MG1655 (pMAC33), MG1655 (pLA33C1) and MG1655 (pLA33C1mc) strains (Fig. 4.18).

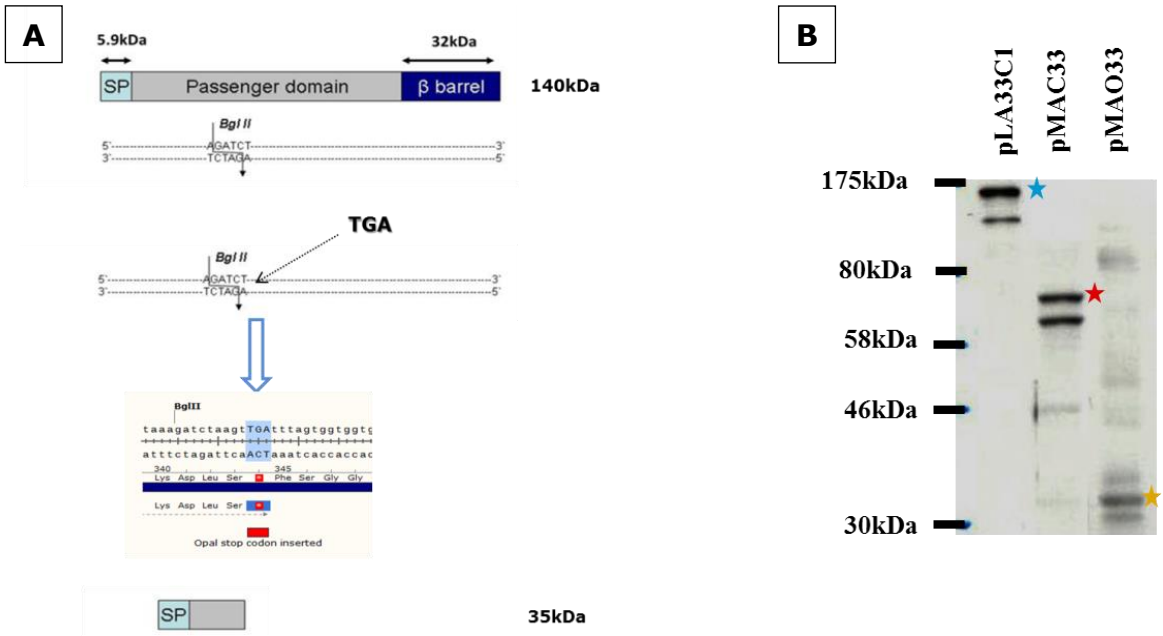


Figure 4.17: Construction of pMAO33 to generate truncated EspC lacking mCherry. The cartoon illustrates insertion of an opal stop codon at amino acid position 334 of EspC by SDM to create a new truncated EspC version without the mCherry fusion ~35 kDa **(A)**. The overnight culture of MG1655 (pLA33C1), MG1655 (pMAC33) and MG1655 (pMAO33) were diluted 1:100 and concurrently induced with 0.02% arabinose. After 4 h whole cell lysates were prepared and separated through 9% SDS-PAGE gel as described in chapter 2. Subsequent immunoblotting using α-EspC detected the native 140 kDa EspC (blue asterisk), truncated ~70 kDa EspC-mCherry (red asterisk), and the new truncated version of EspC without mCherry ~35 kDa (yellow asterisk) **(B)**.

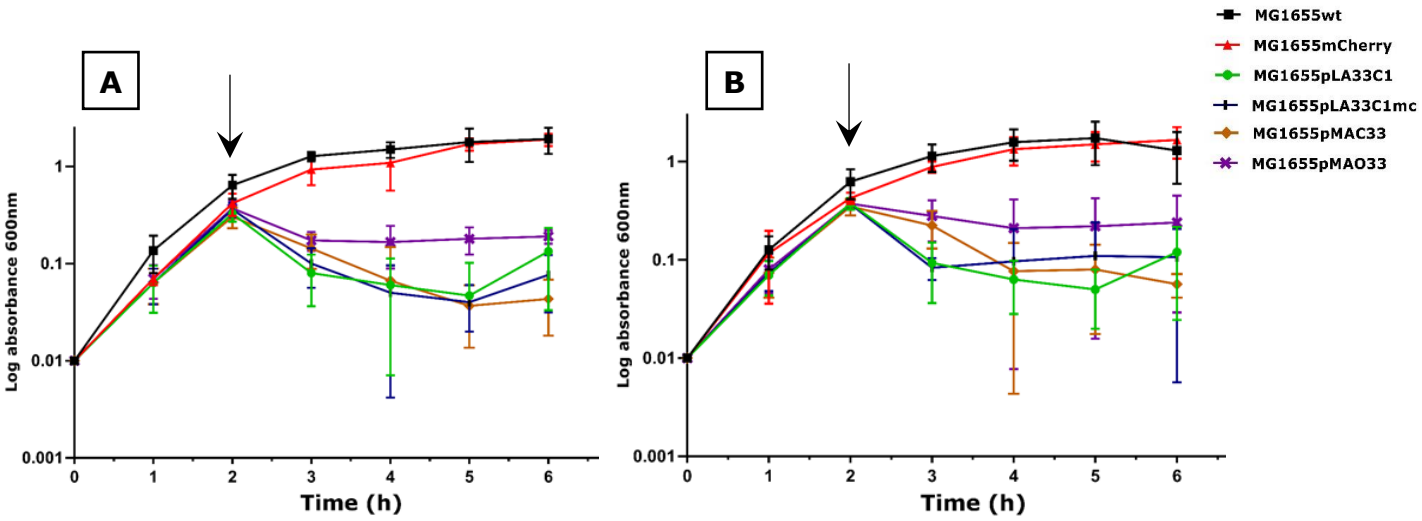


Figure 4.18: 1% SDS reduces the viability of MG1655 producing EspC with or without mCherry or the β-barrel. MG1655 wt, MG1655 (pmCherry), MG1655 (pLA33C1), MG1655 (pLA33C1mc), MG1655 (pMAC33) and MG1655 (pMAO33) were diluted and concurrently induced with either 0.02% **(A)** or 0.2% arabinose **(B)**. 1% SDS was added to the cultures 2 h after induction, and the cell density (OD_{600}) was measured at the times indicated. Black arrows indicate the time point of addition of 1% SDS. Error bars represent standarad deviation (n=3 replicate reads).

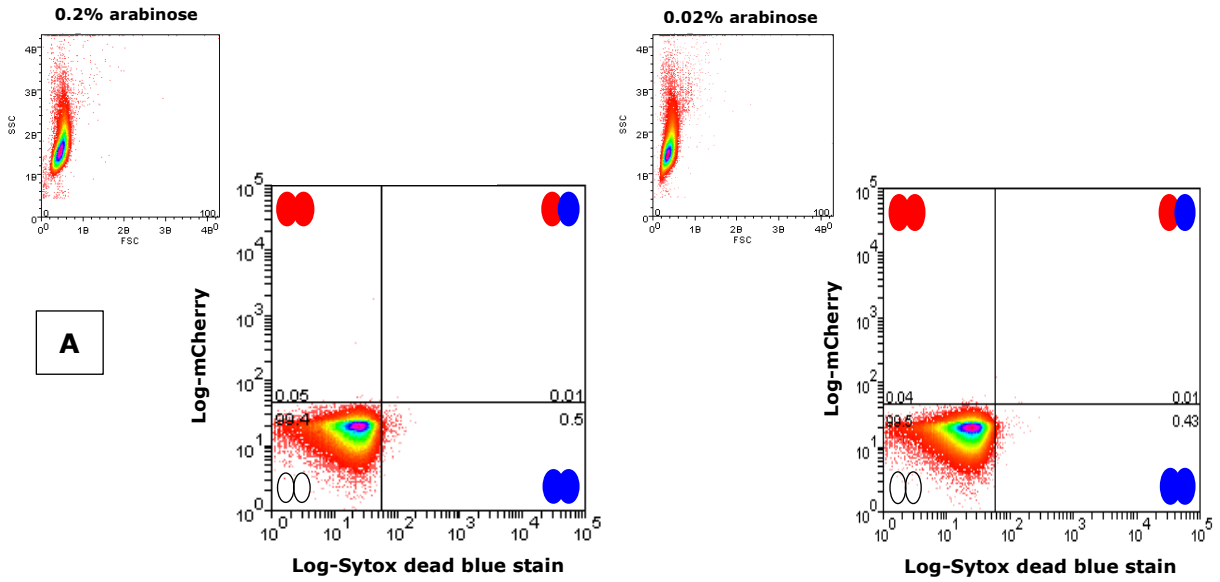
Since addition of 1% SDS (Fig. 4.18) to MG1655 producing EspC with or without mCherry fusion reduced the integrity of the bacterial membrane, the population of viable bacteria present following induction with 0.2% and 0.02% arabinose was quantified. To do this, 4 h induced MG1655 wt, MG1655 (pmCherry), MG1655 (pLA33C1mc) and MG1655 (pMAC33) cultures were washed with ice cold PBS and resuspended to 0.5 OD_{600} units/ml in PBS and stained with 1 µl SYTOX® dead blue stain. Samples were then analysed in duplicate with a Beckman Coulter MoFlo XDP flow cytometry.

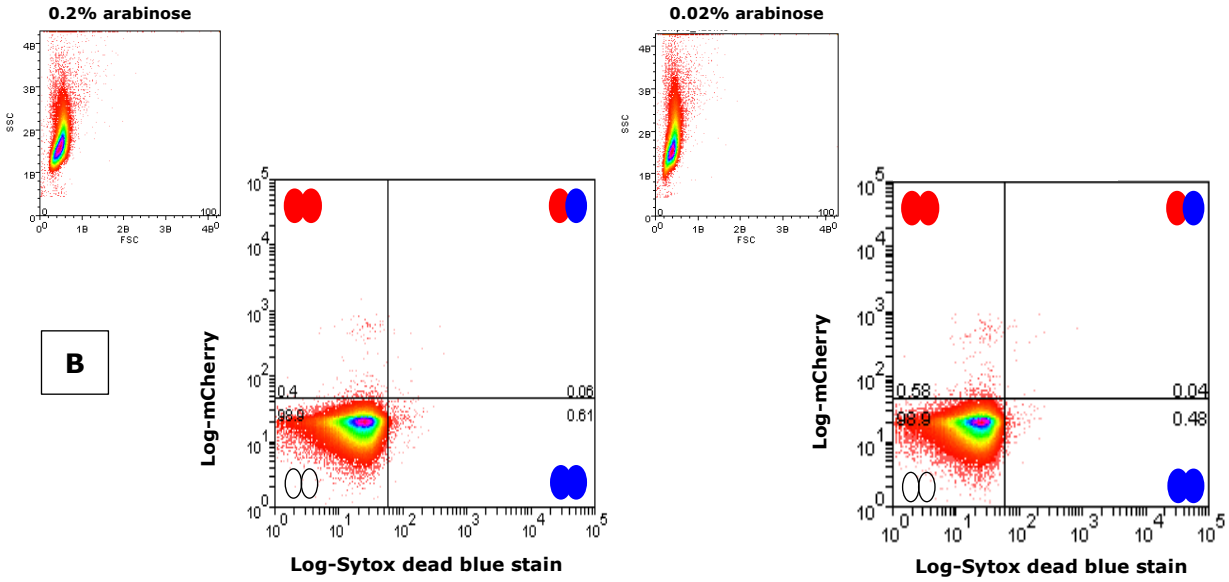
Interestingly, forward and side scatter dot plots indicated that production of the full length 174 kDa EspC-mCherry increased the cell size (Fig. 4.19 C) whereas the truncated EspC-mCherry producing strain lost cell shape uniformity, becoming granulated and smaller (Fig. 4.19 D). No obvious differences in cell size were noticed between the two different arabinose concentrations (Fig. 4.19).

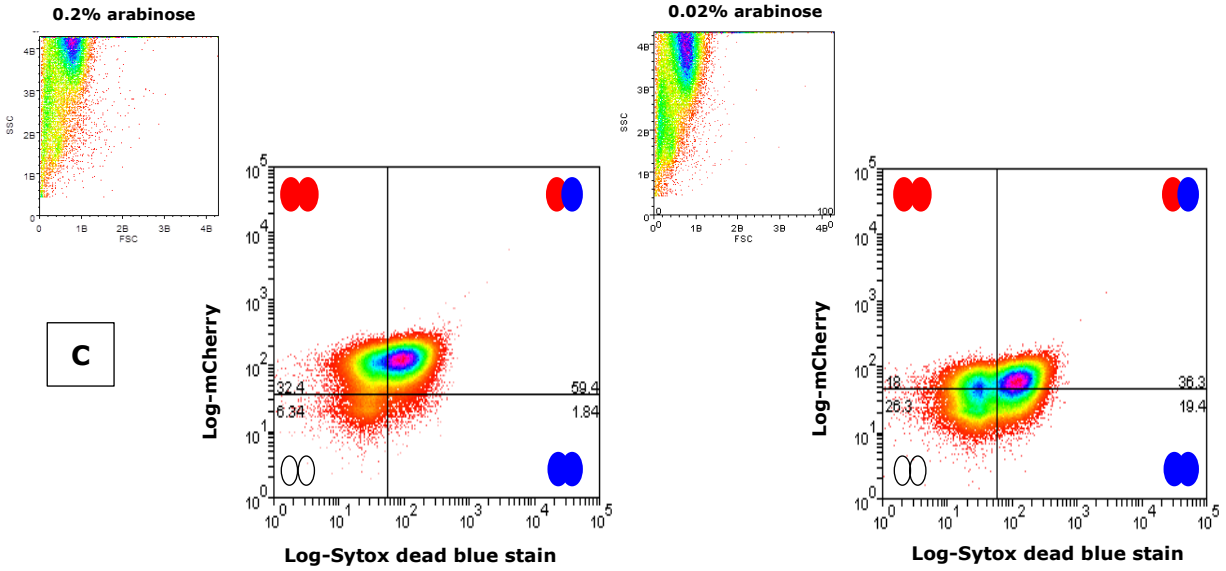
To define the viability of cells in a population and correlate this with EspC production, a quadrant marker was placed to divide the two-fluorescent parameters (X parameter: Log-Sytox dead blue stain to indicate the blue fluorescent bacteria and Y parameter: Log-mCherry to indicate the red fluorescent bacteria). The four sections created distinguish the negative, single positive or double positive cell populations (see cartoon colour indications in Fig. 4.19). Surprisingly, the blue staining revealed that almost 60% of MG1655 (pLA33C1mc) cells had leaky membranes compared to 28% of MG1655 (pMAC33) and these percentages were almost similar in the two arabinose

concentrations (Fig. 4.19 C and D, respectively). In contrast to the fluorescent microscopy, these percentages did change significantly in the two arabinose concentrations (Fig. 4.14 B and C) and (Fig. 4.15 B and C). Furthermore, although the percentage of MG1655 (pLA33C1mc) cells emitting red fluorescence was high, it was almost absent in MG1655 (pMAC33) (Fig. 4.19 C and D, respectively). It seems that the growth defect caused by production of the truncated EspC-mCherry largely perturbs the bacterial cell shapes leading to cell lysis and fragility, which made it difficult to define and quantify the particle-associated fluorescence.

One possible explanation for the apparent presence of EspC derivatives that lack the β-barrel transporter domain in culture supernatants is that the growth defects and loss of membrane integrity are linked to the release of membrane vesicle blebs as bleb release has been reported to occur when bacteria experience internal stresses associated with overproduction or mis-localization of recombinant proteins (267,268). To investigate this, culture supernatants from all MG1655 strains induced by 0.2% or 0.02% arabinose were immunoblotted with α-TolC (OM protein 50 kDa), α-AcrB (IM protein 110 kDa) and α-IscS (cytoplasmic protein 45 kDa) as well as α-EspC (Fig. 4.20). In line with the hypothesis, both MG1655 (pMAC33) and MG1655 (pMAO33) contained considerable levels of cellular proteins in their culture supernatants. In contrast, MG1655 (pLA33C1mc) culture supernatants contained the lowest level of IM and cytoplasmic proteins with no OM protein detected (Fig. 4.20), reflecting the absence of damage cells.


0.2% arabinose
0.02% arabinose
A
Log-mCherry
Log-Sytox dead blue stain
0.05
0.01
99.4
0.5
0.04
0.01
99.5
0.43


0.2% arabinose
0.02% arabinose
B
Log-mCherry
Log-Sytox dead blue stain
0.4
0.06
99.0
0.61
0.58
0.04
98.9
0.48


0.2% arabinose
0.02% arabinose
C
Log-mCherry
Log-Sytox dead blue stain
32.4
59.4
6.34
1.84
18
36.3
26.3
19.4

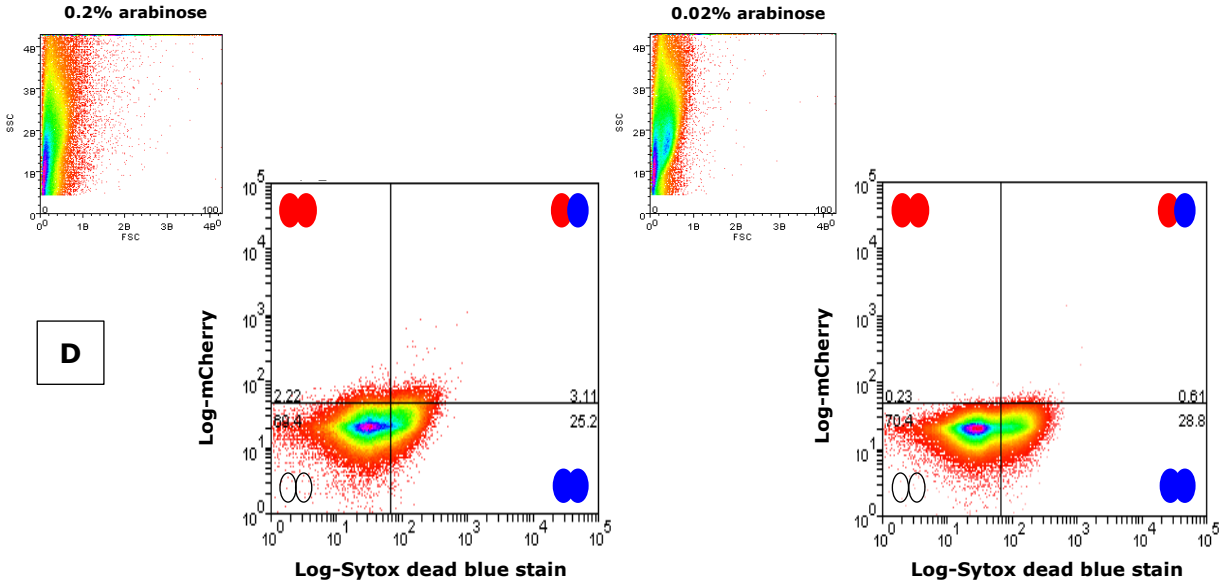


Figure 4.19: Production of the full length 174 kDa EspC-mCherry makes cells larger. Flow cytometry analysis of MG1655 wt **(panel A)**, MG1655 (pmCherry) **(panel B)**, MG1655 (pLA33C1mc) **(panel C)** and MG1655 (pMAC33) **(panel D)** induced with 0.2% (left panel) or 0.02% arabinose (right panel). All strains were stained with SYTOX® dead blue stain as described in materials and methods. Light scatter dot plots indicate cell size (upper plots) and scatterplots with quadrant markers split bacteria into fluorescent subpopulations indicated by the cartoons in the corner: negative (2 white circles), mixed blue/red positive (one blue, one red circle) and double red (two red circles) and blue positive (two blue circles). Log-Sytox dead blue stain X axis is for 405 nm violet laser and Log-mCherry Y axis is 555 nm green laser.

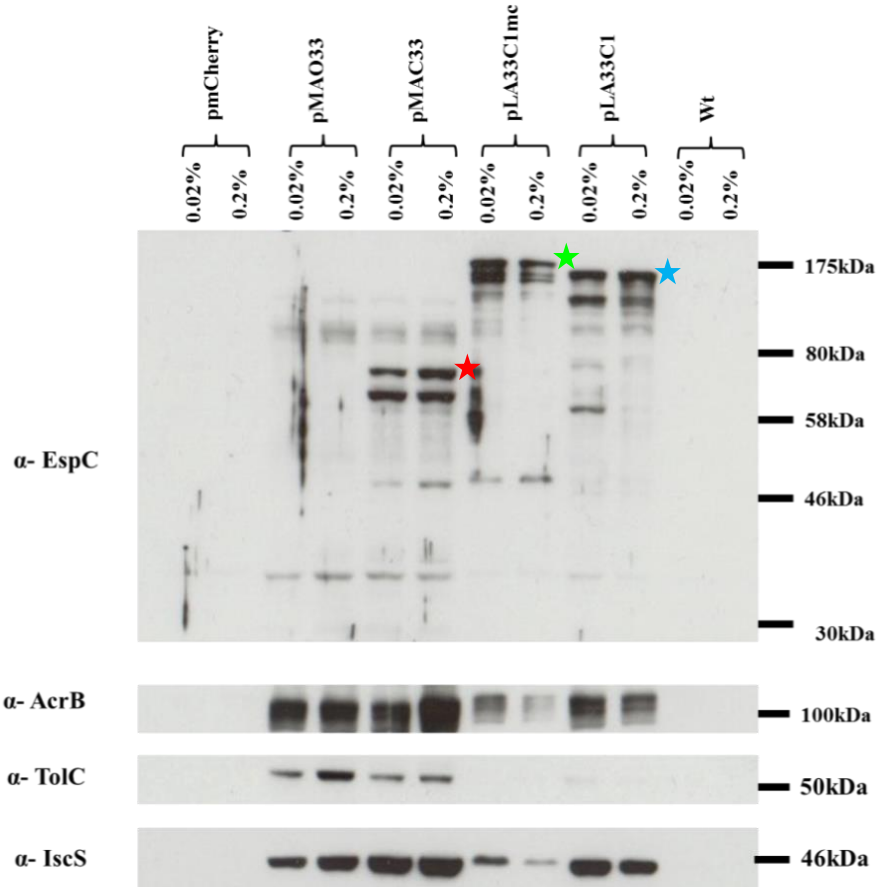
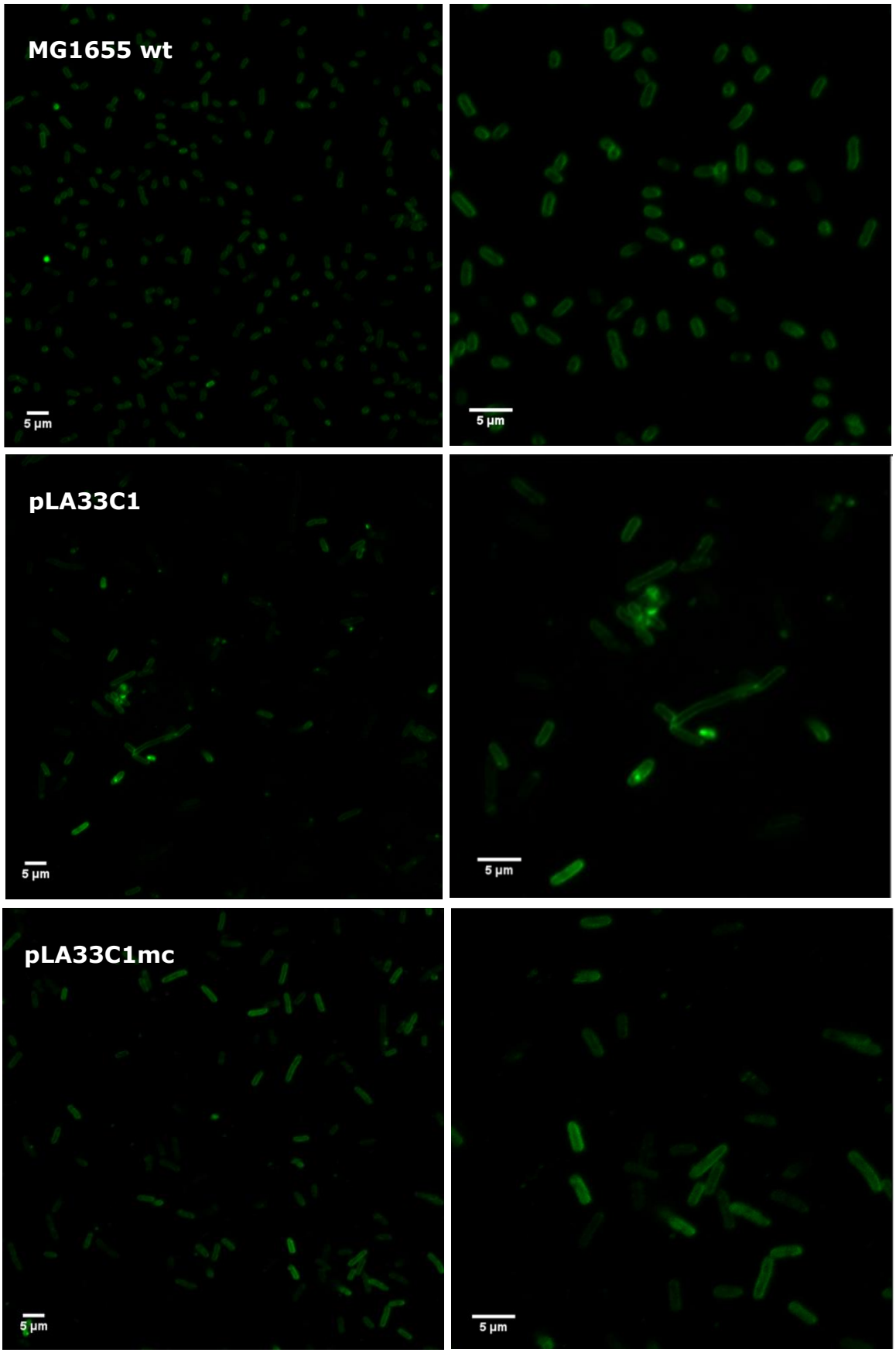


Figure 4.20: Truncated EspC with or without mCherry release IM, OM and cytoplasmic proteins into the culture supernatant. MG1655 wt, MG1655 (pLA33C1), MG1655 (pLA33C1mc), MG1655 (pMAC33), MG1655 (pMAO33) and MG1655 (pmCherry) were grown in LB and induced with 0.2% or 0.02% arabinose for 4 h. TCA precipitated culture supernatants were collected and separately immunoblotted with four antibodies; α-EspC, α-AcrB, α-TolC and α-IscS. α-EspC was able to detect the native 140 kDa EspC (blue asterisk), Full length 174 kDa EspC-mCherry (green asterisk) and truncated ~70 kDa EspC-mCherry (red asterisk). The absence of the truncated EspC lacking mCherry in pMAO33 at ~35 kDa is indicative of degradation on this occasion. The positions of molecular weight markers are indicated in kDa.

As membrane vesicle blebs contain lipids as well as proteins, MG1655 strains were stained with the lipophilic outer membrane dye, FM 1-43. Cultures were induced for 4 h, and cells washed with PBS before staining with FM 1-43 dye. Interestingly, producing truncated EspC with or without mCherry protein caused defects in the growth. Both MG1655 (pMAC33) and MG1655 (pMAO33) had increased amounts of outer membrane containing vesicles (blebs) as well as abnormality in the bacterial shape, presumably forming minicells (Fig. 4.21). Consistent with the FACS analysis, MG1655 (pLA33C1mc) cells were elongated compared to wild-type MG1655 (Figs. 4.19 C and 4.21).

Based on the earlier observation that adding A22 to MG1655 (pMAC33) causes changes in cell shape as well as disrupting protein processing through bacterial compartments in a dose-depended manner, it is possible that it will affect the formation of the minicells/blebs observed in MG1655 (pMAC33) supernatants. To determine whether this occurs, MG1655 (pMAC33) was induced for 4.5 h with 0.2% or 0.02% arabinose, treated with different A22 concentrations and culture supernatants were immunoblotted with α-TolC (OM), α-AcrB (IM) and α-IscS (cytoplasm) (Fig. 4.22). As predicted, the OM protein TolC levels were reduced in the presence of A22 (Fig. 4.22 A and B). This correlates with the reduction in the quantity of the smaller form of truncated EspC-mCherry (~65 kDa), and enhancement of levels of the larger form (~70 kDa). These results indicate that cell shape changes influence the formation of blebs/minicells such that the smaller form of truncated EspC-mCherry is less readily detected.


MG1655 wt
5 µm
5 µm
pLA33C1
5 µm
5 µm
pLA33C1mc
5 µm
5 µm

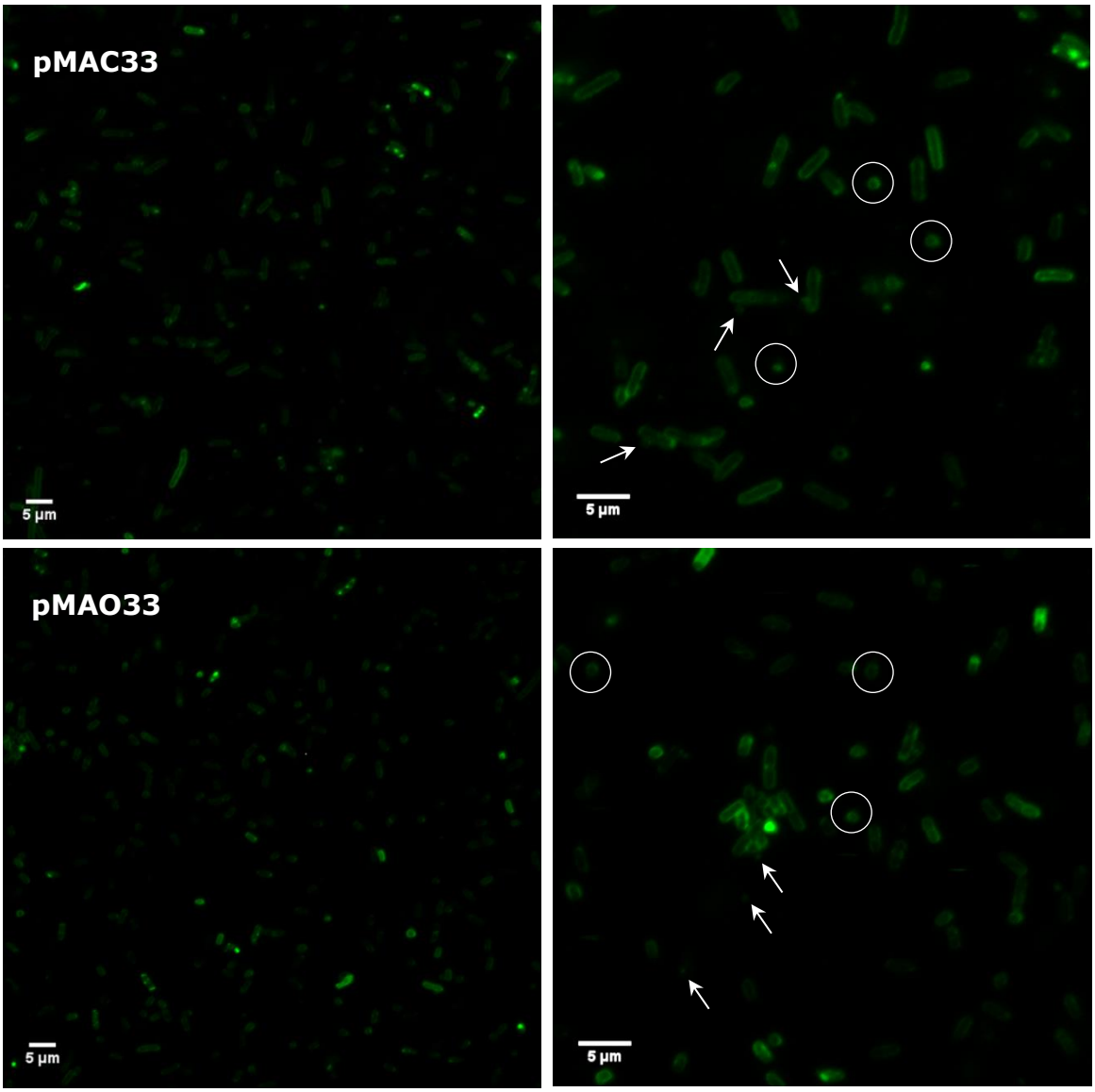


Figure 4.21: MG1655 producing truncated EspC with or without mCherry generates small rounded structures visible by staining with the lipophilic fluorescent membrane dye, FM 1-43. Strains MG1655 wt, MG1655 (pLA33C1), MG1655 (pLA33C1mc), MG1655 (pMAC33), and MG1655 (pMAO33) were grown in LB and induced with 0.2% arabinose for 4 h. Whole cell extracts were collected by centrifugation, washed with PBS and stained with FM 1-43 as described in chapter 2. Images were taken by confocal microscopy and subjected to 488 nm laser to excite the dye. Images on the right hand side show a zoomed view of the left hand side images. White arrows indicate putative blebs while white circles show abnormal cell shapes, possibly minicells. Scale bar represents 5 µm.

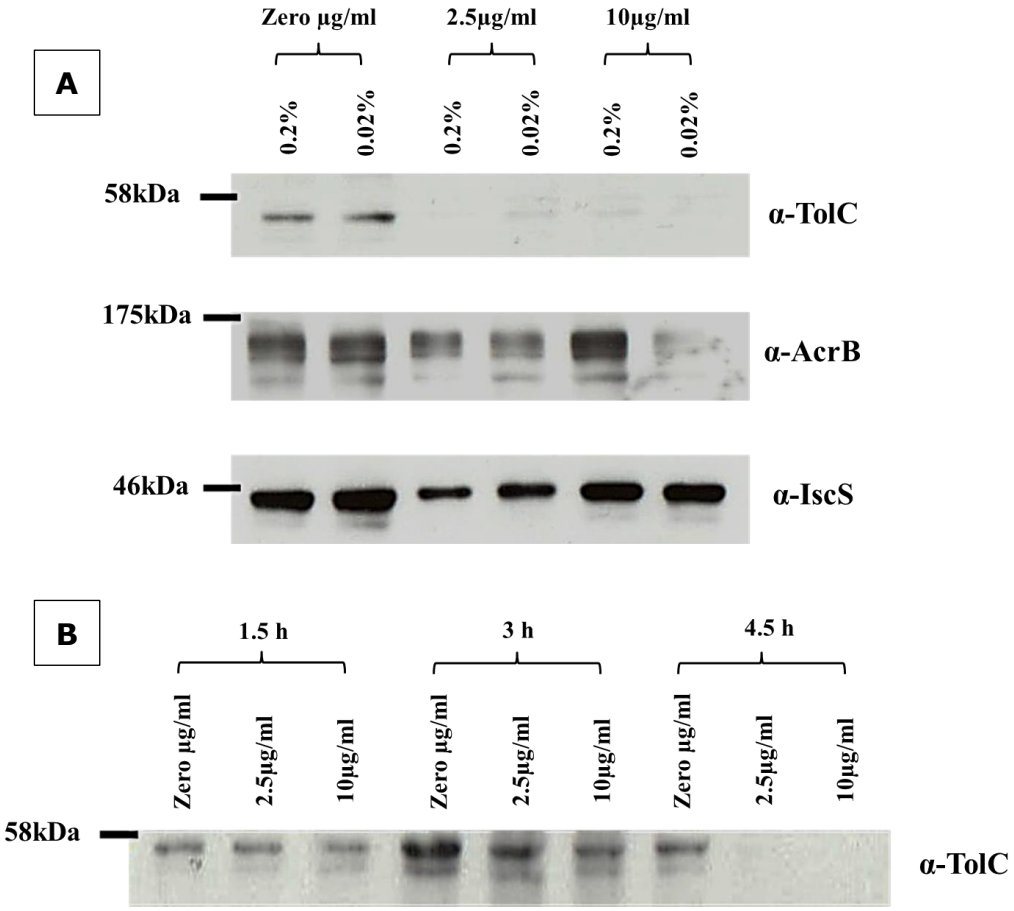


Figure 4.22: A22 reduces the release of outer membrane containing blebs from MG1655 (pMAC33). Immunoblots of supernatant samples from MG1655 (pMAC33) induced with 0.2% or 0.02% arabinose and treated with A22 at different concentrations for 4.5 h **(A)**. Immunoblot of culture supernatants over time from MG1655 (pMAC33) induced with 0.2% arabinose and treated with different A22 concentrations **(B)**. The blots were incubated with α-TolC, α-AcrB, and α-IscS. Proteins were separated in 9% SDS-PAGE.

Together, these results indicate that the expression of full length 174 kDa EspC-mCherry whether in MG1655 or in DH5α creates elongated cells, in which spiral formation is observed. Removal of the β-barrel transporter domain from EspC with or without mCherry causes a growth defect manifested as a loss in membrane integrity with concomitant production of blebs. In the absence of the mCherry fusion, the detrimental influence upon growth of truncated EspC was less severe.

4.2.3 Altering the serine protease motif of overproduced EspC did not repair the observed growth defect

Since MG1655 (pLA33C1) producing EspC exhibited a growth defect (Fig. 4.21), it is possible that the serine protease motif in EspC (GD**S**GS) might be toxic to the cells. Lower OD_{600} measurements obtained from the strains producing all versions of EspC (except pMAO33) support this notion (Fig. 3.12). To determine if this is the case, SDM was performed using primers EspC-F S256I/EspC-R S256I (listed in table 2.4, chapter 2) to substitute isoleucine for the serine at position 256 of the serine protease motif of the EspC passenger domain in all EspC versions. Replacing serine with isoleucine will produce non-functional protein as previously described (73). DNA sequencing confirmed the presence of the desired substitution in pLA33C1, pLA33C1mc, pMAC33 and pMAO33. To test the growth rate of MG1655 harbouring constructs $pLA33C1_{S256I}$, $pLA33C1mc_{S256I}$, $pMAC33_{S256I}$ and $pMAO33_{S256I}$, the overnight cultures of these strains were diluted and concurrently induced with 0.02% arabinose. The OD_{600} was measured after 4 h alongside whole cells lysate preparation followed by immunoblotting with α-EspC to check

protein production. Unexpectedly, all serine protease mutant strains did not grow well and recorded very low OD_{600} compared to wild-type strains except for the MG1655 ($pMAO33_{S256I}$) (Fig. 4.23). Immunoblot analysis revealed similar production levels of original and mutated EspC (data not shown).

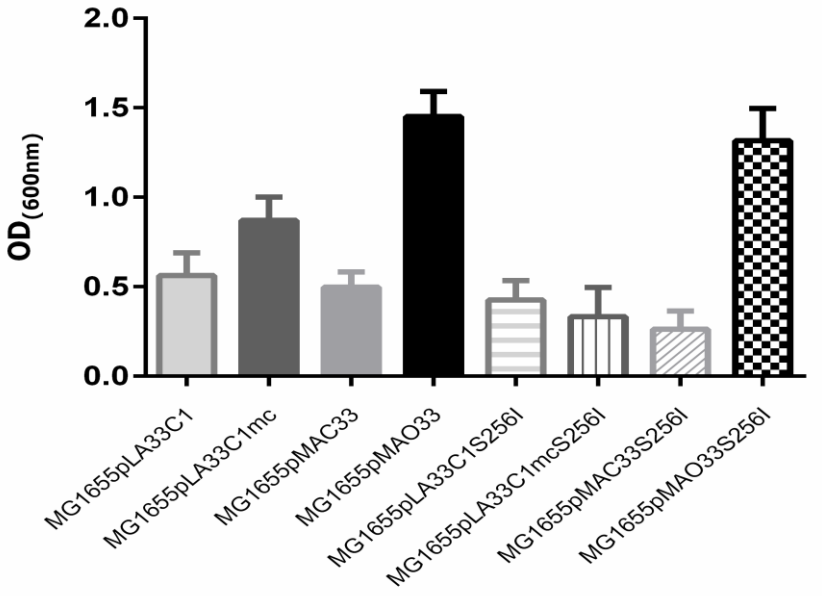


Figure 4.23: No improvement in the growth during overproduction of the EspC serine protease mutant. MG1655 strains listed in the graph hosting mutated or non-mutated serine protease motif variants of EspC were grown in LB with 0.02% arabinose. The optical density OD_{600} was measured after 4 h of induction. Error bar represents standard deviation (n=3 replicate reads).

4.2.4 Inactivation of the motor protein SecA alters the localization of EspC-mCherry

All the forms of EspC evaluated in this study contain an amino-terminal signal peptide for targeting to the IM translocation machinery Sec. There are reports that Sec is maintained in a spiral localization (234). To evaluate whether Sec influences the localization of EspC, pLA33C1mc and pMAC33 were transformed into a SecA mutant of *E. coli* to investigate the localization of EspC in the absence of Sec. Overnight *E. coli*Δ*secA* (pLA33C1mc) and *E. coli*Δ*secA* (pMAC33) cultures were diluted in LB and immediately induced with 0.02% arabinose. Cultures were grown at 30°C until reaching an OD_{600} of 0.05 (approximately 2 h). Subsequently, the cultures were switched to the non-permissive temperature of 42°C to activate the mutation and incubated for 2 h. EspC was induced in *E. coli*Δ*secA* (pLA33C1mc) and *E. coli*Δ*secA* (pMAC33) characterized in whole cell and supernatant lysates at 30 min intervals over 2 h. As shown in Fig. 4.24, both full length and truncated EspC-mCherry accumulated entirely inside the cells and were not detected in any culture supernatants.

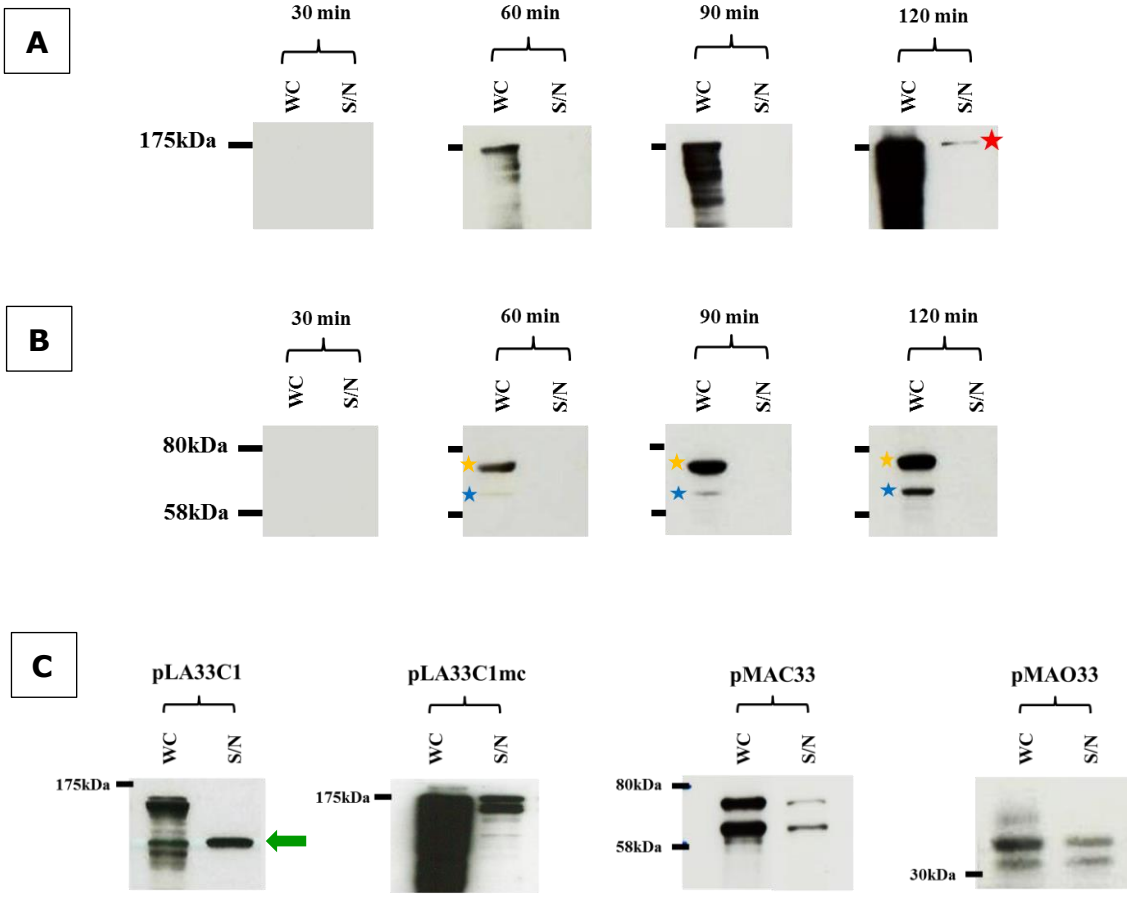


Figure 4.24: EspC-mCherry is not found in culture supernatants of an *E. coli* SecA mutant. Overnight culture of *E. coli*Δ*secA* (pLA33C1mc) **(A)** and *E. coli*Δ*secA* (pMAC33) **(B)** were diluted 1:100 in LB, concurrently induced by 0.02% arabinose and grown at 30˚C with shaking to an OD_{600} of 0.05. The cells were then shifted to the non-permissive temperature of 42˚C and grown for an additional 2 h with shaking. Subsequently, whole cell (WC) and supernatant (S/N) samples were collected at 30 min intervals over 2 h. EspC and truncated forms of EspC induced from MG1655 (pLA33C1), MG1655 (pLA33C1mc), MG1655 (pMAC33) and MG1655 (pMAO33) show that EspC is released into the cell supernatant in the presence of SecA **(C)**. Samples were prepared for SDS-PAGE and Western blotting as described in materials and methods. All Samples were separated through 9% SDS-PAGE and immunoblotted with α-EspC. Red asterisk indicates very low levels of full length EspC-mCherry detected in supernatants after 120 min most probably due to involuntary release as the cells become stressed following high levels of protein expression. The blue asterisks indicate the lower levels of truncated 65 kDa EspC-mCherry (without signal peptide) which mirror the high levels of 70 kDa EspC-mCherry (with signal peptide) (yellow asterisk) detected in whole cell lysates. The green arrow points to the secreted native EspC form lacking the signal peptide ~110 kDa. Both full length and truncated EspC-mCherry forms were previously monitored over time in MG1655 background (see Fig. 3.11).

To visualize the intracellular localization, fluorescent microscopy was undertaken on *E. coli*Δ*secA* (pLA33C1mc) and *E. coli*Δ*secA* (pMAC33) and *E. coli*Δ*secA* (pmCherry). Cells were washed with PBS after 3-4 h at the non-permissive temperature and resuspended to OD_{600} of 0.5 units/ml. Interestingly, both forms of EspC-mCherry exhibited localization patterns different to those observed previously. In *E. coli*Δ*secA* full length EspC-mCherry produced a bipolar and mildly diffuse localization whereas truncated EspC-mCherry was diffusely distributed or unipolar (Fig. 4.25 A and B, respectively). The control *E. coli*Δ*secA* (pmCherry) exhibited only diffuse patterns of fluorescence (Fig. 4.25 C). Zoomed in views of these patterns have clearly shown the distinctive localizations (Fig. 4.25 D). These fluorescent localization patterns did not change when the bacterial actin homologue MreB was perturbed this time (Fig. 4.26). It was clear that *E. coli*Δ*secA* producing full length EspC-mCherry did not increase in size in the same way that MG1655 (pLA33C1mc) did. Moreover, *E. coli*Δ*secA* (pMAC33) grew better than MG1655 (pMAC33) and no damaged cells were observed under confocal microscopy (Fig. 4.25 B). Collectively, these data indicate that the SecA ATPase influences the localization of EspC.

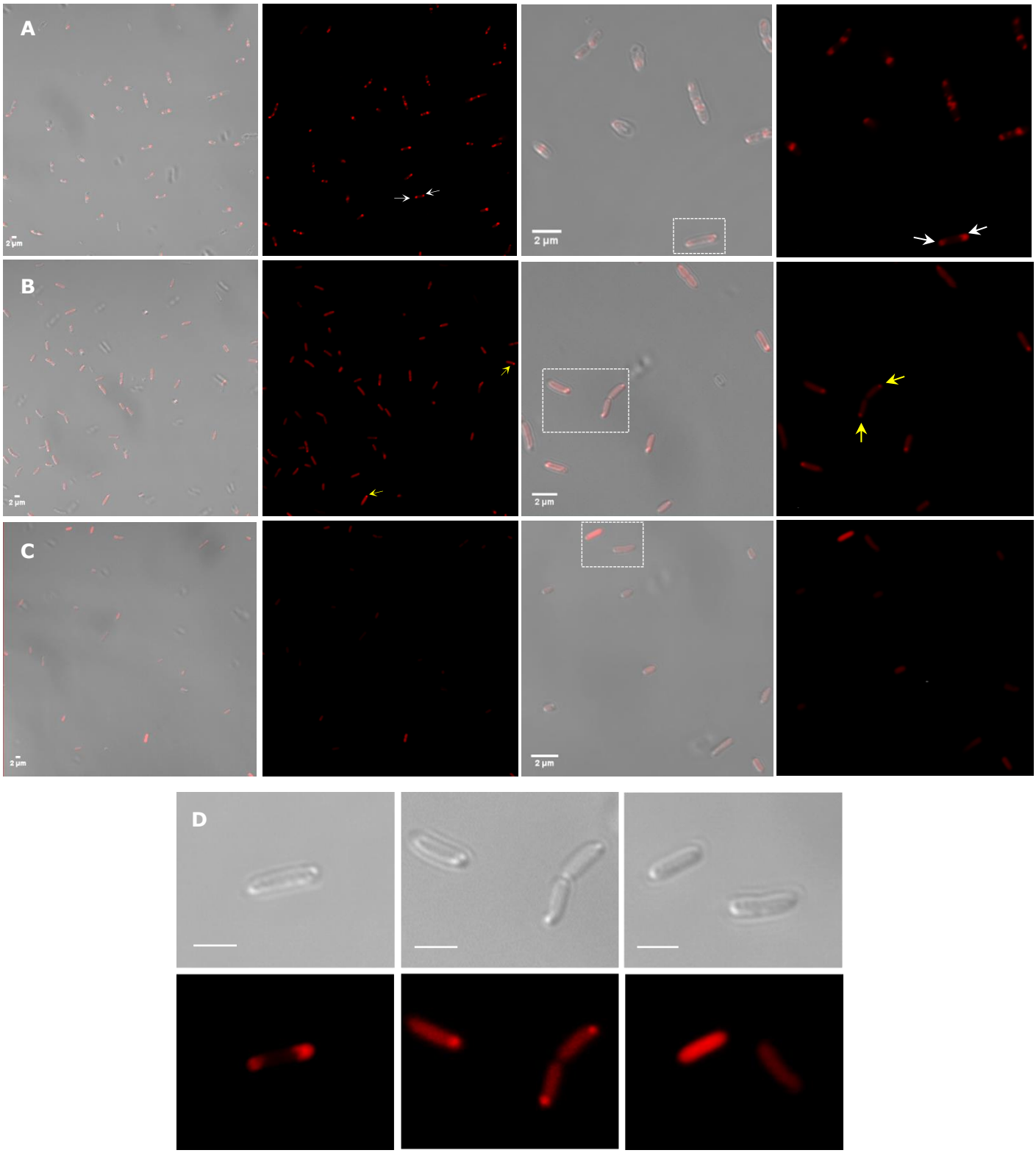


Figure 4.25: In *E. coli*Δ*secA* the full length EspC-mCherry localization becomes predominantly bipolar whilst truncated EspC-mCherry is unipolar. Phase contrast and mCherry fluorescence pictures were taken from *E. coli*Δ*secA* (pLA33C1mc) **(A)**, *E. coli*Δ*secA* (pMAC33) **(B)** and the control *E. coli*Δ*secA* (pmCherry) **(C)**. Zoomed in images were selected from the white rectangles to focus on particular cells **(D)**. Images in D represent the bipolar localization of full length EspC-mCherry **(left column)**, unipolar localization of the truncated EspC-mCherry **(middle column)** and the distinct diffuse pattern from the control mCherry **(right column)**. Images were taken by confocal microscopy. Pictures on the right hand side are closer compared to pictures at the left hand side in **A**, **B** and **C**. White arrows indicate the bipolar localization of the full length 174 kDa EspC-mCherry while the yellow arrows show the unipolar localization of the truncated EspC-mCherry version. Scale bars represent 2 µm.

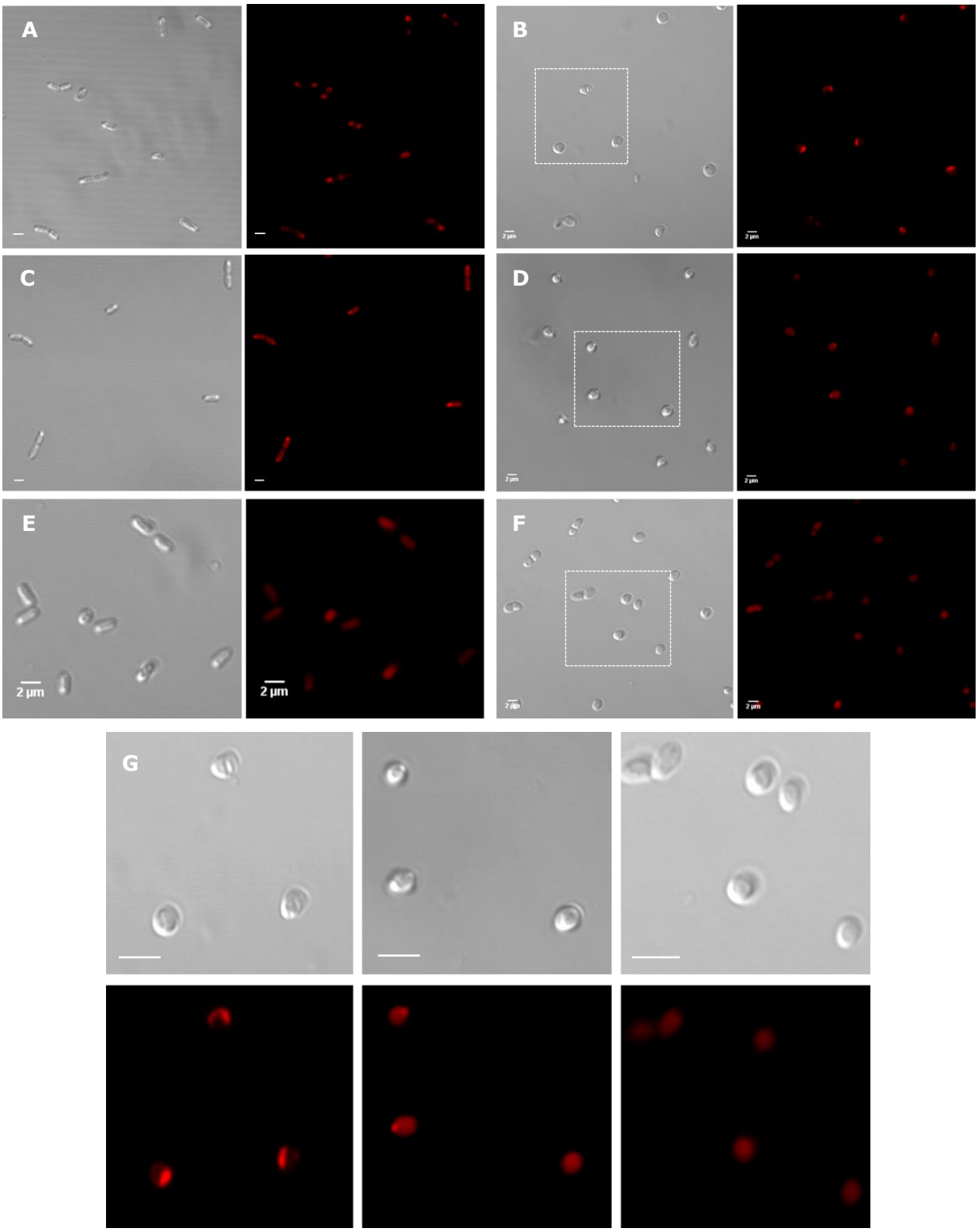


Figure 4.26: Changing the cell shape by A22 did not alter the localization of EspC-mCherry produced from *E. coli* SecA mutant strains. Phase contrast and mCherry fluorescence pictures were taken from *E. coli*Δ*secA* (pLA33C1mc) **(A** and **B)**, *E. coli*Δ*secA* (pMAC33) **(C** and **D)** and the control *E. coli*Δ*secA* (pmCherry) **(E** and **F)**. The overnight cultures were diluted in LB (1:100) and concurrently induced with 0.02% arabinose and incubated at 30°C to grow shaking to OD_{600} of 0.05 then shifting to non-permissive temperature (42°C) and treated with $A22^0$ **(A**, **C** and **E)** or $A22^{10}$ **(B**, **D** and **F)** for 3 to 4 h. As A22 produces rounded cells, the strong curvature at bacterial poles completely disappeared and the full length EspC-mCherry was condensed at one region in the cytoplasm, presumably due to the pressure of the bacterial nucleoid **(B)**. Zoomed images were selected from the white rectangles to focus on particular cells **(G)**. Scale bars represent 2 µm.

4.3 Discussion

Localization of EspC in a helical arrangement has suggested a possible link between T5SS and bacterial cytoskeleton components that are also organized into helices such as the actin homologue MreB and a morphogenic protein, RodZ (214,223). Importantly, these two cytoskeleton proteins interact with each other to maintain the bacterial growth (224). Recently, the Sec machinery that also exhibits a helical conformation was shown to mediate the translocation and insertion of RodZ into the bacterial IM (269). These correlations suggest a common underlying molecular mechanism for the secretion of EspC AT that involves movement towards the bacterial poles in a helical arrangement. The data collected in this chapter clearly present a characteristic set of EspC fluorescent localization patterns that is obtained when the actin homologue MreB, the ATPase SecA and the EspC β-barrel AT domains are all disrupted.

The absence of the β–domain in the truncated EspC-mCherry version causes a significant growth defect manifested by delicate bacterial pellets and low OD_{600} measurements. The data obtained with FACS analysis to assess the bacterial viability during the expression of the truncated EspC-mCherry using SYTOX® blue stain were inconsistent with the microscopy data. Imaging analysis that sometimes requires an increase in the laser gain to be able to observe the blue cells have revealed that the majority of cells have considerably leaky membranes whereas FACS measured differences were not significant, with the percentage of dead cells in a MG1655 (pMAC33) population being 28%.

The inability of the FACS machine to detect weak fluorescent signals from MG1655 (pMAC33) may have misestimated this proportion.

Membrane perturbation might arise as an artefact of mCherry insertion as previously suggested (255). However, a truncated EspC lacking mCherry exhibited similar membrane defects indicating that EspC itself could be attributed to these defects. Mutating the serine protease motif of EspC did not improve the bacterial growth either but instead led to lower OD_{600} measurements suggesting that the protease activity of EspC was not responsible. Addition of 1% SDS confirmed the cell wall weakness in the strains producing different forms of EspC.

The usage of the lipophilic OM FM 1-43 stain to examine the bacterial OM revealed that cultures containing cells producing truncated EspC with or without mCherry also generated structures resembling OM vesicles (blebs) or minicells. These structures were also evident by flow cytometry (Fig. 4.19 D). Immunoblotting with cytoplasmic, IM and OM protein markers as controls supported this (Fig. 4.20). A possible explanation could be that a consequence of stalling truncated EspC in the periplasm is increased turgor pressure on the OM. This would lead to the formation of blebs which are released into the growth medium. Consistent with this prediction, it has been reported that the Gram-negative bacterial cells are able to release harmful incorrectly folded perplasmic proteins into the external milieu by forming OM vesicles (270). Perhaps, another reason to consider is that the truncated EspC could cause aberrant cell division by perturbing the pole-to-pole oscillations of the MinD protein that carries the cell division inhibitor,

MinC, thereby assisting formation of septa at potential sites such as the bacterial poles (268,271). In support of this notion, no growth disturbance was demonstrated in *E. coli*Δ*secA* expressing the truncated EspC.

Full length EspC-mCherry also localized differently in different *E. coli* strains. In both MG1655 and DH5α laboratory strains a spiral distribution was coupled to elongated cells. This fluorescent spiral localization pattern was completely absent in EPECΔ*espC* and cell size was normal, suggesting that laboratory strains lack the EspC secretory machinery components. Overproduction of a large protein that enters membrane translocation channels may create stress on the peptidoglycan sacculus triggering cells to synthesize additional peptidoglycan to fill the pores created (241). Consistent with this, lowering EspC-mCherry production levels by reducing the concentration of the arabinose inducer of expression enabled cell size to return to normal for wild-type cells (Fig. 4.14 D and E). Furthermore, production of the full length EspC-mCherry in *E. coli*Δ*secA* did not create a spiral localization arrangement on secretion or any cell size changes (Figs. 4.25 A and 4.26 A).

Having demonstrated that the bacterial actin homologue MreB is directly responsible for the helical organization of EspC, A22 was used to interrupt the MreB nucleotide binding pocket, thereby preventing it polymerising and forming the helical cytoplasmic filaments (212,263,266). A22 has been used extensively as a tool to understand the function of MreB (207,227,254,263,272). A22 was initially discovered through screening for inhibitors of chromosome partitioning

in *E. coli* and found to convert bacterial cells from rod-shaped to rounded cells (273). To speed this study, A22 was used to perturb MreB and cause cell shape deformation in a manner reminiscent of a MreB loss of function knock-out mutant (254).

Disruption of MreB by A22 affected the localization of both forms of EspC-mCherry. The localization of the full length EspC was disrupted completely and became cloudy without spirals. It may be that a disorientated or delocalized EspC-mCherry is unable to localize to the poles but instead aggregates to form a cloudy fluorescent signal. Truncated EspC-mCherry localization became punctated over time and in an A22 dose-dependent manner, and two forms could be detected by α-dsRed or α-EspC antisera. As A22 concentrations were raised the larger (~70 kDa) form became more abundant whilst levels of the smaller ~65 kDa protein that lacked the signal peptide sequence were reduced (Fig. 4.12 A). Interestingly, the levels of the OM TolC protein in culture supernatants of MG1655 (pMAC33) treated with A22 were similar to those of the smaller form of truncated EspC-mCherry (Figs. 4.22 and 4.12), suggesting either co-localization or perhaps that this form of EspC-mCherry creates greater turgor pressure leading to more blebbing and greater diffusion out of the cells. It is not surprising that blebs/minicells were not detected in *E. coli*Δ*secA* producing truncated EspC-mCherry, presumably because stalling of the truncated EspC-mCherry in the cytoplasm avoids a build-up of turgor pressure in the periplasm.

The results obtained with testing the influence of addition A22 to MG1655 strains clearly demonstrate a slight growth decline in a dose-dependent manner (Fig. 4.8 A), which was consistent with a previous observation (254). It is important to consider that the increase in the optical density in this case might just reflect the change in cell shape (due to increasing the cell size and volume). However, using A22 at a concentration (2.5 µg/ml) that is lower than 3.1 µg/ml (the MIC of A22 in *E. coli*) confirms a slight decline in cell growth (273). It was possible to observe the distorted, patchy localization of the full length EspC-mCherry in cells treated with lower concentrations of A22 ($A22^{2.5}$), with some irregular bands (see the white arrows in Fig. 4.7 A). Nevertheless, at higher A22 levels, protein aggregates and diffused localization became predominant (Fig. 4.9). These results indicate that the bacterial cytoskeleton may be required for EspC secretion since the actin homologue MreB forms a similar helical structure and perturbing it with A22 alters EspC localization.

The distinct bipolar localization of full length EspC-mCherry and polar distribution of truncated EspC-mCherry in *E. coli*Δ*secA* is interesting because of the lack of (i) growth defects and (ii) membrane leakiness. It is possible that the stalled full length EspC-mCherry aggregates in the cytoplasm and then accumulates at poles due to an affinity for concave membranes and the existence of space to accommodate the protein due to the lack of the bacterial nucleoid (271,274). However, when cells became spherical the aggregate proteins appear to have been pushed toward one side possibly by the chromosomal DNA (Fig. 4.26 B). In the case of the truncated EspC-mCherry, localization appeared specific for

the distal poles of daughter cells rather than at the septal site which resembles the localization of the *S. flexneri* AT, IcsA. Interestingly, IcsA is predicted to be directed to one pole before being translocated across the IM in a localization pattern that is conserved among Enterobacteriaceae (200,271). However, the initial process involved in such localization is still undefined. Thus, one prediction is that the truncated EspC-mCherry somehow follows a similar route to be localized at old poles. Further work is required to investigate this and determine whether other hidden factors are involved in such particular polar localization.

There is no doubt that the insertion of the mCherry fluorescent protein into MreB generated a functional fusion similar to that previously reported (221,222). Although few cells exhibited discrete patches with short filaments similar to what been reported recently (242), the majority of cells clearly displayed a diffuse localization pattern which was confirmed by DAPI staining (Fig. 4.4 B). Unexpectedly, after longer induction periods, all cells converted to lemon shapes similar to those treated with A22 at a concentration 2.5 µg/ml (Fig. 4.4 C). A study conducted by Salje *et al*, observed a similar change in the cell shape upon expression of low levels of MreB-mCherry fusion (221). It is not clear why MreB becomes diffuse and upon longer expression times the cells take on a lemon shape. One possibility is that insertion of a large fluorescent mCherry protein (~30 kDa) interferes with the function of MreB by disrupting the protein structure, thus altering the interface between the MreB monomers or the ATP binding pocket leading to an

inability to make the protofilaments necessary for formation the helical filament structures.

Interesting questions raised by these experiments that warrant further investigation include: Would the fluorescent localization patterns of mCherry fusion to EspC or MreB be the same if the protein labelling technique was changed? If the localization pattern was independent of the fluorescent tag, is the spiral localization shared by other autotransporter proteins? Taking advantage of the availability of super-resolution microscopy techniques, recent advances in the Amber suppression approach could be used. This offers exquisite specificity with the ability to incorporate very small fluorophores within recombinant proteins at selected sites leading to minimal changes, if any, in protein structure (275,276). These are important considerations as they will help to unravel a possible common underlying process involved in bacterial protein secretion.

Overall, it is clearly shown here for the first time that the localization of EspC is dependent on its C-terminal transporter domain, the bacterial actin homologue MreB and the Sec translocon. Secretion via a helical distribution along the bacterial cytoskeleton and appears as discrete patches targeted toward bacterial poles. Further investigation is required to examine this possible association between the bacterial helical cytoskeleton and EspC secretion. Different labelling approaches such as using genetically encoded unnatural amino acids with fluorescent labelling to tag EspC instead of mCherry to discount the possibility of any potential protein structure distortions and/or malfunctions. In

addition, using different AT proteins such as the AaaA AT secreted from *P. aeruginosa* in parallel with EspC in protein localization analysis would fuel speculation of a common AT secretion pathway for Gram-negative bacteria. It would be interesting to demonstrate the precise translocation steps and reveal the molecular mechanism involved in the spiral secretion of EspC and be able to inhibit it thus bring new insights and knowledge to unravel the mystery of AT secretion, thereby enabling the development of new therapeutic targets and treatments.

Chapter 5

Can EspC be visualized with a single amino acid tag inserted using Amber suppression combined with click chemistry

5.1 Introduction

The ability to visualize and follow the dynamics of fluorescently labelled proteins as they move through living cells has had a significant impact upon our understanding of their localization. However, current protein labelling techniques with large fluorescent proteins (mCherry and GFP), self-labelling protein tags (for example, Halo and SNAP-tags) or self-labelling tags (tetracysteine and tetraserine tags) requires the use of protein fusions or addition of extra sequences into the target proteins. This may substantially increase the possibility of causing protein structure disruption/misfolding or loss of function (277,278).

Since the majority of data generated in chapters 3 and 4 relied on the insertion of the fluorescent protein mCherry into EspC, other methods of labelling AT proteins with smaller tags were considered to confirm the observed spiral secretion pathway whilst minimising the risk of structural aberrations caused by fusion of the mCherry protein.

The smallest tag identified exploited recent advances in Amber codon suppression. In this approach there is direct incorporation of an unnatural amino acid (UAA) bearing a biorthogonal functional group such as an alkyne or alkene into the protein to be tagged. This is achieved by genetically introducing an amber stop codon (TAG) at a defined site in the target gene and using a unique orthogonal pair of genes *in trans* to incorporate the desired UAA (279,280). Subsequently, a biorthogonal reaction (known as Click Chemistry) is performed to allow selective and rapid ligation of fluorogenic substrates carrying reactive

groups (for example, azide or tetrazine) onto the incorporated UAA. Consequently, the target protein is rendered fluorescent (275,281).

The crucial step in this method is the introduction of the specific orthogonal tRNA/tRNA synthetase (tRNA/RS) pair into the host *E. coli.* The amber suppressor tRNA must not be recognised by any of the endogenous aminoacyl-tRNA synthetases. Instead, only the orthogonal tRNA synthetase (RS) should charge its cognate UAG suppressor tRNA so that the desired UAA is incorporated into the target protein (282,283).

Numerous sets of engineered orthogonal pairs have been used to incorporate UAAs into proteins in the host *E. coli* (277,284). The most popular orthogonal pair for incorporation of such clickable UAAs originates from the methanogenic archaea, *Methanosarcina barkeri* MS (*M.barkeri*) and *Methanosarcina mazei* Go1 (*M. mazei*) (285,286). These organisms contain the 22nd natural amino acid called pyrrolysine (Pyl) which is incorporated into methyltransferases that initiate the formation of methane from methylamines (287). The insertion of Pyl occurs at the position of an amber codon and relies on the specific suppressor $tRNA_{CUA}$ (also known as $tRNA^{Pyl}$) and the pyrrolysyl-tRNA synthetase (PylRS) (286,288). Genetic engineering to insert this orthogonal pair into *E. coli* allows the production of pyrrolysine and its analogues (289,290).

The power of the super-resolution microscopy depends on small and specific fluorogenic probes generated by technology such as UAA labelling. In addition, the freedom to place the label at a particular site in the target protein would be predicted to enable more precise

localization of EspC within cells and hence provide new biological insights (275,291,292).

Attempts were therefore made to incorporate the alkene UAA trans-cyclooct-2-ene–L-lysine (TCOstar) into a specific site in EspC. The plan was to subsequently stably attach the fluorogenic tetrazine-Cy5 organic dye via the strain-promoted inverse-electron-demand Diels–Alder cycloaddition (SPIEDAC) reaction (275). This click chemistry reaction (tetrazine-trans-cyclooctene ligation) offers very fast labelling without the need of a catalyst, excellent biostability and compatibility with aqueous media at low concentrations. So it is ideally suited for live cell imaging as well as *in vitro* labelling studies (275,293,294).

To enable the commercially available TCOstar to be successfully incorporated into EspC in response to an amber codon in *E. coli*, an orthogonal $tRNA_{CUA}$/pyrrolysyl-tRNA synthetase mutant (Y306A and Y384F) pair (*Mm*$tRNA_{CUA}$/*Mm*$PylRS^{AF}$) from *M. mazei* was requested from the European Molecular Biology Laboratory (EMBL), Germany (275-277). Unfortunately, this was not achieved due to a delay in processing the Material Transfer Agreement (MTA). Therefore, to save time a different orthogonal pair*,* *Mb*$tRNA_{CUA}$/*Mb*PylRSΔ from *M. barkeri* was acquired from the Medical Research Council (MRC) Laboratory of molecular Biology, UK (249). Luckily, this time the MTA was accepted and the materials were provided.

The aim of this chapter was to test the ability of TCOstar to be incorporated into EspC using the orthogonal *Mb*$tRNA_{CUA}$/*Mb*PylRSΔ pair. To achieve this, multiple steps of cloning and SDM were carried out to

optimise the *M. barkeri* orthogonal pair to enable it to efficiently incorporate the UAA TCOstar into a specific site in EspC.

5.2 Results

5.2.1 Identification of optimal positions in *espC* to insert the amber stop codon (TAG) by SDM

To identify the best positions in EspC for amber codon insertion, the EspC crystal structure model was created using the I-TASSER server (http://zhanglab.ccmb.med.umich.edu/I-TASSER/) and then mapped in a 3D model using PyMol 3D Zalman software. As shown in Fig. 5.1, two different positions were chosen on the EspC passenger domain crystal structure to insert the UAA at amino acid position 533 or 951 via a TAG codon. These positions appear externally exposed, not embedded inside the protein structure, and so are predicted to be easily accessible by the fluorogenic labels (Fig 5.1). The reason of selecting two positions to label EspC is to increase the chances of successful labelling and imaging.

5.2.1.1 Generation of a truncated version of EspC without the β-barrel domain via genetically encoded amber stop codon for UAA incorporation

In order to insert the amber stop codon (TAG) into the chosen sites, SDM was performed using the pLA33C1 vector as a template and the primer pairs; F-TAG533espC/R-TAG533espC and F-TAG951espC/R-TAG951espC to create two versions of truncated EspC, one at aa positon 533 and the other at 951, respectively (see primer table chapter 2). The successful of creation of these two truncated versions was

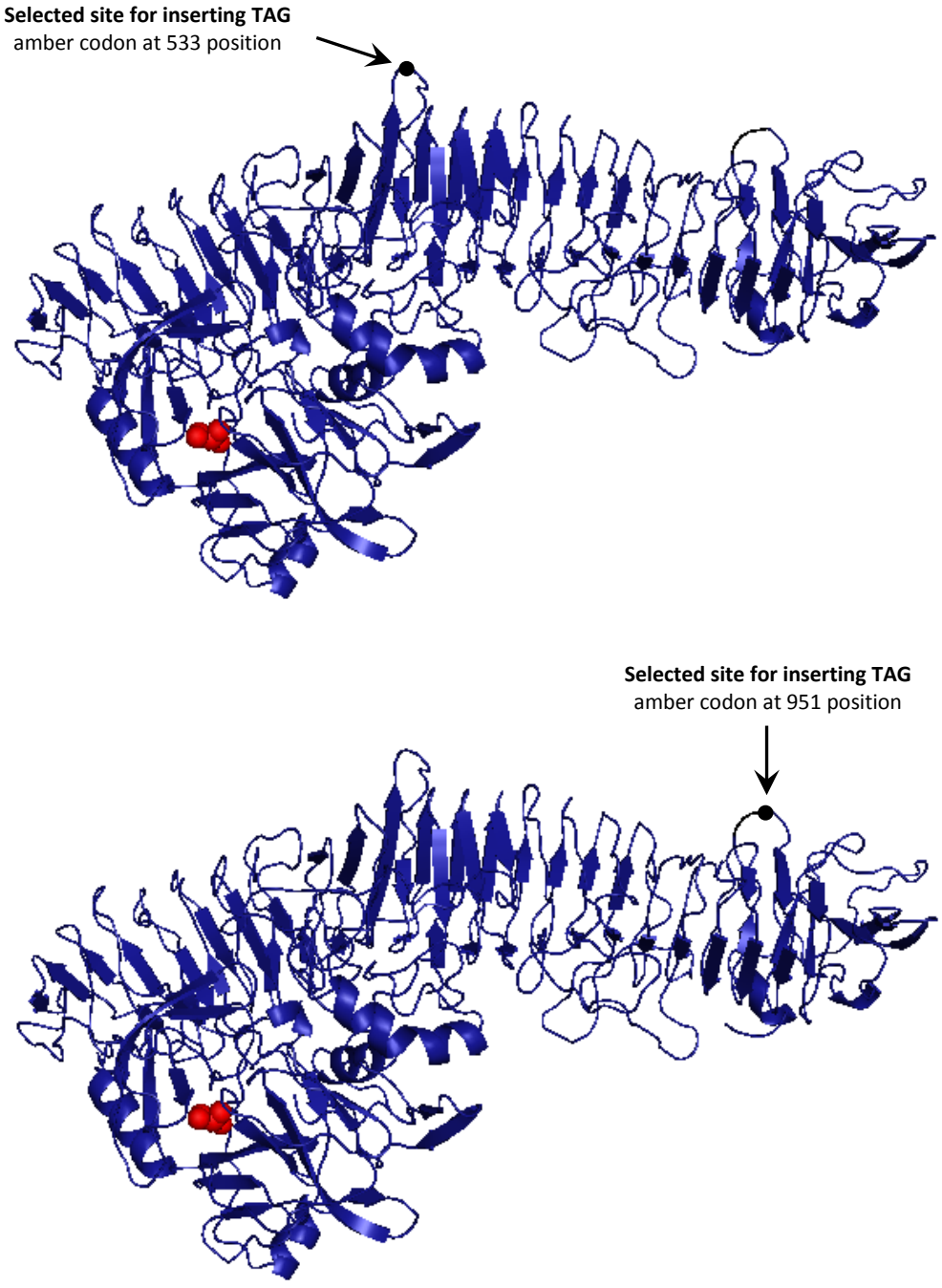


Figure 5.1: The positions selected for UAA insertion mapped onto the EspC passenger domain. The 3D model of the EspC passenger domain developed in PyMol Zalman software showing the locations on the selected external loops for inserting the UAA depicted as black spots (amino acid positions at 533 [top panel] and 951 [bottom panel]). See text for more information. The important catalytic serine residue at position 256 hosted in the motif GD**S**GS is highlighted in red.

confirmed via immunoblotting. α-EspC immunoblotting revealed the production of truncated EspC proteins approximately corresponding to ~55 kDa in the MG1655 culture containing pLA33C1^{TAG533} or ~110 kDa in those having pLA33C1^{TAG951} (Fig. 5.2 A). Furthermore, DNA sequencing confirmed the existence of the amber codon at the chosen sites and verified that no point mutation had occurred elsewhere in *espC*. As is the case when full length EspC is produced, MG1655 producing truncated EspC^{TAG533} or EspC^{TAG951} lacking the β-barrel domain grew more slowly and generated detectable EspC in culture supernatants (Figs. 5.3 and 5.2 B, respectively).

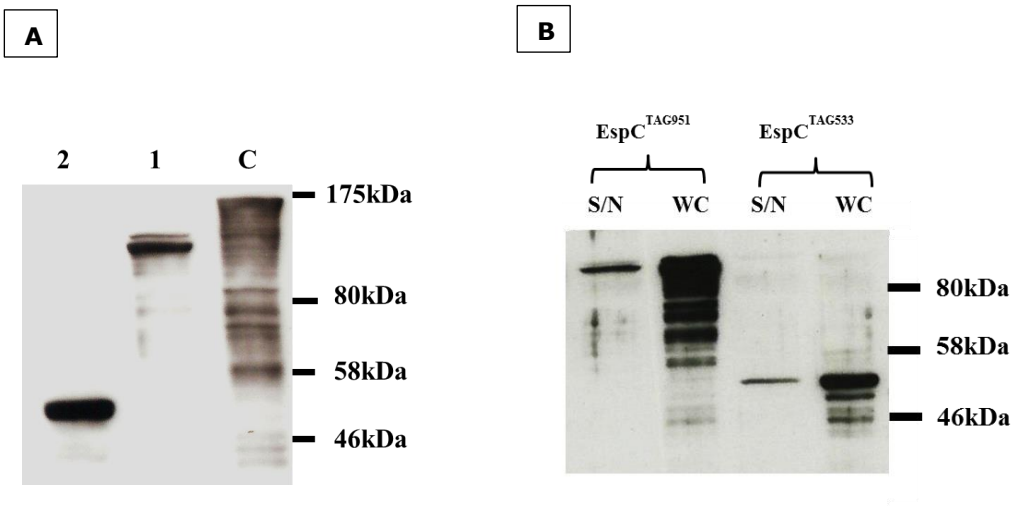


Figure 5.2: Production of short versions of EspC protein in *E. coli* MG1655. The overnight cultures of *E. coli* MG1655 containing pLA33C1^{TAG951} [1], pLA33C1^{TAG533} [2] or the control pLA33C1 plasmid (produces native EspC 140 kDa protein) [C] were diluted 1:100 and concurrently induced with 0.2% arabinose. After 4 h of induction, whole cell lysates (WC) and supernatants (S/N) were prepared as described in Material and Methods, and separated through 9% SDS-PAGE gel which were subjected to immunoblotting using α-EspC. Premature termination of translation at the amber codon equivalent to aa position 533 in EspC amino acid sequence yields production of the expected ~55 kDa truncated protein [2] while at 951 produces larger truncated EspC ~110 kDa [1] **(A)**. These newly truncated EspC forms were also detectable in the culture supernatants (S/N) **(B)**.

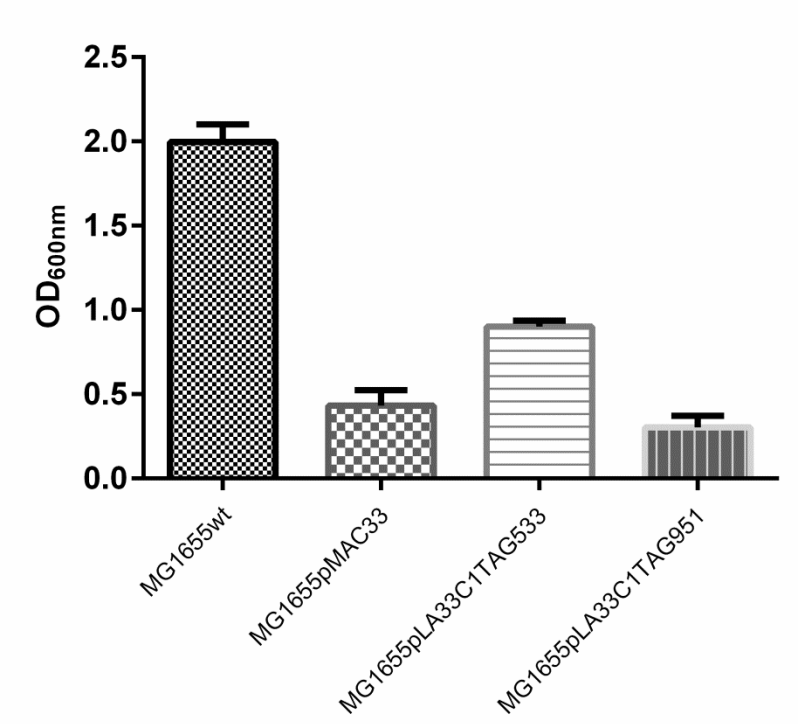


Figure 5.3: Loss of the β-barrel domain in the newly generated EspC mutants causes reduced growth similar to those observed previously. MG1655 wt, MG1655 (pMAC33), MG1655 (pLA33C1^{TAG95}) or MG1655 (pLA33C1^{TAG533}) were grown in LB with 0.2% arabinose and the optical density OD_{600} measured after 4 h of induction. Error bar represent standard deviation (n=3 replicate reads).

5.2.2 Incorporation of N^{ε}-acetyllysine UAA into EspC using the *M. barkeri Mb*tRNA$_{CUA}$/*Mb*PylRSΔ pair

5.2.2.1 Cloning strategy used to insert EspC^{TAG533} and EspC^{TAG951} into p*Myo*4TAGPylT-his$_6$ vector

As shown in Fig. 5.4, the two compatible plasmids received from the MRC Laboratory of Molecular Biology containing the orthogonal pair in *E. coli*. The Km resistant plasmid pBKPylS hosts the *Mb*PylRS mutant (N^{ε}-acetyllysine-tRNA synthetase (ACKRS-1)) under the control of the *E. coli* GlnRS promoter and terminator. The Tc resistant plasmid p*Myo*4TAGPylT-*his$_6$* encodes the amber suppressor *Mb*tRNA$_{CUA}$ (*pylT* gene with *lpp* promoter and *rrnC* terminator). It also encodes a C-terminal hexahistidine tagged sperm whale myoglobin with codon 4 substituted by an amber codon under the control of an arabinose inducible promoter (249). These two vectors have been shown to successfully incorporate a commercially available UAA called N^{ε}-acetyllysine in response to the amber codon and produce full length myoglobin-His$_6$ (248).

In order to incorporate N^{ε}-acetyllysine into EspC at the selected positions, both EspC^{TAG533} and EspC^{TAG951} were cloned into p*Myo*4TAGPylT-*his$_6$*. The strategy used replaced the myoglobin gene for *espC* (Fig. 5.5). Briefly, after releasing *espC* containing the amber codon from its backbone plasmid by digestion with *BamH*I and *Hind*III (Fig. 5.5 A), a PCR amplification was performed using F-espC/R-ApaI-espC primers (listed in table 2.4, chapter 2) to introduce an *Apa*I restriction site downstream of the EspC ORF (Fig. 5.5 B). The amplified

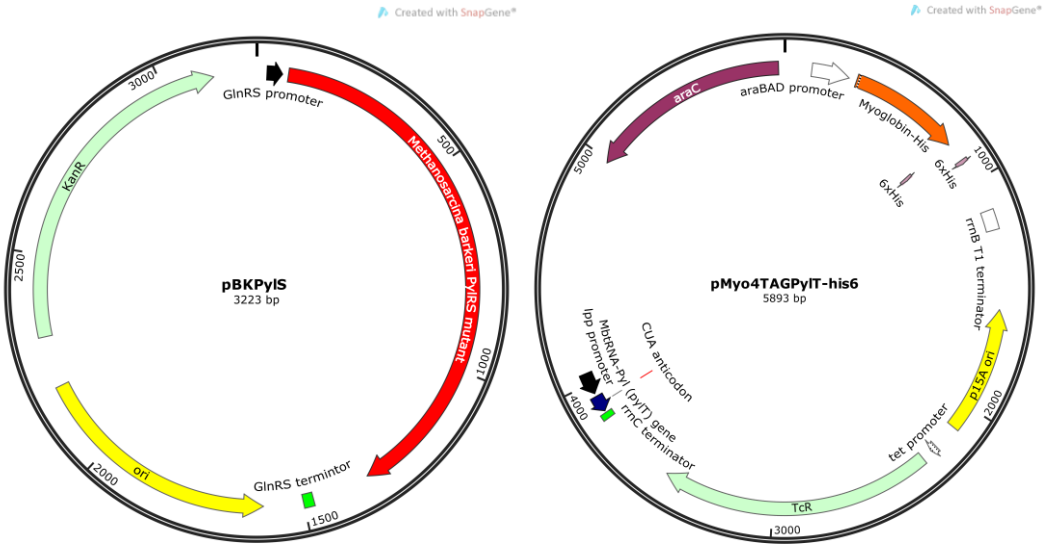


Figure 5.4: The plasmids bearing the orthogonal amber suppressor tRNA$_{CUA}$/pyrrolysyl-tRNA synthetase mutant (*Mb*tRNA$_{CUA}$/*Mb*PylRSΔ) pair from *M. barkeri* received from the MRC Laboratory of Molecular Biology, UK. pBKPylS vector encodes the PylRSΔ (Red arrow) under the control of the GlnRS promoter and terminator that recognises and acylates only its cognate suppressor tRNA$_{CUA}$ (Dark blue arrow) located in the plasmid, p*Myo*4TAGPylT-*his*$_6$. This plasmid also hosts the myoglobin encoding gene with an amber stop codon at position 4 which can be used as a control (orange arrow). The two plasmids are compatible having different origins of replication and antibiotic resistance.

sequence was excised from the gel, digested with restriction enzymes *Sac*I and *Apa*I and ligated into similarly digested p*Myo*4TAGPylT-*his*$_6$ vector (Fig. 5.5 C). Following ligation, the new constructs were transformed into *E. coli* MG1655 and selected on plates with Tc (12.5 µg/ml). Recombinant plasmids were screened by *Sac*I or *Sac*I/*Apa*I digestion for the presence of the cloned DNA fragments and confirmed by DNA sequencing. Verified plasmids were named p*EspC*533TAGPylT and p*EspC*951TAGPylT (Fig. 5.5 D).

5.2.2.2 Inability to incorporate N^{ε}-acetyllysine into amber codons

The production of truncated EspC from the new constructs, p*EspC*533TAGPylT and p*EspC*951TAGPylT was evaluated by induction with arabinose and immunoblotting with α-EspC. To do this, freshly made competent *E. coli* MG1655 was transformed with p*EspC*533TAGPylT or p*EspC*951TAGPylT and prepared as described in chapter 2. MG1655 (pLA33C1) was expressed as a control for full length EspC (140 kDa). As expected, immunoblotting using α-EspC revealed the presence of truncated ~55 kDa and ~110 kDa EspC in lysates hosting MG1655 (p*EspC*533TAGPylT) and (p*EspC*951TAGPylT), respectively (Fig. 5.6 A). This protein profile was similar to that observed in Fig. 5.2, thus further indicating the successful cloning of the *espC* containing amber into p*Myo*4TAG-PylT plasmid.

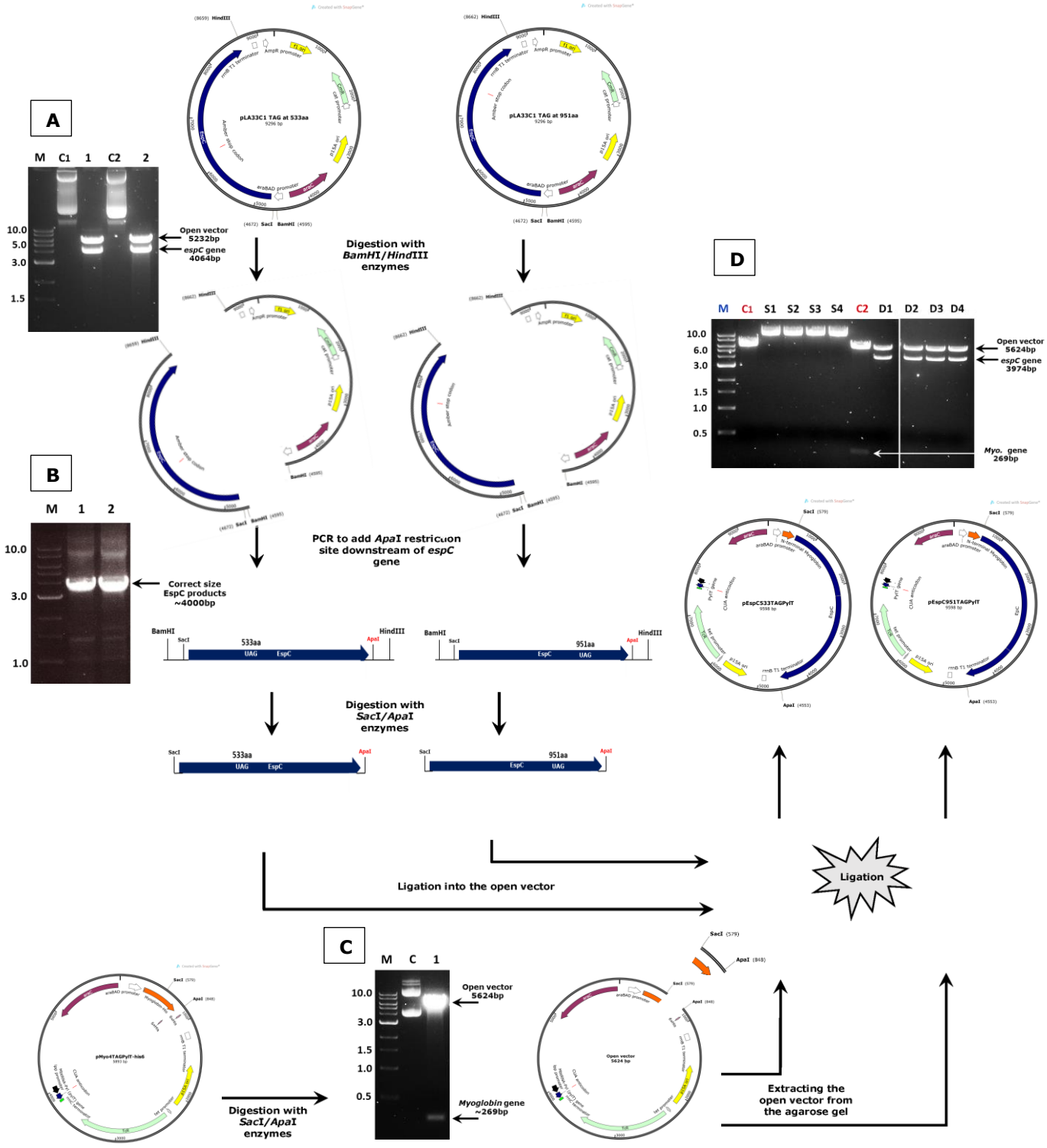


Figure 5.5: The cloning strategy used to replace *myo-his*$_6$ encoding ORF with amber containing *espC*. ~4064 bp template containing the ORF of *espC* was first separated from the pBAD33 vector backbone by *BamH*I/*Hind*III digestion **(Agarose A**: Lane 1 and 2 representing the digested pLA33C1^{TAG533} and pLA33C1^{TAG951} respectively and C is for the control plasmid DNA**)**. The desired fragments were excised from the gel and purified using gel extraction kit. Subsequently, PCR amplification was performed using specific primers (see text) to include *Apa*I restriction site just downstream of the *espC* Opal stop codon. The successful *espC* amplification was confirmed in **agarose B** in both EspC^{TAG533} (lane 1) and EspC^{TAG951} (lane 2). These PCR products were then purified and further digested with *Sac*I/*Apa*I restriction enzymes and ligated into similar digested p*Myo*4TAGPylT-*his*$_6$ plasmid **(Agarose C**: showing the control plasmid DNA and lane 1 displaying the open vector 5624 bp with very small split myoglobin DNA band ~269 bp**)**. The confirmation of the new constructs was through a new digestion with the same restriction enzymes. **Agarose D**: Four randomly selected colonies were selected for evaluation, 1 and 2 are displaying p*EspC*951TAGPylT while 3 and 4 representing p*EspC*533TAGPylT in which single digested by *Apa*I enzyme **(S)** or double digested by *Sac*I/*Apa*I enzymes **(D)**. The expected 3974 bp EspC fragment was detected in D1, D2, D3, and D4. The control p*Myo*4TAGPylT-*his*$_6$ vector was also similarly digested by *Apa*I restriction enzyme (lane C1) or double digested by *Sac*I/*Apa*I restriction enzymes which clearly separated the ~269 bp myoglobin fragment (lane C2). M is for the DNA molecular marker 1 kb.

Having successfully replaced the myoglobin gene by *espC*, the next step was to introduce the N^{ε}-acetyllysine into EspC via the amber codon to enable production of full length EspC, thereby verifying the efficiency of the system. To achieve this aim, *E. coli* MG1655 was transformed with pBKPylSΔ (AcKRS-1) and either p*EspC*533TAGPylT or p*EspC*951TAGPylT. As a control, both pBKPylSΔ (AcKRS-1) and p*Myo*4TAGPylT-his_6 plasmids were transformed into *E. coli* MG1655 to generate the full length sperm whale myoglobin-His. Cells were incubated in LB containing Tc (12.5 µg/ml) and Km (25 µg/ml) overnight with shaking at 37°C. A 1:100 dilution of cultures was prepared the next day, supplemented with antibiotics and 1 mM N^{ε}-acetyllysine UAA as recommended by Neumann *et al*., 2008 (see section 2.16, chapter 2) (248). As a negative control, a similar set of cultures were prepared in parallel but without adding the UAA. After 2 h of growth at 37°C, cultures were induced by 0.2% arabinose to express the recombinant proteins. After a further 3 to 4 h, whole cell lysates were collected for analysis via immunoblotting using α-EspC and α-His-tag antisera for detecting EspC and myoglobin, respectively. Surprisingly, it was not possible to detect the full length EspC protein in lysates containing the N^{ε}-acetyllysine and only truncated proteins were observed (Fig. 5.6 B). Likewise, no full length myoglobin-His_6 (~18 kDa) was observed in the presence of N^{ε}-acetyllysine in the growth medium (Fig. 5.6 D), suggesting incorporation of UAA into EspC had not occurred.

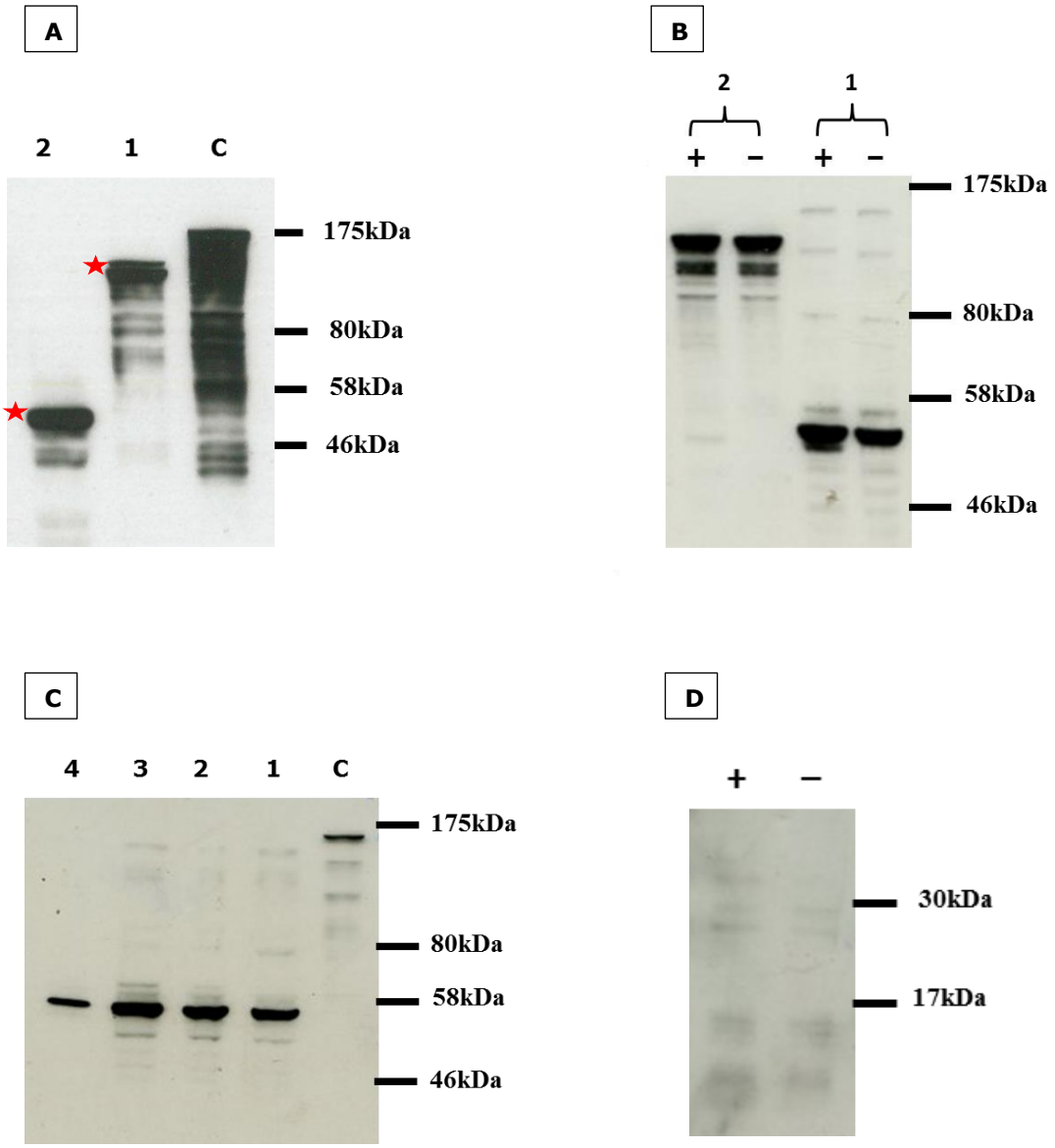


Figure 5.6: Incorporation of N^{ε}-acetyllysine into EspC and Myoglobin-His$_6$ was initially unsuccessful. *E. coli* MG1655 bearing the control pLA33C1 plasmid [C], p*EspC*951TAGPylT [1] and p*EspC*533TAGPylT [2] were grown in LB and concomitantly induced with 0.2% arabinose for 4 h. Truncated EspC products (~55 kDa and ~110 kDa) are indicated by the red asterisks **(Panel A)**. *E. coli* MG1655 bearing p*EspC*533TAGPylT/pBKPylSΔ [1] or p*EspC*951TAGPylT/pBKPylSΔ [2] were prepared as described in the text. Truncated EspC products were produced without (–) or with (+) 1 mM N^{ε}-acetyllysine in the growth medium **(Panel B)**. The truncated ~55 kDa EspC was observed when the *E. coli* MG1655 (p*EspC*533TAGPylT/pBKPylSΔ) culture lacked any N^{ε}-acetyllysine [1] or contained 10 mM N^{ε}-acetyllysine dissolved in LB [2], 1 M HEPES [3] or 80% acetic acid [4] **(Panel C)**. *E. coli* MG1655 hosting p*Myo*4TAGPylT-his$_6$/pBKPylSΔ was induced as described in the text supplemented without (-) or with (+) 1 mM N^{ε}-acetyllysine but it was not possible to detect the Myoglobin-His protein **(Panel D)**. Proteins were separated through a 9% SDS-PAGE and immunoblotted with α-EspC in panel A, B and C while in D the proteins were separated through 12% SDS PAGE and incubated with α-His-tag antisera.

Several optimisation steps were carried out to incorporate the N^{ε}-acetyllysine into the recombinant proteins, for example, dissolving the UAA compound in 80% acetic acid (as recommended by the manufacturer) or 1 M HEPES and adjusting the pH of the growth medium to 7.4. However, similar results indicating a lack of full length EspC were obtained (Fig. 5.6 C). Moreover, using different *E. coli* strains such as DH10B and the T7 expression strain BL21 (DE3) did not alter the outcome (data not shown). To circumvent this issue, sequencing of the orthogonal *Mb*PylRSΔ/tRNA$_{CUA}$ pair as well as the *myo* gene was performed using primers listed in table 2.4, chapter 2. Unexpectedly, the sequencing data revealed that a wild type pyrrolysyl-tRNA synthetase (pylRS^{WT}) was found encoded in the pBKPylS plasmid instead of the expected pylRSΔ (AcKRS-1). With this version of the synthetase, it would not be feasible to use the N^{ε}-acetyllysine UAA as a substrate.

5.2.3 Incorporation of TCOstar UAA into EspC using the *M. mazei Mm*tRNA$_{CUA}$/*Mm*PylRS^{AF} gene pair

It has been reported that the *M. mazei Mm*tRNA^{Pyl}/*Mm*PylRS^{AF} pair efficiently permits incorporation of the UAA, TCOstar (275). Sequence alignment of the *M. mazei* PylRS^{WT} amino acid sequence with the homologous *M. barkeri* PylRS^{WT} using the Basic Local Alignment Search Tool (BLAST) from the National Centre for Biotechnology Information (NCBI) (http://blast.ncbi.nlm.nih.gov/Blast.cgi) revealed only 74% sequence identity. In contrast, DNA sequence alignment of the amber suppressor tRNA^{Pyl} of the two *Methanosarcina* spp. revealed a single nucleotide base difference located at the acceptor stem; the adenine

base at position 3 in *M. mazei* is substituted for guanine in *M. barkeri* (Fig. 5.7). These observations offered a suitable starting point to permit incorporation of TCOstar into EspC. To facilitate this, the *M. barkeri* $PylRS^{WT}$ was replaced with the corresponding $PylRS^{WT}$ of *M. mazei* followed by introduction of the Y306A and Y384F mutations into the protein to allow incorporation of the TCOstar UAA (277). Moreover, changing the guanine base at position 3 in the *M. barkeri* amber suppressor tRNA with adenine would further facilitate the attachment of TCOstar into the acceptor arm of the $tRNA^{Pyl}$.

A

Sequence ID: lcl|Query_127827 Length: 455 Number of Matches: 1

Range 1: 1 to 455 Graphics ▼ Next Match ▲ Previous Match

Score	Expect	Method	Identities	Positives	Gaps
697 bits(1800)	0.0	Compositional matrix adjust.	336/455(74%)	378/455(83%)	35/455(7%)

```
MbPylS   1    MDKKPLDVLISATGLWMSRTGTLHKIKHHEVSRSKIYIEMACGDHLVVNNSRSCRTARAF  60
              MDKKPL+ LISATGLWMSRTGT+HKIKHHEVSRSKIYIEMACGDHLVVNNSRS RTARA
MmPylS   1    MDKKPLNTLISATGLWMSRTGTIHKIKHHEVSRSKIYIEMACGDHLVVNNSRSSRTARAL  60

MbPylS   61   RHHKYRKTCKRCRVSDEDINNFLTRSTESKNSVKVRVVSAP-KVKKAMPKSVSRAPKPLE  119
              RHHKYRKTCKRCRVSDED+N FLT++ E + SVKV+VVSAP + KKAMPKSV+RAPKPLE
MmPylS   61   RHHKYRKTCKRCRVSDEDLNKFLTKANEDQTSVKVKVVSAPTRTKKAMPKSVARAPKPLE  120

MbPylS   120  NSVSAKASTNTSRSVPSPAKSTPNS----------------------------------S  145
              N+ +A+A  + S+  P+   ST  S                                  S
MmPylS   121  NTEAAQAQPSGSKFSPAIPVSTQESVSVPASVSTSISSISTGATASALVKGNTNPITSMS  180

MbPylS   146  VPASAPAPSLTRSQLDRVEALLSPEDKISLNMAKPFRELEPELVTRRKNDFQRLYTNDRE  205
               P  A AP+LT+SQ DR+E LL+P+D+ISLN  KPFRELE EL++RRK D Q++Y  +RE
MmPylS   181  APVQASAPALTKSQTDRLEVLLNPKDEISLNSGKPFRELESELLSRRKKDLQQIYAEERE  240

MbPylS   206  DYLGKLERDITKFFVDRGFLEIKSPILIPAEYVERMGINNDTELSKQIFRVDKNLCLRPM  265
              +YLGKLER+IT+FFVDRGFLEIKSPILIP EY+ERMGI+NDTELSKQIFRVDKN CLRPM
MmPylS   241  NYLGKLEREITRFFVDRGFLEIKSPILIPLEYIERMGIDNDTELSKQIFRVDKNFCLRPM  300

MbPylS   266  LAPTLYNYLRKLDRILPGPIKIFEVGPCYRKESDGKEHLEEFTMVNFCQMGSGCTRENLE  325
              LAP LYNYLRKLDR LP PIKIFE+GPCYRKESDGKEHLEEFTM+NFCQMGSGCTRENLE
MmPylS   301  LAPNLYNYLRKLDRALPDPIKIFEIGPCYRKESDGKEHLEEFTMLNFCQMGSGCTRENLE  360

MbPylS   326  ALIKEFLDYLEIDFEIVGDSCMVYGDTLDIMHGDLELSSAVVGPVSLDREWGIDKPWIGA  385
              ++I +FL++L IDF+IVGDSCMVYGDTLD+MHGDLELSSAVVGP+ LDREWGIDKPWIGA
MmPylS   361  SIITDFLNHLGIDFKIVGDSCMVYGDTLDVMHGDLELSSAVVGPIPLDREWGIDKPWIGA  420

MbPylS   386  GFGLERLLKVMHGFKNIKRASRSESYYNGISTNL*  420
              GFGLERLLKV H FKNIKRA+RSESYYNGISTNL*
MmPylS   421  GFGLERLLKVKHDFKNIKRAARSESYYNGISTNL*  455
```

B

Sequence ID: lcl|Query_162747 Length: 72 Number of Matches: 1

Range 1: 1 to 72 Graphics ▼ Next Match ▲ Previous Match

Score	Expect	Identities	Gaps	Strand
125 bits(138)	6e-35	71/72(99%)	0/72(0%)	Plus/Plus

```
MbPylT   1    GGGAACCTGATCATGTAGATCGAATGGACTCTAAATCCGTTCAGCCGGGTTAGATTCCCG  60
              || ||||||||||||||||||||||||||||||||||||||||||||||||||||||||||
MmPylT   1    GGAAACCTGATCATGTAGATCGAATGGACTCTAAATCCGTTCAGCCGGGTTAGATTCCCG  60

MbPylT   61   GGGTTTCCGCCA  72
              ||||||||||||
MmPylT   61   GGGTTTCCGCCA  72
```

Figure 5.7: Sequence alignment of the pyrrolysyl-tRNA synthetase (PylRS) and the amber suppressor tRNA$_{CUA}$ from *M. barkeri* MS and *M. mazei* Go1 strains. Amino acid sequence alignment of *M. barkeri* PylRS^{WT} (MbPylS) with the *M. mazei* PylRS^{WT} (MmPylS) indicates only 74% of sequence homology **(A)**. Only one nucleotide base difference (red asterisk) was detected during DNA sequence alignment of the *M. barkeri pylT* (MbPylT) with the *M. mazei pylT* (MmPylT) **(B)**.

5.2.3.1 Substitution of *M. barkeri* MS *pylS* gene in the pBKPylS vector for *M. mazei pylS* (*Mm*PylRS^{WT})

TCOstar has been successfully incorporated into GFP via an amber stop codon using the *M. mazei* tRNA^{Pyl}/PylRS^{AF} mutant pair leading to production of full length GFP and hence fluorescence (275). Expanding the catalytic pocket in PylRS^{WT} of *M. mazei,* by introducing the double mutation Y306A/Y384F, significantly increased *in vivo* amber suppression activity with a variety of UAAs (290).

To permit incorporation of TCOstar into *espC*, a cloning strategy involving multiple steps was designed (Fig. 5.8). PCR amplification of *Mm*PylS^{WT} from the whole genome of *M. mazei* (Leibniz institute DSMZ-German collection: https://www.dsmz.de/catalogues/catalogue-microorganisms.html) was performed using primers F-mazei-*Nde*I and R-mazei-*Sal*I (see table 2.4, chapter 2). This introduced *Nde*I and *Sal*I restriction sites into the 5' and 3' ends of the product of 1365 bp (Fig. 5.8 A) which was purified and digested with the same enzymes. In order to insert *Mm*PylRS^{WT} into the pBKPylS vector, SDM was first performed to insert the *Sal*I restriction site downstream of the *Mb*PylRS^{WT} gene in pBKPylS using the primer pair F-pBK-*Sal*I/R-pBK-*Sal*I (listed in table 2.4, chapter 2). Subsequently, the PCR product (3223 bp) was digested with *Dpn*I (Fig. 5.8 B) to remove the parental DNA copies followed by transformation into commercially prepared *E. coli* Top10 competent cells to repair the nicks in mutated plasmid. To confirm the mutation, the plasmid extracted from the selected transformants was subjected to digestion with *Nde*I/*Sal*I enzymes, revealing two DNA fragments (the

open pBK vector backbone 1964 bp and the 1260 bp *pylS* gene of *M. barkeri*). This confirmed the successful introduction of *Sal*I (Fig. 5.8 C). DNA sequencing confirmed the existence of the desired base substitutions to include the *Sal*I restriction site and verified that no point mutations had occurred.

Subsequently the open pBK vector backbone (1964 bp) was excised and purified from the gel (Fig. 5.8 C), and ligated to the *Mm*pylRS digested PCR product. Following transformation into *E. coli* MG1655 with selection on LB containing Km plates, the resultant construct was confirmed by DNA sequencing. Finally, two rounds of SDM were performed to introduce the first Y306A mutation (Fig. 5.8 D) then the second Y384F mutation (Fig. 5.8 E) into the *pylS* gene of *M. mazei*, generating the mutant plasmid, pBKPylS^{AF}.

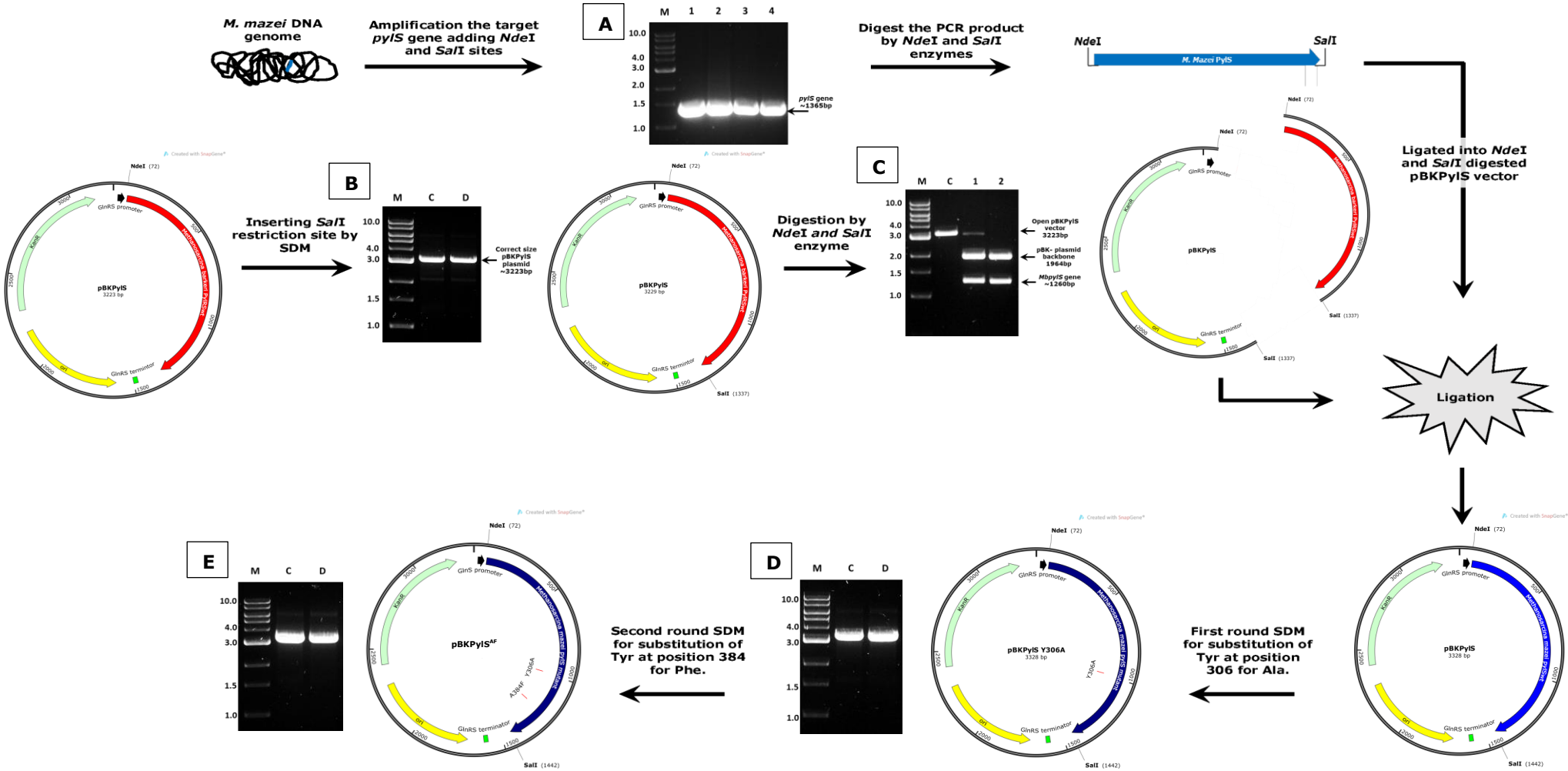


Figure 5.8: Cloning strategy to replace the *Mb*PylRS^{WT} in pBKPylS by the *Mm*PylRS hosting two mutations (Y306A and Y384F) to generate pBKPylS^{AF} vector. The ORF sequence of *M. mazei pylS* gene was PCR amplified to incorporate *Nde*I and *Sal*I restriction sites **(Agarose A**: showing 4 PCR reactions with the expected DNA fragments ~1365 bp corresponding to *pylS* gene). Subsequently, the PCR products were purified and further digested with *Nde*I/*Sal*I enzymes. To enable cloning into the pBKPylS vector, SDM was first performed to incorporate *Sal*I site downstream of *PylS* **(Agarose B)**. For evaluation, the control original plasmid as well as randomly selected two colonies were digested with same set of restriction enzymes **(Agarose C**: Lane C is the control pBKPylS plasmid without (*Sal*I site), lane 1 and 2 showing those having introduced *Sal*I site produce the *Mb*PylRS^{WT} ~1260 bp and vector fragments**)**. Following successful ligation of the digested PCR product into similar digested pBKPylS plasmid, two rounds SDM were carried out to substitute tyrosine amino acid at position 306 and 384 for alanine and phenylalanine **(Agarose D and E**) respectively for producing pBKPylS^{AF} plasmid. Agarose B, D and E showing the SDM PCR; Lanes C are for the control PCR samples and lanes D are PCR samples digested with *Dpn*I restriction enzyme. A small contamination was spotted in lane 1 on agarose C which corresponding to the control sample in lane C.

5.2.3.2 Optimisation of the *M. barkeri* amber suppressor tRNA (*Mb*tRNA$_{CUA}$) to enable TCOstar incorporation efficiency with *Mm*PylRS^{AF}

Having successfully constructed the pBKPylS^{AF} vector containing *M. mazei PylS* gene encoding the double mutant (Y306A/Y384F) to improve the acceptance of the TCOstar, the next step was to optimise the suppressor tRNA acceptor stem and make it homologous with the *M. mazei* pylT (Fig. 5.7). To achieve this, SDM was carried out to substitute guanine for adenine using the primer pair F-tRNA mut/R-tRNA mut (see table 2.4, chapter 2). The procedure of mutagenesis was performed as previously using both p*Myo*4TAGPylT-*his*$_6$ and p*EspC*533TAGPylT plasmids as PCR templates. To save materials and minimise the amount of sample handling, the vector p*EspC*951TAGPylT was not included.

The mutated plasmids were extracted from the selected transformants and the presence of the desired nucleotide substitution was confirmed by DNA sequencing in both vectors, which were named p*Myo*4TAGPylT$_m$ and p*EspC*533TAGPylT$_m$.

5.2.3.3 Inability to incorporate TCOstar using *Mm*PylRS^{AF} and PylT$_m$

To produce EspC containing TCOstar, *E. coli* MG1655 was transformed with pBKPylS^{AF} and p*EspC*533TAGPylT$_m$ and plated on LB agar containing Tc (12.5 µg/ml) and Km (25 µg/ml). For control expression, similar competent *E. coli* cells were transformed with pBKPylS^{AF} and p*Myo*4TAGPylT$_m$ and similarly selected. Subsequently, whole cell lysates

were prepared for SDS-PAGE and immunoblotted as described in section 5.2.2.2. Unfortunately, again, it was not possible to detect the full length of EspC in lysates containing the TCOstar and only truncated EspC were observed. Similarly, no production of myoglobin-His_6 (~18 kDa) was detected (data not shown).

5.2.4 Unexpectedly, N^{ε}-Boc-L-Lysine was successfully incorporated into EspC and myoglobin

Thanks to input from the Chin lab team (MRC Laboratory of Molecular Biology, Cambridge) who provided the orthogonal plasmid pair, pBKPylS/p*Myo*4TAGPylT-*his*$_6$ for this study (Fig. 5.4), the potential of these plasmids to incorporate the UAA called N^{ε}-Boc-L-Lysine into the His-tagged myoglobin rather than N^{ε}-acetyllysine (TCOstar) became evident. Although this conflicts with Neumann *et al*, 2008 (248), *E. coli* MG1655 competent cells were independently transformed with pBKPylS^{WT}/p*EspC*533TAGPylT for EspC production and with pBKPylS^{WT}/p*Myo*4TAGPylT-*his*$_6$ for the control myoglobin production. N^{ε}-Boc-L-Lysine UAA was purchased from Alfa Aesar (Product Number: B21738) and prepared as a stock of 0.05 M, dissolved in LB and used at 1 mM (final concentration). N^{ε}-Boc-L-Lysine was efficiently incorporated into both the control myoglobin-His and EspC (Fig. 5.9). α-His-tag antisera detected the full length myoglobin (~18 kDa) protein in whole cell lysates prepared from cells grown with N^{ε}-Boc-L-Lysine (Fig. 5.9 A).

Although it was not possible to detect the full length of EspC (~140 kDa) in whole cell lysates grown with N^{ε}-Boc-L-Lysine, it was evident that

there were decreased levels of truncated EspC (~55 kDa) accompanied by low levels of EspC (supernatant version lacking β-barrel domain: ~110 kDa) in the supernatant (Fig. 5.9 B). When the experiment was repeated in order to precipitate a larger volume of supernatant, to try to detect EspC more convincingly, no EspC proteins were detected either in the supernatant or whole cell lysate samples containing N^{ε}-Boc-L-Lysine (Fig. 5.9 C). It is possible that EspC had degraded on this occasion, but unfortunately, due to time constraints, it was not possible to investigate this further.

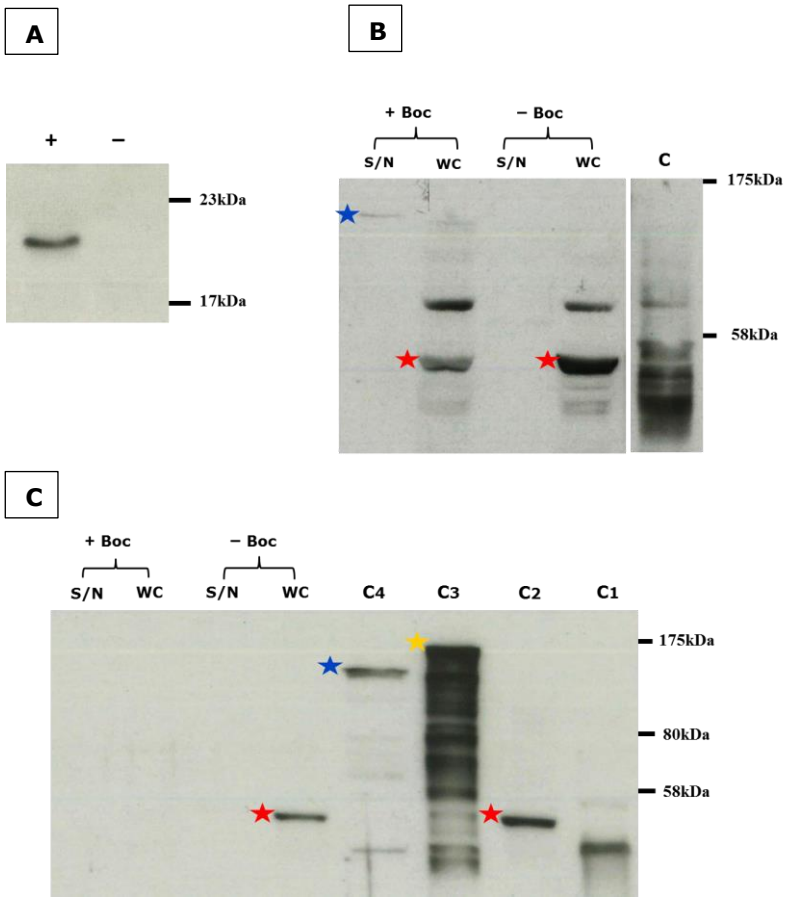


Figure 5.9: Incorporation of N^{ε}-Boc-L-Lysine into EspC and Myoglobin-His$_6$. **(A)** Whole cell lysates of *E. coli* MG1655 containing pBKPylS^{WT}/p*Myo*4TAGPylT-*his*$_6$ with (+) and without (–) N^{ε}-Boc-L-lysine immunoblotted with α-His-tag antisera. The myoglobin-his is indicated at ~18 kDa. **(B)** Whole cell (WC) and supernatant (S/N) lysates of *E. coli* MG1655 containing pBKPylS^{WT}/p*EspC*533TAGPylT with (+) and without (–) N^{ε}-Boc-L-lysine as well as the control MG1655 hosting the empty plasmid pBAD33 immunoblotted with α-EspC antisera. Intracellular truncated EspC (~55 kDa) is indicated by the red asterisks, and secreted EspC lacking the β-barrel (~110 kDa) in the supernatant lysate (Blue asterisk). Note the reduction in truncated EspC in the sample containing N^{ε}-Boc-L-lysine as the UAA is incorporated into EspC. **(C)** Repetition of blot in (B) with controls as follows; C1, *E. coli* MG1655 (pBAD33); C2, *E. coli* MG1655 containing pLA33C1^{TAG533}; C3, whole cell lysate of *E. coli* MG1655 (pLA33C1); C4, supernatant lysate of *E. coli* MG1655 (pLA33C1). Intracellular truncated EspC (~55 kDa) (red asterisks), secreted EspC lacking the β-barrel (~110 kDa) (Blue asterisks) and intracellular native EspC (140 kDa) (yellow asterisk). Cells were grown in LB with selected antibiotics (see text) and supplemented with (+) or without (–) N^{ε}-Boc-L-lysine for 2 h until reached to 0.4-0.5 OD_{600}. Subsequently, samples were induced by 0.02% arabinose and kept to grow for additional 3 h shaking at 37°C. Whole cell (WC) and (S/N) supernatant lysates were prepared as described in Materials and Methods. Samples were loaded on the 12% SDS-PAGE gel **(A)** and 9% SDS-PAGE gels **(B and C)**. Control samples C1, C2 and C3 were induced by 0.02% arabinose prepared as described in section 5.2.2.2.

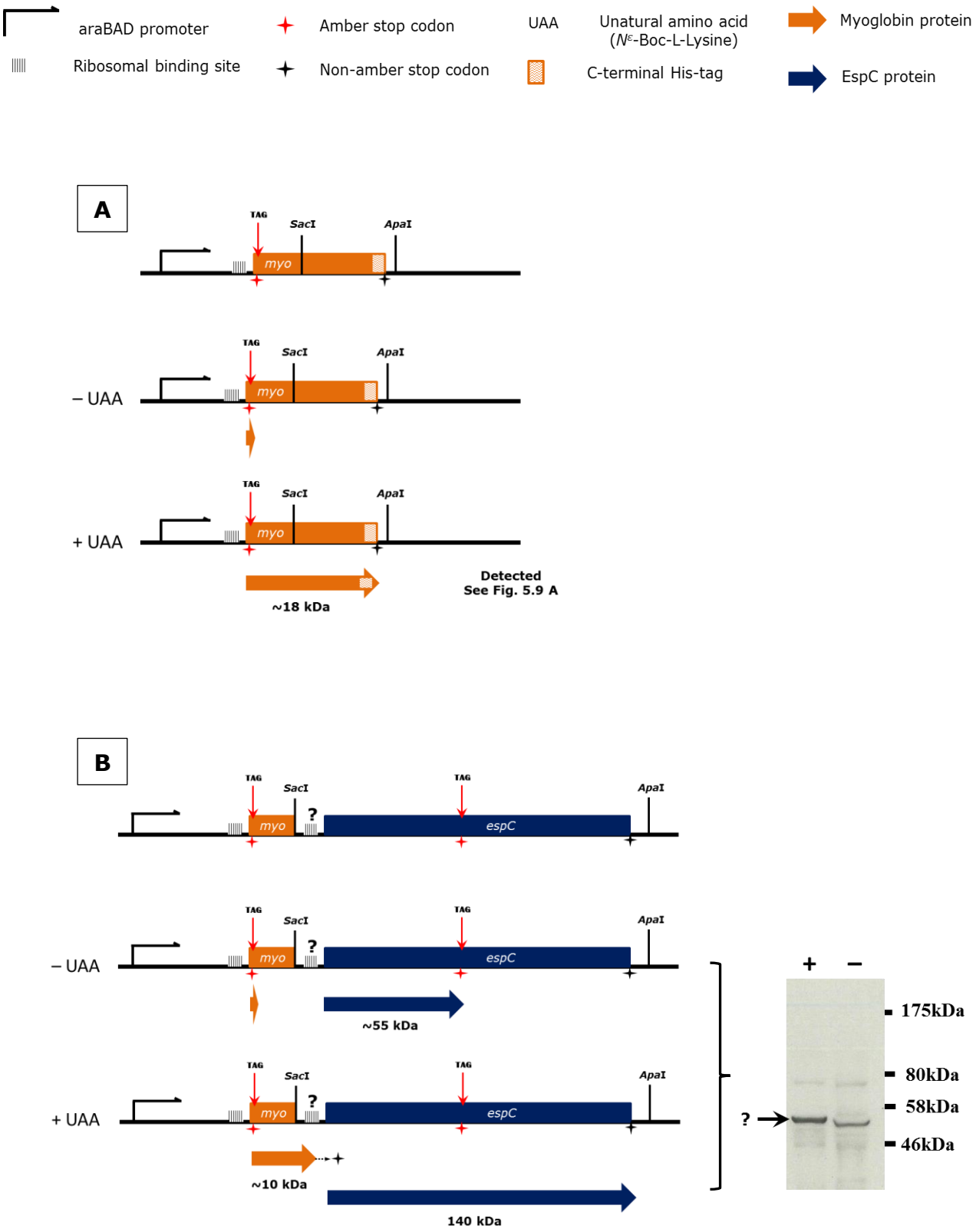
5.3 Discussion

Bioorthogonal click chemistry for visualizing biomolecules within living cells has become a major tool in modern protein localization studies (277). This powerful chemistry relies on the presence of pairs of functional groups that spontaneously, rapidly and selectively interact in an aqueous environment or at the surface of membranes (276). One such reaction, the fast bioconjugation based on SPIEDAC reactivity, tetrazine–trans-cyclooctene ligation was planned in this study (281,293). However, since it was not possible to incorporate TCOstar into EspC, this could not be realised.

According to the study conducted by Neumann *et al,* 2008, N^{ε}-acetyllysine was successfully encoded into myoglobin-his protein using the orthogonal *Mb*tRNA$_{CUA}$/*Mb*PylRS pair in which *Mb*PylRS contains six mutations termed as AcKRS-1. These mutations cause a rearrangement in the binding pocket of *Mb*PylRS to enable binding of the N^{ε}-acetyllysine (248). Unfortunately, this could not be obtained and DNA sequencing confirmed that the available plasmids contained a wild type *Mb*PylRS.

Amber stop codons were successfully inserted at selected sites in *espC* at the amino acid positions 533 and 951 (Fig. 5.1). Immunoblotting confirmed the production of truncated EspC proteins with different sizes (Fig. 5.2). A variety of optimisation steps and strategies were undertaken in the quest to incorporate TCOstar into EspC using the orthogonal *Mb*tRNA$_{CUA}$/*Mb*PylRS pair. For instance, the myoglobin encoding gene in the p*Myo*4TAGPylT-*his*$_6$ vector was replaced with *espC* (see figure 5.5 C and D) to generate a plasmid which fused *myo* (that

included a TAG codon at the position equivalent to amino acid 4) with some upstream DNA including a ribosome binding site to *espC*. Analysis using the Snapgene DNA program revealed that if the amber codon in myoglobin at position 4 is suppressed by UAA, translation will continue to an ochre stop codon. The ochre stop codon is located out of frame of, but within the first few codons of *espC*, and the myoglobin fragment produced would lack a His-tag, and therefore there would be no means to detect its production (Fig. 5.10 B). In the absence of UAA, the expected ~55 kDa EspC product prematurely truncated at the amber stop codon was detected by immunoblotting (Fig. 5.10 B). Growth in N^{ε}-Boc-L-Lysine generated a protein that was recognized by anti-EspC, but that was only marginally altered in its electrophoretic mobility compared to $EspC^{TAG533}$ (Fig. 5.10 B). This indicted that a longer myoglobin fragment was not produced preventing EspC translation. However, it also suggested that EspC was not extended through the amber stop codon to generate full length EspC. To simplify this expression construct, SDM to generate an additional restriction enzyme restriction site (*Sac*I) enabled the remnants of the *myo* gene to be excised from the region whilst retaining the *espC* ribosome binding site (this was confirmed by DNA sequencing) (Fig. 5.10 C). It was expected that incorporation of N^{ε}-Boc-L-Lysine would generate detectable levels of intracellular, full length EspC that could be monitored to track localization during secretion (Fig. 5.10 C). However, this did not occur (Fig. 5.9). This is a crucial limitation making the performance of click chemistry to incorporate a fluorescent label to visualize EspC within live bacteria pointless. Since processed EspC that had been secreted was detected following


araBAD promoter
Ribosomal binding site
Amber stop codon
Non-amber stop codon
UAA
Unatural amino acid
(Nε-Boc-L-Lysine)
C-terminal His-tag
Myoglobin protein
EspC protein
A
TAG
SacI
ApaI
myo
– UAA
+ UAA
~18 kDa
Detected
See Fig. 5.9 A
B
espC
~55 kDa
~10 kDa
140 kDa
+
–
175kDa
80kDa
58kDa
46kDa
?

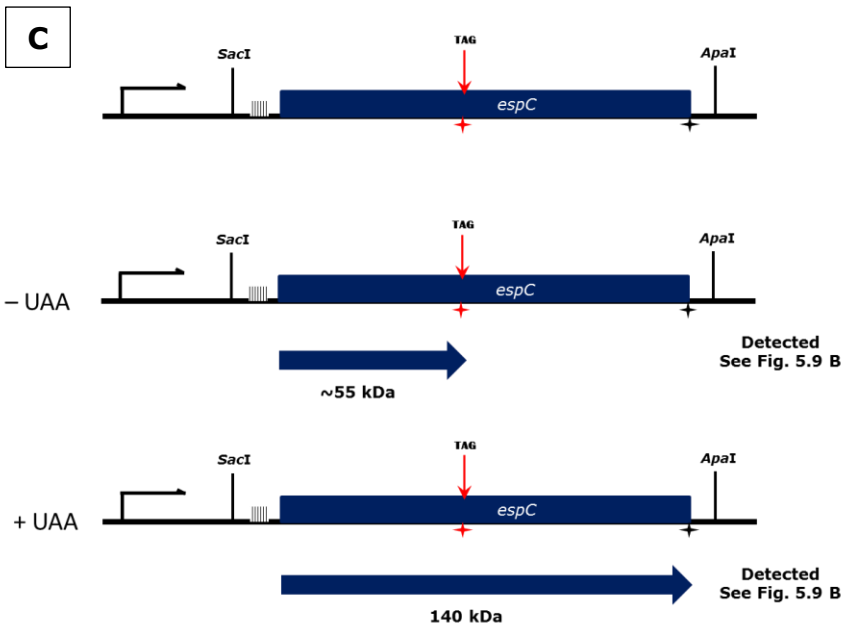


Figure 5.10: Schematic representation shows the predictive expression scenarios of *myo-espC* fusion containing amber codons upon N^{ε}-Boc-L-Lysine incorporation. (A) Detection the expression of the full length myoglobin protein by α-His-tag antisera in presence of N^{ε}-Boc-L-Lysine in the medium (for more details please see Fig. 5.9 A). **(B)** The upstream of *myo* was fused to *espC* containing its RBS and amber codon at position 4 (see text). In absence of UAA, only truncated ~55 kDa EspC is detected. This truncated protein was slightly changed upon adding the UAA (see the western blot immunoblotted using α-EspC antisera). It is not clear here which RBS is driving the translation of the transcript and why there is no product of full length EspC. To circumvent this issue, *myo* with its RBS was excised (data not shown) and generated the construct showing in **(C)**. After successful removing the remaining of *myo* gene region, it was possible to see the full length EspC incorporated with the UAA, N^{ε}-Boc-L-Lysine (Fig. 5.9 B).

incorporation of N^{ε}-Boc-L-Lysine, alternative possibilities for further study are required. For example, it may be possible to use the tools created in this chapter to examine the interaction of EspC with the T3SS during delivery to eukaryotic cells.

EspC may however be unstable when an UAA is incorporated, leading to very low levels of secreted EspC being detectable in an unreproducible manner. It is possible that the structural information used to plan the UAA insertion does not reflect the *in vivo* situation and the UAA was not inserted into an external loop (Fig. 5.1). If so, incorrectly folding may

occur and initiate degradation. Collectively, further investigation is required to test this notion. It would also be beneficial to use the original system designed by the Lemke labs (275) to incorporate TCOstar into EspC as this UAA may be accommodated by the EspC folding pathway more readily.

Chapter 6

The helical distribution of EspC is observed via the small tetracysteine tag technology, and shared by a different AT, AaaA

6.1 Introduction

Chapter 3 clearly showed that EspC fused to mCherry was secreted via a pathway involving a helical structure and/or polar localization. As the large molecular weight of mCherry ~28 kDa (~235 amino acids) could perturb EspC localization, folding and function (295,296), an alternative labelling technique was employed. The chosen bi-arsenical-tetracysteine system relies on the high affinity binding between a small fluorogenic molecule called fluorescein arsenical hairpin binder (FlAsH) and a considerably shorter, site-specific, genetically encoded peptide sequence comprising of two appropriately spaced cysteine pairs. This FlAsH-tag (or tetracysteine-tag (TC) motif) is Cys-Cys-Xaa-Xaa-Cys-Cys (CCXXCC), (where Xaa is not a cysteine residue) (297-299).

Several comprehensive studies have described applications for this labelling system in both eukaryotic and prokaryotic cells; for example, in protein localization studies (141,300-303), fluorescence resonance energy transfer (FRET) experiments for investigating protein conformational changes and protein-protein interactions (304), and in pulse chase analysis (305). It is thus a useful technology to track the dynamics, activity and interactions of molecules inside living cells. The system has a range of advantages listed in table 6.1. Despite all these obvious merits, there are some limitations that need to be considered (table 6.1).

Advantages	Reference	Disadvantages	Reference
The freedom to place the TC motif at a specific site in the target protein.	(306,307)	Poor specificity due to high levels of background staining.	(308,309)
Incorporation of only 6 amino acids (TC-Tag) rather than ~235 amino acids (mCherry) that are less likely to perturb the native structure or activity of the protein of interest.	(298)	Toxicity as a result of the non-specific binding to endogenous cysteine pairs.	(308,309)
FlAsH or ReAsH are available precomplexed to 1,2-ethanedithiol (EDT) which allows membrane permeability, and thus labelling in living cells as well as reducing the non-specific binding of arsenic atoms to endogenous thiols and providing reagent solubility and stability.	(298,310)	The potential effect of TC motif insertion on the protein structure or function.	(309)
Using the optimised TC motif sequence comprising Cys-Cys-Pro-Gly-Cys-Cys (CCPGCC) offers enhanced stability as well as improved affinity for and fast binding to biarsenic compounds.	(306)		
A colour variant with different spectral property is available to be used as an alternative: the resorufin arsenical hairpin binder (ReAsH).	(306,311)		
Brighter labelling can be obtained by introducing multiple biarsenical binding sites into the recombinant protein.	(298)		

Table 6.1: The advantages and disadvantages of FlAsH-tag technology.

Both FlAsH and ReAsH fluorophores are modified to have two arsenic atoms appropriately spaced to match the distance between the two cysteine pairs in the TC motif sequence, and are supplied pre-complexed with two EDT molecules as non-fluorescent FlAsH-EDT_2 and ReAsH-EDT_2 reagents (297,306). The technique is based on the high affinity

interaction of arsenic for thiols. During staining, these membrane permeable reagents bind to the TC-tag in the recombinant protein via formation of four covalent bonds. The covalent bonds are formed between the two arsenic groups in the reagent and pairs of thiols within the TC-tag. Consequently, the reagents become highly fluorescent due to displacement of EDT and emit green in the case of FlAsH or red (ReAsH) light when excited at wavelengths 508 nm and 593 nm respectively (297,309).

This chapter demonstrates the benefit of using this approach in studying the localization of EspC. Here we show that TC-tagged EspC is organized into a helical pattern very similar to that previously observed when it was labelled by mCherry. Likewise, the bacterial cytoskeleton component MreB labelled with FlAsH was detected in a similar pattern. Importantly, another AT with a different function secreted from a different microbe (AaaA, derived from *P. aeruginosa*) was also observed to follow a similar helical localization on secretion when tagged with TC. This suggests a common underlying mechanism for protein secretion of all ATs from Gram-negative bacteria. Interestingly, TC tagging of AaaA without its β-barrel domain had a different localization pattern to AaaA that was slightly perplexing but demonstrated the importance of the entire molecule for competent secretion which remains mysterious.

High resolution 3D images of TC fused ATs (EspC and AaaA) were generated using SR-SIM which show for the first time that both EspC and AaaA ATs are distributed in a dynamic helical structure.

6.2 Results

6.2.1 Labelling MreB and EspC with membrane-permeable FlAsH-EDT_2

Green emitting FlAsH-EDT_2 substrate was chosen for this study rather than the red variant ReAsH-EDT_2 because (i) it has been used widely especially in protein localization studies (141,302,303,312), (ii) it provides a different colour variant with different spectrum compared to mCherry (297), (iii) FlAsh-EDT_2 is less expensive than ReAsH-EDT_2. To deliver a successful interaction between FlAsH-EDT_2 and a biarsenical binding site, a TC motif was genetically engineered into permissive sites within MreB and EspC predicted to be distant from their active sites and externally exposed, and thus easily accessible by the FlAsH dye without affecting the function of the target protein.

6.2.1.1 The TC-tag (CCPGCC) was incorporated into MreB and EspC efficiently

Using a TC-tag containing the two cysteine pairs in close proximity to internal Pro and Gly residues provides enhanced stability to the CCPGCC-FlAsH complex compared with the use of other amino acids acting as spacing residues (306). This enhanced affinity was mainly due to the tendency of the CPGC segment to adopt a hairpin turn confirmation which provides a favourable site for dye binding (306,307,313). Consequently, this unique motif was selected for this work. The CCPGCC motif was successfully created in MreB by insertion of two cysteine residues before and after residues Pro-227–Gly228 using

SDM (primer pair F-MreB CCXXCC/R-MreB CCXXCC listed in the table 2.4, chapter 2). The sequence Cys-Cys-Pro-Gly-Cys-Cys is predicted to be externally exposed at the same position that was previously used to insert mCherry and successfully generate a fluorescent recombinant protein (Fig. 4.2).

Whilst addition of CCPGCC tag to MreB was uncomplicated, for EspC it was slightly more challenging. The positions to insert TC-tag into EspC were previously elucidated in chapter 5 (Fig. 5.1). Initially, the only non-optimal sequence (CCGKCC) was incorporated into EspC nearby to amino acid position 951. This was accomplished by introducing a pair of cysteine residues before and after residues Gly-897–Lys-898 (Fig. 6.1) using primer pair F-EspC CCXXCC/R-EspC CCXXCC (see table 2.4, chapter 2). However, it was not possible to insert the optimal CCPGCC sequence at this site. To generate EspC with the optimal CCPGCC sequence, several optimisation steps were undertaken to troubleshoot the amplification reaction such as addition of DMSO alongside changing the concentration of primer or template. Subsequently, an CCPGCC insertion was achieved in EspC by encoding the whole motif sequence between Gln-530 and Phe-531 residues using primer pair F-EspC CCPGCC/R-EspC CCPGCC (see table 2.4, chapter 2). Ultimately, the optimal sequence Cys-Cys-Pro-Gly-Cys-Cys was introduced at amino acid position 531 that was previously used to incorporate an UAA (Fig. 5.1). All introduced mutations were verified by DNA sequencing. In addition, immunoblotting confirmed the production of the 140 kDa TC-tagged EspC (data not shown).

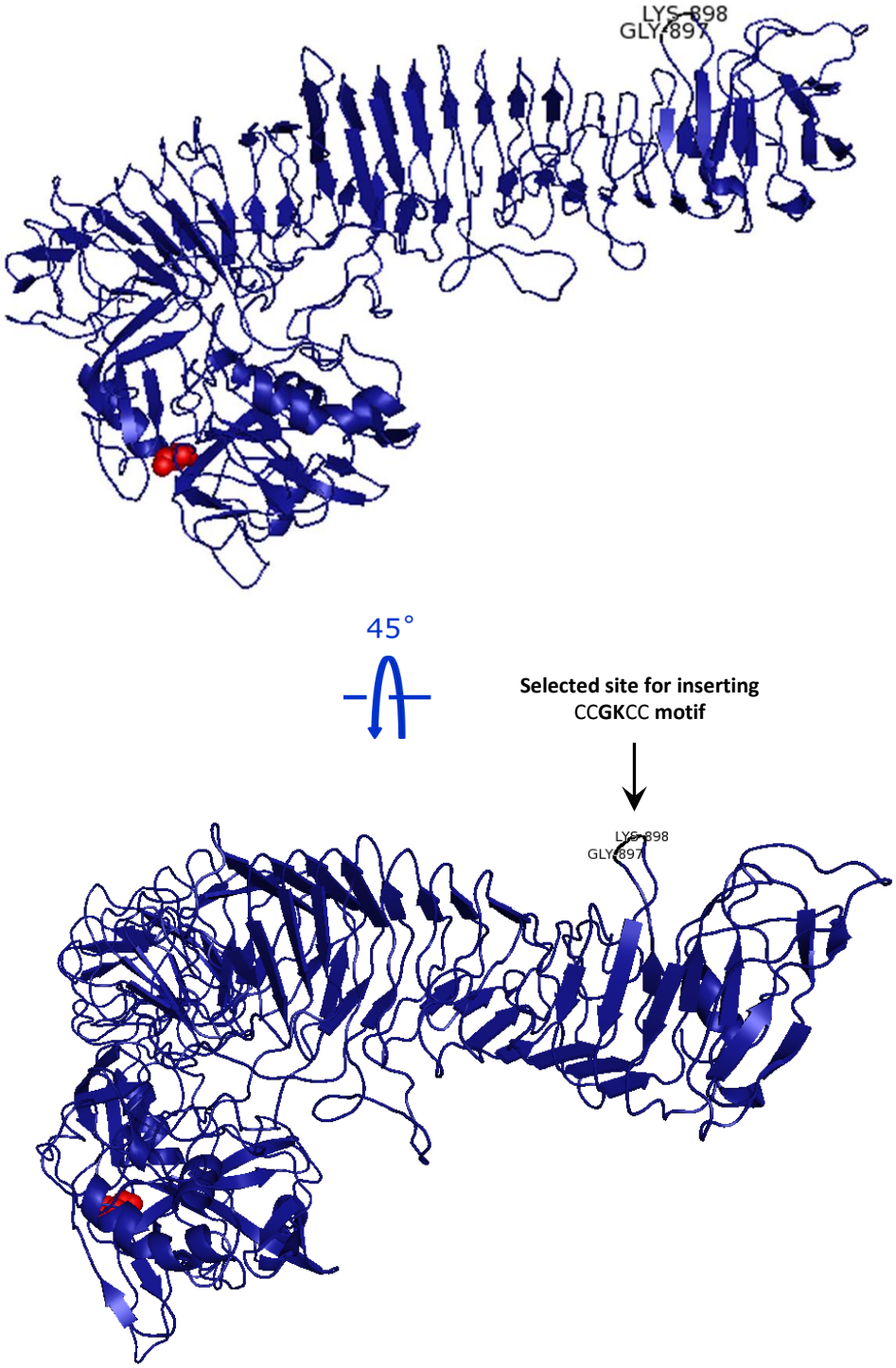


Figure 6.1: The position selected for CCGKCC motif insertion on the predicted native EspC passenger domain structure. The 3D model of EspC passenger domain developed in PyMol Zalman software showing the location of residues on external loops selected for creating the CCGKCC motif. See text for more information. The important catalytic serine residue at position 256 hosted in motif GD**S**GS is highlighted in red.

6.2.1.2 EspC is distributed in a spiral, patchy structure seen encircling cells in super-resolution microscope

In order to detect the TC-tagged proteins and reveal their localization, it was necessary first to design a FlAsH-EDT_2 labelling protocol suitable for our experiment. Based on the information provided in the Tetracysteine Tag Detection Kit, a standard protocol was written and described in chapter 2. To establish an optimally efficient FlAsH-EDT_2 staining protocol, several optimisation steps were performed to improve the signal over the noise of the fluorescence background. Initially, overnight MG1655 cells hosting the empty vector pBAD33 (control), pLA33mreB (control), and pLA33mreB-TC were diluted 1:100 in LB containing Cm and concurrently induced with 0.02% arabinose for 2 h. Subsequently, cells were collected and stained with 1 µM to 2 µM final FlAsH-EDT_2 diluted in phosphate-buffered saline (PBS) and incubated for 15 to 20 min in darkness at room temperature. To minimise any interference by non-specific background staining, cells were washed twice with British Anti-Lewisite (BAL) wash buffer as recommended by the manufacturer.

Despite the poor signal quality in all MG1655 strains, it was possible to detect the spiral patchy localization pattern of MreB in single cells expressing MreB-TC using confocal microscopy (Fig. 6.2 C and D). The pattern was very similar to what had been previously observed when tagged with mCherry (Fig. 4.4 A). The weak fluorescence detected in the control samples was due to non-specific binding of FlAsH which quickly fades upon exposure to the blue laser (Fig. 6.2 A and B).

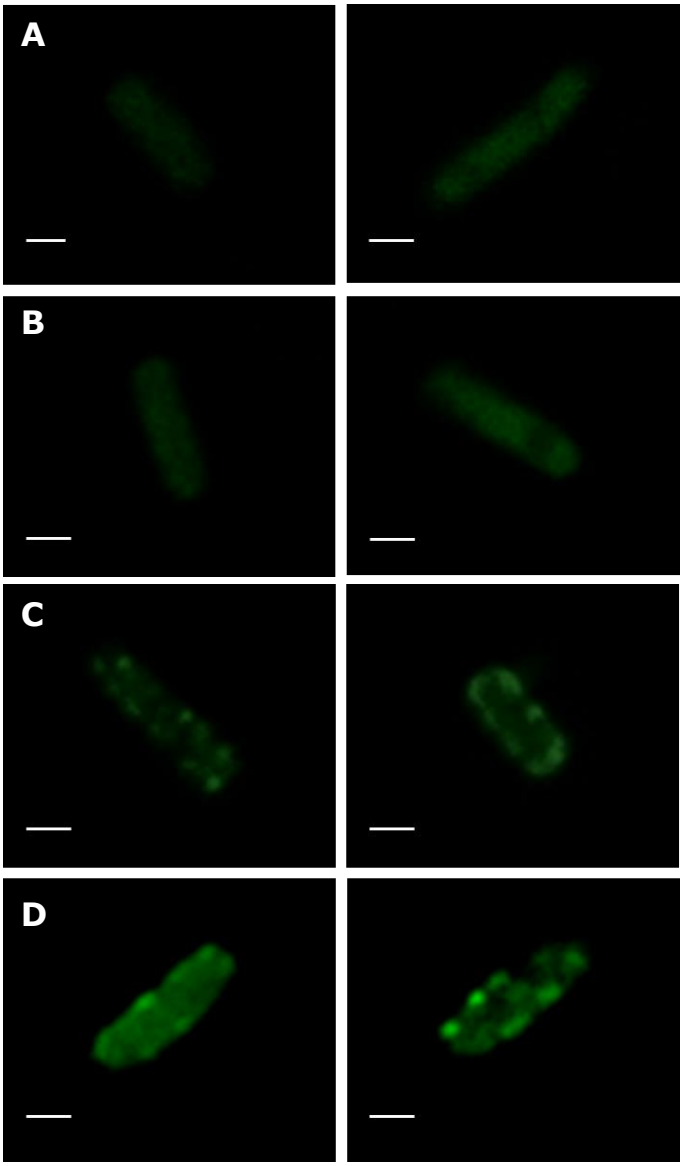


Figure 6.2: Detection of a helical patchy arrangement of TC-tagged MreB during FlAsH staining. Images of FlAsH labelled MG1655 (pBAD33) **(A)**, MG1655 (pLA33mreB) **(B)** and MG1655 (pLA33mreB-TC) **(C** and **D)** induced with 0.02% arabinose for 2 h and prepared for staining as described in the text (for more details see chapter 2). Scale bars represent 1 μm.

To improve the signal quality, the labelling experiment was repeated under the following conditions; (i) the concentration of FlAsH labelling reagent was increased to 5 μM, (ii) the stain incubation period was increased to 45 min, (iii) ultra-pure HEPES buffered saline was used as the labelling medium, (iv) an extra final washing step using HEPES buffer was added to reduce background staining, (v) the recombinant protein was produced for a longer period of time.

Under these modified conditions, an improvement of the fluorescent signal with lower background staining was achieved. FlAsH staining of strain MG1655 (pLA33mreB-TC) producing TC-tagged MreB induced for 2.5 h clearly appears helically arranged in patches which are very bright compared to the control sample producing MreB lacking the TC-tag (Fig. 6.3 A). Likewise, the spiral localization of 4 h induced EspC-TC was readily apparent compared with controls (Fig. 6.3 B and C). Consistent with previous findings, the brightness of the FlAsH-EspC-TC complex containing the optimal tetracysteine sequence CCPGCC (Fig. 6.3 B) is greater than that generated by the non-optimal motif, CCGKCC (Fig. 6.3 C) (306). Importantly, only diffusely distributed fluorescence was detected in all control samples (Fig. 6.3). To improve microscopic resolution and hence interpretation of protein localization, individual FlAsH stained cells producing TC tagged proteins were imaged by confocal microscopy (Fig. 6.4 A, B, and C). As it was difficult to image the MG1655 cells producing EspC tagged via the non-optimal motif due to the poor FlAsH signal quality, EspC tagged with the CCGKCC motif was excluded from any further study.

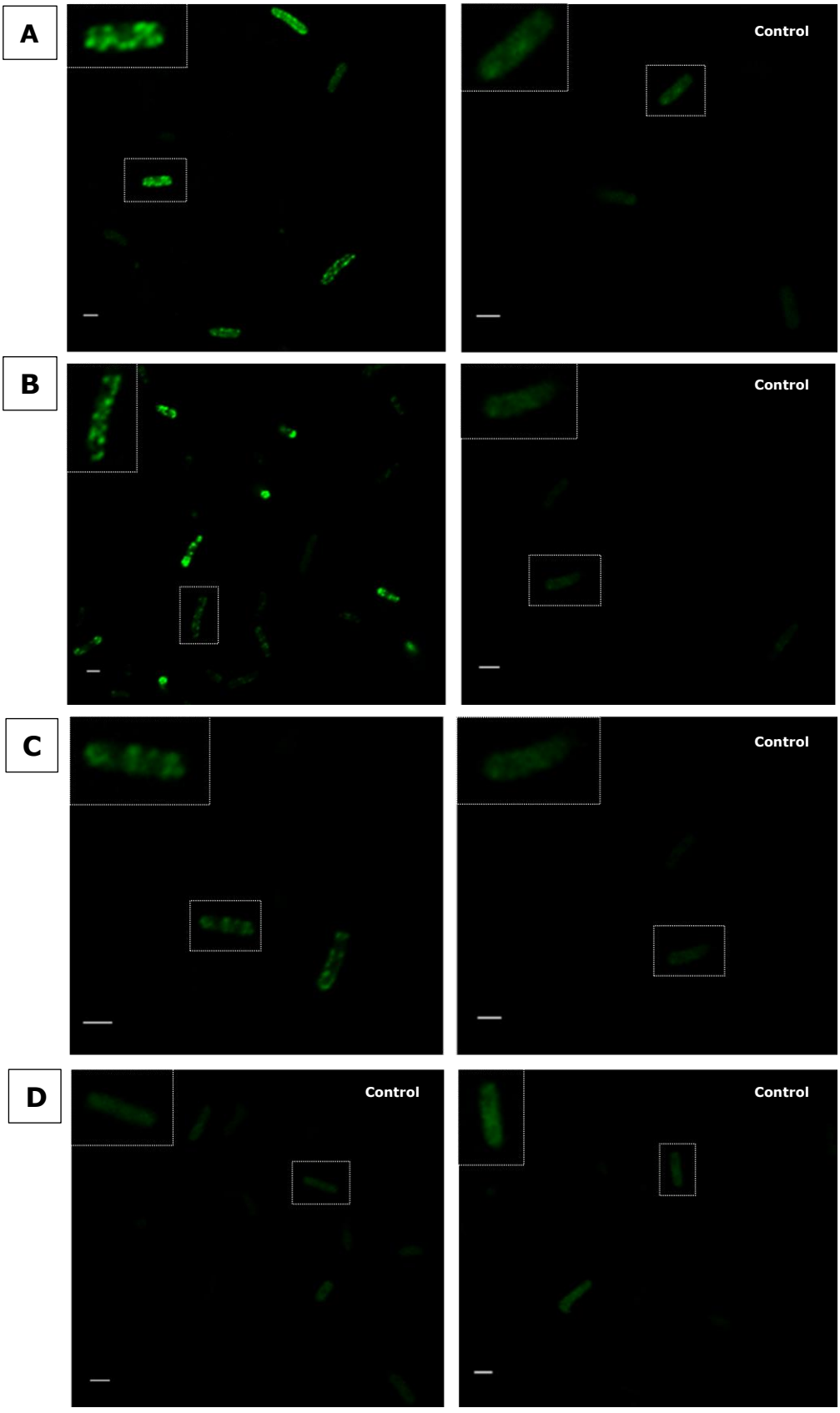


Figure 6.3: Detection of bright spiral localization signals of FlAsH-tagged MreB and EspC hosting the optimal TC motif (CCPGCC). Images of FlAsH labelled MG1655 (pLA33mreB-TC) with the control MG1655 (pLA33mreB) **(A),** MG1655 (pLA33C1-TC^{CCPGCC}) with the control MG1655 (pLA33C1) **(B)** MG1655 (pLA33C1-TC^{CCGKCC}) with the control MG1655 (pLA33C1) **(C)** and the controls MG1655 wt **(D *left* panel)** and MG1655 (pBAD33) **(D *right* panel)**. Protein overproduction and sample preparation as described in the text. Scale bars indicate 1 µm.

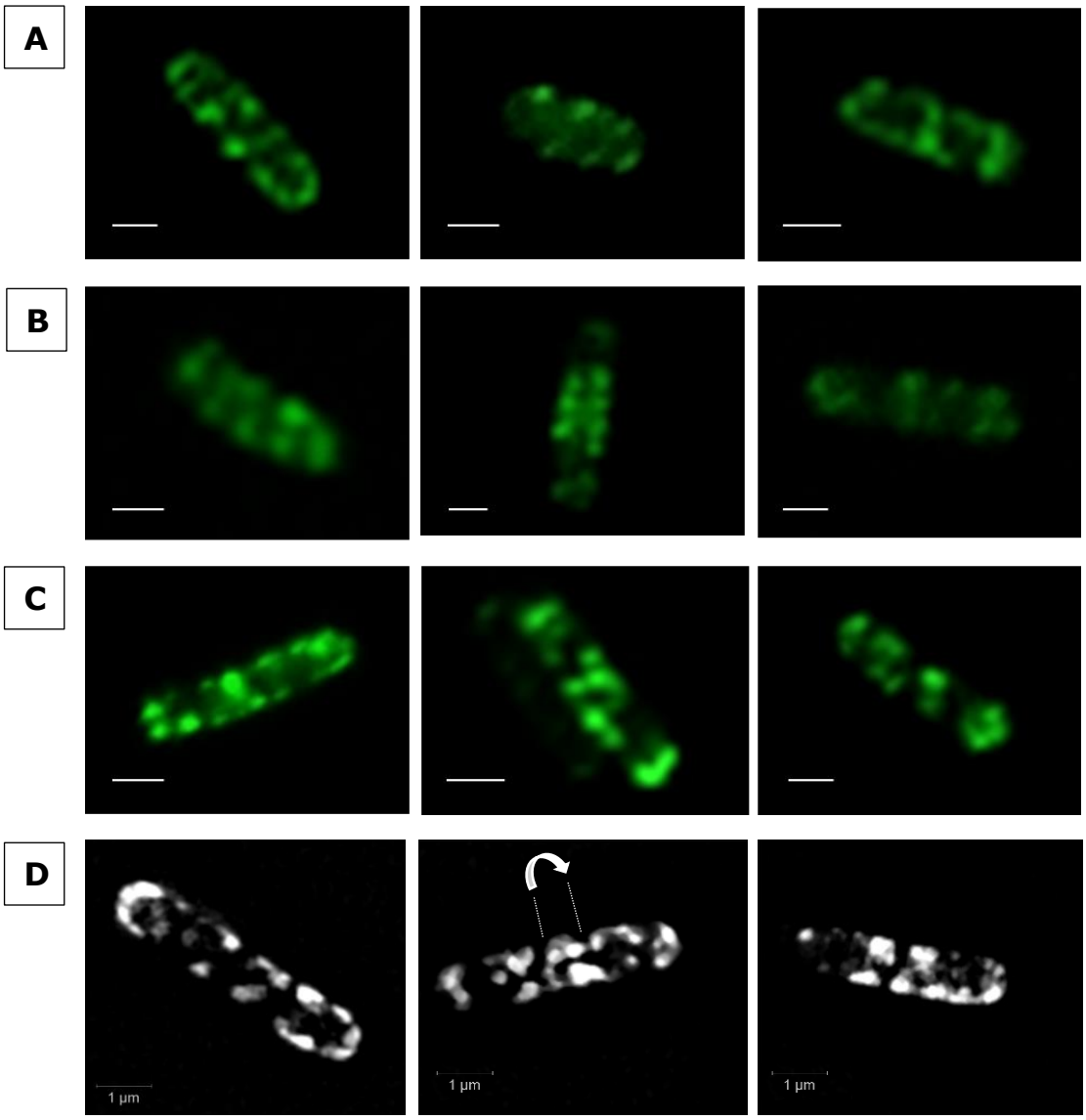


Figure 6.4: EspC forms a spiral structure resembling the bacterial cytoskeleton actin homologue MreB. MG1655 producing MreB-TC **(A)**, EspC-TC^{CCGKCC} **(B)** and EspC-TC^{CCPGCC} **(C** and **D)** were prepared for FlAsH staining as described in text (for more details see chapter 2). Images in **panel A**, **B** and **C** were taken by confocal microscopy while the images in **panel D** were imaged by SR-SIM. The arrow in the middle picture in panel D mirrors the diagonal moves of EspC around the bacterial cell circumference. Scale bars indicate 1 µm.

To investigate the helical distribution of EspC using advanced microscopy techniques, SR-SIM was exploited for imaging FlAsH tagged EspC-TC^{CCPGCC} within a live cell. Interestingly, a precise 3D helix arrangement was formulated from patches of protein encircling the cell wall of the bacterium (Fig. 6.4 D). Construction of 3D rendering of structured illumination images allowed a panoramic inspection inside the bacterium during EspC secretion (Fig. 6.5). A striking spiral distribution of EspC molecules was evident on the boundary of the membranes or within the periplasm. Patches of fluorescence were clearly apparent around the cell membranes, stretching along the bacterial cytoskeleton from pole to pole (Fig. 6.5). Most notably the lack of the FlAsH labelled EspC within the bacterial cytoplasm highlighted the distinct possibility that the bacterial cytoskeleton could be driving some kind of localization during AT secretion.

To support the hypothesis that the spiral localization of EspC is MreB dependent, the protein patches of EspC and MreB were examined using two independent fluorescent labelling techniques (mCherry and FlAsH tag). Moreover, visualization by different super resolution techniques, SIM and direct stochastic optical reconstruction microscopy (dSTORM) were performed. Although co-localization of EspC-mCherry with FlAsH tagged MreB-TC could not be studied in the same cell, the patchy structural patterns seem to have a similar distribution (Fig. 6.6).

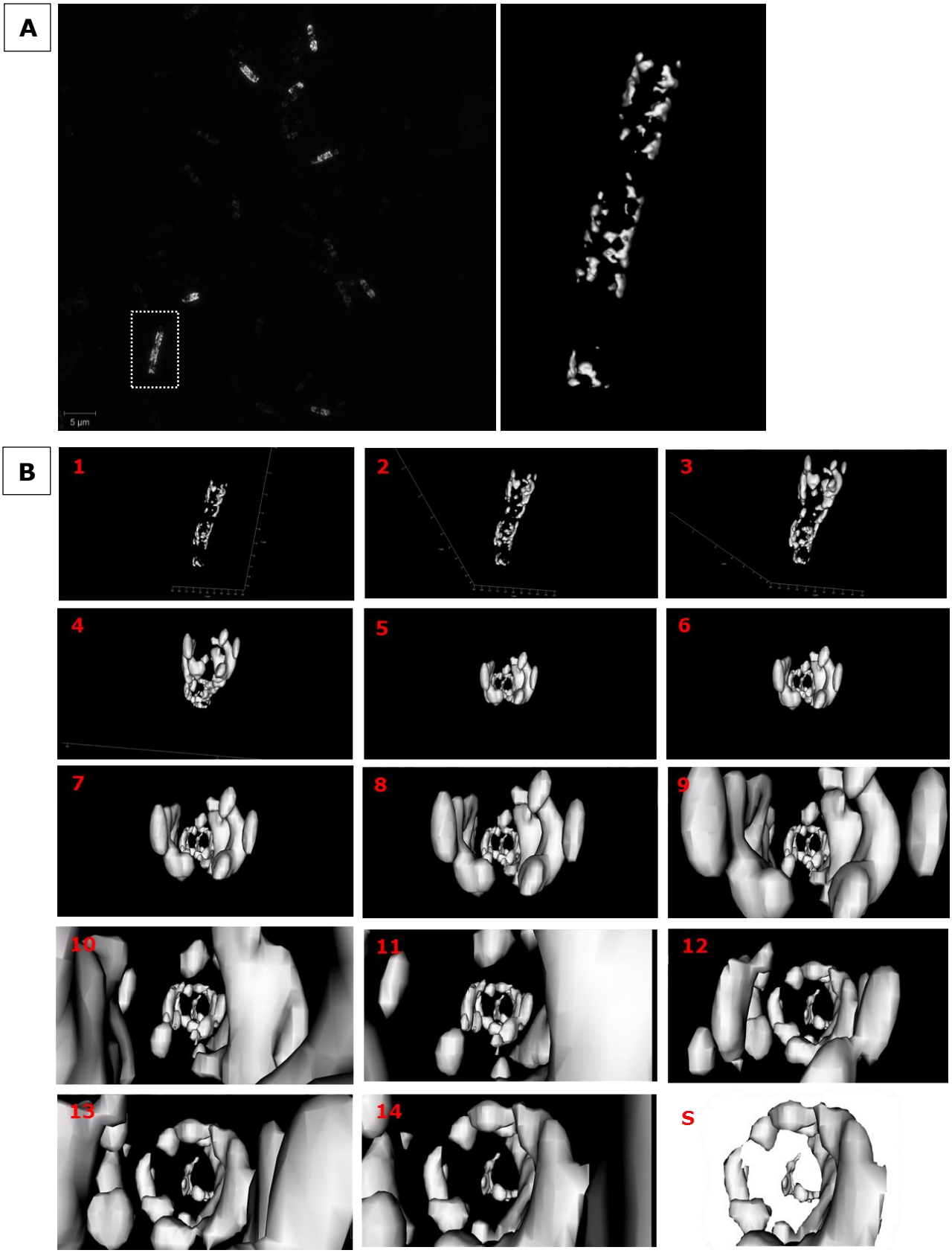


Figure 6.5: 3D rendering of structured illumination images reveal the spiral localization of FlAsH labelled TC-tagged EspC inside the living bacterium. FlAsH staining of MG1655 (pLA33C1-TC) induced by 0.02% arabinose for 4 h and prepared for SR-SIM imaging as described in chapter 2. An elongated cell was selected from the population **(A)** to illustrate the pattern of EspC localization. A 3D animation movie was created, and individual frames from 1-14 are shown here **(B)**. The bacterium was tilted and rotated virtually to reveal the spiral structure. The patchy helix without the black background is indicated **(S)**.

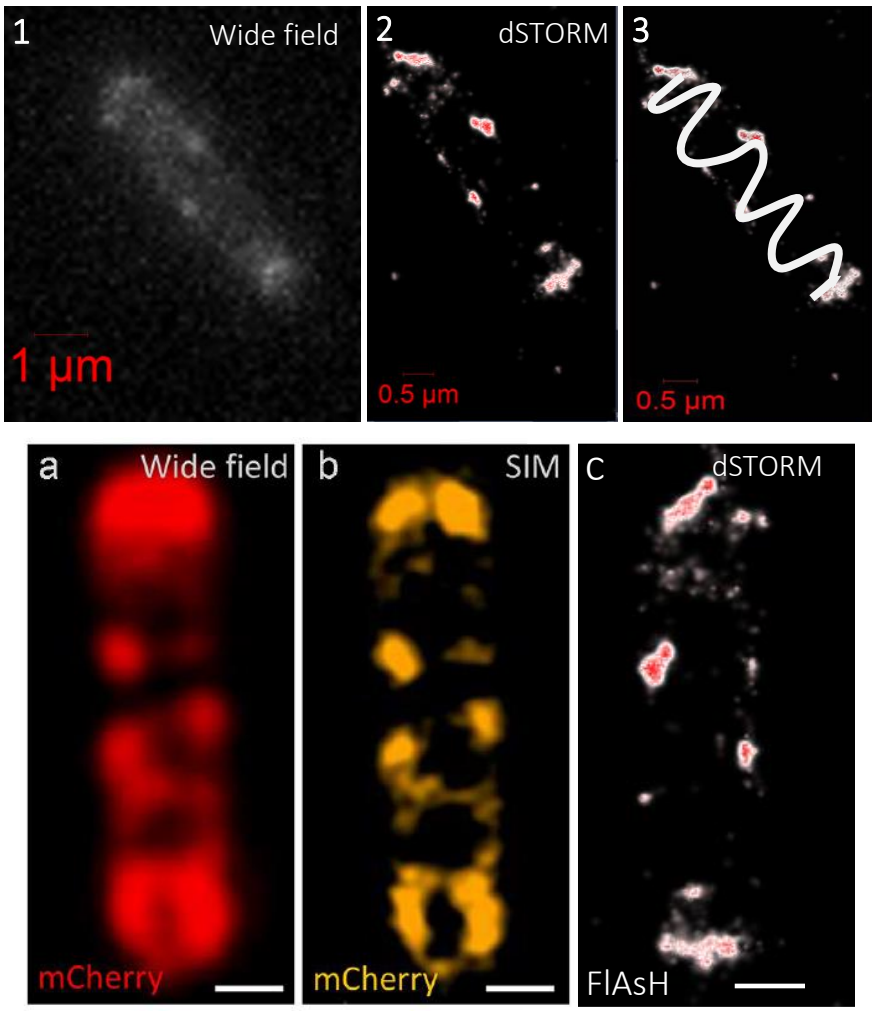


Figure 6.6: High precision dSTORM image of FlAsH-tagged MreB reveals similar patchy distribution to EspC-mCherry fusion in MG1655. Super resolution images of FlAsH labelled MG1655 cell producing TC-tagged MreB via 0.02% arabinose induction for 2-3 h **(1, 2, 3** and **c)**. dSTORM image shows the precise details of MreB localization at bacterial cell wall (the centroids of the localized molecules in red pixels and the actual localization of molecules in white clusters) which appears as a patchy distribution along the cell membranes **(2** and **c).** Connecting the localized patches from pole to pole created a drawing of a spiral structure **(3).** Scale bars in bottom row represent 0.5 µm.

6.2.2 The spiral localization of EspC is shared by the AT AaaA

Since EspC produces a spiral-like structure when it was tagged with two different fluorescent labels, it was predicted that the helical localization pattern might also be conserved in a different AT protein and possibly represent a common underlying mechanism in rod-shaped Gram-negative bacteria. To test this, the surface exposed AaaA AT secreted from *P. aeruginosa* was selected and its localization compared with that of EspC. In order to monitor its secretion, AaaA was first cloned into pBAD33. The optimal CCPGCC sequence was then inserted by SDM.

6.2.2.1 Cloning strategy used to insert *aaaA* into pBAD33 vector

The strategy employed to transfer *aaaA* gene from pET21a+::*aaaA* (created by Esteban Paredes-Osses) to pBAD33 is indicated in Fig. 6.7 (314). Simply, pET21a+::*aaaA* was digested with *Sal*I and *Bgl*II enzymes to release a product of 2065 bp that contained *aaaA* (Fig. 6.7 A). In order to ligate the purified *aaaA* into pBAD33 vector, the construct pLA33C1 containing an extra *Bgl*II restriction site that was previously inserted by SDM during construction of pLA33mCherry and pLA33mreB (Figs. 3.4 and 4.1 B respectively) was used. Digestion of pLA33C1$_{BglII}$ with *Sal*I and *Bgl*II liberated *espC* from pLA33C1$_{BglII}$ and yielded a linearized open *Bgl*II/*Sal*I pBAD33 backbone (Fig. 6.7 B). Following successful ligation, the resultant construct was transformed into MG1655 competent cells (Fig. 6.7 C).

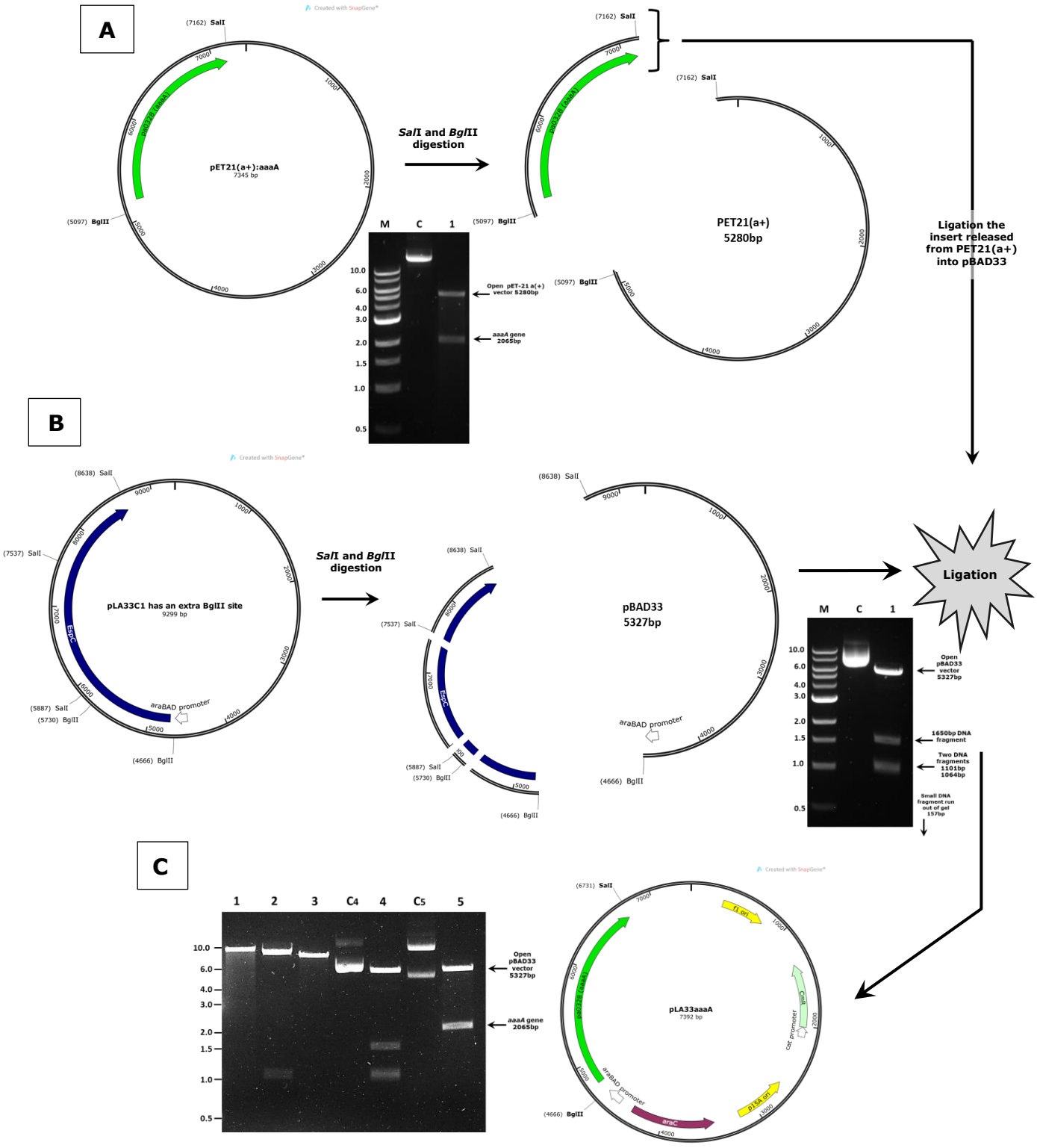


Figure 6.7: Cloning strategy adopted for construction of pLA33aaaA. Digestion of pET21(a+)::aaaA with *Bgl*II and *Sal*I enzymes was performed to release a 2065 bp DNA fragment containing the *aaaA* gene (agarose gel in **(A)**; M, C and 1 showing the 1 kb DNA ladder, the control plasmid DNA and the plasmid digestion with *Bgl*II and *Sal*I respectively). The *aaaA* DNA fragment was ligated into 5327 bp open pBAD33 vector which was digested with the same enzymes (agarose gel in **(B)**; M, C and 1 indicating the 1 kb DNA ladder, the control pLA33C1$_{BglII}$ plasmid DNA and the pLA33C1$_{BglII}$ digestion with *Bgl*II and *Sal*I respectively). The confirmation of the new construct (pLA33aaaA) was achieved by DNA sequencing or as shown in **(C)** via digestion with the same restriction enzymes; 1, 2, and 3 showing single *Bgl*II digestion of pLA33C1 (used here as a control), pLA33C1$_{BglII}$ and pLA33aaaA plasmids respectively (note that a fragment of ~1064 bp represents the upstream portion of *espC* released in lane 2) whereas 4 and 5 represent a double *Bgl*II and *Sal*I digestion of pLA33C1$_{BglII}$ and pLA33aaaA plasmids respectively. C4 and C5 are control DNA plasmids. A double digestion with *Bgl*II and *Sal*I of pLA33aaaA confirms the release of *aaaA* gene (lane 5).

Plasmid DNA present in the resultant colonies were evaluated by single restriction digestion with *BglII* or double digestion with *SalI* and *Bgl*II for the existence of the expected DNA fragment (Fig. 6.7 C). DNA sequencing was performed to verify this. Confirmed plasmids were named pLA33aaaA.

6.2.2.2 AaaA forms patchy helices resembling the EspC AT, but appears very bright

The results obtained in section 6.2.1.2 indicated the usefulness of using the optimal TC (CCPGCC) tag in this study which provides a better signal to noise ratio compared with the CCGKCC motif sequence. It therefore would be appropriate to incorporate it into AaaA AT. Towards this end, the predicted structure of the AaaA passenger domain model was first created using I-TASSER server and then mapped in a 3D model using PyMol 3D Zalman software (Fig. 6.8). By looking at the predicted AaaA 3D structure, an ideal site that was externally presented and distant from the protein active sites was chosen for TC insertion (Fig. 6.8). In order to encode the CCPGCC motif sequence at the nominated place, SDM was performed using primers F-AaaA CCPXCC/R-AaaA CCPXCC (see table 2.4, chapter 2). These primers were designed to insert two cysteine residues plus a proline (CCP) before and two cysteine residues after the Gly residue at 292 position. Thus, the optimal CCPGCC tag was successfully introduced and confirmed by DNA sequencing.

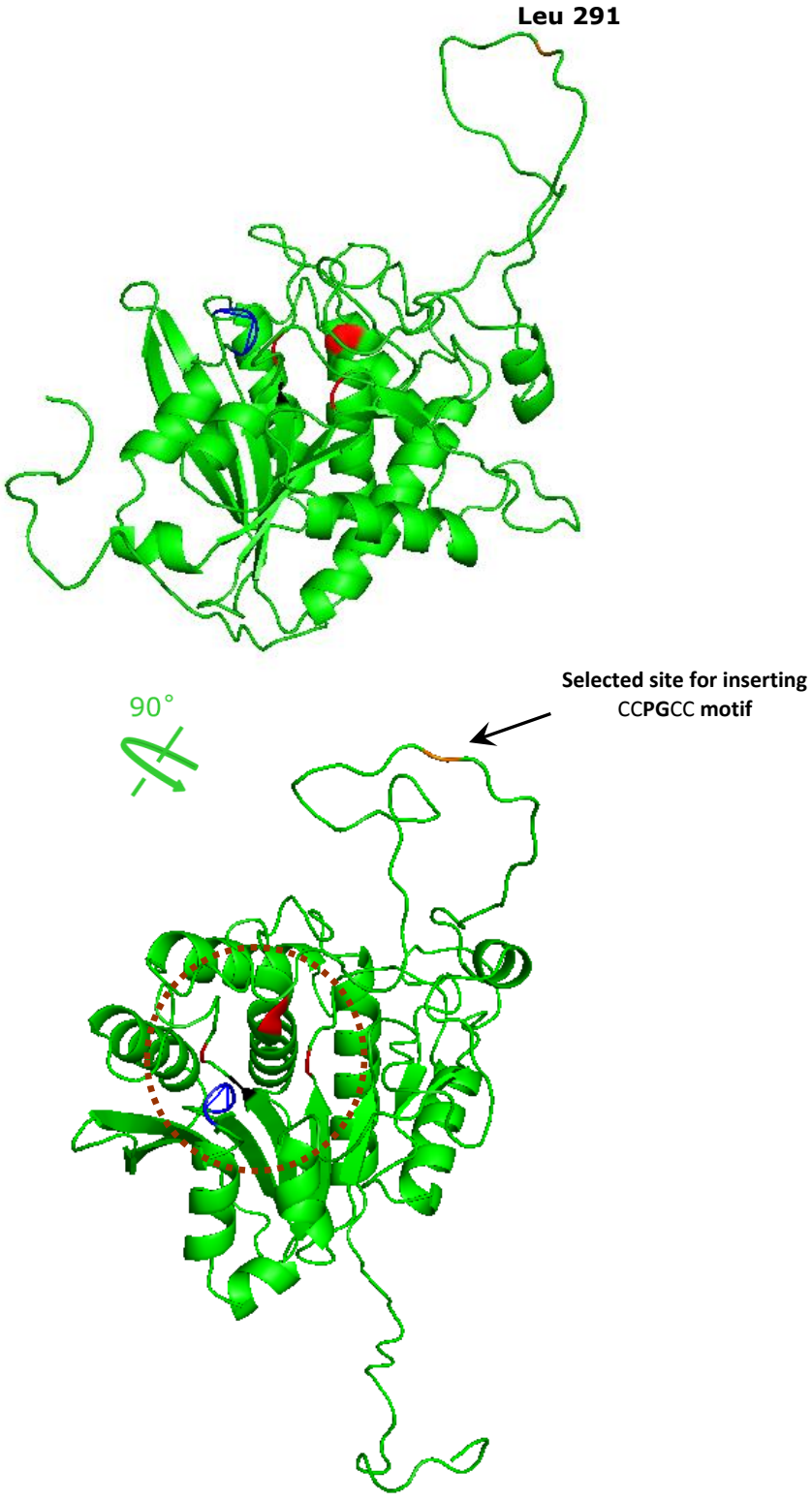


Figure 6.8: Position of the optimal TC-tag insertion on the AaaA passenger domain structure. The 3D model of AaaA developed in PyMol Zalman software showing the selected location on the external loop for inserting the CCPGCC sequence. TC-tag was inserted after Leu residue at position 291. The active site residues residing inside the AaaA binding pocket (Brown dotted circle) including His^{100} (Black), Asp^{102}, Asp^{115}, Asp^{176} (Red) and Glu^{147}, Glu^{148}, Glu^{148} (Blue) are highlighted.

In order to track the secretion of the AaaA, the intracellular FlAsH labelling procedure for TC-tagged AaaA was carried out according to the conditions described previously in section 6.2.1.2. Briefly, the overnight cultures of MG1655 hosting pLA33aaaA (control) and pLA33aaaA-TC were diluted 1:100 in LB containing Cm, grown to OD_{600} of 0.05 and induced with 0.02% arabinose for approximately 2.5 h. Subsequently, cells were collected and prepared for FlAsH staining following the protocol described in chapter 2. Remarkably, confocal fluorescence images revealed that FlAsH-tagged AaaA is localized in spirals orientating circumferentially around and along the long axis of the cell (Fig. 6.9 A). Moreover, unusually strong FlAsH signals were predominantly observed in the majority of cells with lower non-specific background binding of FlAsH (Fig. 6.9 A). Z-stack confocal images further supports the AaaA localization as a helical array (Fig. 6.10).

Unexpectedly, the control MG1655 sample producing the native AaaA without the TC-tag (control) also showed good fluorescence signals also adopting a patchy spiral distribution (Figs. 6.9 B and 6.11 A). To investigate this aberration, the amino acid sequence of the AaaA was analysed with SnapGene software. Interestingly, the sequence analysis revealed the existence of two consecutive cysteine amino acids (CC) at positions 232 and 233. It is possible that consecutive cysteines might be enough to lead to efficient binding to FlAsH-EDT_2, and thus generate a fluorescent state. Notably, producing AaaA (whether native or TC-tagged) for long time periods (over 2.5 h) caused the production of very elongated cells (Fig. 6.11 B).

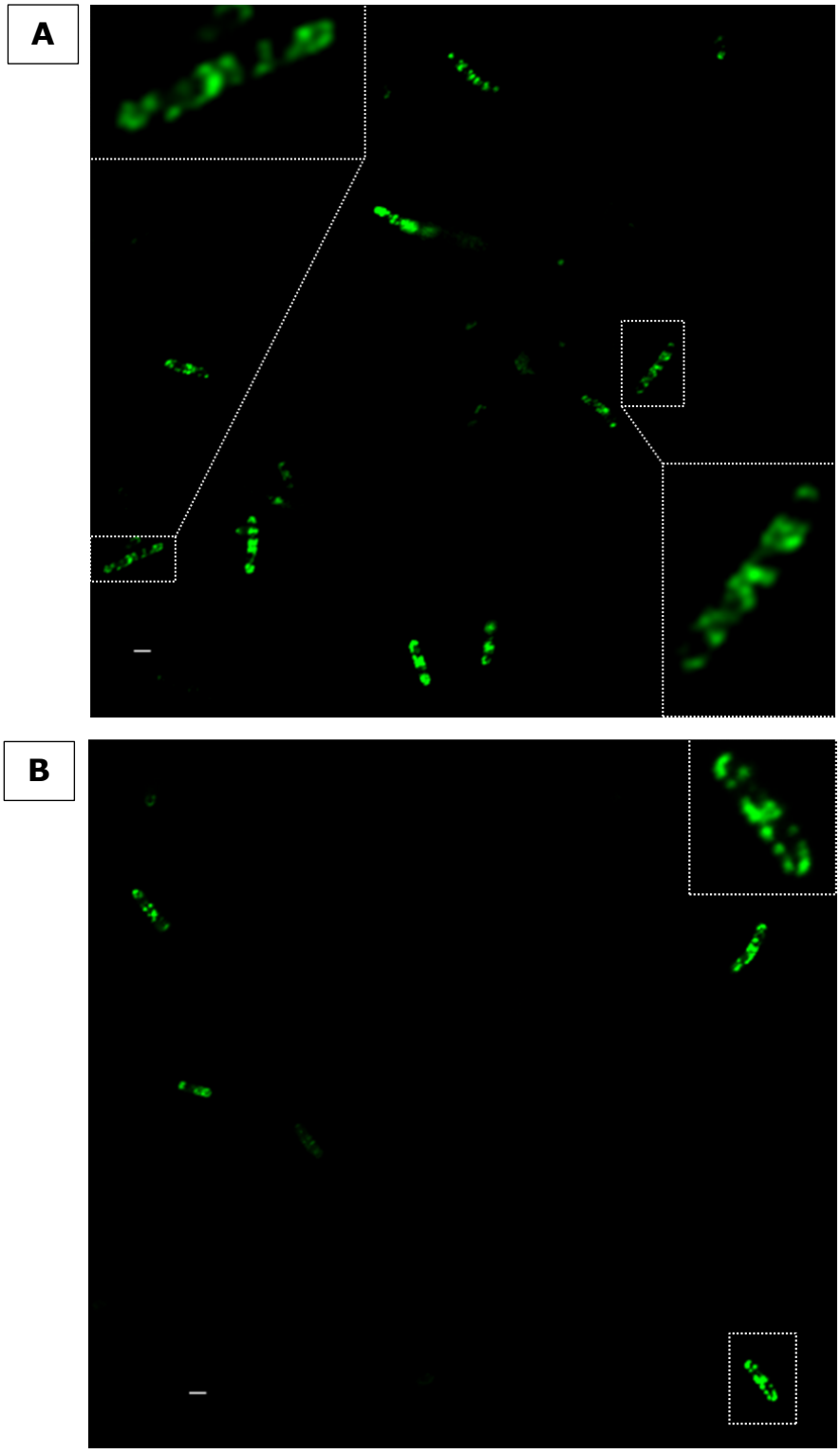


Figure 6.9: FlAsH-stained AaaA-TC AT adopts a bright helical patchy configuration. The overnight cultures of MG1655 hosting pLA33aaaA-TC **(A)** and pLA33aaaA (control) **(B)** were diluted 1:100 in LB containing 30 µg/mL Cm and grown until OD_{600} of 0.05. Then the cultures were induced by 0.02% arabinose for 2.5 h. Cells were prepared for FlAsH staining following the protocol described in chapter 2, and the conditions stated in the text. White rectangles indicate zoomed view of randomly selected cells to clarify the protein localization pattern. Scale bars indicate 2 µm.

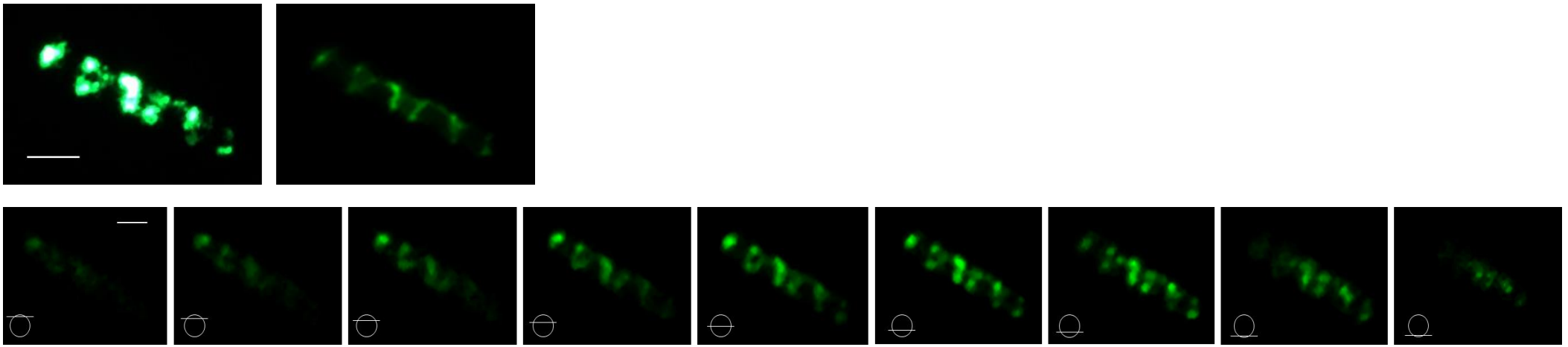


Figure 6.10: TC-tagged AaaA localizes as an extended helix in *E. coli*. The overnight cultures of MG1655 hosting pLA33aaaA-TC were diluted 1:100 in LB containing 30 µg/mL Cm and grown until OD_{600} of 0.05. Subsequently, the culture was induced by 0.02% arabinose for 2.5 h. Cells were prepared for FlAsH labelling following the protocol described in chapter 2 and the conditions stated in the text. The top two processed images demonstrate the the spiral arrangement as distinct patches of AaaA protein. The bottom row represents the individual unprocessed confocal images of a focal stack through a cell with an extended spiral fluorescence pattern. The diagrams show where the focal plane was in the cell for each image. Scale bar represents 1 µm.

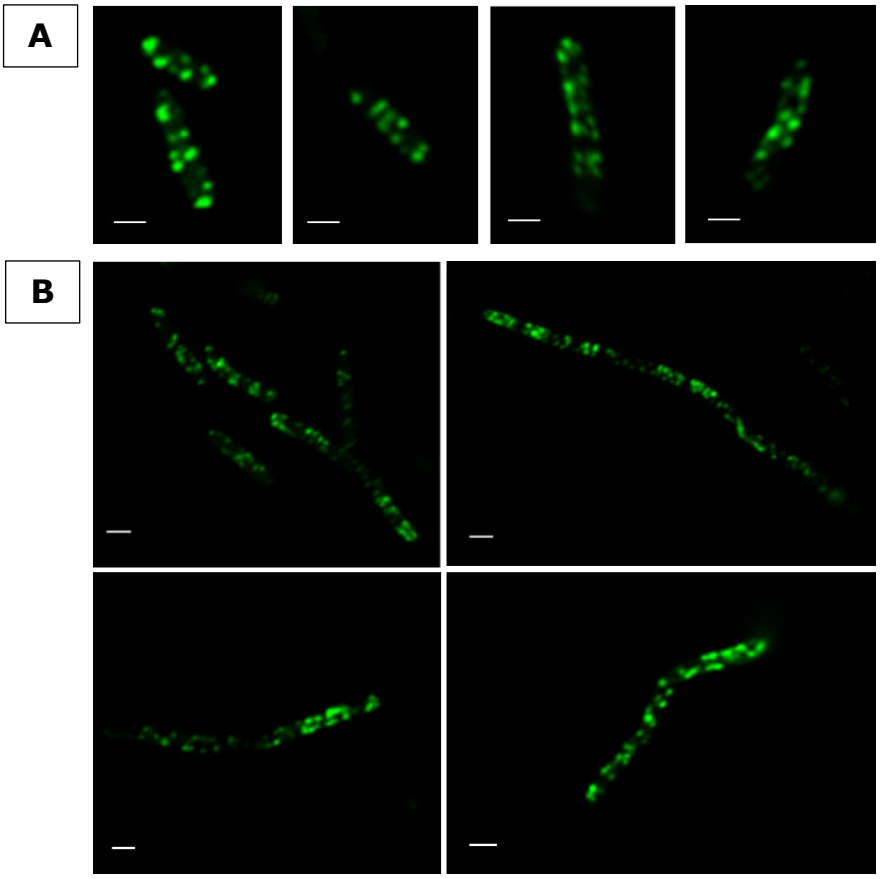


Figure 6.11: AaaA distributes in patches in elongated cells when expressed during extended times. The overnight cultures of MG1655 hosting pLA33aaaA (A and the bottom row of panel B) and pLA33aaaA-TC (top row of panel B) were diluted 1:100 in LB containing 30 µg/mL Cm and grown until OD_{600} of 0.05. Then the cultures were induced by 0.02% arabinose for 2.5 h **(A)** or over 3 h **(B)**. Cells were prepared for FlAsH staining following the protocol described in chapter 2 and the conditions stated in the text. Scale bar represents 1 µm.

6.2.2.3 Substitution of cysteine for serine at position 233 in AaaA abolished the fluorescent signal

It has been reported that FlAsH-EDT_2 reagent is able to bind non-specifically to endogenous cysteine pairs or cysteine-rich proteins (306,308). However, Adams *et al*., 2002 has provided a method to suppress this non-specific binding by including washing steps using BAL or EDT (306). FlAsH staining of arabinose induced MG1655 wt or MG1655 (pBAD33) did not show high levels of non-specific background labelling, so it is likely the background fluorescence evident in Fig. 6.9 is derived from AaaA. AaaA is not a cysteine-rich protein but it contains 3 cysteine residues, two of which are consecutively located at position 232 and 233 while the third one is at position 13.

Because of the brightly fluorescent cells obtained during FlAsH labelling of TC-tagged AaaA compared to EspC-TC^{CCPGCC} or MreB-TC, it was hypothesized that there might be binding of the reagent in two places within AaaA, at the inserted CCPGCC motif sequence and also at the two consecutive native cysteine residues (CC). To investigate this, SDM was performed with the native AaaA using primers F-AaaA C233S/R-AaaA C233S (listed in table 2.4, chapter 2) to replace the cysteine amino acid with serine at position 233. The resulting pLA33aaaA^{C233S} mutant was confirmed by DNA sequencing and subsequently transformed into MG1655 competent cells for FlAsH staining analysis. Interestingly, FlAsH staining of MG1655 expressing the mutant aaaA^{C233S} (induced by 0.02% arabinose for 2.5 h) showed undetectable fluorescent signals and only a weak diffuse fluorescent pattern was apparent in certain cells (Fig.

6.12), suggesting that the two consecutive cysteine residues were responsible for the strong fluorescence signal in the TC-tagged AaaA.

6.2.2.4 Super-resolution imaging of TC-tagged AaaA revealed the similarity of localization with EspC

Introducing the advanced microscopy techniques to biology gives the ability to directly visualize the dynamic processes of biomolecules inside of living cells (315). This has had a huge impact on understanding the molecular mechanisms involved in the secretion of virulence proteins (316). Here, SR-SIM has shown that secretion of EspC occurs in a helical arrangement stretched between bacterial poles and is localized to distinct patches (Fig. 6.5). In order to produce more precise details of the localization of AaaA and see if the localization pattern is shared with EspC, FlAsH-treated MG1655 cells expressing TC-tagged AaaA were imaged by SR-SIM. Interestingly, very similar patchy helices were observed during AaaA secretion (Fig. 6.13), suggesting that the spiral localization is conserved amongst ATs.

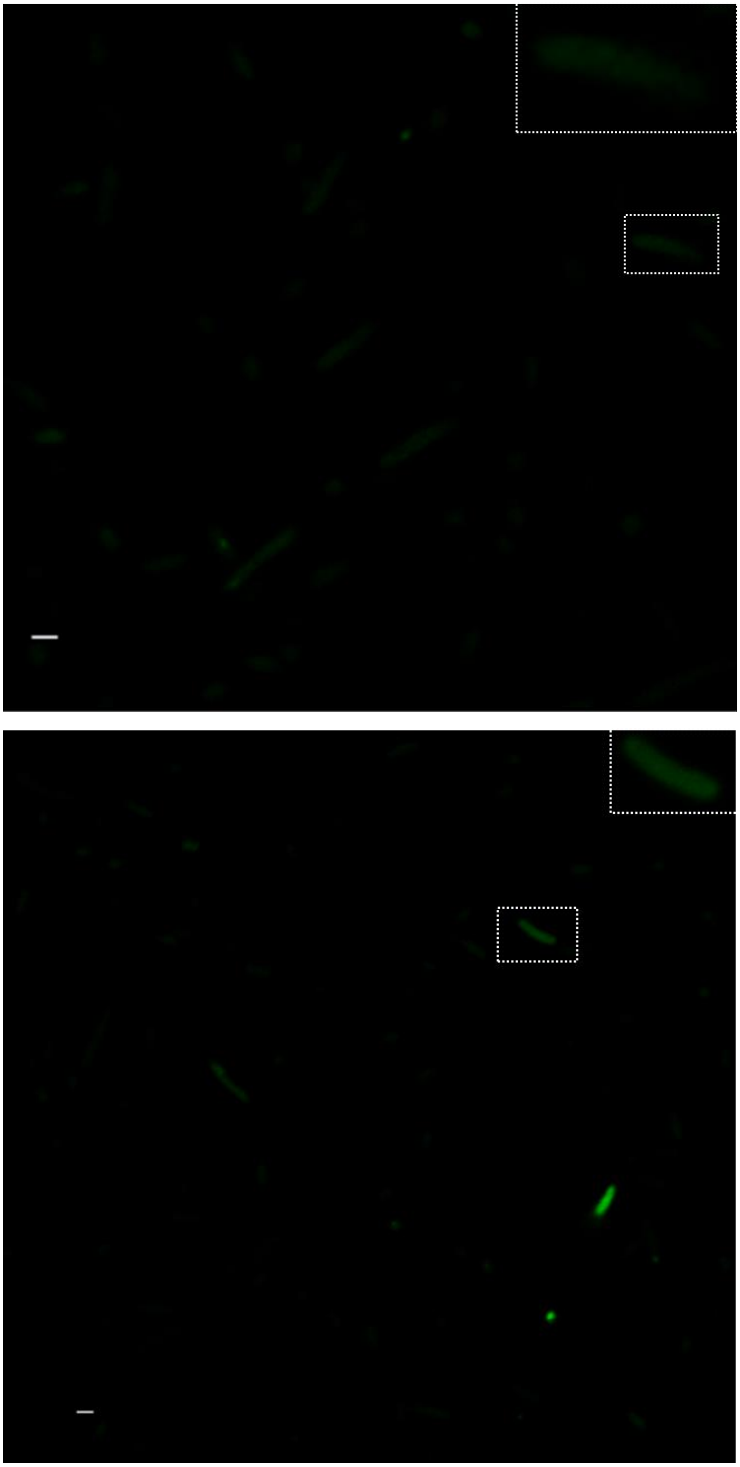


Figure 6.12: Replacement of the cysteine residue with serine at position 233 in AaaA leads to remarkable loss in background FlAsH signals. The overnight culture of MG1655 hosting pLA33aaaA^{C233S} was diluted 1:100 in LB containing 30 µg/mL Cm and grown until OD_{600} of 0.05. Then the culture was induced by 0.02% arabinose for 2.5 h. Cells were prepared for FlAsH staining following the protocol described in chapter 2 and the conditions stated in the text. Only weak diffuse fluorescence was detected. The laser gain was increased in these pictures to be able to capture some cells. White rectangles indicate zoomed view of randomly selected cells to clarify the protein localization pattern. Scale bars indicate 2 µm.

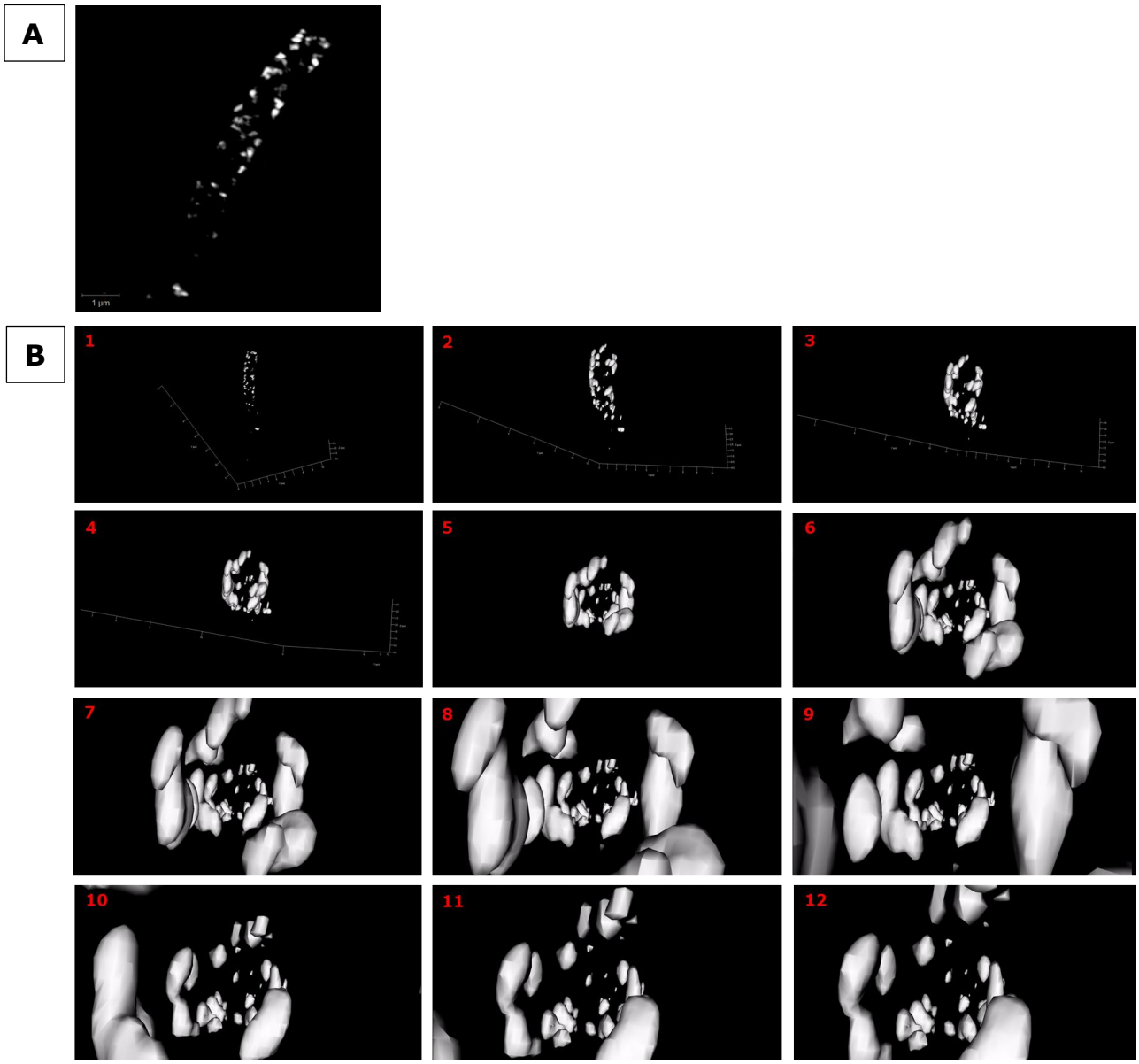


Figure 6.13: 3D rendering of structured illumination images reveal the spiral localization of FlAsH labelled AaaA-TC inside the living bacterium. The overnight culture of MG1655 hosting pLA33aaaA-TC was diluted 1:100 in LB containing 30 µg/mL Cm and grown until OD_{600} of 0.05. Subsequently, the culture was induced by 0.02% arabinose for 2.5 h. Cells were prepared for FlAsH staining following the protocol described in chapter 2 and the conditions described in the text. The elongated cell in picture **(A)** was chosen for analysis to illustrate a detailed arrangement pattern of AaaA localization. A 3D animation movie was created, and individual frames from 1-12 are shown here **(B)**. The bacterium was tilted and rotated virtually to reveal the spiral structure.

6.2.3 FlAsH labelling of TC-tagged AaaA lacking the β-barrel domain shows distinct localization

6.2.3.1 Generation of a truncated version of TC-tagged AaaA without the C-terminal β-barrel domain

From the results in chapter 3, the diffuse localization pattern of the truncated EspC-mCherry fusion indicated the importance of the β-barrel domain in the secretion of EspC. It was hypothesized that the AT β-barrel domain has a key role in targeting the protein towards the bacterial poles. To reach the poles, a helical path provided by the bacterial cytoskeleton MreB could be utilized to enable the AT to interact with the secretion pathway assistant, the OM located BAM complex. Therefore, removal of the AT β-barrel domain would cause protein mis-localization inside the periplasmic space, and thereby a different localization pattern would be observed.

Having constructed AaaA with a TC-tag, this hypothesis was tested again, but this time in AaaA by deleting the C-terminal β-barrel domain. SDM was performed using the mutagenic primers F-aaaATAG343/R-aaaATAG343 (see primer table, chapter 2) to insert an amber stop codon TAG at amino acid position 343 in the sequence of TC tagged AaaA which is equivalent to position 338 in the native AaaA sequence. The plasmid pLA33aaaA-TC was used as a template for the PCR reaction. The resultant construct called pLA33aaaA-TCΔ was transformed into MG1655 competent cells for FlAsH staining. DNA sequencing confirmed the successful insertion of TAG stop codon at position 343 and verified the absence of point mutations in *aaaA*.

Position 338 was chosen as the site of AaaA truncation because it had been previously made, resulting in overproduced and active AaaA (personal communication, Kim Hardie). This work was carried out in collaboration with an MSc student, Mathulah Sriskandarajah.

6.2.3.2 Truncated FlAsH-tagged AaaA without the β-barrel domain assumed a bulky spotty localization, and appeared to lack the helical organization

To examine the localization of TC-tagged AaaA lacking the β-barrel, an overnight culture of MG1655 (pLA33aaaA-TCΔ) was diluted 1:100 in LB containing 30 μg/mL Cm and left to grow at 37°C with shaking for approximately 1 h (0.05 OD_{600}). Following an induction step with 0.02% arabinose for 2.5 h, the cells were prepared for FlAsH staining as previously described. Interestingly, the localization of FlAsH stained truncated AaaA-TC exhibited a different fluorescence pattern. Confocal microscopy revealed that it localized in spots. However, these spots were very condensed and lacked the helical arrangement seen previously (Fig. 6.14). Optical sections of a cell expressing FlAsH labelled truncated AaaA-TC confirmed the absence of the spiral localization array (Fig. 6.15). Consistent with these findings, imaging this localization pattern from inside the bacterial cytoplasm via construction of a structured series of 3D rendered illumination images using SR-SIM, revealed that the bulky spotty distribution of truncated AaaA was completely devoid of any helical organization (Fig. 6.16).

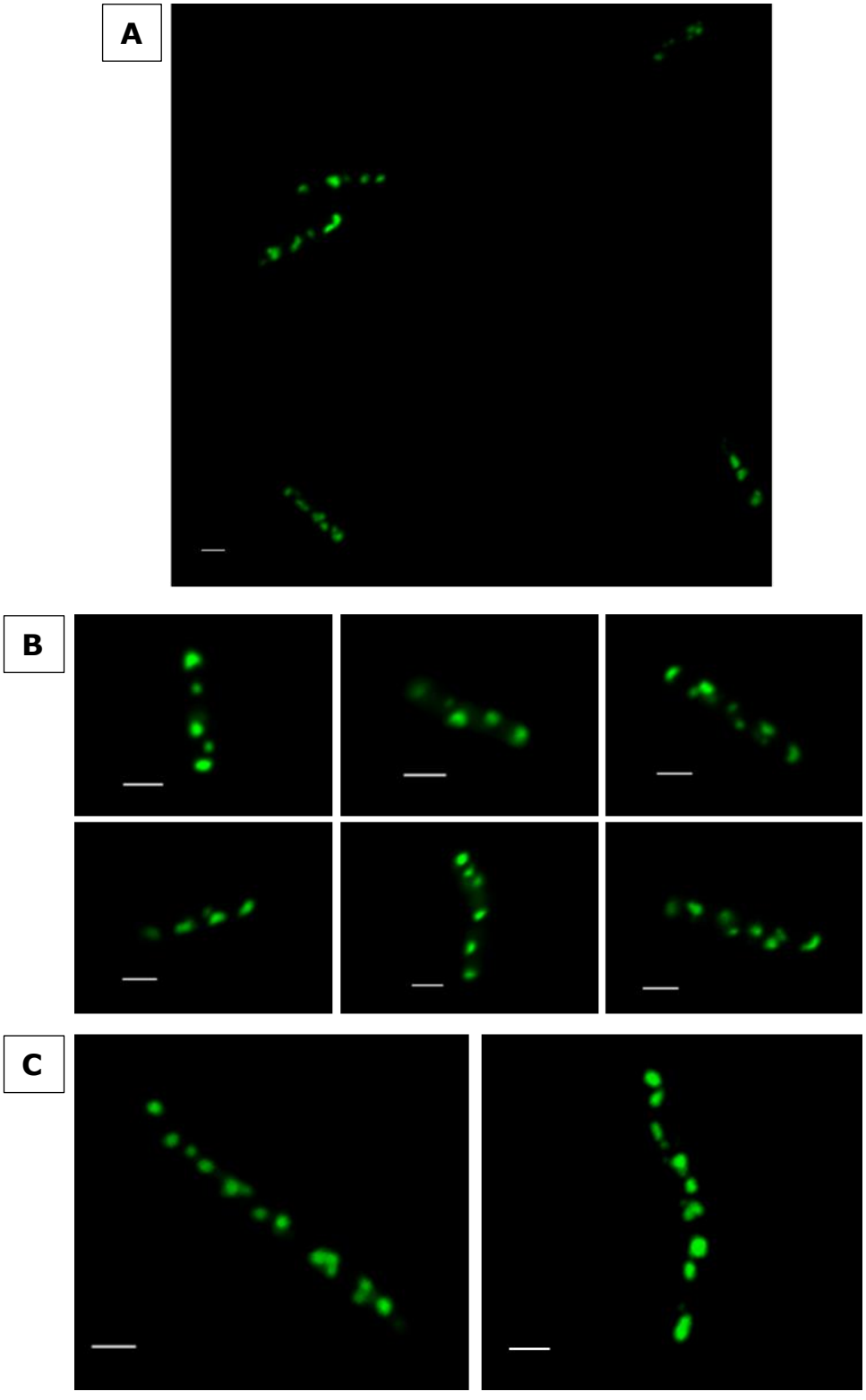


Figure 6.14: Cells expressing FlAsH stained truncated AaaA-TC display a dense random distribution of fluorescent spots with no structured helical arrangement. The overnight culture of MG1655 hosting MG1655 (pLA33aaaA-TCΔ) was grown and prepared for FlAsH staining as described in the text. Cells in wide field **(A)**, expanded magnification **(B)** or a particularly elongated example **(C)** are shown. Scale bars indicate 2 μm. Thanks to MSc Mathulah Sriskandarajah who kindly helped with the experiment.

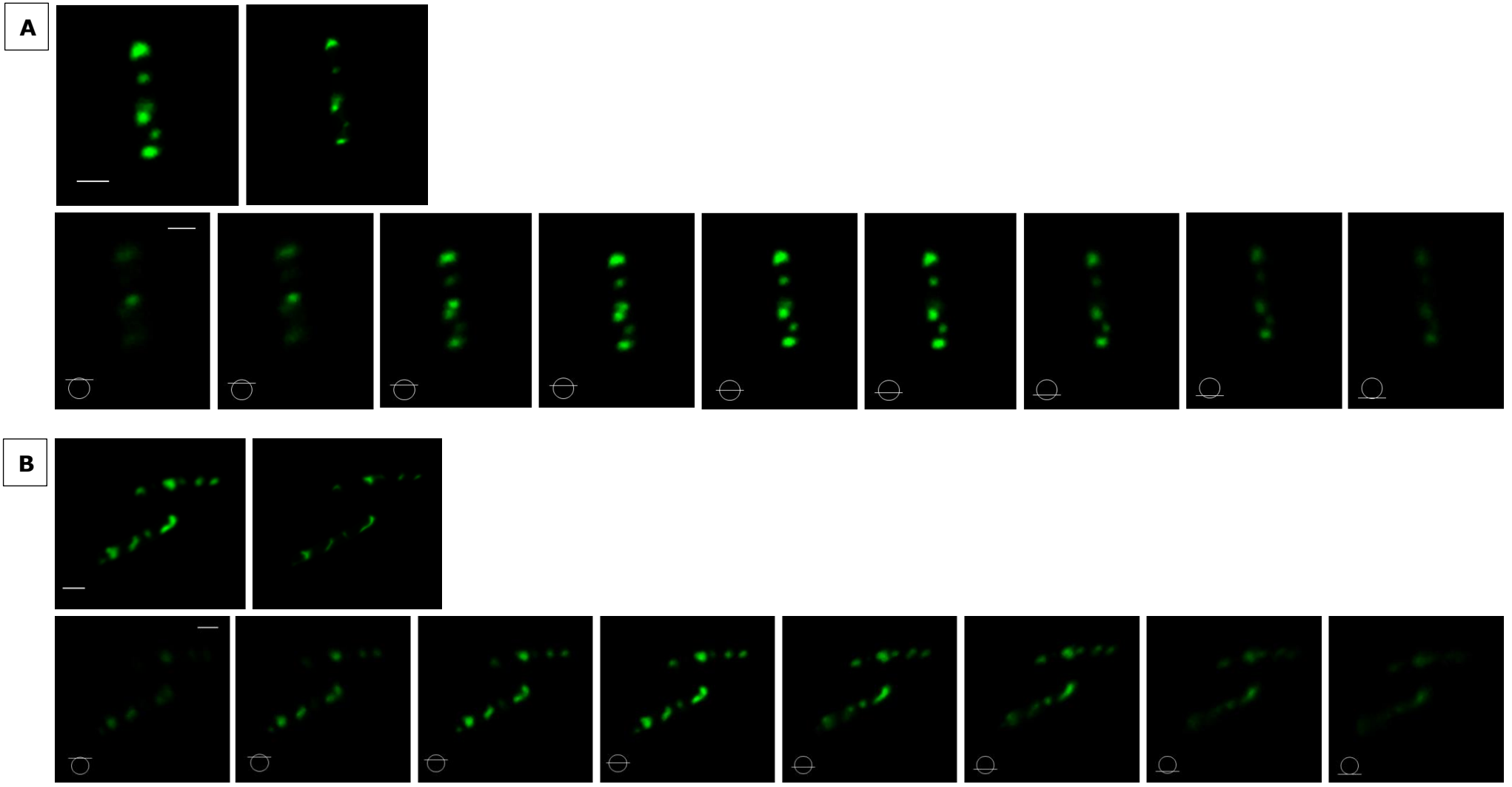


Figure 6.15: An absence of the extended helix during production of TC-tagged AaaA lacking the β-barrel domain in MG1655. The overnight culture of MG1655 hosting pLA33aaaA-TCΔ was diluted 1:100 in LB containing 30 µg/mL Cm and grown until OD_{600} of 0.05. Subsequently, the culture was induced by 0.02% arabinose for 2.5 h. Cells were prepared for FlAsH labelling following the protocol described in chapter 2 and the conditions stated in the text. The top (unprocessed and processed) images in **A** and **B** clarify the spotty localization of truncated AaaA. The bottom row in **A** and **B** shows the confocal Z-stack images of the same cells which clearly illustrates the absence of spirals compared to Fig. 6.10. The diagrams show where the focal plane was in the cell for each image. Scale bar represents 2 µm.

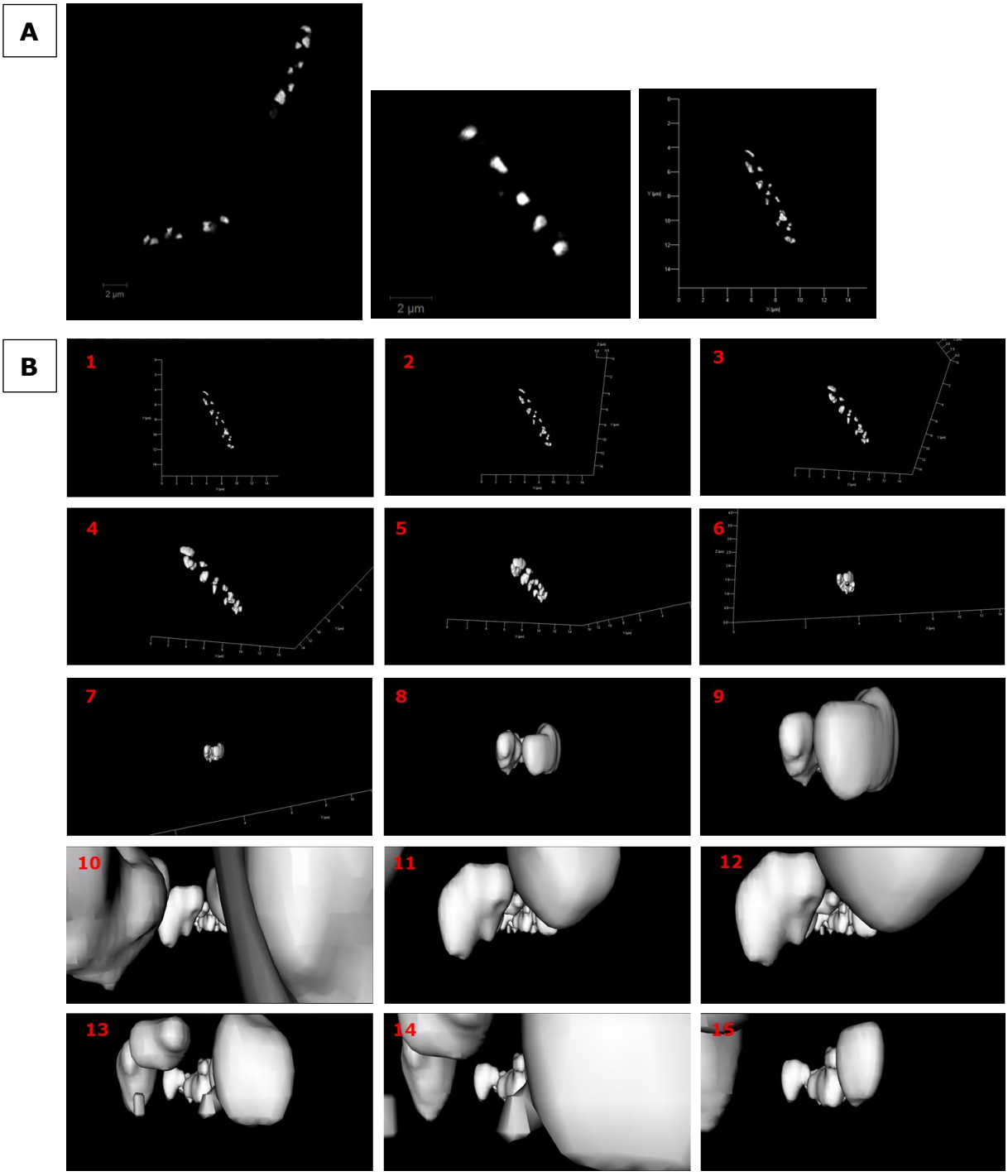


Figure 6.16: Inconsistent spotty distribution of FlAsH labelled truncated AaaA-TC at bacterial membranes appears bulky and lacking the helical organization. The overnight culture of MG1655 hosting pLA33aaaA-TCΔ was diluted 1:100 in LB containing 30 µg/mL Cm and grown until OD_{600} of 0.05. Subsequently, the culture was induced by 0.02% arabinose for 2.5 h. Cells were prepared for FlAsH staining following the protocol described in chapter 2. The top row of images show the localization pattern of the truncated AaaA which appears very dense **(A)**. The image with XY axis (top, right) was selected to create a 3D animation movie, and individual frames from 1-15 are shown **(B)**. The bacterium was tilted and rotated virtually (using Zeiss software) to reveal the pattern of the truncated protein localization. These images illustrate the thickness of localized molecules at bacterial membranes as well as the absence of the spiral organization compared to the full length molecules.

6.2.3.3 All forms of AaaA are active and detectable by immunoblotting

Although it has been clearly illustrated that the TC-tagged AaaA is localized in patchy helices, the consequences of inserting 5 amino acid residues on the AaaA structure and function are still undefined. This is an important question to answer as it will help to assess the selected position for TC insertion and see whether this causes protein perturbation or malfunction. The identity of all forms of AaaA made in this study including; native AaaA, AaaA-TC, mutant AaaA with cysteine substitution for serine at 233 position and the truncated AaaA-TC which has been created by insertion of an amber codon at position 343 were successfully detected by immunoblotting using the polyclonal antibody α-AaaA at dilution 1:2000 (Fig. 6.17) (126). This was achieved by 1:100 dilution of the overnight cultures of MG1655 carrying the pLA33aaaA, pLA33aaaA-TC, pLA33aaaA^{C233S}, pLA33aaaA-TCΔ or the empty vector pBAD33 in LB containing 30 µg/ml Cm and left to grow until reaching OD_{600} of 0.05. Following the induction step with 0.02% arabinose for 2.5 h, 1 ml from each culture was collected and centrifuged to collect the cells' pellet. After that, cells were resuspended in 200 µl 1X SDS loading dye, and subjected to immunoblotting.

As shown in Fig. 6.17, all forms of AaaA were successfully identified using the AaaA antiserum. All forms were detected at the same molecular weight ~80 kDa except for the truncated form which is only 342 amino acid long yields a shorter product around 38 kDa. The native

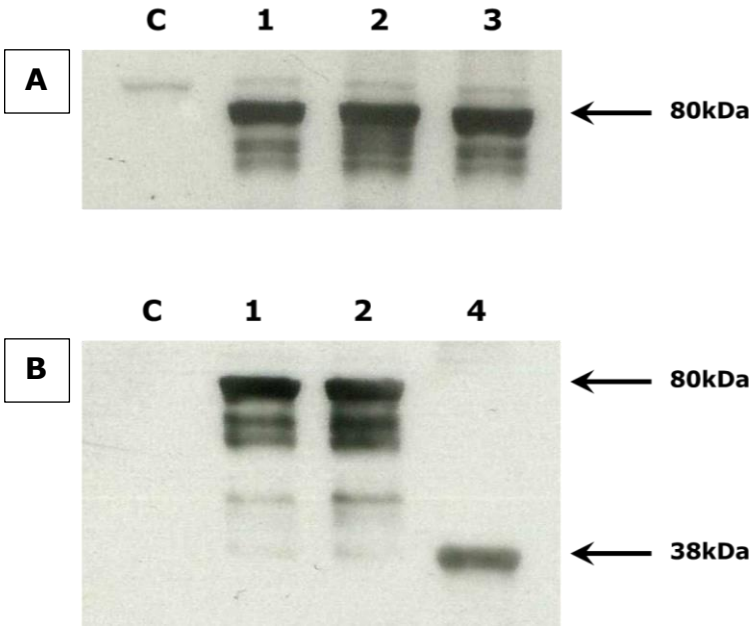


Figure 6.17: All AaaA versions produce full length protein except for the truncated AaaA. *E. coli* MG1655 containing pBAD33 (empty vector) **[C]**, pLA33aaaA **[1]**, pLA33aaaA-TC **[2]**, pLA33aaaA^{C233S} **[3]** and pLA33aaaA-TCΔ **[4]** were grown in LB medium containing 30 µg/ml Cm overnight at 37°C shaking. Next day, cells were resuspended in fresh LB medium (1:100) containing similar amount of antibiotic and incubated until reaching OD_{600} of 0.05. Following the induction period of 2.5 h with 0.02% arabinose, whole cell lysates were prepared as described in chapter 2 and separated through a 9% SDS-PAGE gel which was subjected to immunoblotting using α-AaaA serum at dilution 1:2000. The blot in panel B reveals the presence of truncated AaaA protein (around 38 kDa) [4] while panel A shows the successful production of full length native AaaA [1], TC-tagged AaaA [2] and AaaA with substituted cysteine for serine at position 233 [3]. No protein detected with the negative control lysate [C]. Samples C, 1 and 2 were reloaded in panel B in parallel with sample 4. Thanks to MSc Mathulah Sriskandarajah who kindly helped with the experiment.

AaaA has 647 amino acids in addition to 5 resides for those with TC tagged.

To determine the activity of AaaA, a *p*-nitroanilide degradation assay was undertaken. This assay was previously utilized in a study conducted by Luckett *et al*., 2012 to determine the functionality of AaaA (126). This study confirms the efficient ability of AaaA to degrade the arginine-*p*-nitroanilide substrate and release a chromophore (4-nitroanilide) into the media which can be monitored over time by observing OD_{405} at 37°C in a Lucy Plate Reader.

To test the activity of all forms of AaaA produced in this study especially those with a TC-tag, the cultures of MG1655 hosting pLA33aaaA, pLA33aaaA-TC, pLA33aaaA^{C233S}, pLA33aaaA-TCΔ or the empty vector pBAD33 (control) were grown overnight in LB medium containing 30 µg/ml Cm shaking at 37°C. The next day, samples were prepared for the *p*-nitroanilide degradation assay following the protocol described in chapter 2. Briefly, the overnight cultures were diluted 1:100 in LB containing 30 µg/ml Cm and left to grow at 37°C shaking for approximately 1 h (0.05 OD_{600}) then induction with 0.02% arabinose for 2.5 h was performed. Subsequently, the cells were washed, resuspended in MMP and normalised to 0.25 of OD_{600}, mixed with the arginine-*p*-nitroanilide substrate (1 mM) and loaded into a 96 well-plate for measuring in Lucy Plate Reader (405 nm) at 37°C over time. It is worth mentioning here that once the cells are mixed with the *p*-nitroanilide assay medium, no growth would occur and only enzymatic activity is being monitored.

As shown in Fig. 6.18, all forms of AaaA exhibited similar high levels of degradation of the arginine-*p*-nitroanilide substrate and fully release 4-nitroanilide within a short period of time, 2-3 h. The negative control strain hosting pBAD33 (empty vector) did not show any significant degradation. A slight degradation delay was spotted with the strain carrying TC-tagged AaaA compared to the native AaaA protein. However, the TC-tagged truncated AaaA showed a significant delay in the activity compared to full length AaaA (Fig. 6.19). These results indicate that all AaaA forms are active and confirm that the site selected for TC motif insertion was ideal and did not perturb the function of the protein.

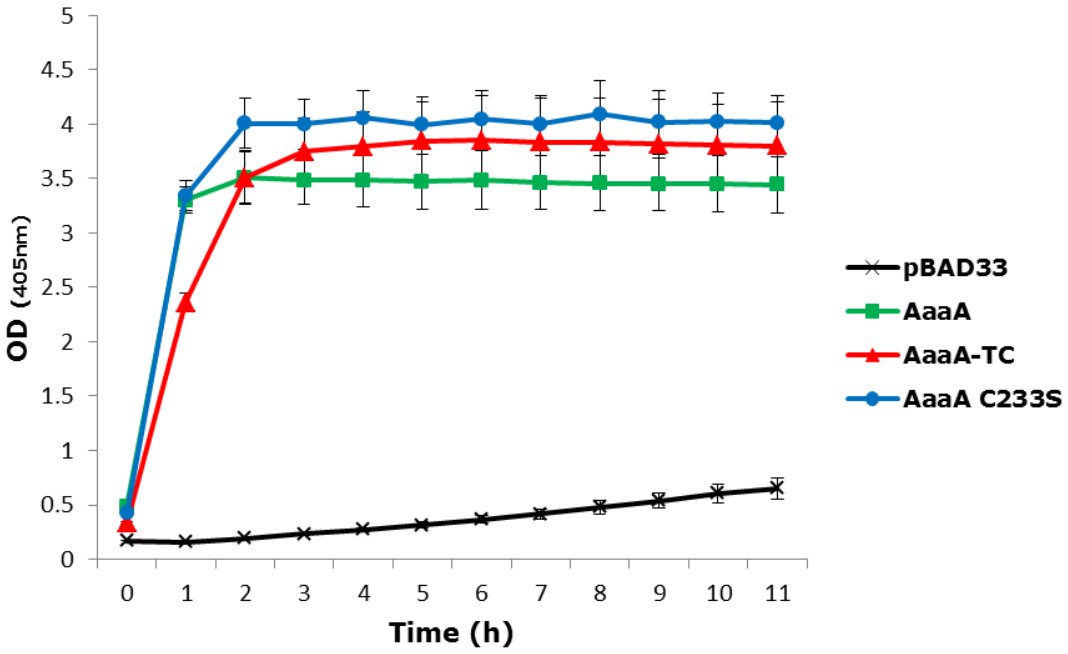


Figure 6.18: All AaaA forms release arginine form the substrate. MG1655 carrying the empty vector pBAD33 (×), pLA33aaaA (■), pLA33aaaA-TC (▲) and pLA33aaaA^{C233S} (●) were grown in LB medium containing 30 µg/ml Cm overnight at 37˚C shaking. Next day, cells were resuspended in fresh LB medium (1:100) containing similar amounts of antibiotic and incubated until reaching OD_{600} of 0.05. Following the induction period of 2.5 h with 0.02% arabinose, cells were collected for the *p*-nitroanalide assay. Cells were washed, resuspended in MMP and normalised to OD_{600} of 0.25. Subsequently, cells were mixed with arginine-*p*-nitroanilide (1 mM), and moved to clear bottomed 96 well plate to be monitored in Lucy Plate Reader (405 nm) at 37˚C for 12 h. This experiment was performed in triplicate and error bars indicate the standard deviation.

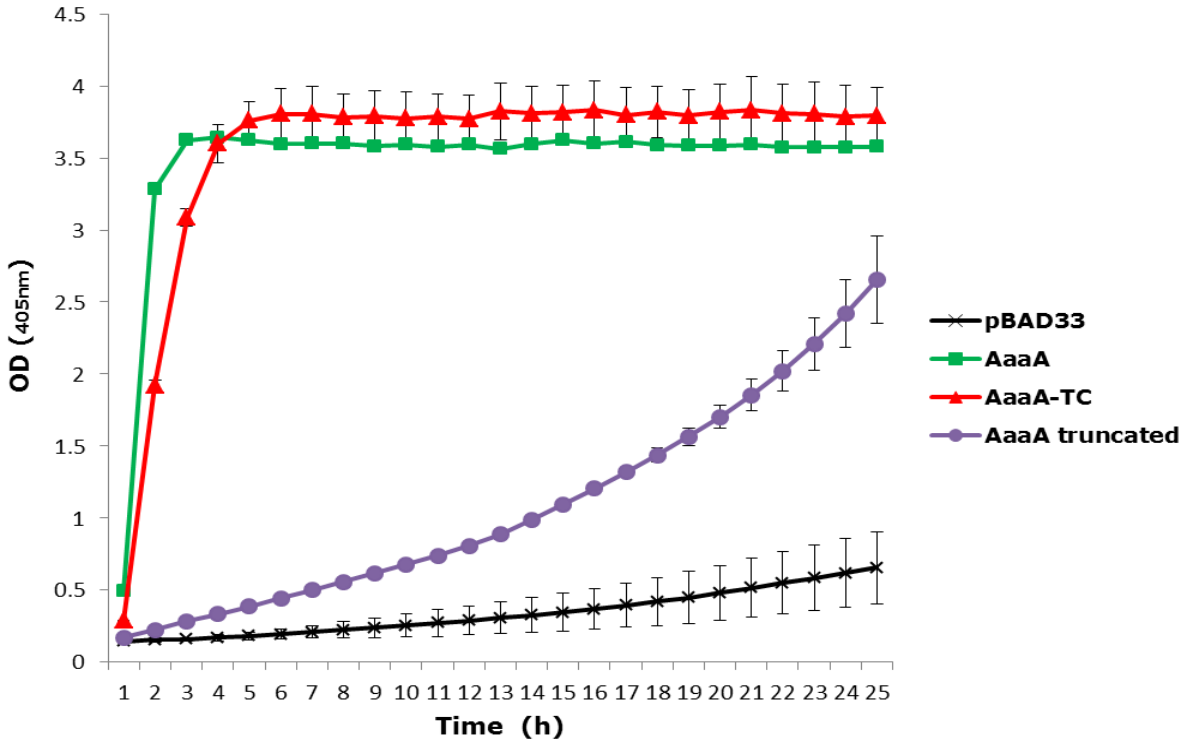


Figure 6.19: Truncated AaaA is active but was delayed and did not achieve the maximum activity compared with the full length AaaA forms during 24 h of incubation. MG1655 carrying the empty vector pBAD33 (×), pLA33aaaA (■), pLA33aaaA-TC (▲) and pLA33aaaA-TCΔ (expressing truncated TC-tagged AaaA without β-barrel domain) (●) were grown in LB medium containing 30 µg/ml Cm overnight at 37°C shaking. Next day, cells were resuspended in fresh LB medium (1:100) containing similar amounts of antibiotic and incubated until reaching OD_{600} of 0.05. Following the induction period of 2.5 h with 0.02% arabinose, cells were collected for the *p*-nitroanalide assay. Cells were washed, resuspended in MMP and normalised to OD_{600} of 0.25. Subsequently, cells were mixed with arginine-*p*-nitroanilide (1 mM), and moved to clear bottomed 96 well plate to be monitored in Lucy Plate Reader (405 nm) at 37°C for almost 24 h. This experiment was performed in triplicate and error bars indicating the standard deviation. Thanks to MSc Mathulah Sriskandarajah who kindly run the experiment.

6.2.3.4 Overproduction of AaaA causes a significant reduction in the bacterial growth

Having demonstrated that the production of the membrane tethered AaaA for extended times altered the cell morphology in particular cells, it was hypothesized that the accumulation at the outer membrane affected cell integrity, leading to growth defects. To investigate the consequences of the arabinose induction levels on the cell viability, the strains MG1655 (pBAD33), MG1655 (pLA33aaaA), MG1655 (pLA33aaaA-TC) and MG1655 (pLA33aaaA-TCΔ) were grown as previously described but induced with different arabinose concentrations. Cells were induced with zero%, 0.2%, 0.02% and 0.002% arabinose at an OD_{600} of 0.05 and allowed to grow at 37°C shaking for a further 2.5 h. As expected, overproduction of AaaA at 0.2% arabinose caused a significant growth reduction compared to 0.02% and 0.002% as well as to the control MG1655 hosting the empty vector, pBAD33 (Fig. 6.20).

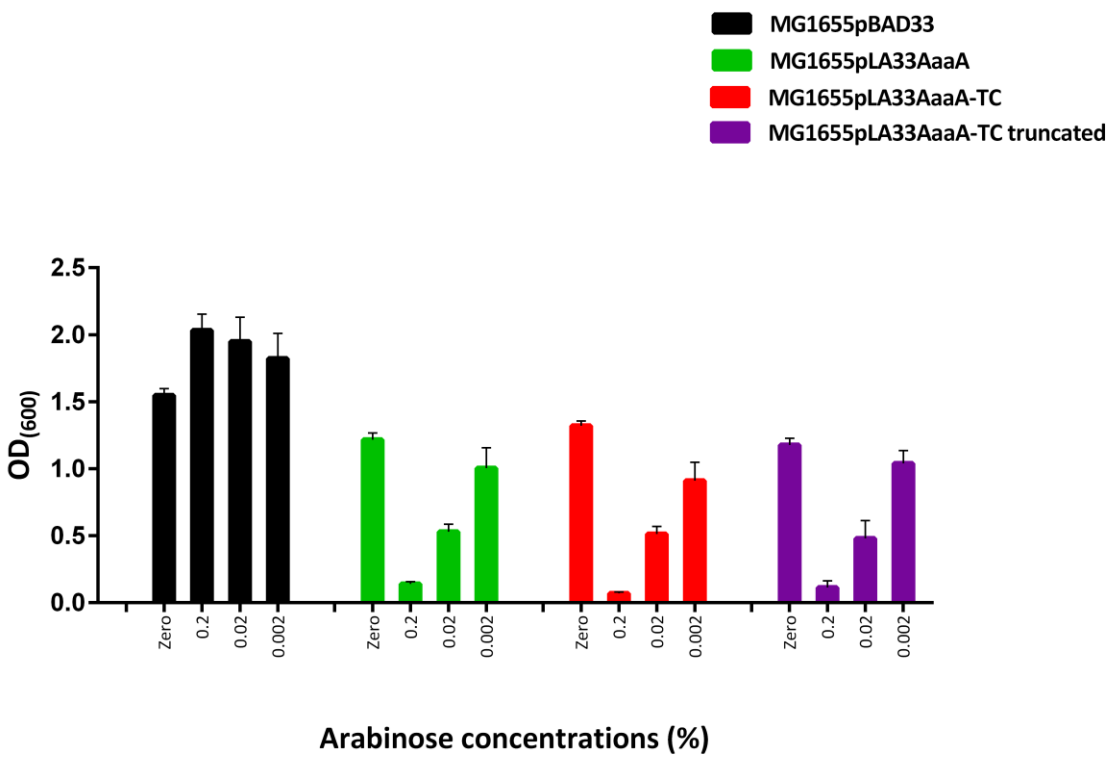


Figure 6.20: High doses of arabinose suppress the growth in cells producing AaaA. The overnight cultures of MG1655 (pBAD33), MG1655 (pLA33aaaA), MG1655 (pLA33aaaA-TC) and MG1655 (pLA33aaaA-TCΔ) were diluted 1:100 in LB supplemented with 30 µg/ml Cm and incubated to grow at 37˚C shaking until reaching OD_{600} of 0.05. Next, each strain was divided into aliquots to be induced with Zero%, 0.2%, 0.02% and 0.002% arabinose. Samples were then taken to measure the cell density (OD_{600}). The experiment was performed in triplicate; error bars indicate the standard deviation.

6.2.4 EspC-mCherry fusion detects that the spiral structure is dynamic, but the FlAsH tagged AaaA control does not

The circumferentially distributed disconnected patches of both EspC and AaaA hint at a dynamic spiral path being followed by the ATs during secretion. The MreB association demonstrated here could provide a mechanism to spatially guide these molecules during their journey toward the cell surface.

To assess the potential dynamic nature of these patches, fluorescence recovery after photobleaching (FRAP) was used in live cells producing EspC-mCherry fusion to determine if new molecules are added to existing patches. MG1655 (pLA33C1mc) was grown, induced by 0.02% arabinose for 4 h and prepared for confocal imaging as previously described. As shown in Fig. 6.21, a selected single fluorescent patch (green circle) located close to the middle of bacterium was photobleached using a focused laser beam and the recovery of fluorescence was monitored for up to 35 min. Using ZenZeiss software, it was possible to calculate the recovery of fluorescence over the time of the experiment. The values collected from the bleached area were normalised against a control unbleached area (blue circle) on the same bacteria (Fig. 6.21 B). A table was generated of the fraction of mobile versus immobile molecules, providing information about molecule dynamics (Fig. 6.21 D). Interestingly, the EspC-mCherry patch showed a good recovery of fluorescence over time (Fig. 6.21 D). The Zeiss FRAP analysis revealed that the percentage of mobile and immobile fractions was 67.93% and 32.07% respectively inside the green circle.

The different fluorescent labelling technique that requires addition of a substrate (FlAsH-EDT_2) to produce fluorescence for AaaA was used as a control in this experiment because in the absence of substrate, there should be no recovery of fluorescence after bleaching. As expected, bleaching one discrete patch of fluorescent AaaA on the cell did not show any fluorescence recovery over time (Fig. 6.21 A and C). Here, the percentage of mobile and immobile fractions was 0.4% and 99.6% respectively inside the green circle. These results support the notion that the EspC-mCherry molecules are mobile, and when newly synthesized they are able to enter pathways of secretion that are visualized as fluorescent patches in this study.

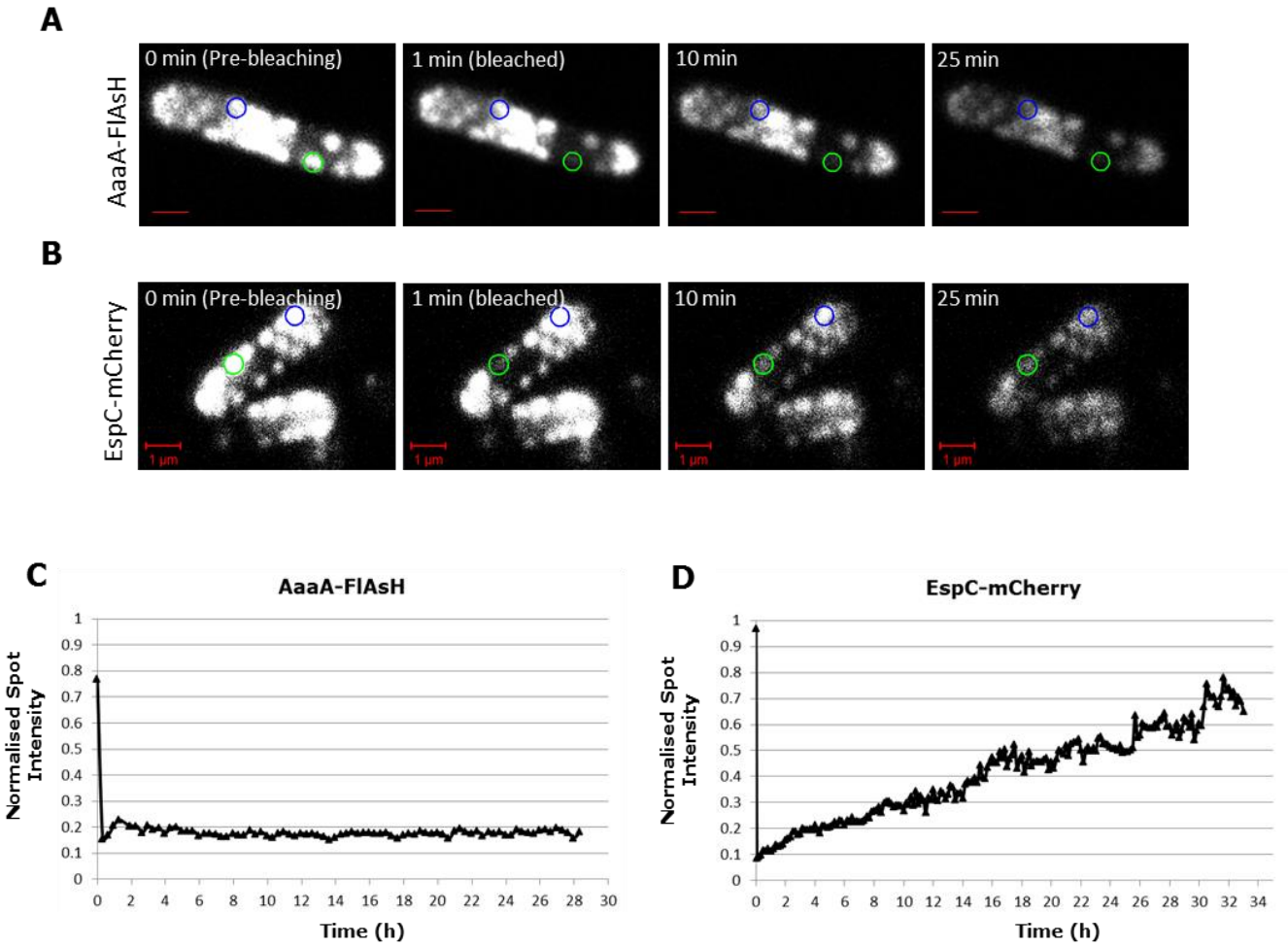


Figure 6.21: Fluorescence recovery after photobleaching reveals the dynamic nature of the molecules of EspC in patches. The overnight culture of MG1655 (pLA33aaaA-TC) **(A)**, (used in this experiment as a control), was diluted 1:100 in LB containing 30 µg/mL Cm and grown until OD_{600} of 0.05. Subsequently, the culture was induced by 0.02% arabinose for 2.5 h. Cells were prepared for FlAsH staining following the protocol described in chapter 2. 8.0 µl of washed cells were applied to microscopic slides and covered with a coverslip and sealed with transparent nail polish. The overnight culture of MG1655 (pLA33C1mc) **(B)** was diluted 1:100 in fresh LB containing 30 µg/mL Cm and concurrently induced by 0.02% arabinose to grow for 4 h at 37°C shaking. Next, the cells were collected and washed with PBS and normalised to OD_{600} of 0.5. Cells were prepared for microscope analysis as described above. The representative images of AaaA-FlAsH **(A)** and EspC-mCherry **(B)** show fluorescent intensity before and after photobleaching at the region of interest marked by the green circle. The intensity of fluorescence within the blue circles was used as reference to normalise over time. Blue circles indicate the control unbleached regions. The fluorescence recovery over time graphs revealing the recovery of fluorescence of EspC-mCherry **(D)** compared with AaaA-FlAsH **(C)**. The Black triangles in graph C and D show the normalised fluorescent intensity of zones marked by the green circles in each single frame for images in A and B respectively over time.

6.3 Discussion

This chapter addresses a number of potential technical problems important for FlAsH labelling and provides solutions to resolve these issues. The data presented here indicate the usefulness of tetracysteine tag technology in monitoring the localization and trafficking of recombinant proteins in living cells. The combination of a small inserted TC motif with a small permeable fluorophore detection reagent offers a better observation of localization due to minimal structural perturbation of the target protein and lower levels of host cell damage compared to using a large fluorescent protein tag. The results presented here support our hypothesis that EspC is secreted via patches that are (i) disconnected, (ii) helically distributed along the bacterial cytoskeleton, and (iii) dynamic.

The preliminary images obtained during FlAsH staining of TC-tagged MreB in live bacteria (Fig. 6.2), confirms the patchy distribution of MreB observed in fixed *E. coli* cells labelled with α-MreB antibodies (219,317). This patchy pattern of MreB was also observed in a small proportion of cells that produced the MreB-mCherry fusion (Fig. 4.4 A). However, fusion of the large mCherry protein with MreB potentially disrupted MreB folding leading to an inability to form the protofilaments leaving it diffuse in the cytoplasm (Fig. 4.4 B). This was not the case when the FlAsH tag was used since, consistent with previous studies, FlAsH tagged MreB appeared as disconnected patches that were helically distributed (Fig. 6.2 C and D) (242), and sometimes formed helical streaks of variable lengths that encircled the cell (Fig. 6.4 A) (240). The high

precision patchy localization patterns of FlAsH tagged MreB by dSTORM (Fig. 6.6), suggests that the TC tag did not significantly perturb the overall folding and function of MreB.

It has been postulated that the use of biarsenical dyes for single molecule labelling tends to be too nonspecific (315,318,319). This may be due to the level of background staining, cellular toxicity of the arsenic compounds and the likely disruption of protein structure or function as a consequence of the TC-tag sequence insertion (309). Background staining was minimized here by (i) washing the cells twice with the competitor 1,2-dithiol antidote (BAL) to eliminate the thiol-dependent background, (ii) using HEPES ultra-pure buffer as a labelling media instead of PBS, and (iii) introducing a final HEPES wash. These measures substantially improved the signal to noise ratio and reduced background fluorescence (Figs. 6.3 and 6.2 respectively). However, the background fluorescence can also be generated by non-specific binding to endogenous proteins rich in cysteines such as cytoskeleton proteins and protein kinases (308). This possibility was discounted in this study by arabinose induction of the host bacteria lacking any plasmids, or hosting the empty cloning vector (pBAD33) and treating with FlAsH-EDT_2 which resulted in no substantial fluorescence (Fig. 6.3 D).

In fact, the presence of only three cysteine residues in MreB and four in EspC which are scattered across the protein limits the probability of non-specific binding. In support of this, fluorescent intensity was low in controls (Fig. 6.3 A, B and C). In case of AaaA, the scenario was different. The intensity of green fluorescence from FlAsH labelled TC-

AaaA was noticeably greater than that from FlAsH labelled MreB-TC or EspC-TC^{CCPGCC} (Fig. 6.9 A). Moreover, control cells producing native AaaA exhibited patchy fluorescence, although this was not as bright as that from TC-tagged AaaA. Although AaaA has only three cysteines in a total of 647 amino acid residues, two are consecutive cysteines (at positions 232 and 233), and might be responsible for providing half a FlAsH-EDT_2 substrate binding site (Fig. 6.9 B). Substitution of the second cysteine residue (at position 233) for serine abolished the patchy fluorescence associated with FlAsH substrate binding. Only a low level diffuse fluorescence was detected, even when the laser power was increased (Fig. 6.12). Perhaps, if these cysteines were spaced with one amino acid in between (C-X-C), or presented as four consecutive cysteines (CCCC), the affinity for the biarsenic compounds could also be reduced (309).

The high resolution information achieved during imaging FlAsH stained EspC-TC^{CCPGCC} was remarkable. The localization of EspC-TC^{CCPGCC} in patchy helices was very clear compared to EspC-mCherry (Figs. 6.5 and 6.6 b respectively). There is no doubt that switching from mCherry (~28 kDa) to the smaller sized FlAsH-EDT_2/TC-motif (<2 kDa) reduces the pitfalls of improper protein folding (298). Consequently, a better localization pattern could be detected. This successful outcome vindicates the choice to insert the FlAsH binding site in an externally exposed loop of the target proteins so that it was accessible to the dye even if they are folded, and unlikely to interfere with function or structure. Although both optimal CCPGCC and non-optimal CCGKCC motifs were engineered into EspC, the optimised motif clearly generated a stronger and more stable fluorescence (Fig. 6.3 B and C) which was

consistent with previous studies (306). This optimal motif has been further improved and optimised to include extra residues flanking the core motif. Two optimised motifs, FLNCCPGCCMEP and HRWCCPGCCKTF were shown to have increased affinity and improved fluorescence quantum yields (320-322). However, due to the large number of amino acids required to insert these, only the optimal motif (CCPGCC) was utilized in this study.

Having investigated alternative approaches to fluorescent labelling to exclude technical artefacts and confirm the EspC localization pattern, it was important to demonstrate whether this pattern might be conserved between different ATs as this would reveal if common underlying machineries are involved in the spiral pathway of secretion. Interestingly, optical sections of MG1655 cell producing FlAsH tagged AaaA-TC exhibited a spiral localization of fluorescence that extended along the long axis of the cell (Fig. 6.10). This helical patchy pattern was evident in the elongated cells and consistent with the MreB localization in cells treated by cephalexin (cell division inhibitor) (219). Furthermore, looking at the structure from inside the cell, the helical pattern was reminiscent of those of the FlAsH labelled EspC-TC^{CCPGCC} (Fig. 6.13), indicating that the patchy spiral secretion pathway seems to be conserved among ATs. Further analysis is required to gather further insight into the mechanism of spiral formation. Perhaps testing a wide range of ATs with diverse functions would provide some clues and shed light on the secretion mechanism used by ATs.

It has been speculated that using smaller fluorescent tags and membrane permeable organic dyes to monitor the localization of proteins in living cells, more insight into their localization journey would be gained (271). However, concerns about the impact of protein overproduction levels on the cell must be considered. For this reason, the *espC*, *aaaA* and *mreB* were expressed from an *araBAD* promoter to ensure tight control of their expression (323). Furthermore, the addition of low L-arabinose concentrations (0.02% final concentration) decreased the impact of the overproduced proteins. The production of proteins at near-native levels might not be suitable for this study because the tetracysteine tag technology works best when the target proteins are abundantly expressed (308,324).

It could be argued that the production of AaaA for long periods of time resulting in a filamentous phenotype in a proportion of cells (Fig. 6.11 B) indicates a high production level. Certainly, overproduction of membrane proteins alters the integrity of the bacterial cell wall and thus cell viability (325). This was not observed, however in EspC. It can therefore be assumed that due to the nature of AaaA (AaaA needs to be tethered to the cell surface), accumulation of such a protein in the outer membrane might influence the membrane integrity, and thus interrupt the cell division. Similarly, truncated AaaA lacking the C-terminal domain in the periplasmic space also appeared to hamper division in particular cells, causing filamentous growth (Fig. 6.14 C). In both scenarios, it is reasonable to suspect that the production of AaaA (either full length or truncated) via addition of arabinose reduces growth in a dose dependant manner (Fig. 6.20). The strong reduction in the growth

observed upon production of AaaA at higher levels, suggests possible cell toxicity (325). This could perhaps be minimised by lowering the inducer concentration (326).

The finding that both EspC and AaaA localize in very similar patchy helical arrays raised a possibility that they may be following the same secretion route which starts from the first gate (Sec translocon) and continues to the exit gate (BAM complex). This route was suggested in this study to be associated somehow with MreB (chapter 4), as perturbing MreB with A22 caused mistargeting of EspC (Fig. 4.7). Importantly, the Sec machinery itself was demonstrated to arrange in a helical array, but this helical pattern was distinct from the MreB spiral organization (234,235). It was hypothesized that the C-terminal domain of ATs is involved in targeting the proteins towards their destination at the cell poles. In support of this hypothesis, the FlAsH tagged AaaA-TC lacking the β-barrel domain was localized as bulky spots which were very condensed, bright and missing the spiral pattern of distribution. It can be speculated that truncated AaaA has lost its trafficking guide, and thus accumulates at the SecYEG gate (Figs. 6.14, 6.15 and 6.16). This localization appears consistent with the helical arrangement of FlAsH tagged SecY and SecE (141) or SecA-GFP and SecY-GFP fusions (234). It however would be appropriate to further examine whether the truncated AaaA co-localizes with the SecYEG or perhaps by producing the FlAsH tagged truncated AaaA-TC in MM52 *E. coli* cells which lack a functional Sec machinery. Unfortunately, time constraints prevented these experiments.

The predicted co-localization of patchy helices of EspC and MreB (Fig. 6.6) is also interesting. Despite examining their localization in cells grown at different times with different imaging techniques, the patches of EspC and MreB seem overlapped perfectly. The patchy helical structure of EspC appeared to have a similar helical pitch to MreB suggesting at least a transient association of MreB with EspC. Supporting this notion, EspC patches were dynamic (Fig. 6.21). It is vital to conduct direct co-localization studies to confirm this possible association.

In agreement with previous work, AaaA degraded arginine-*p*-nitroanilide (126). As shown in Figs. 6.18 and 6.19, the optimal release of 4-nitroanilide was accomplished within 2 h by MG1655 (plA33aaaA), whilst MG1655 (pBAD33) did not degrade arginine-*p*-nitroanilide. Moreover, the TC-tagged AaaA maintained this arginine specific aminopeptidase activity, thus insertion of the TC-tag in AaaA did not affect its activity suggesting that the structure and function of AaaA was maintained. Interestingly, the TC-tagged AaaA without the β-barrel domain was significantly delayed in its activity compared to other AaaA versions (Fig. 6.19). This is consistent with removal of the AT C-terminal domain having a major effect on the translocation of passenger domains causing mislocalization (160,327). The delayed activity could reflect stalling of AaaA in the periplasm, slower acquisition of the final active structure and/or reduced contact with the exogenously added extracellular substrate. Although AaaA belongs to the AT family, it is apparent that ATs are not autonomously secreted proteins. Instead, additional factors including periplasmic chaperones and the BAM complex are required to

successfully delivery passenger domains to the OM surface (99,174,328). Unfortunately, it was not possible to assess the activity of EspC in this study. Attempts to test the ability of EspC and $EspC_{S256I}$ (chapter 4) to degrade the human fodrin were unsuccessful. It may be necessary to used purified EspC as described by Navarro-García *et al* (73). Unfortunately, due to the time constraints, it was not possible to optimise this.

Further defining the molecular mechanism involved in the spiral secretion of EspC and AaaA would facilitate the uncovering of new targets for the development novel therapies to overcome infections caused by antibiotic resistant bacteria (329,330). ATs are (i) the largest family of secreted proteins by Gram negative bacteria, (ii) often associated with virulence, (iii) widely distributed, (iv) share conserved unique structural properties (93,126), making them an ideal target for novel antimicrobial agents (331). As an example, the availability of the crystal structure of the *E. coli* AT Haemoglobin protease (Hbp) passenger domain, made it possible to design an Hbp platform for the efficient secretion and surface display of heterologous proteins, utilizing the *Mycobacterium tuberculosis* vaccine target ESAT6 as a model protein. This study also showed that ESAT6 fusion to the passenger domain of EspC was successfully secreted, suggesting this approach can be applicable to different ATs (332). So far, it seems that the majority of publications focus on ATs as novel targets for vaccine development rather than as a target for antibiotics (331,333-336).

Overall, there does not appear to be any evidence in the literature where it is shown that ATs are localized in a helix or coupled to the bacterial cytoskeleton, MreB. Hence, the results obtained in this work are considered to be important and will definitely provide additional insight to identify new potential targets for the development of inhibitors to tackle the emergence of antibiotic resistance bacteria.

Chapter 7

Final conclusions and further directions

In this study, the mechanisms of secretion of two different AT proteins, EspC and AaaA were investigated to compare individual localization patterns and establish whether there is a common AT secretion pathway. Two separate methods were used to fluorescently label proteins and monitor localization patterns in an innovative way. For the first time it was shown that localization of both EspC and AaaA (i) is dependent upon a combination of the AT β-barrel domain, the bacterial cytoskeleton actin homologue MreB plus the Sec translocon, and (ii) that it occurs via discrete patches that are distributed in a helical pattern along the bacterial cytoskeleton. Importantly, given that a similar spiral localization arrangement is shared by both ATs this indicates that a conserved underlying secretion machinery might be responsible for the spiral secretion of classical ATs from rod-shaped bacteria.

The patchy localization observed for EspC was also evident when the actin homologue MreB was labelled with FlAsH-EDT_2 (Figs. 6.3 A and 6.4 A) or fused to the mCherry fluorescent protein (Fig. 4.4 A). Moreover, monitoring over time revealed the dynamic nature of the patches as they moved around the cell circumference in a helical pattern in a manner that is consistent with recent reports (242). The similarity of this pattern of MreB localization to that of EspC elucidated for the first time a novel patchy spiral pattern of localization for T5SS (Fig. 6.6). However, the mechanism of this is still not fully defined. The use of high resolution imaging technologies to characterize AT localization will enable further advancements into the molecular interactions that are involved in the localization of EspC. For example, co-localization studies of EspC with MreB or other morphogenetic proteins such as MreD, MreC,

RodA and RodZ would identify whether similar patchy arrangements exist to suggest interaction with the AT secretion pathway. Preliminary data obtained from the predicted co-localization of patchy helices of MreB and EspC suggests this will be the case (Fig. 6.6). To use a different approach, interaction of EspC with cytoskeleton proteins can also be elucidated by performing two-hybrid screening using the bacterial two-hybrid system.

In rod-shaped bacteria, MreB is essential for lateral cell wall growth and thus maintenance of the bacterial bacillus shape (217). In the absence of MreB, as shown in chapter 4, when the MreB-inhibitor A22 was added to growing cells, the bacterial cells transform into lemon/rounded-shaped morphology in an A22 dose dependent manner (Fig. 4.5). Inhibition of MreB by A22 also altered the spiral fluorescence pattern of the full length EspC-mCherry and only cloudy red fluorescence cells were observed (Fig. 4.7), supporting the association of EspC with the spiral cytoskeleton of *E. coli*.

In addition, it was noticed that complete spiral localization of EspC into discrete patches is particularly evident in a population of cells that are slightly elongated (Figs. 3.8 and 6.5). The spiral-like structures of EspC in these cells were clearly visible under confocal microscopy as the patchy appearance was extended across the entire length of the cytoskeleton from pole to pole. It has been reported that the cytoplasmic filaments of MreB rotate around the bacterial cell in a process that is driven by peptidoglycan synthesis (212,213). It is plausible to link the cell wall elongation machinery to EspC secretion as

its role in the driving force for MreB patchy motion. The remarkable spiral organization of FlAsH tagged EspC imaged through an elongated cell by super-resolution microscopy support this inference (Fig. 6.5).

The other potential structure in *E. coli* that has been shown to organize into helical patterns is the Sec machinery. Perturbing the spiral localization of EspC by producing it in an *E. coli* Δ*secA* mutant strain provided strong evidence for the implication of the Sec machinery in the localization of EspC (Fig. 4.25). The spiral pattern of Sec is different from MreB as Sec spirals seem to have a larger pitch than their MreB equivalents (235). Interestingly, expression of the truncated FlAsH tagged AaaA in MG1655 revealed dense spots (blobs) distributed randomly over the entire length of the cell (Fig. 6.14). Z-stack as well as super-resolution images of such cells confirmed that these dense spots/blobs clearly lacking a structured helical arrangement (Figs 6.15 and 6.16, respectively). It is possible to speculate that due to the lack of the β-barrel domain, truncated AaaA did not integrate into the OM and rather accumulated nearby or at the SecYEG channel interfaces thus leading to the formation of these random blobs. Further experiments to investigate the localization of TC-tagged AaaA lacking the β-barrel domain in *E. coli* Δ*secA* would clarify if these blobs mirrored the localization pattern of the Sec translocon or were genuinely random events.

It was hoped that incorporation of TCOstar into EspC for bio-orthogonal incorporation of localized fluorescence in living cells would allow improved fluorescent studies on the localization of EspC. The major

advantage in this labelling approach is the insertion of very small UAA tag that would result in minimal or no alteration to the global protein properties (275). Unfortunately, this was not achieved. In fact, the inability to detect good levels of secreted EspC in the supernatant lysate upon incorporated with N^{ε}-Boc-L-Lysine (Fig. 5.9) indicated that insertion of the amber codon at the position equivalent to amino acid 533 in the peptide sequence of EspC might be responsible for causing changes in the overall structure that led to protein degradation. N^{ε}-Boc-L-Lysine did not bear a trans-cyclooctene functionalized ring, and thus it was not possible to perform tetrazine-trans-cyclooctene ligation (Click reaction). To overcome these issues, it would be beneficial to use the previously reported plasmids (pEvolv $tRNA^{Pyl}$/$PylRS^{AF}$ and $pBAD^{GFPY39TAG}$) that have been shown to genetically encode numerous UAAs such as TCOstar into GFP (275).

In contrast to the Amber suppression work, the utilization of the small FlAsH-tag in this study was very advantageous. As previously mentioned, proteins engineered with TC motif are less likely to have detrimental effects on the protein folding and function due to the small size of the inserted tag. Consequently, the protein of interest would be correctly folded, localized and functional. Investigating the influence of inserting the TC-tag on the AaaA structure and function via assaying its enzyme activity *in vitro* showed that all versions of the TC-tagged AaaA exhibited good activity (Figs. 6.18 and 6.19). Unfortunately due to the time constraints it was not possible to perform an activity assay with the EspC to show that it had no loss of the cytotoxic activity when it was fused with mCherry or tagged with the TC-motif. To do this, EspC could

be purified using anion exchange chromatography as described by Drago-Serrano *et al*., 2006 (74).

The creation of truncated AT proteins without their β-barrel domains provides the potential to generate applicable and comparable controls for evaluation of the hypothesis that MreB is important for governing the localization of ATs to cell poles by a mechanism that recruits the AT β-barrel domain. Despite differences in the size of the truncated EspC-mCherry compared with the size of truncated FlAsH tagged AaaA, the data collected here strongly suggest that the C-terminal β-barrel of ATs is required for the spiral distribution. Not only did these truncated proteins localize in a pattern that was different to that of full length versions, but strikingly, major perturbations resulting from loss of membrane integrity with concomitant production of minicells was observed in cells containing truncated AT proteins that were produced for long periods of time (chapter 4). Indeed, bacterial viability of MG1655 was affected following long periods of EspC production which was not relieved by the Ser256Ile substitution of the serine protease motif of EspC (Fig. 4.23).

One of the interesting observations of this work was the variation in the localization of full length EspC-mCherry when it was expressed in an EPEC background. Unlike expression of full length EspC-mCherry in the *E. coli* K-12 laboratory strains (MG1655 and DH5α), full length EspC-mCherry secretion in the parental EPECΔ*espC* background did not appear to show the same structured helical localization with concentrated patches under the same growth conditions (Fig. 3.18).

However, as the localization of the truncated EspC-mCherry in both *E. coli* K-12 and EPECΔ*espC* was very similar. It is possible that the bacterial OM is importance in governing the helical organization of EspC because no integration with the BAM complex would occur with the truncated EspC-mCherry in both *E.coli* strain backgrounds. The crucial role of the BAM complex in directing the spatiotemporal dynamics of bacterial OMPs has recently been elucidated (337). By using both FRAP and total internal reflection fluorescence (TIRF) microscopy, co-localization of the OMPs with the main BAM complex component, BamA occurs within large clusters of the OM termed OMP islands (337,338). In addition, it has been established that these islands move toward bacterial poles during growth and this movement is driven by new OMP biosynthesis in *E. coli* (337,339). Detecting the dynamic nature of EspC in patches by FRAP here in chapter 6 supports this notion. As all ATs contain a β-barrel and require BamA for insertion into the OM, this raises the question as to whether their mechanism of insertion in the OM is similar or distinct to that of OMPs? Further analyses such as performing fluorescence loss in photobleaching (FLIP) would be useful to measure the mobility and dynamics of EspC patches towards the poles in living bacterial cells.

An important factor for the differences in the localization patterns of full length EspC-mCherry within *E. coli* K-12 and EPECΔ*espC* strains are the differences between both strains in their membrane fluidity. Because the laboratory *E. coli* strains contain high membrane fluidity (due to the presence of an incomplete LPS), diffusion of molecules in the OM would be increased thereby interfering with the distribution of membrane

proteins. Supporting this notion, a study conducted by Jain *et al*., 2006 has demonstrated that polar localization of ATs such as IcsA, SepA, AIDA-I and BrkA are non-polar when expressed in *E. coli* K-12. The proteins are found instead diffusely localized in the OM (199). Contradicting this hypothesis however is a recent report conducted by Doyle *et al*., 2015 which refutes the membrane diffusion models because the surface distribution of IcsA was equivalent between complete and incomplete LPS strains (202). Repeating the EspC secretion with an *E. coli* K-12 MG1655 strain that has a complete LPS (340) would encompass the role of OM fluidity on AT localization and provide additional insight into the mechanisms by which EspC AT traverses the bacterial cell envelope.

Future investigations in this research could be focused on the delivery system of AT proteins to eukaryotic cells. With the information of the FlAsH and UAA labelling approaches, this could shed light on how EspC is been delivered to host cell via the T3SS which is still unknown. Also, while this study has compared localization of AaaA with EspC, it can also be extended to other types of ATs that are secreted using other AT secretion pathways such as those listed in the Table 1.2. It would be interesting to see if the spiral localization of EspC and AaaA is highly conserved among the different types of ATs. In addition, to further address the possible association of the spiral patchy localization of EspC with the MreB patches, a proper co-localization study could be performed within a single living cell using the EspC-mCherry and TC tagged MreB.

In conclusion, this study has clearly shown for the first time that EspC and AaaA are secreted in discrete patches. These patches rotate around the cell circumference along the long axis of the cell spanning the entire length of the cell cytoskeleton from pole to pole and maintaining a spiral confirmation. The presence of intact β-barrel domain and a functional MreB and Sec translocon are important for preserving the helical organization of EspC and AaaA. The work presented in this thesis offers potential for mechanistic understanding of the AT secretion system. By characterizing the precise translocation process to reveal the molecular mechanism involved in the spiral secretion of EspC this would offer the potential to discover inhibitors that might serve as a novel antimicrobial. Novel antimicrobial agents are desperately needed because those currently available have become ineffective due to the emergence of antibiotic resistance in hospitals and communities (329,330). Therefore, immediate action needs to be taken to contain this situation. Here, it has been illustrated that interfering with EspC-mCherry secretion perturbs cell shape and leads to growth defects and this perhaps provides potential for a novel antimicrobial strategy. Other possible therapeutic targets that can be focused on AT biogenesis for development of novel anti-virulence compounds are shown in Fig. 7.1

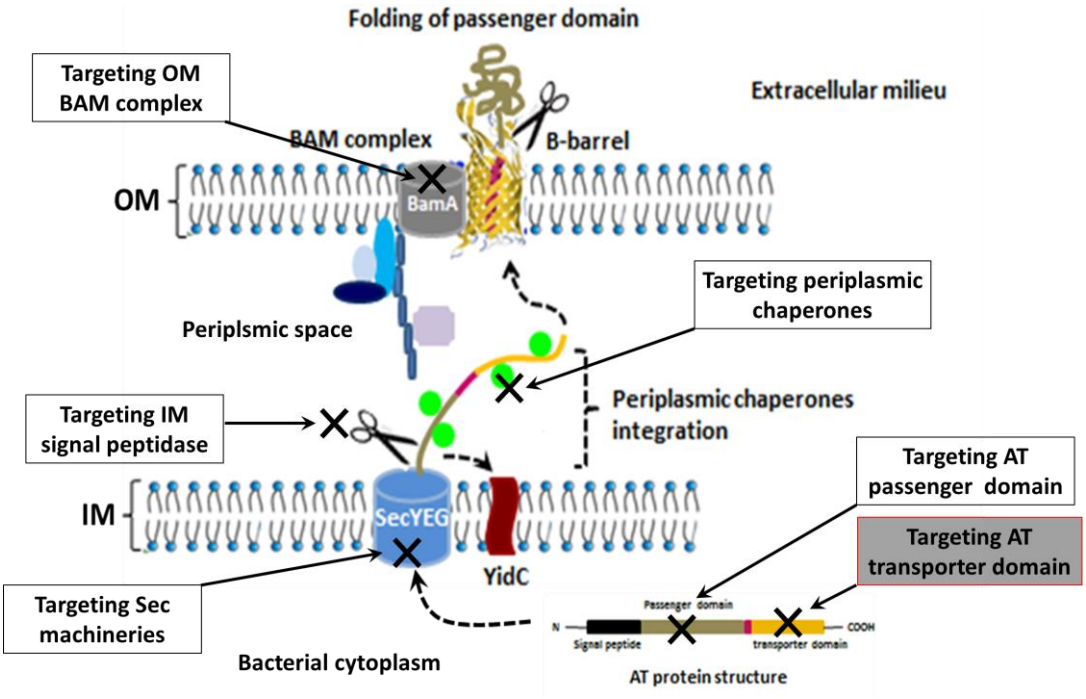


Figure 7.1: Schematic presentation of the AT secretion pathway and the prediction of possible targets for novel antimicrobials. ATs are synthesized in the cytoplasm and then targeted to the IM channel SecYEG which releases them to the periplasm. After integration with the BAM complex, translocation across the OM and release to the outside occurs. Potential therapeutic targets (**X**) are shown. The consequences of perturbing the AT transporter domain is already elucidated in this study.

References

1. Croxen, M. A., Law, R. J., Scholz, R., Keeney, K. M., Wlodarska, M., and Finlay, B. B. (2013) Recent advances in understanding enteric pathogenic *Escherichia coli*. *Clinical Microbiology Reviews* **26**, 822-880

2. Lai, Y., Rosenshine, I., Leong, J. M., and Frankel, G. (2013) Intimate host attachment: enteropathogenic and enterohaemorrhagic *Escherichia coli*. *Cellular Microbiology* **15**, 1796-1808

3. Donnenberg, M. S., and Whittam, T. S. (2001) Pathogenesis and evolution of virulence in enteropathogenic and enterohemorrhagic *Escherichia coli*. *The Journal of Clinical Investigation* **107**, 539-548

4. Iguchi, A., Thomson, N. R., Ogura, Y., Saunders, D., Ooka, T., Henderson, I. R., Harris, D., Asadulghani, M., Kurokawa, K., Dean, P., Kenny, B., Quail, M. A., Thurston, S., Dougan, G., Hayashi, T., Parkhill, J., and Frankel, G. (2009) Complete genome sequence and comparative genome analysis of enteropathogenic *Escherichia coli* O127:H6 strain E2348/69. *Journal of Bacteriology* **191**, 347-354

5. Clements, A., Young, J. C., Constantinou, N., and Frankel, G. (2012) Infection strategies of enteric pathogenic *Escherichia coli*. *Gut Microbes* **3**, 71-87

6. Servin, A. L. (2014) Pathogenesis of human diffusely adhering *Escherichia coli* expressing Afa/Dr adhesins (Afa/Dr DAEC): current insights and future challenges. *Clinical Microbiology Reviews* **27**, 823-869

7. Lee, D. W., Gwack, J., and Youn, S. K. (2012) Enteropathogenic *Escherichia coli* outbreak and its incubation period: is it short or long? *Osong Public Health and Research Perspectives* **3**, 43-47

8. Nataro, J. P., and Kaper, J. B. (1998) Diarrheagenic *Escherichia coli*. *Clinical Microbiology Reviews* **11**, 142-201

9. Baldwin, T. J. (1998) The 18th C.L. Oakley Lecture. Pathogenicity of enteropathogenic *Escherichia coli*. *Journal of Medical Microbiology* **47**, 283-293

10. Shulman, S. T. (2004) The history of pediatric infectious diseases. *Pediatric Research* **55**, 163-176

11. Ochoa, T. J., and Contreras, C. A. (2011) Enteropathogenic *Escherichia coli* infection in children. *Current Opinion in Infectious Diseases* **24**, 478-483

12. Lacher, D. W., Steinsland, H., Blank, T. E., Donnenberg, M. S., and Whittam, T. S. (2007) Molecular evolution of typical enteropathogenic *Escherichia coli*: clonal analysis by multilocus sequence typing and virulence gene allelic profiling. *Journal of Bacteriology* **189**, 342-350

13. Ochoa, T. J., Barletta, F., Contreras, C., and Mercado, E. (2008) New insights into the epidemiology of enteropathogenic *Escherichia coli* infection. *Transactions of the Royal Society of Tropical Medicine and Hygiene* **102**, 852-856

14. Robins-Browne, R. M., Yam, W. C., O'Gorman, L. E., and Bettelheim, K. A. (1993) Examination of archetypal strains of enteropathogenic *Escherichia coli* for properties associated with bacterial virulence. *Journal of Medical Microbiology* **38**, 222-226

15. Levine, M. M., Bergquist, E. J., Nalin, D. R., Waterman, D. H., Hornick, R. B., Young, C. R., and Sotman, S. (1978) *Escherichia coli* strains that cause diarrhoea but do not produce heat-labile or heat-stable enterotoxins and are non-invasive. *Lancet* **1**, 1119-1122

16. Vallance, B. A., and Finlay, B. B. (2000) Exploitation of host cells by enteropathogenic *Escherichia coli*. *Proceedings of the National Academy of Sciences of the United States of America* **97**, 8799-8806

17. Frankel, G., Phillips, A. D., Rosenshine, I., Dougan, G., Kaper, J. B., and Knutton, S. (1998) Enteropathogenic and enterohaemorrhagic *Escherichia coli*: more subversive elements. *Molecular Microbiology* **30**, 911-921

18. Clarke, S. C., Haigh, R. D., Freestone, P. P., and Williams, P. H. (2003) Virulence of enteropathogenic *Escherichia coli*, a global pathogen. *Clinical Microbiology Reviews* **16**, 365-378

19. Navarro-Garcia, F., Serapio-Palacios, A., Ugalde-Silva, P., Tapia-Pastrana, G., and Chavez-Duenas, L. (2013) Actin cytoskeleton manipulation by effector proteins secreted by diarrheagenic *Escherichia coli* pathotypes. *BioMed Research International* **2013**, 374395

20. Chen, H. D., and Frankel, G. (2005) Enteropathogenic *Escherichia coli*: unravelling pathogenesis. *Federation of European Microbiological Societies Microbiology Reviews* **29**, 83-98

21. Jerse, A. E., Yu, J., Tall, B. D., and Kaper, J. B. (1990) A genetic locus of enteropathogenic *Escherichia coli* necessary for the production of attaching and effacing lesions on tissue culture cells. *Proceedings of the National Academy of Sciences of the United States of America* **87**, 7839-7843

22. Franzin, F. M., and Sircili, M. P. (2015) Locus of enterocyte effacement: a pathogenicity island involved in the virulence of enteropathogenic and enterohemorragic *Escherichia coli* subjected to a complex network of gene regulation. *BioMed Research International* **2015**, 534738

23. McDaniel, T. K., and Kaper, J. B. (1997) A cloned pathogenicity island from enteropathogenic *Escherichia coli* confers the attaching and effacing phenotype on *E. coli* K-12. *Molecular Microbiology* **23**, 399-407

24. Kenny, B. (2002) Enteropathogenic *Escherichia coli* (EPEC)-- a crafty subversive little bug. *Microbiology (Reading, England)* **148**, 1967-1978

25. Elliott, S. J., Wainwright, L. A., McDaniel, T. K., Jarvis, K. G., Deng, Y. K., Lai, L. C., McNamara, B. P., Donnenberg, M. S., and Kaper, J. B. (1998) The complete sequence of the locus of enterocyte effacement (LEE) from enteropathogenic *Escherichia coli* E2348/69. *Molecular Microbiology* **28**, 1-4

26. Navarro-Garcia, F., Sonnested, M., and Teter, K. (2010) Host-toxin interactions involving EspC and Pet, two serine protease autotransporters of the Enterobacteriaceae. *Toxins* **2**, 1134-1147

27. Kenny, B., Lai, L. C., Finlay, B. B., and Donnenberg, M. S. (1996) EspA, a protein secreted by enteropathogenic *Escherichia coli*, is required to induce signals in epithelial cells. *Molecular Microbiology* **20**, 313-323

28. Lai, L. C., Wainwright, L. A., Stone, K. D., and Donnenberg, M. S. (1997) A third secreted protein that is encoded by the enteropathogenic *Escherichia coli* pathogenicity island is required for transduction of signals and for attaching and effacing activities in host cells. *Infection and Immunity* **65**, 2211-2217

29. Taylor, K. A., O'Connell, C. B., Luther, P. W., and Donnenberg, M. S. (1998) The EspB protein of enteropathogenic *Escherichia coli* is targeted to the cytoplasm of infected HeLa cells. *Infection and Immunity* **66**, 5501-5507

30. McNamara, B. P., and Donnenberg, M. S. (1998) A novel proline-rich protein, EspF, is secreted from enteropathogenic *Escherichia coli* via the type III export pathway. *Federation of European Microbiological Societies Microbiology Letters* **166**, 71-78

31. Shaw, R. K., Smollett, K., Cleary, J., Garmendia, J., Straatman-Iwanowska, A., Frankel, G., and Knutton, S. (2005) Enteropathogenic *Escherichia coli* type III effectors EspG and EspG2 disrupt the microtubule network of intestinal epithelial cells. *Infection and Immunity* **73**, 4385-4390

32. Garmendia, J., Frankel, G., and Crepin, V. F. (2005) Enteropathogenic and enterohemorrhagic *Escherichia coli* infections: translocation, translocation, translocation. *Infection and Immunity* **73**, 2573-2585

33. Dean, P., Maresca, M., and Kenny, B. (2005) EPEC's weapons of mass subversion. *Current Opinion in Microbiology* **8**, 28-34

34. Vidal, J. E., and Navarro-Garcia, F. (2006) Efficient translocation of EspC into epithelial cells depends on enteropathogenic *Escherichia coli* and host cell contact. *Infection and Immunity* **74**, 2293-2303

35. Vidal, J. E., and Navarro-Garcia, F. (2008) EspC translocation into epithelial cells by enteropathogenic *Escherichia coli* requires a concerted participation of type V and III secretion systems. *Cellular Microbiology* **10**, 1975-1986

36. Mellies, J. L., Navarro-Garcia, F., Okeke, I., Frederickson, J., Nataro, J. P., and Kaper, J. B. (2001) *espC* pathogenicity island of enteropathogenic *Escherichia coli* encodes an enterotoxin. *Infection and Immunity* **69**, 315-324

37. Dean, P., and Kenny, B. (2009) The effector repertoire of enteropathogenic *E. coli*: ganging up on the host cell. *Current Opinion in Microbiology* **12**, 101-109

38. Ruano-Gallego, D., Alvarez, B., and Fernandez, L. A. (2015) Engineering the controlled assembly of filamentous injectisomes in *E. coli* K-12 for protein translocation into mammalian cells. *American Chemical Society Synthetic Biology* **4**, 1030-1041

39. Glotfelty, L. G., Zahs, A., Hodges, K., Shan, K., Alto, N. M., and Hecht, G. A. (2014) Enteropathogenic *E. coli* effectors EspG1/G2 disrupt microtubules, contribute to tight junction perturbation and inhibit restoration. *Cellular Microbiology* **16**, 1767-1783

40. Elliott, S. J., Krejany, E. O., Mellies, J. L., Robins-Browne, R. M., Sasakawa, C., and Kaper, J. B. (2001) EspG, a novel type III system-secreted protein from enteropathogenic *Escherichia coli* with similarities to VirA of *Shigella flexneri*. *Infection and Immunity* **69**, 4027-4033

41. Glotfelty, L. G., and Hecht, G. A. (2012) Enteropathogenic *E. coli* effectors EspG1/G2 disrupt tight junctions: new roles and mechanisms. *Annals of the New York Academy of Sciences* **1258**, 149-158

42. Lee, C. A. (1997) Type III secretion systems: machines to deliver bacterial proteins into eukaryotic cells? *Trends in Microbiology* **5**, 148-156

43. Zhou, M., Guo, Z., Duan, Q., Hardwidge, P. R., and Zhu, G. (2014) *Escherichia coli* type III secretion system 2: a new kind of T3SS? *Veterinary Research* **45**, 32

44. Luo, W., and Donnenberg, M. S. (2011) Interactions and predicted host membrane topology of the enteropathogenic *Escherichia coli* translocator protein EspB. *Journal of Bacteriology* **193**, 2972-2980

45. Knutton, S., Rosenshine, I., Pallen, M. J., Nisan, I., Neves, B. C., Bain, C., Wolff, C., Dougan, G., and Frankel, G. (1998) A novel EspA-associated surface organelle of enteropathogenic *Escherichia coli* involved in protein translocation into epithelial cells. *The European Molecular Biology Organization Journal* **17**, 2166-2176

46. Kenny, B., DeVinney, R., Stein, M., Reinscheid, D. J., Frey, E. A., and Finlay, B. B. (1997) Enteropathogenic *E. coli* (EPEC) transfers its receptor for intimate adherence into mammalian cells. *Cell* **91**, 511-520

47. Kenny, B. (1999) Phosphorylation of tyrosine 474 of the enteropathogenic *Escherichia coli* (EPEC) Tir receptor molecule is essential for actin nucleating activity and is preceded by additional host modifications. *Molecular Microbiology* **31**, 1229-1241

48. Campellone, K. G. (2010) Cytoskeleton-modulating effectors of enteropathogenic and enterohaemorrhagic *Escherichia coli*: Tir, EspFU and actin pedestal assembly. *The Federation of European Biochemical Societies journal* **277**, 2390-2402

49. Phillips, N., Hayward, R. D., and Koronakis, V. (2004) Phosphorylation of the enteropathogenic *E. coli* receptor by the Src-family kinase c-Fyn triggers actin pedestal formation. *Nature Cell Biology* **6**, 618-625

50. Scaletsky, I. C., Silva, M. L., and Trabulsi, L. R. (1984) Distinctive patterns of adherence of enteropathogenic *Escherichia coli* to HeLa cells. *Infection and Immunity* **45**, 534-536

51. Aroeti, B., Friedman, G., Zlotkin-Rivkin, E., and Donnenberg, M. S. (2012) Retraction of enteropathogenic *E. coli* type IV pili promotes efficient host cell colonization, effector translocation and tight junction disruption. *Gut Microbes* **3**, 267-271

52. Zahavi, E. E., Lieberman, J. A., Donnenberg, M. S., Nitzan, M., Baruch, K., Rosenshine, I., Turner, J. R., Melamed-Book, N., Feinstein, N., Zlotkin-Rivkin, E., and Aroeti, B. (2011) Bundle-forming pilus retraction enhances enteropathogenic *Escherichia coli* infectivity. *Molecular Biology of The Cell* **22**, 2436-2447

53. Anantha, R. P., Stone, K. D., and Donnenberg, M. S. (2000) Effects of *bfp* mutations on biogenesis of functional enteropathogenic *Escherichia coli* type IV pili. *Journal of Bacteriology* **182**, 2498-2506

54. Bieber, D., Ramer, S. W., Wu, C. Y., Murray, W. J., Tobe, T., Fernandez, R., and Schoolnik, G. K. (1998) Type IV pili, transient bacterial aggregates, and virulence of enteropathogenic *Escherichia coli*. *Science* **280**, 2114-2118

55. Bustamante, V. H., Villalba, M. I., Garcia-Angulo, V. A., Vazquez, A., Martinez, L. C., Jimenez, R., and Puente, J. L. (2011) PerC and GrlA independently regulate Ler expression in enteropathogenic *Escherichia coli*. *Molecular Microbiology* **82**, 398-415

56. Elliott, S. J., Sperandio, V., Giron, J. A., Shin, S., Mellies, J. L., Wainwright, L., Hutcheson, S. W., McDaniel, T. K., and Kaper, J. B. (2000) The locus of enterocyte effacement (LEE)-encoded regulator controls expression of both LEE- and non-LEE-encoded virulence factors in enteropathogenic and enterohemorrhagic *Escherichia coli*. *Infection and Immunity* **68**, 6115-6126

57. Deng, W., Puente, J. L., Gruenheid, S., Li, Y., Vallance, B. A., Vazquez, A., Barba, J., Ibarra, J. A., O'Donnell, P., Metalnikov, P., Ashman, K., Lee, S., Goode, D., Pawson, T., and Finlay, B. B. (2004) Dissecting virulence: systematic and functional analyses of a pathogenicity island. *Proceedings of the National Academy of Sciences of the United States of America* **101**, 3597-3602

58. Padavannil, A., Jobichen, C., Mills, E., Velazquez-Campoy, A., Li, M., Leung, K. Y., Mok, Y. K., Rosenshine, I., and Sivaraman, J. (2013) Structure of GrlR-GrlA complex that prevents GrlA activation of virulence genes. *Nature Communications* **4**, 2546

59. Gomez-Duarte, O. G., and Kaper, J. B. (1995) A plasmid-encoded regulatory region activates chromosomal *eaeA* expression in enteropathogenic *Escherichia coli*. *Infection and Immunity* **63**, 1767-1776

60. Bustamante, V. H., Santana, F. J., Calva, E., and Puente, J. L. (2001) Transcriptional regulation of type III secretion genes in enteropathogenic *Escherichia coli*: Ler antagonizes H-NS-dependent repression. *Molecular Microbiology* **39**, 664-678

61. Friedberg, D., Umanski, T., Fang, Y., and Rosenshine, I. (1999) Hierarchy in the expression of the locus of enterocyte effacement genes of enteropathogenic *Escherichia coli*. *Molecular Microbiology* **34**, 941-952

62. Levine, J. A., Hansen, A. M., Michalski, J. M., Hazen, T. H., Rasko, D. A., and Kaper, J. B. (2014) H-NST induces LEE expression and the formation of attaching and effacing lesions in enterohemorrhagic *Escherichia coli*. *Public Library of Science one* **9**, e86618

63. Goldberg, M. D., Johnson, M., Hinton, J. C., and Williams, P. H. (2001) Role of the nucleoid-associated protein Fis in the regulation of virulence properties of enteropathogenic *Escherichia coli*. *Molecular Microbiology* **41**, 549-559

64. Grant, A. J., Farris, M., Alefounder, P., Williams, P. H., Woodward, M. J., and O'Connor, C. D. (2003) Co-ordination of pathogenicity island expression by the BipA GTPase in enteropathogenic *Escherichia coli* (EPEC). *Molecular Microbiology* **48**, 507-521

65. MacRitchie, D. M., Acosta, N., and Raivio, T. L. (2012) DegP is involved in Cpx-mediated posttranscriptional regulation of the type III secretion apparatus in enteropathogenic *Escherichia coli*. *Infection and Immunity* **80**, 1766-1772

66. Bhatt, S., Edwards, A. N., Nguyen, H. T., Merlin, D., Romeo, T., and Kalman, D. (2009) The RNA binding protein CsrA is a pleiotropic regulator of the locus of enterocyte effacement pathogenicity island of enteropathogenic *Escherichia coli*. *Infection and Immunity* **77**, 3552-3568

67. Puente, J. L., Bieber, D., Ramer, S. W., Murray, W., and Schoolnik, G. K. (1996) The bundle-forming pili of enteropathogenic *Escherichia coli*: transcriptional regulation by environmental signals. *Molecular Microbiology* **20**, 87-100

68. Sircili, M. P., Walters, M., Trabulsi, L. R., and Sperandio, V. (2004) Modulation of enteropathogenic *Escherichia coli* virulence by quorum sensing. *Infection and Immunity* **72**, 2329-2337

69. Sperandio, V., Li, C. C., and Kaper, J. B. (2002) Quorum-sensing *Escherichia coli* regulator A: a regulator of the LysR family involved in the regulation of the locus of enterocyte effacement pathogenicity island in enterohemorrhagic *E. coli*. *Infection and Immunity* **70**, 3085-3093

70. Sperandio, V., Torres, A. G., Jarvis, B., Nataro, J. P., and Kaper, J. B. (2003) Bacteria-host communication: the language of hormones. *Proceedings of the National Academy of Sciences of the United States of America* **100**, 8951-8956

71. Abreu, A. G., Bueris, V., Porangaba, T. M., Sircili, M. P., Navarro-Garcia, F., and Elias, W. P. (2013) Autotransporter protein-encoding genes of diarrheagenic *Escherichia coli* are found in both typical and atypical enteropathogenic *E. coli* strains. *Applied and Environmental Microbiology* **79**, 411-414

72. Henderson, I. R., Navarro-Garcia, F., Desvaux, M., Fernandez, R. C., and Ala'Aldeen, D. (2004) Type V protein secretion pathway: the autotransporter story. *Microbiology and Molecular Biology Reviews* **68**, 692-744

73. Navarro-Garcia, F., Canizalez-Roman, A., Sui, B. Q., Nataro, J. P., and Azamar, Y. (2004) The serine protease motif of EspC from enteropathogenic *Escherichia col*i produces epithelial damage by a mechanism different from that of Pet toxin from enteroaggregative *E. coli*. *Infection and Immunity* **72**, 3609-3621

74. Drago-Serrano, M. E., Parra, S. G., and Manjarrez-Hernandez, H. A. (2006) EspC, an autotransporter protein secreted by enteropathogenic *Escherichia coli* (EPEC), displays protease activity on human hemoglobin. *Federation of European Microbiological Societies microbiology Letters* **265**, 35-40

75. Stein, M., Kenny, B., Stein, M. A., and Finlay, B. B. (1996) Characterization of EspC, a 110-kilodalton protein secreted by enteropathogenic *Escherichia coli* which is homologous to members of the immunoglobulin A protease-like family of secreted proteins. *Journal of Bacteriology* **178**, 6546-6554

76. Orth, D., Ehrlenbach, S., Brockmeyer, J., Khan, A. B., Huber, G., Karch, H., Sarg, B., Lindner, H., and Wurzner, R. (2010) EspP, a serine protease of enterohemorrhagic *Escherichia coli*, impairs complement activation by cleaving complement factors C3/C3b and C5. *Infection and Immunity* **78**, 4294-4301

77. Schmidt, H., Zhang, W. L., Hemmrich, U., Jelacic, S., Brunder, W., Tarr, P. I., Dobrindt, U., Hacker, J., and Karch, H. (2001) Identification and characterization of a novel genomic island integrated at selC in locus of enterocyte effacement-negative, Shiga toxin-producing *Escherichia coli*. *Infection and Immunity* **69**, 6863-6873

78. Weiss, A., Joerss, H., and Brockmeyer, J. (2014) Structural and functional characterization of cleavage and inactivation of human serine protease inhibitors by the bacterial SPATE protease EspPalpha from enterohemorrhagic *E. coli*. *Public Library of Science one* **9**, e111363

79. Dutta, P. R., Sui, B. Q., and Nataro, J. P. (2003) Structure-function analysis of the enteroaggregative *Escherichia coli* plasmid-encoded toxin autotransporter using scanning linker mutagenesis. *The Journal of Biological Chemistry* **278**, 39912-39920

80. Henderson, I. R., Czeczulin, J., Eslava, C., Noriega, F., and Nataro, J. P. (1999) Characterization of pic, a secreted protease of *Shigella flexneri* and enteroaggregative *Escherichia coli*. *Infection and Immunity* **67**, 5587-5596

81. Patel, S. K., Dotson, J., Allen, K. P., and Fleckenstein, J. M. (2004) Identification and molecular characterization of EatA, an autotransporter protein of enterotoxigenic *Escherichia coli*. *Infection and Immunity* **72**, 1786-1794

82. Guignot, J., Chaplais, C., Coconnier-Polter, M. H., and Servin, A. L. (2007) The secreted autotransporter toxin, Sat, functions as a virulence factor in Afa/Dr diffusely adhering *Escherichia coli* by promoting lesions in tight junction of polarized epithelial cells. *Cellular Microbiology* **9**, 204-221

83. Elsinghorst, E. A., and Weitz, J. A. (1994) Epithelial cell invasion and adherence directed by the enterotoxigenic *Escherichia coli* tib locus is associated with a 104-kilodalton outer membrane protein. *Infection and Immunity* **62**, 3463-3471

84. Torres, A. G., Perna, N. T., Burland, V., Ruknudin, A., Blattner, F. R., and Kaper, J. B. (2002) Characterization of Cah, a calcium-binding and heat-extractable autotransporter protein of enterohaemorrhagic *Escherichia coli*. *Molecular Microbiology* **45**, 951-966

85. Wells, T. J., Sherlock, O., Rivas, L., Mahajan, A., Beatson, S. A., Torpdahl, M., Webb, R. I., Allsopp, L. P., Gobius, K. S., Gally, D. L., and Schembri, M. A. (2008) EhaA is a novel autotransporter protein of enterohemorrhagic *Escherichia coli* O157:H7 that contributes to adhesion and biofilm formation. *Environmental Microbiology* **10**, 589-604

86. Easton, D. M., Totsika, M., Allsopp, L. P., Phan, M. D., Idris, A., Wurpel, D. J., Sherlock, O., Zhang, B., Venturini, C., Beatson, S. A., Mahony, T. J., Cobbold, R. N., and Schembri, M. A. (2011) Characterization of EhaJ, a new autotransporter protein from enterohemorrhagic and enteropathogenic *Escherichia coli*. *Frontiers in Microbiolog* **2**, 120

87. Navarro-Garcia, F., Serapio-Palacios, A., Vidal, J. E., Salazar, M. I., and Tapia-Pastrana, G. (2014) EspC promotes epithelial cell detachment by enteropathogenic *Escherichia coli* via sequential cleavages of a cytoskeletal protein and then focal adhesion proteins. *Infection and Immunity* **82**, 2255-2265

88. Guignot, J., Segura, A., and Tran Van Nhieu, G. (2015) The serine protease EspC from enteropathogenic *Escherichia coli* regulates pore formation and cytotoxicity mediated by the type III secretion system. *Public Library of Science pathogens* **11**, e1005013

89. Ruiz-Perez, F., and Nataro, J. P. (2014) Bacterial serine proteases secreted by the autotransporter pathway: classification, specificity, and role in virulence. *Cellular and Molecular Life Sciences* **71**, 745-770

90. Dautin, N. (2010) Serine protease autotransporters of Enterobacteriaceae (SPATEs): biogenesis and function. *Toxins* **2**, 1179-1206

91. Yen, Y. T., Kostakioti, M., Henderson, I. R., and Stathopoulos, C. (2008) Common themes and variations in serine protease autotransporters. *Trends in Microbiology* **16**, 370-379

92. Yen, M. R., Peabody, C. R., Partovi, S. M., Zhai, Y., Tseng, Y. H., and Saier, M. H. (2002) Protein-translocating outer membrane porins of Gram-negative bacteria. *Biochimica et biophysica acta* **1562**, 6-31

93. Leyton, D. L., Rossiter, A. E., and Henderson, I. R. (2012) From self sufficiency to dependence: mechanisms and factors important for autotransporter biogenesis. *Nature Reviews. Microbiology* **10**, 213-225

94. Gawarzewski, I., Smits, S. H., Schmitt, L., and Jose, J. (2013) Structural comparison of the transport units of type V secretion systems. *Biological Chemistry* **394**, 1385-1398

95. Leo, J. C., Grin, I., and Linke, D. (2012) Type V secretion: mechanism(s) of autotransport through the bacterial outer membrane. *Philosophical Transactions of The Royal Society of London. Series B, Biological sciences* **367**, 1088-1101

96. McBride, M. J., and Zhu, Y. (2013) Gliding motility and Por secretion system genes are widespread among members of the phylum bacteroidetes. *Journal of Bacteriology* **195**, 270-278

97. Abby, S. S., Cury, J., Guglielmini, J., Neron, B., Touchon, M., and Rocha, E. P. (2016) Identification of protein secretion systems in bacterial genomes. *Scientific Reports* **6**, 23080

98. Chagnot, C., Zorgani, M. A., Astruc, T., and Desvaux, M. (2013) Proteinaceous determinants of surface colonization in bacteria: bacterial adhesion and biofilm formation from a protein secretion perspective. *Frontiers in Microbiology* **4**, 303

99. Costa, T. R., Felisberto-Rodrigues, C., Meir, A., Prevost, M. S., Redzej, A., Trokter, M., and Waksman, G. (2015) Secretion systems in Gram-negative bacteria: structural and mechanistic insights. *Nature Reviews. Microbiology* **13**, 343-359

100. Fan, E., Chauhan, N., Udatha, D. B., Leo, J. C., and Linke, D. (2016) Type V secretion systems in bacteria. *Microbiology Spectrum* **4**

101. Grijpstra, J., Arenas, J., Rutten, L., and Tommassen, J. (2013) Autotransporter secretion: varying on a theme. *Research in Microbiology* **164**, 562-582

102. Pohlner, J., Halter, R., Beyreuther, K., and Meyer, T. F. (1987) Gene structure and extracellular secretion of *Neisseria gonorrhoeae* IgA protease. *Nature* **325**, 458-462

103. Henderson, I. R., and Nataro, J. P. (2001) Virulence functions of autotransporter proteins. *Infection and Immunity* **69**, 1231-1243

104. Oliver, D. C., Huang, G., Nodel, E., Pleasance, S., and Fernandez, R. C. (2003) A conserved region within the *Bordetella pertussis* autotransporter BrkA is necessary for folding of its passenger domain. *Molecular Microbiology* **47**, 1367-1383

105. Velarde, J. J., and Nataro, J. P. (2004) Hydrophobic residues of the autotransporter EspP linker domain are important for outer membrane translocation of its passenger. *The Journal of Biological Chemistry* **279**, 31495-31504

106. Kostakioti, M., and Stathopoulos, C. (2006) Role of the alpha-helical linker of the C-terminal translocator in the biogenesis of the serine protease subfamily of autotransporters. *Infection and Immunity* **74**, 4961-4969

107. Desvaux, M., Parham, N. J., and Henderson, I. R. (2004) Type V protein secretion: simplicity gone awry? *Current Issues in Molecular Biology* **6**, 111-124

108. Peterson, J. H., Tian, P., Ieva, R., Dautin, N., and Bernstein, H. D. (2010) Secretion of a bacterial virulence factor is driven by the folding of a C-terminal segment. *Proceedings of The National Academy of Sciences of the United States of America* **107**, 17739-17744

109. Soprova, Z., Sauri, A., van Ulsen, P., Tame, J. R., den Blaauwen, T., Jong, W. S., and Luirink, J. (2010) A conserved aromatic residue in the autochaperone domain of the autotransporter Hbp is critical for initiation of outer membrane translocation. *The Journal of Biological Chemistry* **285**, 38224-38233

110. Drobnak, I., Braselmann, E., and Clark, P. L. (2015) Multiple driving forces required for efficient secretion of autotransporter virulence proteins. *The Journal of Biological Chemistry* **290**, 10104-10116

111. Bishop, K. (2009) Dissecting protein-protein interactions facilitating secretion of the virulence factor EspC by enteropathogenic *Escherichia coli.* MPhil thesis. The University of Nottingham.

112. van Ulsen, P., Rahman, S., Jong, W. S., Daleke-Schermerhorn, M. H., and Luirink, J. (2014) Type V secretion: from biogenesis to biotechnology. *Biochimica et Biophysica acta* **1843**, 1592-1611

113. Meng, G., Surana, N. K., St Geme, J. W., 3rd, and Waksman, G. (2006) Structure of the outer membrane translocator domain of the *Haemophilus influenzae* Hia trimeric autotransporter. *The European Molecular Biology Organization journal* **25**, 2297-2304

114. Weiss, A., and Brockmeyer, J. (2013) Prevalence, biogenesis, and functionality of the serine protease autotransporter EspP. *Toxins* **5**, 25-48

115. Abreu, A. G., Abe, C. M., Nune, K. O., Moraes, C. T., Chavez-Duenas, L., Navarro-Garcia, F., Barbosa, A. S., Piazza, R. M., and Elias, W. P. (2016) The serine protease Pic as a virulence factor of atypical enteropathogenic *Escherichia coli*. *Gut Microbes* **7**, 115-125

116. Benjelloun-Touimi, Z., Sansonetti, P. J., and Parsot, C. (1995) SepA, the major extracellular protein of *Shigella flexneri*: autonomous secretion and involvement in tissue invasion. *Molecular Microbiology* **17**, 123-135

117. Parreira, V. R., and Gyles, C. L. (2003) A novel pathogenicity island integrated adjacent to the thrW tRNA gene of avian pathogenic *Escherichia coli* encodes a vacuolating autotransporter toxin. *Infection and Immunity* **71**, 5087-5096

118. Nishimura, K., Yoon, Y. H., Kurihara, A., Unzai, S., Luirink, J., Park, S. Y., and Tame, J. R. (2010) Role of domains within the autotransporter Hbp/Tsh. *Acta crystallographica. Section D, Biological Crystallography* **66**, 1295-1300

119. van Ulsen, P., van Alphen, L., ten Hove, J., Fransen, F., van der Ley, P., and Tommassen, J. (2003) A Neisserial autotransporter NalP modulating the processing of other autotransporters. *Molecular Microbiology* **50**, 1017-1030

120. Fink, D. L., Green, B. A., and St Geme, J. W., 3rd. (2002) The *Haemophilus influenzae* Hap autotransporter binds to fibronectin, laminin, and collagen IV. *Infection and Immunity* **70**, 4902-4907

121. Reyrat, J. M., Charrel, M., Pagliaccia, C., Burroni, D., Lupetti, P., de Bernard, M., Ji, X., Norais, N., Papini, E., Dallai, R., Rappuoli, R., and Telford, J. L. (1998) Characterisation of a monoclonal antibody and its use to purify the cytotoxin of *Helicobacter pylori*. *Federation of European Microbiological Societies Microbiology Letters* **165**, 79-84

122. Goldberg, M. B., Barzu, O., Parsot, C., and Sansonetti, P. J. (1993) Unipolar localization and ATPase activity of IcsA, a *Shigella flexneri* protein involved in intracellular movement. *Journal of Bacteriology* **175**, 2189-2196

123. Benz, I., and Schmidt, M. A. (1992) AIDA-I, the adhesin involved in diffuse adherence of the diarrhoeagenic *Escherichia coli* strain 2787 (O126:H27), is synthesized via a precursor molecule. *Molecular Microbiology* **6**, 1539-1546

124. Cote, J. P., and Mourez, M. (2011) Structure-function analysis of the TibA self-associating autotransporter reveals a modular organization. *Infection and Immunity* **79**, 1826-1832

125. Kjaergaard, K., Schembri, M. A., Hasman, H., and Klemm, P. (2000) Antigen 43 from *Escherichia coli* induces inter- and intraspecies cell aggregation and changes in colony morphology of *Pseudomonas fluorescens*. *Journal of Bacteriology* **182**, 4789-4796

126. Luckett, J. C., Darch, O., Watters, C., Abuoun, M., Wright, V., Paredes-Osses, E., Ward, J., Goto, H., Heeb, S., Pommier, S., Rumbaugh, K. P., Camara, M., and Hardie, K. R. (2012) A novel virulence strategy for *Pseudomonas aeruginosa* mediated by an autotransporter with arginine-specific aminopeptidase activity. *Public Library of Science Pathogens* **8**, e1002854

127. Wilhelm, S., Gdynia, A., Tielen, P., Rosenau, F., and Jaeger, K. E. (2007) The autotransporter esterase EstA of *Pseudomonas aeruginosa* is required for rhamnolipid production, cell motility, and biofilm formation. *Journal of Bacteriology* **189**, 6695-6703

128. Hoopman, T. C., Wang, W., Brautigam, C. A., Sedillo, J. L., Reilly, T. J., and Hansen, E. J. (2008) *Moraxella catarrhalis* synthesizes an autotransporter that is an acid phosphatase. *Journal of Bacteriology* **190**, 1459-1472

129. Barenkamp, S. J., and Leininger, E. (1992) Cloning, expression, and DNA sequence analysis of genes encoding nontypeable *Haemophilus influenzae* high-molecular-weight surface-exposed proteins related to filamentous hemagglutinin of *Bordetella pertussis*. *Infection and Immunity* **60**, 1302-1313

130. Guedin, S., Willery, E., Tommassen, J., Fort, E., Drobecq, H., Locht, C., and Jacob-Dubuisson, F. (2000) Novel topological features of FhaC, the outer membrane transporter involved in the secretion of the *Bordetella pertussis* filamentous hemagglutinin. *The Journal of Biological Chemistry* **275**, 30202-30210

131. Uphoff, T. S., and Welch, R. A. (1990) Nucleotide sequencing of the *Proteus mirabilis* calcium-independent hemolysin genes (hpmA and hpmB) reveals sequence similarity with the *Serratia marcescens* hemolysin genes (shlA and shlB). *Journal of Bacteriology* **172**, 1206-1216

132. Braun, V., Ondraczek, R., and Hobbie, S. (1993) Activation and secretion of Serratia hemolysin. *Zentralblatt fur Bakteriologie :International Journal of Medical Microbiology* **278**, 306-315

133. Surana, N. K., Cutter, D., Barenkamp, S. J., and St Geme, J. W., 3rd. (2004) The *Haemophilus influenzae* Hia autotransporter contains an unusually short trimeric translocator domain. *The Journal of Biological Chemistry* **279**, 14679-14685

134. Roggenkamp, A., Ackermann, N., Jacobi, C. A., Truelzsch, K., Hoffmann, H., and Heesemann, J. (2003) Molecular analysis of transport and oligomerization of the *Yersinia enterocolitica* adhesin YadA. *Journal of Bacteriology* **185**, 3735-3744

135. Scarselli, M., Serruto, D., Montanari, P., Capecchi, B., Adu-Bobie, J., Veggi, D., Rappuoli, R., Pizza, M., and Arico, B. (2006) *Neisseria meningitidis* NhhA is a multifunctional trimeric autotransporter adhesin. *Molecular Microbiology* **61**, 631-644

136. Griffiths, N. J., Hill, D. J., Borodina, E., Sessions, R. B., Devos, N. I., Feron, C. M., Poolman, J. T., and Virji, M. (2011) Meningococcal surface fibril (Msf) binds to activated vitronectin and inhibits the terminal complement pathway to increase serum resistance. *Molecular Microbiology* **82**, 1129-1149

137. Leo, J. C., Lyskowski, A., Hattula, K., Hartmann, M. D., Schwarz, H., Butcher, S. J., Linke, D., Lupas, A. N., and Goldman, A. (2011) The structure of *E. coli* IgG-binding protein D suggests a general model for bending and binding in trimeric autotransporter adhesins. *Structure (London, England: 1993)* **19**, 1021-1030

138. Salacha, R., Kovacic, F., Brochier-Armanet, C., Wilhelm, S., Tommassen, J., Filloux, A., Voulhoux, R., and Bleves, S. (2010) The *Pseudomonas aeruginosa* patatin-like protein PlpD is the archetype of a novel Type V secretion system. *Environmental Microbiology* **12**, 1498-1512

139. da Mata Madeira, P. V., Zouhir, S., Basso, P., Neves, D., Laubier, A., Salacha, R., Bleves, S., Faudry, E., Contreras-Martel, C., and Dessen, A. (2016) Structural basis of lipid targeting and destruction by the Type V secretion system of *Pseudomonas aeruginosa. Journal of Molecular Biology* **428**, 1790-1803

140. Green, E. R., and Mecsas, J. (2016) Bacterial secretion systems: An overview. *Microbiology Spectrum* **4**

141. Gold, V. A., Robson, A., Bao, H., Romantsov, T., Duong, F., and Collinson, I. (2010) The action of cardiolipin on the bacterial translocon. *Proceedings of the National Academy of Sciences of the United States of America* **107**, 10044-10049

142. Dautin, N., and Bernstein, H. D. (2007) Protein secretion in gram-negative bacteria via the autotransporter pathway. *Annual Review of Microbiology* **61**, 89-112

143. Desvaux, M., Cooper, L. M., Filenko, N. A., Scott-Tucker, A., Turner, S. M., Cole, J. A., and Henderson, I. R. (2006) The unusual extended signal peptide region of the type V secretion system is phylogenetically restricted. *Federation of European Microbiological Societies Microbiology Letters* **264**, 22-30

144. Peterson, J. H., Szabady, R. L., and Bernstein, H. D. (2006) An unusual signal peptide extension inhibits the binding of bacterial presecretory proteins to the signal recognition particle, trigger factor, and the SecYEG complex. *The Journal of Biological Chemistry* **281**, 9038-9048

145. Desvaux, M., Scott-Tucker, A., Turner, S. M., Cooper, L. M., Huber, D., Nataro, J. P., and Henderson, I. R. (2007) A conserved extended signal peptide region directs posttranslational protein translocation via a novel mechanism. *Microbiology (Reading, England)* **153**, 59-70

146. Jong, W. S., ten Hagen-Jongman, C. M., Ruijter, E., Orru, R. V., Genevaux, P., and Luirink, J. (2010) YidC is involved in the biogenesis of the secreted autotransporter hemoglobin protease. *The Journal of Biological Chemistry* **285**, 39682-39690

147. Szabady, R. L., Peterson, J. H., Skillman, K. M., and Bernstein, H. D. (2005) An unusual signal peptide facilitates late steps in the biogenesis of a bacterial autotransporter. *Proceedings of the National Academy of Sciences of the United States of America* **102**, 221-226

148. Okuda, S., and Tokuda, H. (2011) Lipoprotein sorting in bacteria. *Annual Review of Microbiology* **65**, 239-259

149. Roussel-Jazede, V., Grijpstra, J., van Dam, V., Tommassen, J., and van Ulsen, P. (2013) Lipidation of the autotransporter NalP of *Neisseria meningitidis* is required for its function in the release of cell-surface-exposed proteins. *Microbiology (Reading, England)* **159**, 286-295

150. Ruiz-Perez, F., Henderson, I. R., Leyton, D. L., Rossiter, A. E., Zhang, Y., and Nataro, J. P. (2009) Roles of periplasmic chaperone proteins in the biogenesis of serine protease autotransporters of Enterobacteriaceae. *Journal of Bacteriology* **191**, 6571-6583

151. Purdy, G. E., Fisher, C. R., and Payne, S. M. (2007) IcsA surface presentation in *Shigella flexneri* requires the periplasmic chaperones DegP, Skp, and SurA. *Journal of Bacteriology* **189**, 5566-5573

152. Ruiz-Perez, F., Henderson, I. R., and Nataro, J. P. (2010) Interaction of FkpA, a peptidyl-prolyl cis/trans isomerase with EspP autotransporter protein. *Gut Microbes* **1**, 339-344

153. Veiga, E., de Lorenzo, V., and Fernandez, L. A. (2004) Structural tolerance of bacterial autotransporters for folded passenger protein domains. *Molecular Microbiology* **52**, 1069-1080

154. Tapia-Pastrana, G., Chavez-Duenas, L., Lanz-Mendoza, H., Teter, K., and Navarro-Garcia, F. (2012) VirK is a periplasmic protein required for efficient secretion of plasmid-encoded toxin from enteroaggregative *Escherichia coli*. *Infection and Immunity* **80**, 2276-2285

155. Wagner, J. K., Heindl, J. E., Gray, A. N., Jain, S., and Goldberg, M. B. (2009) Contribution of the periplasmic chaperone Skp to efficient presentation of the autotransporter IcsA on the surface of *Shigella flexneri*. *Journal of Bacteriology* **191**, 815-821

156. Rizzitello, A. E., Harper, J. R., and Silhavy, T. J. (2001) Genetic evidence for parallel pathways of chaperone activity in the periplasm of *Escherichia coli*. *Journal of Bacteriology* **183**, 6794-6800

157. Sklar, J. G., Wu, T., Kahne, D., and Silhavy, T. J. (2007) Defining the roles of the periplasmic chaperones SurA, Skp, and DegP in *Escherichia coli*. *Genes and Development* **21**, 2473-2484

158. Jacob-Dubuisson, F., Guerin, J., Baelen, S., and Clantin, B. (2013) Two-partner secretion: as simple as it sounds? *Research in Microbiology* **164**, 583-595

159. Barnard, T. J., Dautin, N., Lukacik, P., Bernstein, H. D., and Buchanan, S. K. (2007) Autotransporter structure reveals intra-barrel cleavage followed by conformational changes. *Nature Structural and Molecular Biology* **14**, 1214-1220

160. Dautin, N., and Bernstein, H. D. (2011) Residues in a conserved alpha-helical segment are required for cleavage but not secretion of an *Escherichia coli* serine protease autotransporter passenger domain. *Journal of Bacteriology* **193**, 3748-3756

161. Roussel-Jazede, V., Van Gelder, P., Sijbrandi, R., Rutten, L., Otto, B. R., Luirink, J., Gros, P., Tommassen, J., and Van Ulsen, P. (2011) Channel properties of the translocator domain of the autotransporter Hbp of *Escherichia coli*. *Molecular Membrane Biology* **28**, 158-170

162. Zhai, Y., Zhang, K., Huo, Y., Zhu, Y., Zhou, Q., Lu, J., Black, I., Pang, X., Roszak, A. W., Zhang, X., Isaacs, N. W., and Sun, F. (2011) Autotransporter passenger domain secretion requires a hydrophobic cavity at the extracellular entrance of the beta-domain pore. *The Biochemical Journal* **435**, 577-587

163. Leyton, D. L., Sevastsyanovich, Y. R., Browning, D. F., Rossiter, A. E., Wells, T. J., Fitzpatrick, R. E., Overduin, M., Cunningham, A. F., and Henderson, I. R. (2011) Size and conformation limits to secretion of disulfide-bonded loops in autotransporter proteins. *The Journal of Biological Chemistry* **286**, 42283-42291

164. Selkrig, J., Mosbahi, K., Webb, C. T., Belousoff, M. J., Perry, A. J., Wells, T. J., Morris, F., Leyton, D. L., Totsika, M., Phan, M. D., Celik, N., Kelly, M., Oates, C., Hartland, E. L., Robins-Browne, R. M., Ramarathinam, S. H., Purcell, A. W., Schembri, M. A., Strugnell, R. A., Henderson, I. R., Walker, D., and Lithgow, T. (2012) Discovery of an archetypal protein transport system in bacterial outer membranes. *Nature Structural and Molecular Biology* **19**, 506-510, S501

165. Ieva, R., Skillman, K. M., and Bernstein, H. D. (2008) Incorporation of a polypeptide segment into the beta-domain pore during the assembly of a bacterial autotransporter. *Molecular Microbiology* **67**, 188-201

166. Junker, M., Besingi, R. N., and Clark, P. L. (2009) Vectorial transport and folding of an autotransporter virulence protein during outer membrane secretion. *Molecular Microbiology* **71**, 1323-1332

167. Skillman, K. M., Barnard, T. J., Peterson, J. H., Ghirlando, R., and Bernstein, H. D. (2005) Efficient secretion of a folded protein domain by a monomeric bacterial autotransporter. *Molecular Microbiology* **58**, 945-958

168. Veiga, E., Sugawara, E., Nikaido, H., de Lorenzo, V., and Fernandez, L. A. (2002) Export of autotransported proteins proceeds through an oligomeric ring shaped by C-terminal domains. *The European Molecular Biology Organization Journal* **21**, 2122-2131

169. Barnard, T. J., Gumbart, J., Peterson, J. H., Noinaj, N., Easley, N. C., Dautin, N., Kuszak, A. J., Tajkhorshid, E., Bernstein, H. D., and Buchanan, S. K. (2012) Molecular basis for the activation of a catalytic asparagine residue in a self-cleaving bacterial autotransporter. *Journal of Molecular Biology* **415**, 128-142

170. May, K. L., and Morona, R. (2008) Mutagenesis of the *Shigella flexneri* autotransporter IcsA reveals novel functional regions involved in IcsA biogenesis and recruitment of host neural Wiscott-Aldrich syndrome protein. *Journal of Bacteriology* **190**, 4666-4676

171. Junker, M., Schuster, C. C., McDonnell, A. V., Sorg, K. A., Finn, M. C., Berger, B., and Clark, P. L. (2006) Pertactin beta-helix folding mechanism suggests common themes for the secretion and folding of autotransporter proteins. *Proceedings of the National Academy of Sciences of the United States of America* **103**, 4918-4923

172. Gangwer, K. A., Mushrush, D. J., Stauff, D. L., Spiller, B., McClain, M. S., Cover, T. L., and Lacy, D. B. (2007) Crystal structure of the *Helicobacter pylori* vacuolating toxin p55 domain.

Proceedings of the National Academy of Sciences of the United States of America **104**, 16293-16298

173. Renn, J. P., and Clark, P. L. (2008) A conserved stable core structure in the passenger domain beta-helix of autotransporter virulence proteins. *Biopolymers* **89**, 420-427

174. Sauri, A., Soprova, Z., Wickstrom, D., de Gier, J. W., Van der Schors, R. C., Smit, A. B., Jong, W. S., and Luirink, J. (2009) The Bam (Omp85) complex is involved in secretion of the autotransporter haemoglobin protease. *Microbiology (Reading, England)* **155**, 3982-3991

175. Voulhoux, R., Bos, M. P., Geurtsen, J., Mols, M., and Tommassen, J. (2003) Role of a highly conserved bacterial protein in outer membrane protein assembly. *Science (New York, N.Y.)* **299**, 262-265

176. Bernstein, H. D. (2007) Are bacterial 'autotransporters' really transporters? *Trends in Microbiology* **15**, 441-447

177. Oomen, C. J., van Ulsen, P., van Gelder, P., Feijen, M., Tommassen, J., and Gros, P. (2004) Structure of the translocator domain of a bacterial autotransporter. *The European Molecular Biology Organization Journal* **23**, 1257-1266

178. Webb, C. T., Heinz, E., and Lithgow, T. (2012) Evolution of the beta-barrel assembly machinery. *Trends in Microbiology* **20**, 612-620

179. Rossiter, A. E., Leyton, D. L., Tveen-Jensen, K., Browning, D. F., Sevastsyanovich, Y., Knowles, T. J., Nichols, K. B., Cunningham, A. F., Overduin, M., Schembri, M. A., and Henderson, I. R. (2011) The essential beta-barrel assembly machinery complex components BamD and BamA are required for autotransporter biogenesis. *Journal of Bacteriology* **193**, 4250-4253

180. Hagan, C. L., Kim, S., and Kahne, D. (2010) Reconstitution of outer membrane protein assembly from purified components. *Science (New York, N.Y.)* **328**, 890-892

181. Gatzeva-Topalova, P. Z., Warner, L. R., Pardi, A., and Sousa, M. C. (2010) Structure and flexibility of the complete periplasmic domain of BamA: the protein insertion machine of the outer membrane. *Structure (London, England: 1993)* **18**, 1492-1501

182. Bakelar, J., Buchanan, S. K., and Noinaj, N. (2016) The structure of the beta-barrel assembly machinery complex. *Science (New York, N.Y.)* **351**, 180-186

183. Malinverni, J. C., Werner, J., Kim, S., Sklar, J. G., Kahne, D., Misra, R., and Silhavy, T. J. (2006) YfiO stabilizes the YaeT complex and is essential for outer membrane protein assembly in *Escherichia coli*. *Molecular Microbiology* **61**, 151-164

184. Noinaj, N., Fairman, J. W., and Buchanan, S. K. (2011) The crystal structure of BamB suggests interactions with BamA and its role within the BAM complex. *Journal of Molecular Biology* **407**, 248-260

185. Noinaj, N., Kuszak, A. J., Gumbart, J. C., Lukacik, P., Chang, H., Easley, N. C., Lithgow, T., and Buchanan, S. K. (2013) Structural insight into the biogenesis of beta-barrel membrane proteins. *Nature* **501**, 385-390

186. Noinaj, N., Kuszak, A. J., Balusek, C., Gumbart, J. C., and Buchanan, S. K. (2014) Lateral opening and exit pore formation are required for BamA function. *Structure (London, England: 1993)* **22**, 1055-1062

187. Sinnige, T., Weingarth, M., Daniels, M., Boelens, R., Bonvin, A. M., Houben, K., and Baldus, M. (2015) Conformational plasticity of the POTRA 5 domain in the outer membrane protein assembly factor BamA. *Structure (London, England: 1993)* **23**, 1317-1324

188. Han, L., Zheng, J., Wang, Y., Yang, X., Liu, Y., Sun, C., Cao, B., Zhou, H., Ni, D., Lou, J., Zhao, Y., and Huang, Y. (2016) Structure of the BAM complex and its implications for biogenesis of outer-membrane proteins. *Nature Structural and Molecular Biology* **23**, 192-196

189. Yen, Y. T., Tsang, C., Cameron, T. A., Ankrah, D. O., Rodou, A., and Stathopoulos, C. (2010) Importance of conserved residues of the serine protease autotransporter beta-domain in passenger domain processing and beta-barrel assembly. *Infection and Immunity* **78**, 3516-3528

190. Ieva, R., Tian, P., Peterson, J. H., and Bernstein, H. D. (2011) Sequential and spatially restricted interactions of assembly factors with an autotransporter beta domain. *Proceedings of the National Academy of Sciences of the United States of America* **108**, E383-391

191. Pavlova, O., Peterson, J. H., Ieva, R., and Bernstein, H. D. (2013) Mechanistic link between beta barrel assembly and the initiation of autotransporter secretion. *Proceedings of the National Academy of Sciences of the United States of America* **110**, E938-947

192. Bernstein, H. D. (2015) Looks can be deceiving: recent insights into the mechanism of protein secretion by the autotransporter pathway. *Molecular Microbiology* **97**, 205-215

193. Gruss, F., Zahringer, F., Jakob, R. P., Burmann, B. M., Hiller, S., and Maier, T. (2013) The structural basis of autotransporter translocation by TamA. *Nature Structural and Molecular Biology* **20**, 1318-1320

194. Heinz, E., Selkrig, J., Belousoff, M. J., and Lithgow, T. (2015) Evolution of the translocation and assembly module (TAM). *Genome Biology and Evolution* **7**, 1628-1643

195. Dautin, N., Barnard, T. J., Anderson, D. E., and Bernstein, H. D. (2007) Cleavage of a bacterial autotransporter by an evolutionarily convergent autocatalytic mechanism. *The European Molecular Biology Organization Journal* **26**, 1942-1952

196. Charbonneau, M. E., Janvore, J., and Mourez, M. (2009) Autoprocessing of the *Escherichia coli* AIDA-I autotransporter: a new mechanism involving acidic residues in the junction region. *The Journal of Biological Chemistry* **284**, 17340-17351

197. Shere, K. D., Sallustio, S., Manessis, A., D'Aversa, T. G., and Goldberg, M. B. (1997) Disruption of IcsP, the major Shigella protease that cleaves IcsA, accelerates actin-based motility. *Molecular Microbiology* **25**, 451-462

198. Kenjale, R., Meng, G., Fink, D. L., Juehne, T., Ohashi, T., Erickson, H. P., Waksman, G., and St Geme, J. W., 3rd. (2009) Structural determinants of autoproteolysis of the *Haemophilus influenzae* Hap autotransporter. *Infection and Immunity* **77**, 4704-4713

199. Jain, S., van Ulsen, P., Benz, I., Schmidt, M. A., Fernandez, R., Tommassen, J., and Goldberg, M. B. (2006) Polar localization of the autotransporter family of large bacterial virulence proteins. *Journal of Bacteriology* **188**, 4841-4850

200. Charles, M., Perez, M., Kobil, J. H., and Goldberg, M. B. (2001) Polar targeting of Shigella virulence factor IcsA in Enterobacteriacae and Vibrio. *Proceedings of the National Academy of Sciences of the United States of America* **98**, 9871-9876

201. Brandon, L. D., Goehring, N., Janakiraman, A., Yan, A. W., Wu, T., Beckwith, J., and Goldberg, M. B. (2003) IcsA, a polarly localized autotransporter with an atypical signal peptide, uses the Sec apparatus for secretion, although the Sec apparatus is circumferentially distributed. *Molecular Microbiology* **50**, 45-60

202. Doyle, M. T., Grabowicz, M., May, K. L., and Morona, R. (2015) Lipopolysaccharide surface structure does not influence IcsA polarity. *Federation of European Microbiological Societies Microbiology Letters* **362**, fnv042

203. Janakiraman, A., Fixen, K. R., Gray, A. N., Niki, H., and Goldberg, M. B. (2009) A genome-scale proteomic screen identifies a role for DnaK in chaperoning of polar autotransporters in Shigella. *Journal of Bacteriology* **191**, 6300-6311

204. Fixen, K. R., Janakiraman, A., Garrity, S., Slade, D. J., Gray, A. N., Karahan, N., Hochschild, A., and Goldberg, M. B. (2012) Genetic reporter system for positioning of proteins at the bacterial pole. *American Society for Microbiology* **3**

205. Greenfield, D., McEvoy, A. L., Shroff, H., Crooks, G. E., Wingreen, N. S., Betzig, E., and Liphardt, J. (2009) Self-organization of the *Escherichia coli* chemotaxis network imaged with super-resolution light microscopy. *Public Library of Science Biology* **7**, e1000137

206. Davis, B. M., and Waldor, M. K. (2013) Establishing polar identity in gram-negative rods. *Current Opinion in Microbiology* **16**, 752-759

207. Cowles, K. N., and Gitai, Z. (2010) Surface association and the MreB cytoskeleton regulate pilus production, localization and function in *Pseudomonas aeruginosa*. *Molecular Microbiology* **76**, 1411-1426

208. Nilsen, T., Yan, A. W., Gale, G., and Goldberg, M. B. (2005) Presence of multiple sites containing polar material in spherical *Escherichia coli* cells that lack MreB. *Journal of Bacteriology* **187**, 6187-6196

209. Gitai, Z., Dye, N., and Shapiro, L. (2004) An actin-like gene can determine cell polarity in bacteria. *Proceedings of the National Academy of Sciences of the United States of America* **101**, 8643-8648

210. Shih, Y. L., Kawagishi, I., and Rothfield, L. (2005) The MreB and Min cytoskeletal-like systems play independent roles in prokaryotic polar differentiation. *Molecular Microbiology* **58**, 917-928

211. Wagner, J. K., Galvani, C. D., and Brun, Y. V. (2005) *Caulobacter crescentus* requires RodA and MreB for stalk synthesis and prevention of ectopic pole formation. *Journal of Bacteriology* **187**, 544-553

212. Garner, E. C., Bernard, R., Wang, W., Zhuang, X., Rudner, D. Z., and Mitchison, T. (2011) Coupled, circumferential motions of the cell wall synthesis machinery and MreB filaments in *B. subtilis*. *Science (New York)* **333**, 222-225

213. van Teeffelen, S., Wang, S., Furchtgott, L., Huang, K. C., Wingreen, N. S., Shaevitz, J. W., and Gitai, Z. (2011) The bacterial actin MreB rotates, and rotation depends on cell-wall

assembly. *Proceedings of the National Academy of Sciences of the United States of America* **108**, 15822-15827

214. van Teeffelen, S., and Gitai, Z. (2011) Rotate into shape: MreB and bacterial morphogenesis. *The European Molecular Biology Organization Journal* **30**, 4856-4857

215. Carballido-Lopez, R. (2006) The bacterial actin-like cytoskeleton. *Microbiology and Molecular Biology Reviews* **70**, 888-909

216. Shaevitz, J. W., and Gitai, Z. (2010) The structure and function of bacterial actin homologs. *Cold Spring Harbor Perspectives in Biology* **2**, a000364

217. Strahl, H., Burmann, F., and Hamoen, L. W. (2014) The actin homologue MreB organizes the bacterial cell membrane. *Nature Communications* **5**, 3442

218. Oswald, F., Varadarajan, A., Lill, H., Peterman, E. J., and Bollen, Y. J. (2016) MreB-dependent organization of the *E. coli* cytoplasmic membrane controls membrane protein diffusion. *Biophysical Journal* **110**, 1139-1149

219. Kruse, T., Bork-Jensen, J., and Gerdes, K. (2005) The morphogenetic MreBCD proteins of *Escherichia coli* form an essential membrane-bound complex. *Molecular Microbiology* **55**, 78-89

220. Vats, P., Shih, Y. L., and Rothfield, L. (2009) Assembly of the MreB-associated cytoskeletal ring of *Escherichia coli*. *Molecular Microbiology* **72**, 170-182

221. Salje, J., van den Ent, F., de Boer, P., and Lowe, J. (2011) Direct membrane binding by bacterial actin MreB. *Molecular Cell* **43**, 478-487

222. Bendezu, F. O., Hale, C. A., Bernhardt, T. G., and de Boer, P. A. (2009) RodZ (YfgA) is required for proper assembly of the MreB actin cytoskeleton and cell shape in *E. coli*. *The European Molecular Biology Organization Journal* **28**, 193-204

223. van den Ent, F., Johnson, C. M., Persons, L., de Boer, P., and Lowe, J. (2010) Bacterial actin MreB assembles in complex with cell shape protein RodZ. *The European Molecular Biology Organization Journal* **29**, 1081-1090

224. Alyahya, S. A., Alexander, R., Costa, T., Henriques, A. O., Emonet, T., and Jacobs-Wagner, C. (2009) RodZ, a component of the bacterial core morphogenic apparatus. *Proceedings of the National Academy of Sciences of the United States of America* **106**, 1239-1244

225. Shiomi, D. (2014) Regulation of determination of bacterial shape. *Nihon saikingaku zasshi. Japanese Journal of Bacteriology* **69**, 557-564

226. Gerdes, K. (2009) RodZ, a new player in bacterial cell morphogenesis. *The European Molecular Biology Organization Journal* **28**, 171-172

227. van den Ent, F., Izore, T., Bharat, T. A., Johnson, C. M., and Lowe, J. (2014) Bacterial actin MreB forms antiparallel double filaments. *eLife* **3**, e02634

228. Celler, K., Koning, R. I., Koster, A. J., and van Wezel, G. P. (2013) Multidimensional view of the bacterial cytoskeleton. *Journal of Bacteriology* **195**, 1627-1636

229. Kim, S. Y., Gitai, Z., Kinkhabwala, A., Shapiro, L., and Moerner, W. E. (2006) Single molecules of the bacterial actin MreB undergo directed treadmilling motion in *Caulobacter crescentus*. *Proceedings of the National Academy of Sciences of the United States of America* **103**, 10929-10934

230. Defeu Soufo, H. J., and Graumann, P. L. (2006) Dynamic localization and interaction with other *Bacillus subtilis* actin-like proteins are important for the function of MreB. *Molecular Microbiology* **62**, 1340-1356

231. Dominguez-Escobar, J., Chastanet, A., Crevenna, A. H., Fromion, V., Wedlich-Soldner, R., and Carballido-Lopez, R. (2011) Processive movement of MreB-associated cell wall biosynthetic complexes in bacteria. *Science (New York)* **333**, 225-228

232. Vollmer, W., and Seligman, S. J. (2010) Architecture of peptidoglycan: more data and more models. *Trends in Microbiology* **18**, 59-66

233. Typas, A., Banzhaf, M., Gross, C. A., and Vollmer, W. (2012) From the regulation of peptidoglycan synthesis to bacterial growth and morphology. *Nature Reviews. Microbiology* **10**, 123-136

234. Campo, N., Tjalsma, H., Buist, G., Stepniak, D., Meijer, M., Veenhuis, M., Westermann, M., Muller, J. P., Bron, S., Kok, J., Kuipers, O. P., and Jongbloed, J. D. (2004) Subcellular sites for bacterial protein export. *Molecular Microbiology* **53**, 1583-1599

235. Shiomi, D., Yoshimoto, M., Homma, M., and Kawagishi, I. (2006) Helical distribution of the bacterial chemoreceptor via colocalization with the Sec protein translocation machinery. *Molecular Microbiology* **60**, 894-906

236. Cougnoux, A., Gibold, L., Robin, F., Dubois, D., Pradel, N., Darfeuille-Michaud, A., Dalmasso, G., Delmas, J., and Bonnet, R. (2012) Analysis of structure-function relationships in the colibactin-maturating enzyme ClbP. *Journal of Molecular Biology* **424**, 203-214

237. Margolin, W. (2012) The price of tags in protein localization studies. *Journal of Bacteriology* **194**, 6369-6371

238. Swulius, M. T., and Jensen, G. J. (2012) The helical MreB cytoskeleton in *Escherichia coli* MC1000/pLE7 is an artifact of the N-Terminal yellow fluorescent protein tag. *Journal of Bacteriology* **194**, 6382-6386

239. Swulius, M. T., Chen, S., Jane Ding, H., Li, Z., Briegel, A., Pilhofer, M., Tocheva, E. I., Lybarger, S. R., Johnson, T. L., Sandkvist, M., and Jensen, G. J. (2011) Long helical filaments are not seen encircling cells in electron cryotomograms of rod-shaped bacteria. *Biochemical and Biophysical Research Communications* **407**, 650-655

240. Olshausen, P. V., Defeu Soufo, H. J., Wicker, K., Heintzmann, R., Graumann, P. L., and Rohrbach, A. (2013) Superresolution imaging of dynamic MreB filaments in *B. subtilis*--a multiple-motor-driven transport? *Biophysical Journal* **105**, 1171-1181

241. Turner, R. D., Hurd, A. F., Cadby, A., Hobbs, J. K., and Foster, S. J. (2013) Cell wall elongation mode in Gram-negative bacteria is determined by peptidoglycan architecture. *Nature Communications* **4**, 1496

242. Errington, J. (2015) Bacterial morphogenesis and the enigmatic MreB helix. *Nature Reviews. Microbiology* **13**, 241-248

243. Sambrook, J. F., Fritsch, E. F., and Maniatis, T. (1989) *Molecular Cloning: A Laboratory Manual,* 2nd ed., Cold Spring Harbor Laboratory Press, Cold Spring Harbor, NY.

244. Jensen, K. F. (1993) The *Escherichia coli* K-12 "wild types" W3110 and MG1655 have an *rph* frameshift mutation that leads to pyrimidine starvation due to low *pyrE* expression levels. *Journal of Bacteriology* **175**, 3401-3407

245. Oliver, D. B., and Beckwith, J. (1981) *E. coli* mutant pleiotropically defective in the export of secreted proteins. *Cell* **25**, 765-772

246. Arnold, L. (2003) Characterisation of factors involved in the secretion of EspC in enteropathogenic *E. coli*. PhD thesis. The University of Nottingham.

247. Ashawesh, M. (2007) Tracking autotransporter secretion with fluorescent tags. MSc dissertation. The University of Nottingham

248. Neumann, H., Peak-Chew, S. Y., and Chin, J. W. (2008) Genetically encoding N(epsilon)-acetyllysine in recombinant proteins. *Nature Chemical Biology* **4**, 232-234

249. Nguyen, D. P., Lusic, H., Neumann, H., Kapadnis, P. B., Deiters, A., and Chin, J. W. (2009) Genetic encoding and labeling of aliphatic azides and alkynes in recombinant proteins via a pyrrolysyl-tRNA Synthetase/tRNA(CUA) pair and click chemistry. *Journal of The American Chemical Society* **131**, 8720-8721

250. Chin, J. W., Martin, A. B., King, D. S., Wang, L., and Schultz, P. G. (2002) Addition of a photocrosslinking amino acid to the genetic code of *Escherichia coli*. *Proceedings of The National Academy of Sciences of the United States of America* **99**, 11020-11024

251. Saiki, R. K., Gelfand, D. H., Stoffel, S., Scharf, S. J., Higuchi, R., Horn, G. T., Mullis, K. B., and Erlich, H. A. (1988) Primer-directed enzymatic amplification of DNA with a thermostable DNA polymerase. *Science (New York, N.Y.)* **239**, 487-491

252. Cooksley, C., Jenks, P. J., Green, A., Cockayne, A., Logan, R. P., and Hardie, K. R. (2003) NapA protects *Helicobacter pylori* from oxidative stress damage, and its production is influenced by the ferric uptake regulator. *Journal of Medical Microbiolog* **52**, 461-469

253. Hardie, K. R., Lory, S., and Pugsley, A. P. (1996) Insertion of an outer membrane protein in *Escherichia coli* requires a chaperone-like protein. *The European Molecular Biology Organization Journal* **15**, 978-988

254. Gitai, Z., Dye, N. A., Reisenauer, A., Wachi, M., and Shapiro, L. (2005) MreB actin-mediated segregation of a specific region of a bacterial chromosome. *Cell* **120**, 329-341

255. Shemiakina, II, Ermakova, G. V., Cranfill, P. J., Baird, M. A., Evans, R. A., Souslova, E. A., Staroverov, D. B., Gorokhovatsky, A. Y., Putintseva, E. V., Gorodnicheva, T. V., Chepurnykh, T. V., Strukova, L., Lukyanov, S., Zaraisky, A. G., Davidson, M. W., Chudakov, D. M., and Shcherbo, D. (2012) A monomeric red fluorescent protein with low cytotoxicity. *Nature Communications* **3**, 1204

256. Chudakov, D. M., Matz, M. V., Lukyanov, S., and Lukyanov, K. A. (2010) Fluorescent proteins and their applications in imaging living cells and tissues. *Physiological Reviews* **90**, 1103-1163

257. Rao, C. V. S., De Waelheyns, E., Economou, A., and Anne, J. (2014) Antibiotic targeting of the bacterial secretory pathway. *Biochimica et Biophysica acta* **1843**, 1762-1783

258. Fan, J. Y., Cui, Z. Q., Wei, H. P., Zhang, Z. P., Zhou, Y. F., Wang, Y. P., and Zhang, X. E. (2008) Split mCherry as a new red bimolecular fluorescence complementation system for visualizing protein-protein interactions in living cells. *Biochemical and Biophysical Research Communications* **367**, 47-53

259. Shaner, N. C., Campbell, R. E., Steinbach, P. A., Giepmans, B. N., Palmer, A. E., and Tsien, R. Y. (2004) Improved monomeric red, orange and yellow fluorescent proteins derived from *Discosoma* sp. red fluorescent protein. *Nature Biotechnology* **22**, 1567-1572

260. Tikhonova, E. B., and Zgurskaya, H. I. (2004) AcrA, AcrB, and TolC of *Escherichia coli* form a stable intermembrane multidrug efflux complex. *The Journal of Biological Chemistry* **279**, 32116-32124

261. Kim, J. S., Jeong, H., Song, S., Kim, H. Y., Lee, K., Hyun, J., and Ha, N. C. (2015) Structure of the tripartite multidrug efflux pump AcrAB-TolC suggests an alternative assembly mode. *Molecules and Cells* **38**, 180-186

262. Legaree, B. A., Adams, C. B., and Clarke, A. J. (2007) Overproduction of penicillin-binding protein 2 and its inactive variants causes morphological changes and lysis in *Escherichia coli*. *Journal of Bacteriology* **189**, 4975-4983

263. Bean, G. J., Flickinger, S. T., Westler, W. M., McCully, M. E., Sept, D., Weibel, D. B., and Amann, K. J. (2009) A22 disrupts the bacterial actin cytoskeleton by directly binding and inducing a low-affinity state in MreB. *Biochemistry* **48**, 4852-4857

264. van den Ent, F., Amos, L. A., and Lowe, J. (2001) Prokaryotic origin of the actin cytoskeleton. *Nature* **413**, 39-44

265. Formstone, A., and Errington, J. (2005) A magnesium-dependent mreB null mutant: implications for the role of mreB in *Bacillus subtilis*. *Molecular Microbiology* **55**, 1646-1657

266. Wu, X., Iwai, N., and Chen, W. L. (2011) Effects of S-(3,4-dichlorobenzyl) isothiourea on different cellular events in the cyanobacterium Anabaena sp. strain PCC 7120. *Research in Microbiology* **162**, 375-381

267. McBroom, A. J., and Kuehn, M. J. (2007) Release of outer membrane vesicles by Gram-negative bacteria is a novel envelope stress response. *Molecular Microbiology* **63**, 545-558

268. Zhou, L., Srisatjaluk, R., Justus, D. E., and Doyle, R. J. (1998) On the origin of membrane vesicles in gram-negative bacteria. *Federation of European Microbiological Societies Microbiology Letters* **163**, 223-228

269. Rawat, S., Zhu, L., Lindner, E., Dalbey, R. E., and White, S. H. (2015) SecA drives transmembrane insertion of RodZ, an unusual single-span membrane protein. *Journal of Molecular Biology* **427**, 1023-1037

270. Saier, M. H., Jr., and Bogdanov, M. V. (2013) Membranous organelles in bacteria. *Journal of Molecular Microbiology and Biotechnology* **23**, 5-12

271. Laloux, G., and Jacobs-Wagner, C. (2014) How do bacteria localize proteins to the cell pole? *Journal of Cell Science* **127**, 11-19

272. White, C. L., Kitich, A., and Gober, J. W. (2010) Positioning cell wall synthetic complexes by the bacterial morphogenetic proteins MreB and MreD. *Molecular Microbiology* **76**, 616-633

273. Iwai, N., Nagai, K., and Wachi, M. (2002) Novel S-benzylisothiourea compound that induces spherical cells in *Escherichia coli* probably by acting on a rod-shape-determining protein(s) other than penicillin-binding protein 2. *Bioscience, Biotechnology and Biochemistry* **66**, 2658-2662

274. Ramamurthi, K. S., and Losick, R. (2009) Negative membrane curvature as a cue for subcellular localization of a bacterial protein. *Proceedings of the National Academy of Sciences of the United States of America* **106**, 13541-13545

275. Nikic, I., Plass, T., Schraidt, O., Szymanski, J., Briggs, J. A., Schultz, C., and Lemke, E. A. (2014) Minimal tags for rapid dual-color live-cell labeling and super-resolution microscopy. *Angewandte Chemie (International ed. in English)* **53**, 2245-2249

276. Plass, T., Milles, S., Koehler, C., Szymanski, J., Mueller, R., Wiessler, M., Schultz, C., and Lemke, E. A. (2012) Amino acids for Diels-Alder reactions in living cells. *Angewandte Chemie (International ed. in English)* **51**, 4166-4170

277. Plass, T., Milles, S., Koehler, C., Schultz, C., and Lemke, E. A. (2011) Genetically encoded copper-free click chemistry. *Angewandte Chemie (International ed. in English)* **50**, 3878-3881

278. Lang, K., Davis, L., Torres-Kolbus, J., Chou, C., Deiters, A., and Chin, J. W. (2012) Genetically encoded norbornene directs site-specific cellular protein labelling via a rapid bioorthogonal reaction. *Nature Chemistry* **4**, 298-304

279. Summerer, D., Chen, S., Wu, N., Deiters, A., Chin, J. W., and Schultz, P. G. (2006) A genetically encoded fluorescent amino acid. *Proceedings of the National Academy of Sciences of the United States of America* **103**, 9785-9789

280. Wals, K., and Ovaa, H. (2014) Unnatural amino acid incorporation in *E. coli*: current and future applications in the design of therapeutic proteins. *Frontiers in Chemistry* **2**, 15

281. Ramil, C. P., and Lin, Q. (2013) Bioorthogonal chemistry: strategies and recent developments. *Chemical Communications (Cambridge, England)* **49**, 11007-11022

282. Liu, D. R., Magliery, T. J., Pastrnak, M., and Schultz, P. G. (1997) Engineering a tRNA and aminoacyl-tRNA synthetase for the site-specific incorporation of unnatural amino acids into proteins *in vivo*. *Proceedings of the National Academy of Sciences of the United States of America* **94**, 10092-10097

283. Wang, L., and Schultz, P. G. (2001) A general approach for the generation of orthogonal tRNAs. *Chemistry and Biology* **8**, 883-890

284. Krueger, A. T., and Imperiali, B. (2013) Fluorescent amino acids: modular building blocks for the assembly of new tools for chemical biology. *Chembiochem: a European Journal of Chemical Biology* **14**, 788-799

285. Schneider, S., Gattner, M. J., Vrabel, M., Flugel, V., Lopez-Carrillo, V., Prill, S., and Carell, T. (2013) Structural insights into incorporation of norbornene amino acids for click modification of proteins. *Chembiochem: a European Journal of Chemical Biology* **14**, 2114-2118

286. Nozawa, K., O'Donoghue, P., Gundllapalli, S., Araiso, Y., Ishitani, R., Umehara, T., Soll, D., and Nureki, O. (2009) Pyrrolysyl-tRNA synthetase-tRNA(Pyl) structure reveals the molecular basis of orthogonality. *Nature* **457**, 1163-1167

287. Krzycki, J. A. (2005) The direct genetic encoding of pyrrolysine. *Current Opinion in Microbiology* **8**, 706-712

288. Blight, S. K., Larue, R. C., Mahapatra, A., Longstaff, D. G., Chang, E., Zhao, G., Kang, P. T., Green-Church, K. B., Chan, M. K., and Krzycki, J. A. (2004) Direct charging of tRNA(CUA) with pyrrolysine *in vitro* and *in vivo*. *Nature* **431**, 333-335

289. Liu, C. C., and Schultz, P. G. (2010) Adding new chemistries to the genetic code. *Annual Review of Biochemistry* **79**, 413-444

290. Yanagisawa, T., Ishii, R., Fukunaga, R., Kobayashi, T., Sakamoto, K., and Yokoyama, S. (2008) Multistep engineering of pyrrolysyl-tRNA synthetase to genetically encode N(epsilon)-(o-azidobenzyloxycarbonyl) lysine for site-specific protein modification. *Chemistry and Biology* **15**, 1187-1197

291. Lukinavicius, G., Umezawa, K., Olivier, N., Honigmann, A., Yang, G., Plass, T., Mueller, V., Reymond, L., Correa, I. R., Jr., Luo, Z. G., Schultz, C., Lemke, E. A., Heppenstall, P., Eggeling, C., Manley, S., and Johnsson, K. (2013) A near-infrared fluorophore for live-cell super-resolution microscopy of cellular proteins. *Nature Chemistry* **5**, 132-139

292. Nikic, I., and Lemke, E. A. (2015) Genetic code expansion enabled site-specific dual-color protein labeling: superresolution microscopy and beyond. *Current Opinion in Chemical Biology* **28**, 164-173

293. Blackman, M. L., Royzen, M., and Fox, J. M. (2008) Tetrazine ligation: fast bioconjugation based on inverse-electron-demand Diels-Alder reactivity. *Journal of The American Chemical Society* **130**, 13518-13519

294. Devaraj, N. K., Weissleder, R., and Hilderbrand, S. A. (2008) Tetrazine-based cycloadditions: application to pretargeted live cell imaging. *Bioconjugate Chemistry* **19**, 2297-2299

295. Gahlmann, A., and Moerner, W. E. (2014) Exploring bacterial cell biology with single-molecule tracking and super-resolution imaging. *Nature Reviews Microbiology* **12**, 9-22

296. Landgraf, D., Okumus, B., Chien, P., Baker, T. A., and Paulsson, J. (2012) Segregation of molecules at cell division reveals native protein localization. *Nature Methods* **9**, 480-482

297. Griffin, B. A., Adams, S. R., and Tsien, R. Y. (1998) Specific covalent labeling of recombinant protein molecules inside live cells. *Science (New York, N.Y.)* **281**, 269-272

298. Griffin, B. A., Adams, S. R., Jones, J., and Tsien, R. Y. (2000) Fluorescent labeling of recombinant proteins in living cells with FlAsH. *Methods in Enzymology* **327**, 565-578

299. Hoffmann, C., Gaietta, G., Zurn, A., Adams, S. R., Terrillon, S., Ellisman, M. H., Tsien, R. Y., and Lohse, M. J. (2010) Fluorescent labeling of tetracysteine-tagged proteins in intact cells. *Nature Protocols* **5**, 1666-1677

300. Crivat, G., Tokumasu, F., Sa, J. M., Hwang, J., and Wellems, T. E. (2011) Tetracysteine-based fluorescent tags to study protein localization and trafficking in Plasmodium falciparum-infected erythrocytes. *Public Library of Science one* **6**, e22975

301. Estevez, J. M., and Somerville, C. (2006) FlAsH-based live-cell fluorescent imaging of synthetic peptides expressed in Arabidopsis and tobacco. *BioTechniques* **41**, 569-570, 572-564

302. Cabeen, M. T., Charbon, G., Vollmer, W., Born, P., Ausmees, N., Weibel, D. B., and Jacobs-Wagner, C. (2009) Bacterial cell curvature through mechanical control of cell growth. *The European Molecular Biology Organization Journal* **28**, 1208-1219

303. Cabeen, M. T., Murolo, M. A., Briegel, A., Bui, N. K., Vollmer, W., Ausmees, N., Jensen, G. J., and Jacobs-Wagner, C. (2010) Mutations in the Lipopolysaccharide biosynthesis pathway interfere with crescentin-mediated cell curvature in *Caulobacter crescentus*. *Journal of Bacteriology* **192**, 3368-3378

304. Hoffmann, C., Gaietta, G., Bunemann, M., Adams, S. R., Oberdorff-Maass, S., Behr, B., Vilardaga, J. P., Tsien, R. Y., Ellisman, M. H., and Lohse, M. J. (2005) A FlAsH-based FRET approach to determine G protein-coupled receptor activation in living cells. *Nature Methods* **2**, 171-176

305. Gaietta, G., Deerinck, T. J., Adams, S. R., Bouwer, J., Tour, O., Laird, D. W., Sosinsky, G. E., Tsien, R. Y., and Ellisman, M. H. (2002) Multicolor and electron microscopic imaging of connexin trafficking. *Science (New York, N.Y.)* **296**, 503-507

306. Adams, S. R., Campbell, R. E., Gross, L. A., Martin, B. R., Walkup, G. K., Yao, Y., Llopis, J., and Tsien, R. Y. (2002) New biarsenical ligands and tetracysteine motifs for protein labeling *in vitro* and *in vivo*: synthesis and biological applications. *Journal of the American Chemical Society* **124**, 6063-6076

307. Ignatova, Z., and Gierasch, L. M. (2004) Monitoring protein stability and aggregation *in vivo* by real-time fluorescent labeling. *Proceedings of the National Academy of Sciences of the United States of America* **101**, 523-528

308. Stroffekova, K., Proenza, C., and Beam, K. G. (2001) The protein-labeling reagent FLASH-EDT2 binds not only to CCXXCC motifs but also non-specifically to endogenous cysteine-rich proteins. *Pflugers Archiv: European Journal of Physiology* **442**, 859-866

309. Crivat, G., and Taraska, J. W. (2012) Imaging proteins inside cells with fluorescent tags. *Trends in Biotechnology* **30**, 8-16

310. Yang, H., He, J., Hu, F., Zheng, C., and Yu, Z. (2010) Detection of *Escherichia coli* enoyl-ACP reductase using biarsenical-tetracysteine motif. *Bioconjugate Chemistry* **21**, 1341-1348

311. Adams, S. R., and Tsien, R. Y. (2008) Preparation of the membrane-permeant biarsenicals FlAsH-EDT2 and ReAsH-EDT2 for fluorescent labeling of tetracysteine-tagged proteins. *Nature Protocols* **3**, 1527-1534

312. Romantsov, T., Battle, A. R., Hendel, J. L., Martinac, B., and Wood, J. M. (2010) Protein localization in *Escherichia coli* cells: comparison of the cytoplasmic membrane proteins ProP, LacY, ProW, AqpZ, MscS, and MscL. *Journal of Bacteriology* **192**, 912-924

313. Madani, F., Lind, J., Damberg, P., Adams, S. R., Tsien, R. Y., and Graslund, A. O. (2009) Hairpin structure of a biarsenical-tetracysteine motif determined by NMR spectroscopy. *Journal of the American Chemical Society* **131**, 4613-4615

314. Paredes-Osses, E. (2014) A novel virulence strategy for *Pseudomonas aeruginosa* mediated by an autotransporter with arginine-specific aminopeptidase activity. The Universtiy of Nottingham

315. Tuson, H. H., and Biteen, J. S. (2015) Unveiling the inner workings of live bacteria using super-resolution microscopy. *Analytical Chemistry* **87**, 42-63

316. Ishitsuka, Y., Nienhaus, K., and Nienhaus, G. U. (2014) Photoactivatable fluorescent proteins for super-resolution microscopy. *Methods in Molecular Biology (Clifton, N.J.)* **1148**, 239-260

317. Kruse, T., Moller-Jensen, J., Lobner-Olesen, A., and Gerdes, K. (2003) Dysfunctional MreB inhibits chromosome segregation in *Escherichia coli*. *The European Molecular Biology Organization Journal* **22**, 5283-5292

318. Uttamapinant, C., White, K. A., Baruah, H., Thompson, S., Fernandez-Suarez, M., Puthenveetil, S., and Ting, A. Y. (2010) A fluorophore ligase for site-specific protein labeling inside living cells. *Proceedings of the National Academy of Sciences of the United States of America* **107**, 10914-10919

319. Hinner, M. J., and Johnsson, K. (2010) How to obtain labeled proteins and what to do with them. *Current Opinion in Biotechnology* **21**, 766-776

320. Martin, B. R., Giepmans, B. N., Adams, S. R., and Tsien, R. Y. (2005) Mammalian cell-based optimization of the biarsenical-binding tetracysteine motif for improved fluorescence and affinity. *Nature Biotechnology* **23**, 1308-1314

321. Gaietta, G. M., Giepmans, B. N., Deerinck, T. J., Smith, W. B., Ngan, L., Llopis, J., Adams, S. R., Tsien, R. Y., and Ellisman, M. H. (2006) Golgi twins in late mitosis revealed by genetically encoded tags for live cell imaging and correlated electron microscopy. *Proceedings of the National Academy of Sciences of the United States of America* **103**, 17777-17782

322. Zurn, A., Klenk, C., Zabel, U., Reiner, S., Lohse, M. J., and Hoffmann, C. (2010) Site-specific, orthogonal labeling of proteins in intact cells with two small biarsenical fluorophores. *Bioconjugate Chemistry* **21**, 853-859

323. Guzman, L. M., Belin, D., Carson, M. J., and Beckwith, J. (1995) Tight regulation, modulation, and high-level expression by vectors containing the arabinose PBAD promoter. *Journal of Bacteriology* **177**, 4121-4130

324. Snapp, E. (2005) Design and use of fluorescent fusion proteins in cell biology. *Current Protocols in Cell Biology / editorial board, Juan S. Bonifacino ... [et al.]* **Chapter 21**, Unit 21 24

325. Wagner, S., Baars, L., Ytterberg, A. J., Klussmeier, A., Wagner, C. S., Nord, O., Nygren, P. A., van Wijk, K. J., and de Gier, J. W. (2007) Consequences of membrane protein overexpression in *Escherichia coli*. *Molecular & Cellular Proteomics : MCP* **6**, 1527-1550

326. Wagner, S., Bader, M. L., Drew, D., and de Gier, J. W. (2006) Rationalizing membrane protein overexpression. *Trends in Biotechnology* **24**, 364-371

327. Roman-Hernandez, G., Peterson, J. H., and Bernstein, H. D. (2014) Reconstitution of bacterial autotransporter assembly using purified components. *eLife* **3**, e04234

328. Ieva, R., and Bernstein, H. D. (2009) Interaction of an autotransporter passenger domain with BamA during its translocation across the bacterial outer membrane. *Proceedings of the National Academy of Sciences of the United States of America* **106**, 19120-19125

329. Huttner, A., Harbarth, S., Carlet, J., Cosgrove, S., Goossens, H., Holmes, A., Jarlier, V., Voss, A., and Pittet, D. (2013) Antimicrobial resistance: a global view from the 2013 World Healthcare-Associated Infections Forum. *Antimicrobial Resistance and Infection Control* **2**, 31

330. WHO. (2014) Antimicrobial resistance: global report on surveillance.

331. Wells, T. J., Tree, J. J., Ulett, G. C., and Schembri, M. A. (2007) Autotransporter proteins: novel targets at the bacterial cell surface. *Federation of European Microbiological Societies Microbiology Letters* **274**, 163-172

332. Jong, W. S., Soprova, Z., de Punder, K., ten Hagen-Jongman, C. M., Wagner, S., Wickstrom, D., de Gier, J. W., Andersen, P., van der Wel, N. N., and Luirink, J. (2012) A structurally informed autotransporter platform for efficient heterologous protein secretion and display. *Microbial Cell Factories* **11**, 85

333. Samo, M., Choudhary, N. R., Riebe, K. J., Shterev, I., Staats, H. F., Sempowski, G. D., and Leduc, I. (2016) Immunization with the *Haemophilus ducreyi* trimeric autotransporter adhesin DsrA with alum, CpG or imiquimod generates a persistent humoral immune response that recognizes the bacterial surface. *Vaccine* **34**, 1193-1200

334. Bentancor, L. V., Routray, A., Bozkurt-Guzel, C., Camacho-Peiro, A., Pier, G. B., and Maira-Litran, T. (2012) Evaluation of the trimeric autotransporter Ata as a vaccine candidate against *Acinetobacter baumannii* infections. *Infection and Immunity* **80**, 3381-3388

335. Hjelm, A., Soderstrom, B., Vikstrom, D., Jong, W. S., Luirink, J., and de Gier, J. W. (2015) Autotransporter-based antigen display in bacterial ghosts. *Applied and Environmental Microbiology* **81**, 726-735

336. Jong, W. S., Daleke-Schermerhorn, M. H., Vikstrom, D., Ten Hagen-Jongman, C. M., de Punder, K., van der Wel, N. N., van de Sandt, C. E., Rimmelzwaan, G. F., Follmann, F., Agger, E. M., Andersen, P., de Gier, J. W., and Luirink, J. (2014) An autotransporter display platform for the development of multivalent recombinant bacterial vector vaccines. *Microbial Cell Factories* **13**, 162

337. Kleanthous, C., Rassam, P., and Baumann, C. G. (2015) Protein-protein interactions and the spatiotemporal dynamics of bacterial outer membrane proteins. *Current Opinion in Structural Biology* **35**, 109-115

338. Rassam, P., Copeland, N. A., Birkholz, O., Toth, C., Chavent, M., Duncan, A. L., Cross, S. J., Housden, N. G., Kaminska, R., Seger, U., Quinn, D. M., Garrod, T. J., Sansom, M. S., Piehler, J., Baumann, C. G., and Kleanthous, C. (2015) Supramolecular assemblies underpin turnover of outer membrane proteins in bacteria. *Nature* **523**, 333-336

339. Ursell, T. S., Trepagnier, E. H., Huang, K. C., and Theriot, J. A. (2012) Analysis of surface protein expression reveals the growth pattern of the gram-negative outer membrane. *Public Library of Science Computational Biology* **8**, e1002680

340. Hong, Y., and Reeves, P. R. (2014) Diversity of o-antigen repeat unit structures can account for the substantial sequence variation of wzx translocases. *Journal of Bacteriology* **196**, 1713-1722